Dynamics and Stability of Shock Waves in Granular Gases Undergoing Activated Inelastic Collisions

by

Nick Sirmas

Thesis submitted in partial fulfillment
of the requirements for the
PhD in Mechanical Engineering degree

The Ottawa-Carleton Institute for Mechanical and Aerospace Engineering
Faculty of Engineering
University of Ottawa

© Nick Sirmas, Ottawa, Canada, 2017

Abstract

The present work investigates the dynamics and stability of shock waves in granular gases. The problem was modelled for a piston propagating into a system of disks that can undergo inelastic collisions if an impact threshold is exceeded. The model was addressed numerically at the microscopic and macroscopic levels. The molecular dynamics methodology employed the Event-Driven Molecular Dynamics method, and the continuum model was formulated using the Navier-Stokes equations for granular gases with the transport terms of Jenkins and Richman and a modified cooling rate term.

The inviscid steady state shock structure was derived and analyzed. The results indicated that a relaxing shock structure is expected for sufficiently strong shock waves. Beyond this limit the structure was shown to be independent of the initial energy, a finding similar to the strong shock approximation in molecular gases.

One-dimensional simulations demonstrated that the molecular dynamics and continuum models yield similar evolutions and structures of the shock wave, validating the continuum description of this study. Two-dimensional results showed that sufficiently strong shock waves can exhibit multi-dimensional instability with high density non-uniformities and convective rolls within the structure, with the size of instabilities shown to scale with the relaxation length of the shock structure. Instabilities were observed with the continuum description *only* with the inclusion of statistical fluctuations to density mimicking the molecular model. The cases that were unstable were shown to be in a regime whereby statistical fluctuations can become important, following the description for this regime by Bird.

Based on these findings, it is proposed that unstable shock behaviour can be observed for highly dissipative shock waves that yield short relaxation length scales, where fluctuations become important. The current work may shed light on unstable shock behaviour observed in dissipative gases, having implications for both granular media and molecular gases.

Acknowledgements

The author would like to thank his supervisor, Dr. Matei Radulescu, for his guidance and support throughout the duration of the project. His mentoring has played a significant role in the completion of the current work and in the author's development within the field.

The author would also like to acknowledge and thank his fellow graduate students at the University of Ottawa for their input and help.

Funding for the work presented in this thesis has been provided by the Natural Sciences and Engineering Research Council of Canada (NSERC) via the Alexander Graham Bell Scholarship, and from the Ontario Ministry of Training, Colleges and Universities via an Ontario Graduate Scholarship.

Dedication

This work is dedicated to my family, friends, and four-legged pals for their patience, support and understanding during this process.

Contents

List of Figures

Nomenclature

Roman Symbols

A	Area of domain
c	Sound speed
D	Velocity of shock wave
d	Diameter of particle
dx	Side length for square perturbations
e	Specific internal energy
e_{tot}	Specific total energy
E_{A}	Activation energy
g_2	Pair correlation function
k	Boltzmann constant
l_{R}	Relaxation length scale
L_x	Length of domain in x-direction
L_y	Length of domain in y-direction
M	Mach number
m	Mass of particle
N	Number of particles
n	Number density of particles
q	Heat flux
T	Temperature
u	Velocity of entity
u^*	Activation impact velocity threshold
V	Volume of domain
v	Specific volume

x x-coordinate of entity

y y-coordinate of entity

Z Compressibility factor

z Position in shock fixed frame of reference

Greek Symbols

Δ Resolution at the finest scale after refinement

δ Mean spacing between particles

ε Coefficient of restitution

γ Isentropic exponent

η Packing factor, $\eta = \frac{\pi d^2 n}{4}$

κ Thermal conductivity

λ Mean free path

μ_2 Shear viscosity

μ_1 Bulk viscosity

ρ Density

σ Standard deviation for statistical fluctuations

τ Mean free time

θ Thermicity

ψ Shock strength parameter

ζ Cooling rate

Superscripts

$\tilde{(\,)}$ Dimensional term

Subscripts

$(\,)_{\mathrm{o}}$ Initial state

$(\,)_{\infty}$ Equilibrated shocked state

$(\,)_{\mathrm{i}}$ Property of ith particle

$(\,)_{\mathrm{p}}$ Property of piston

$(\,)_{\mathrm{rms}}$ Root mean squared

$(\,)_{\mathrm{s}}$ Shocked state

$(\,)_{\mathrm{x}}$ Property in x-direction

$(\,)_{\mathrm{y}}$ Property in y-direction

Acronyms

MD Molecular Dynamics

N-S Navier-Stokes

Chapter 1

Introduction

1.1 Shock Waves in Granular Media

A granular medium is a system of solid, macroscopic sized particles that undergo dissipative collisions. When looking at large systems of granular particles, granular materials are complex, as they can exhibit solid, liquid and gaseous behaviour [1]. Due to the dissipative nature of the medium, some type of energy input is necessary for the flow to become fluidized. This may be accomplished by gravity acting on particles that are free to move, (e.g., an avalanche), by agitating the particles, or in multiphase flows with an influential interstitial fluid (i.e., particles within a moving liquid or gas). The understanding of these processes is important, especially in the handling and processing of granular materials in industrial applications, for example, in the handling of ingredients for food processing or pharmaceuticals.

By including a source of energy input, a granular medium may also experience shock-like dynamics. Sharp gradients appear for macroscopic properties, such as the number density and kinetic energy of the particles. Interestingly, cases where shock dynamics are present in granular materials have also been shown to become unstable. The most common example is

in the pattern formation of granular media subjected to a vertically oscillating driver, which has been observed both experimentally and numerically [2, 3]. In this case, the periodic agitation of the container walls drives strong shocks and expansion waves into the non-uniform granular gas. Unstable formations have also been observed for rapid granular flows down a chute, with the front of flow exhibiting finger-like patterns [4, 5]. Experiments have also identified unstable formations of finger-like jets in granular media dispersed by shock waves driven through air [6, 7], although the complex multi-phase dynamics have prevented the authors from clearly identifying the mechanisms controlling the instability. The goal of this thesis is to investigate such instabilities, limiting the study to only the granular gas phase.

Few studies have investigated the classical problem of a piston propagating into a granular gas to study shock wave formation [8, 9]. These studies have addressed the one-dimensional structure and evolution of shock waves driven by a piston into granular gases, as sketched out in Fig. 1.1. For simplicity, these studies model the granular medium as a system composed of smooth, solid particles that interact inelastically, whereby hydrodynamic equations can be obtained [10].

In an early study, Goldshtein *et al.* showed that the steady shock structure in granular media is composed of three distinct regions [8]. The shock structure is shown in Fig. 1.1 for the *granular temperature* of the medium, which represents the kinetic energy of the particles [10]. In such a structure, a piston propagates forward, supporting a shock wave travelling ahead at some velocity D. The first region of the shock structure follows immediately behind the shock front. This region is characterized by a rapid increase in granular temperature which identifies the 'excitation' region (region I). Due to the inelasticity and increased rate of collisions, the granular temperature decreases and density increases with distance behind the excitation region; this marks the 'relaxing' region (region II). Eventually, the density becomes sufficiently high as the equilibrium region tends to zero granular temperature, which

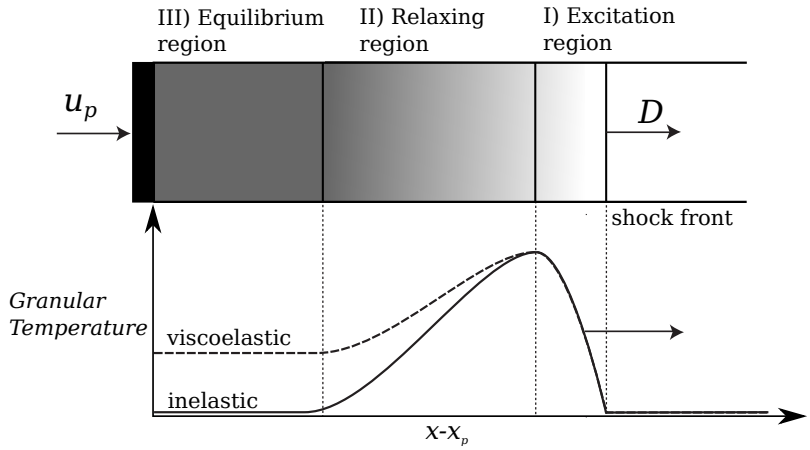

Figure 1.1: Granular temperature distributions in the piston frame of reference for a shock wave propagating at a velocity D, supported by a piston travelling at a velocity u_p into a granular medium.

is characterized by the 'equilibrium' region (region III). In reality, collisions have been shown to become elastic for sufficiently low impact energies, yielding viscoelastic collisions [11, 12]. For such a medium, a similar structure is expected as compared to a purely inelastic mixture, although some kinetic energy is expected in the equilibrium region.

The evolution of the shock structure due to the piston propagating into a granular medium was addressed by Kamenetsky *et al.* [9], who investigated the evolution of such a structure numerically by solving the one-dimensional Euler equations for smooth, inelastic disks. Kamenetsky *et al.* revealed interesting dynamics prior to the shock wave attaining the developed structure illustrated in Fig. 1.1. In particular, the authors found that the lead shock front pulls back towards the piston for a short period, before attaining a constant velocity. The dynamics of this stage were not explained nor further explored. The influence of initial packing fraction of particles and their degree of inelasticity were explored in this context, although the study was not extended to systems involving viscoelastic collisions.

1.2 Analogues to Shock Instability in Molecular Gases

Qualitatively, a structure similar to that shown in Fig. 1.1 is observed for sufficiently strong shock waves driven into molecular gases, whereby the shock is strong enough to bring about inelastic collisions between molecules (i.e., via endothermic reactions or vibrational relaxation) [13].

Interestingly, these types of relaxing shock waves have also been shown to sometimes become unstable. In this context, instability refers to the presence of ripples or corrugations along the shock front. Experimentally, unstable shock structures have been observed in sufficiently strong shocks leading to ionization [14–16]. Similar instabilities have also been observed for strong shock waves leading to molecular dissociation [16]. Further experiments have revealed that shock waves can also become unstable when neither ionization or dissociation is expected. This has been observed in shock waves through gases composed of heavy molecules, characterized by a high specific heat and influenced by vibrational relaxation, such as carbon dioxide [16–18], propane [18], and freon [19].

The similarity between granular media and molecular gases, whereby there are strong relaxation effects *within* the shock structure, suggests that investigating the stability of shock waves through granular media may shed light on the instabilities seen in molecular gases.

1.3 Mechanisms of Shock Instability

Current models for predicting shock instabilities are mostly based on jump conditions between the initial and final equilibrium states, without knowledge of the kinetic processes linking the two states. Traditionally, these states are represented on the Hugoniot curve, which represents the locus of the post shock states, usually represented in a pressure-specific volume diagram [13]. A configuration of the Hugoniot that is expected to be stable is represented in Fig. 1.2. The Rayleigh line, also shown in Fig. 1.2, shows the locus of non-equilibrium states

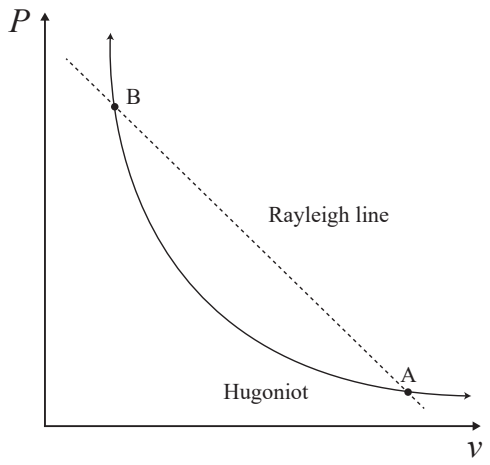

Figure 1.2: Hugoniot structure in which stable shock waves are predicted on a pressure-specific volume plot, where the post shock state B is found from the intersection of the Rayleigh line (dashed) and the Hugoniot curve (solid line), with the Rayleigh line extending from the initial state A.

that satisfy the one-dimensional inviscid mass and momentum conservation laws; steeper Rayleigh lines correspond to a stronger shock. The Rayleigh line intersects the Hugoniot curve at two points, the initial state (point A), and the post shock state (point B) expected for a specific shock strength.

For unstable shock waves, the Hugoniot is expected to take on a more complex shape, as sketched out in the Fig. 1.3 [13, 20]. Figure 1.3(a) shows the Hugoniot characteristic of a material undergoing a phase transition, which is shown to become unstable in the vicinity of the phase transition point (C) [20]. Due to the multiple states characterized by the intersection of the Hugoniot and Rayleigh lines, the shock wave is no longer a single shock structure, but can split into two sequential shock waves.

Media characterized by the Hugoniot shown in Fig. 1.3(b) are also expected to sustain unstable shock waves. Instability is expected when the Rayleigh line intersects a segment of the Hugoniot with a positive slope (B). Instability caused by the positive slope is associated with the D'yakov-Kontorovich instability. The D'yakov-Kontorovich criterion, based on the slope of the Hugoniot, identifies whether the shock wave will be stable (negative slope) or unstable (positive slope) [21, 22].

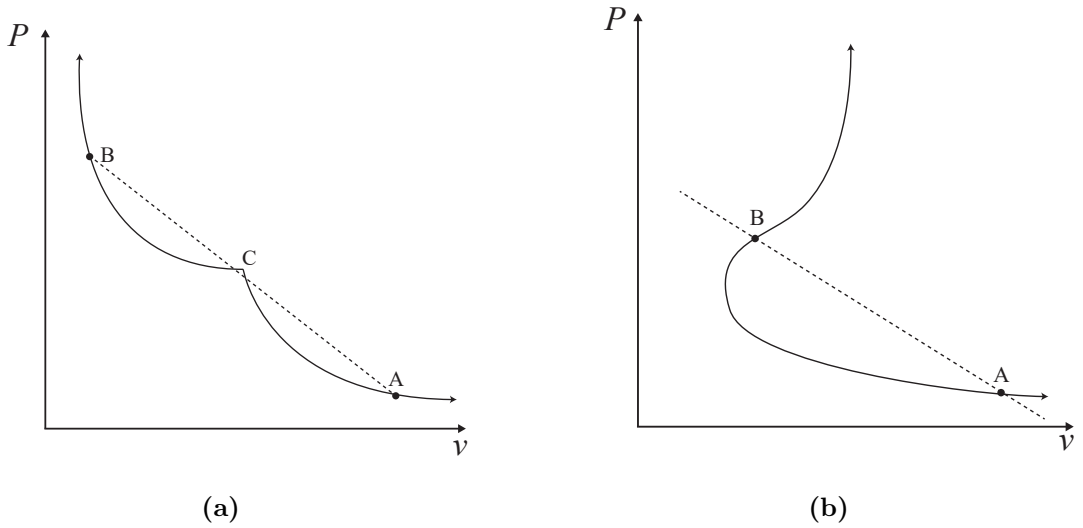

Figure 1.3: Expected Hugoniot-Rayleigh interactions where unstable shock waves are expected based on the intersection of the Rayleigh line (dashed) and Hugoniot curve (solid) in a) media undergoing a phase transition and b) media experiencing D'yakov-Kontorovich instability.

Although the Hugoniot curves can be obtained experimentally for a given substance in order to predict instability, experiments that were predicted to generate stable shock waves based on their Hugoniot demonstrated unstable shock structures [16, 18].

Another mechanism of interest involving shock dynamics is that of Richtmyer-Meshkov and Rayleigh-Taylor type instabilities. In such a multi-dimensional instability, misaligned gradients of density and pressure lead to vorticity production [23]. Richtmyer-Meshkov instability can occur when the contact surface between fluids of two different densities interact with a shock wave. The shock wave causes any perturbations along the contact surface of the two fluids to amplify, as shown in Fig. 1.4. This type of instability is a universal physical phenomenon encountered, for example, in gases [24], plasmas [25], Bose-Einstein condensates [26], and combustion [27]. This instability is localized at the contact surface and not at the shock front, yet the mechanism is still of interest for some cases where granular media exhibit shock dynamics: for example, in the case of oscillating granular beds, where compression waves are periodically driven through density gradients [28].

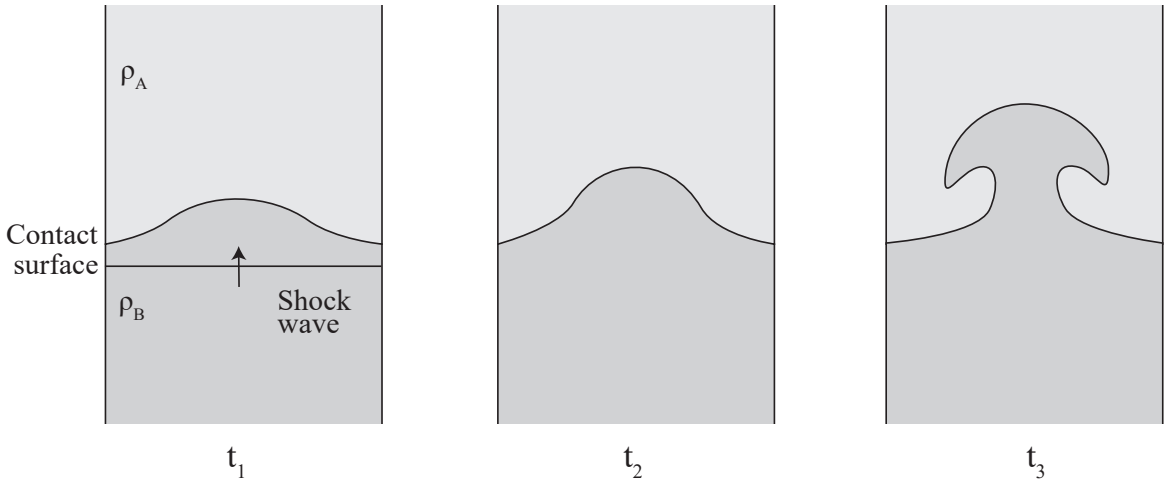

Figure 1.4: Sketch of Richtmyer-Meshkov instability evolving over time from a shock wave interacting with a contact surface between fluids of different densities.

Models for predicting the instability of relaxing shocks involving the kinetics of the relaxation process have only very recently been formulated. Direct numerical simulations at the continuum level in the case of ionizing shocks have indeed recovered the instability [29, 30], suggesting that it is related to the hydrodynamic coupling with the kinetics of the relaxation process. This suggests that an account for the kinetics of the relaxation process may be required to predict the shock instability in relaxing media.

1.4 Motivation

This thesis studies the effect that dissipative collisions have on the stability of shock wave structures in granular gases. Specifically, the current work uses a similar model to that used by Goldshtein *et al.* [8] and Kamenetsky *et al.* [9] in studying the shock dynamics of granular media via the classical problem of a shock wave driven by a moving piston. Such a model is used to investigate the stability of the ensuing shock waves.

Although these previous studies have thoroughly investigated the shock wave development and structure in granular media via the piston problem, they have been limited to

purely inelastic mixtures. The understanding of shock waves in mixtures characterized by viscoelastic collisions, whereby kinetic energy is retained in the equilibrium region, is still lacking. Therefore, prior to investigating the shock stability of such a medium, the expected shock structure must first be derived and characterized. Once the expected characteristics are established, they can be applied to investigating multi-dimensional instabilities.

A microscopic and a macroscopic approach are used in this study to determine if both descriptions exhibit the same shock behaviour. Traditionally, granular flows have been studied using Molecular Dynamics (MD), whereby each particle is modelled deterministically. In this technique, the collision rules can be easily adjusted to treat viscoelastic collisions. Although MD is the most popular technique, it can be computationally expensive when simulating systems with a large number of particles. Motivated by this, there is a large interest in modelling granular flows at the continuum level, albeit with some challenges [31–33]. The major challenges are linked to the rarefied effects of granular flows due to a lack of scale separation between microscopic and macroscopic changes, whereby large macroscopic changes occur over short lengths.

1.5 Objective and Organization of Thesis

This thesis considers the problem of a shock wave driven by a moving piston into a medium characterized by viscoelastic collisions. The medium is assumed to be a system of smooth hard disks (2D) that can collide inelastically. In order to model viscoelastic collisions, a simple formalism is adopted whereby collisions between particles are inelastic with a coefficient of restitution ε if the impact velocity exceeds some threshold velocity. This is a simple treatment for viscoelastic collisions [34, 35]. In such a way, the equilibrium region in the shock structure can be easily controlled by varying the activation threshold. The proposed model can thus also serve as an analogue to molecular gases.

The model is simulated using the hard particle molecular dynamics approach used for granular flows. Continuum modelling is also conducted and compared with the MD results. A thorough review of the two techniques and their applications to rapid granular flows is presented in Ch. 2 prior to their implementation.

1.5.1 Objectives

Using the methods outlined above, the following objectives are investigated in the present thesis:

- Obtain and characterize the structure and evolution of shock waves in media characterized by activated inelastic collisions, extending the previous work that is limited to purely inelastic media.
- Investigate the stability of shock waves through dissipative medium with finite relaxation.
- Determine the role that microscopic and macroscopic effects play on ensuing phenomena by comparing the results given from the molecular dynamics and continuum descriptions.
- Investigate ensuing shock instability in the framework of current shock stability theory.

1.5.2 Organization

The remainder of the thesis is organized as follows. Chapter 2 contains a literature review on what has been completed for shock-like dynamics in granular flows, and the methods that have been used for these investigations. The model that was used in this study and the numerical implementation is presented in Chapter 3. The steady state shock structure and properties derived from the continuum description is given in Chapter 4. The one-dimensional

structure and evolution obtained from the MD and continuum models is presented in Chapter 5. Chapter 6 presents the two-dimensional structure and evolution obtained from the different models, discussing the role that statistical fluctuations play on the shock stability. Discussion and analyses of the mechanisms influencing shock instability seen in the current work is conveyed in Chapter 7. Finally, Chapter 8 contains concluding remarks about the present study.

Chapter 2

Review on Rapid Granular Flows

It is well established that granular media can act like a solid, liquid or gas [1]. Due to the inelastic nature of collisions for such a media, methods of energy input are required for fluid like behaviour to persist. This may be accomplished by gravity acting on particles that are free to move, (e.g., an avalanche), by agitating the particles, or in multiphase flows with an influential interstitial fluid (i.e., particles within a moving liquid or gas). The understanding of these processes is important, especially in the handling and processing of granular materials in industrial applications, for example, in the handling of ingredients for food processing or pharmaceuticals.

Interestingly, fluidized granular material can exhibit shock-like dynamics, as seen in molecular gases. These shock dynamics are seen by sharp gradients in macroscopic properties, such as number density and granular temperature (kinetic energy of particles). Such a phenomena has been seen in granular flow around obstacles, which generate oblique shock waves [36], or in vertically agitated flows, where the media is continuously subjected to compression and expansion waves [28]. Shock dynamics can also be observed in multiphase flows, whereby granular media may be compressed by a shock wave travelling through air, for example, in explosively dispersed granular media [6].

The incentive to understand granular flows, with and without any shock dynamics, has driven a significant amount of research in the past few decades. In particular, research has been driven by the need to model these flows numerically, due to the ability to scale up to larger systems that are not possible, nor economical, experimentally. Numerical modelling of such flows also allows for a broader range of properties to be simulated, with the ability to visualize and extract properties that are not feasible experimentally.

In this chapter, a review of the advancements in research related to granular flows with the presence of shock-like dynamics is presented. First, numerical methods used for such flows are reviewed in Sec. 2.1. A review on the experimental and numerical work that has been completed on this topic is presented in Sec. 2.2.

2.1 Numerical Methods for Granular Flows

2.1.1 Molecular Dynamics Modelling

The most popular method to simulate granular flows has been via molecular dynamics (MD) modelling, with granular particles treated as discrete elements, i.e., discrete element modelling. This modelling technique is commonly done by using the Event Driven Molecular Dynamics method [37]. In this method, particles can be represented by any shape, although the common method is with solid sphere (3D) or disks (2D). In such MD simulations, hard particles are translated within a bounded volume. The hard particles are chosen since there are no force potentials between the molecules, which enables calculation of the kinematics of the system, which follow simple Newtonian dynamics of each particle. This allows for simulations to progress between 'events' (collisions), as opposed to fixed time steps needed in force based algorithms.

In order to address the behaviour of particles, the necessary dynamics for collisions between particles, or boundaries, must be implemented [37]. For granular media, this requires

the inelasticity and friction to be represented by the necessary coefficients of normal and tangential restitution. These values may be treated as constants, or dependent on the impact velocity between collisions, representing the viscoelastic nature of collisions.

2.1.2 Continuum Modelling

Modelling granular flows at the continuum level, using macroscopic equations of motion, has received significant interest due to the capability of treating much larger systems, unlike MD models, which are limited by the number of particles. The continuum description also allows for the stability of different types of flows to be identified via perturbation theory and stability analysis.

The similarity of granular flow to molecular gases has motivated the continuum descriptions to be established. However, the difference in scales between molecules and granular particles, and the non-equilibrium effects due to dissipative collisions make this a difficult task. In particular, rarefied effects dominate due to the lack of scale separation between microscopic and macroscopic changes, whereby large macroscopic changes occur over short lengths [38]. More thorough descriptions of these challenges are discussed in Refs. [31–33].

With these challenges in mind, many authors have attempted to derive approximations to the equations of motion using kinetic theory. Equations up to Burnett order have been established for systems of disks or spheres, which are summarized and compared in the reviews by Campbell [31] and Goldhirsch [33]. Descriptions established by Jenkins *et al.* [39, 40] have been favoured by many authors in comparing MD with continuum results, which have been in good agreement. This gives promise to the ongoing development of continuum modelling of granular flows.

2.2 Investigations on Shock-like Dynamics in Granular Media

2.2.1 Piston Driven Granular Shocks

The classical methodology to characterize shock waves in granular media has been via the piston problem, with a piston propagating into a granular gas, generating a compression wave.

One of the earliest investigations on shock wave structures for granular gases was the theoretical work by Goldshtein *et al.* [8]. This fundamental work identified the unique self-similar structure, which can be broken up into three distinct regions when considering an inviscid medium, as shown in Fig. 2.1. In this structure, there is a piston propagating forward at a velocity U. This causes a shock wave to form, which is the interface of the *undisturbed region* and the *fluidized region*. The shock wave causes the granular mixture, initially at rest, to obtain some kinetic energy. Because of the inelasticity and increased rate of the collisions within this fluidized region, the granular temperature of the material decreases, while density increases. Eventually, the density becomes high enough and the region tends to zero granular temperature, which is characterized by the *solid block* region. Goldshtein *et al.* characterized the expected shock structure for different initial packing factors, piston velocities, and coefficients of normal restitution.

Kamenetsky *et al.* extended on the work by Goldshtein *et al.* by investigating the evolution of the shock wave for the piston problem in granular mixtures [9]. This work was done numerically by solving the one-dimensional Euler equations for smooth, inelastic disks. The authors revealed interesting dynamics prior to the shock wave attaining the developed structure illustrated in Fig. 2.1. One particular finding was that the lead shock front pulls back towards the piston for a short period, before attaining a constant velocity, and forming

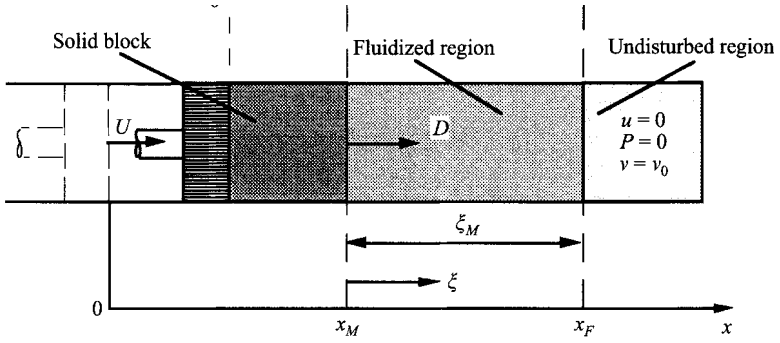

Figure 2.1: Schematic of piston driven shock wave through granular gas, from [8].

the steady structure. The influence of initial packing fraction of particles and their degree of inelasticity were explored in this context.

Most recently, the piston problem has also been investigated experimentally by Vilquin *et al.* [41]. This was done by investigating the shock structure formed by a flat obstacle propagating into a mixture of vibro-fluidized steel beads. The specific interest of this work was to investigate velocity distributions of particles within the shock front and the departure from a distribution expected for local equilibrium. Interestingly, this study also demonstrated that investigating the shock structure in granular gases can also be used to address issues in molecular gases. Specifically, the results for the granular medium were linked to velocity distributions across as shock wave in molecular gases, which exhibit similar non-equilibrium behaviour at high Mach numbers.

2.2.2 Vertically Oscillating Flows

Shock-like dynamics have been seen for granular particles that are subjected to vertical oscillations. An example of this can be seen in Fig. 2.2, where an oscillating bed impacting a layer of inelastic spheres brings rise to compression and expansion waves, fluidizing the particles. In addition to studying this method of energy input for granular flow, significant interest is led by the ensuing pattern formations. The earliest of these investigations was completed by Faraday in 1831, who noticed a pattern formation within powders subjected to

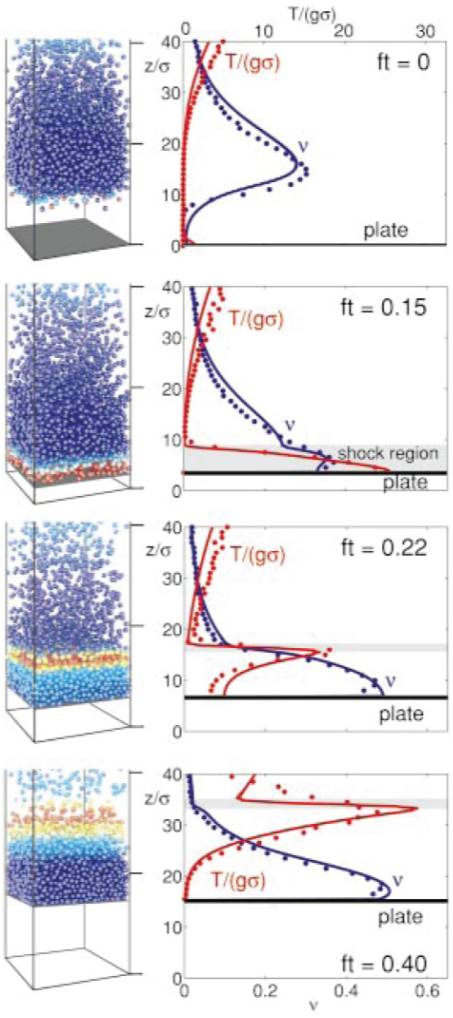

Figure 2.2: Snapshots of MD simulations (left) and dimensionless distribution of temperature and volume fraction (right) for a vertically oscillating bed of inelastic spheres. Particles in MD simulations are colour coded according to temperature: high T in red, low T in blue, and the bottom plate of the container shaded solid gray. For the distribution on the right, results from MD simulation are shown as dots, and continuum results are solid lines, from [28].

vertical oscillations [42]. With the growing interest in granular flows in the past few decades, many studies have since investigated this phenomena.

Early experimental work identified the regimes of different patterns, based on the amplitude and frequency of the driven oscillations [2, 43]. These results were supplemented by MD simulations, completed in 2D and 3D to investigate different phenomena in vibrated flows [2, 44–46].

Continuum simulations using the descriptions by Jenkins and Richman have recently been used to study vibrated flows, showing good agreement with MD. Such simulations have shown agreement in comparing the shock-like dynamics [28], as seen in Fig. 2.2, and the formation of patterns due to oscillations in 2D [3] and 3D [47]. An example of results obtained in 2D can be seen from Carillo *et al.* in Fig. 2.3 [3].

Theoretically, linear stability analysis has been completed on this instability [48], accomplished by following the linear theory established for Faraday instabilities within viscous fluids [49, 50].

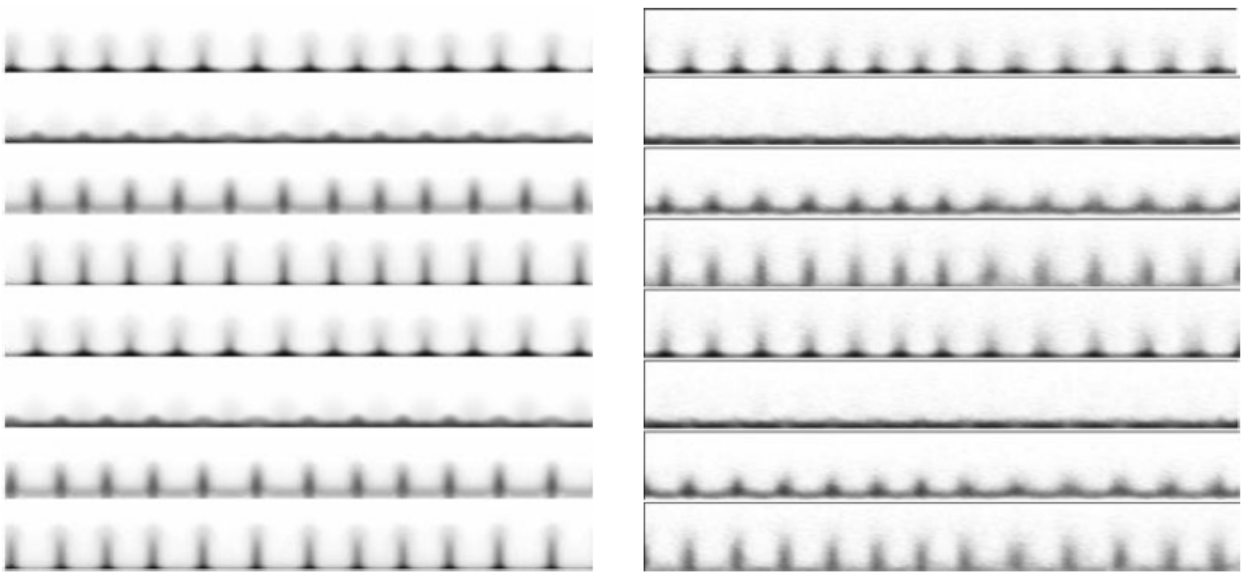

Figure 2.3: Snapshots of the density evolution over time (top to bottom) on an oscillating bed of inelastic disks, as obtained from the continuum (left) and MD simulations (right), from [3].

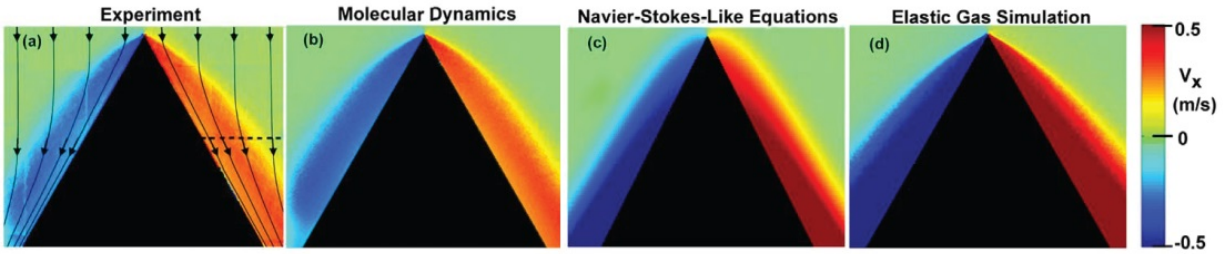

Figure 2.4: Horizontal component of the velocity field of a granular flow around a wedge, obtained by (a) experiment, (b) molecular dynamics of inelastic disks (c) Navier-Stokes equations using Jenkins-Richman description, and (d) molecular dynamics of a hard sphere elastic gas, from [36].

2.2.3 Flows Down an Incline

Flows down an inclined surface have received a large amount of interest due to their application for transport and handling of granular material [31, 33]. Understanding the dynamics of avalanches has also driven studies on this type of flow [51–54].

Some studies have treated the front of the avalanche as a shock front [55–57]. Interestingly, such flows have generated a fingering like instability, which have been attributed to blast-like behaviour [4] or friction along the surface [5].

Shock like dynamics have also been observed for granular flows around obstacles, either down an incline [58, 59], or free falling [36, 60, 61]. An example of such a flow can be seen in Fig. 2.4 for quasi-2D flow around a wedge, generating an oblique shock wave [36]. This study showed fair agreement between experimental, MD, and continuum results for this flow, where the Jenkins-Richman description was used for Navier-Stokes equations.

2.2.4 Multiphase Flows

One of the most recent interests involving shock-like dynamics in granular material has been in investigating the dynamics of granular material subjected to a shock wave through air [6, 7, 62–68]. This has been seen on large scales, such as dry and wet granular media dispersed by an explosive [6, 62, 65], as demonstrated in Fig. 2.5, or on smaller scales, such

as that shown in Fig. 2.6 for an inert shock wave striking a small amount of flour [7, 68].

Regardless of scale, experiments have demonstrated the generation of a similar non-uniform cloud, with jetting of the granular media. Due to the complex nature of this multiphase problem, most results have been limited to experiments, although multiphase simulations have recently been conducted for this problem [64]. However, the mechanism controlling this jetting phenomena is still not well understood.

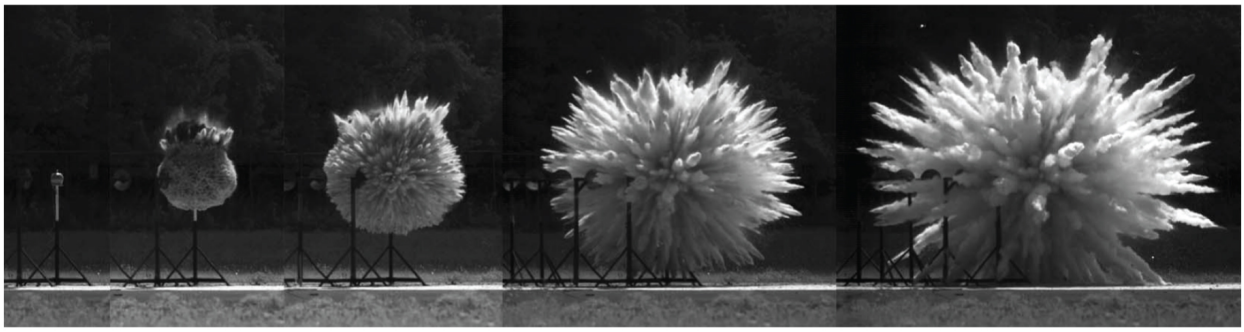

Figure 2.5: Explosive dispersal of a packed bed of sand particles contained within a glass sphere, from [6].

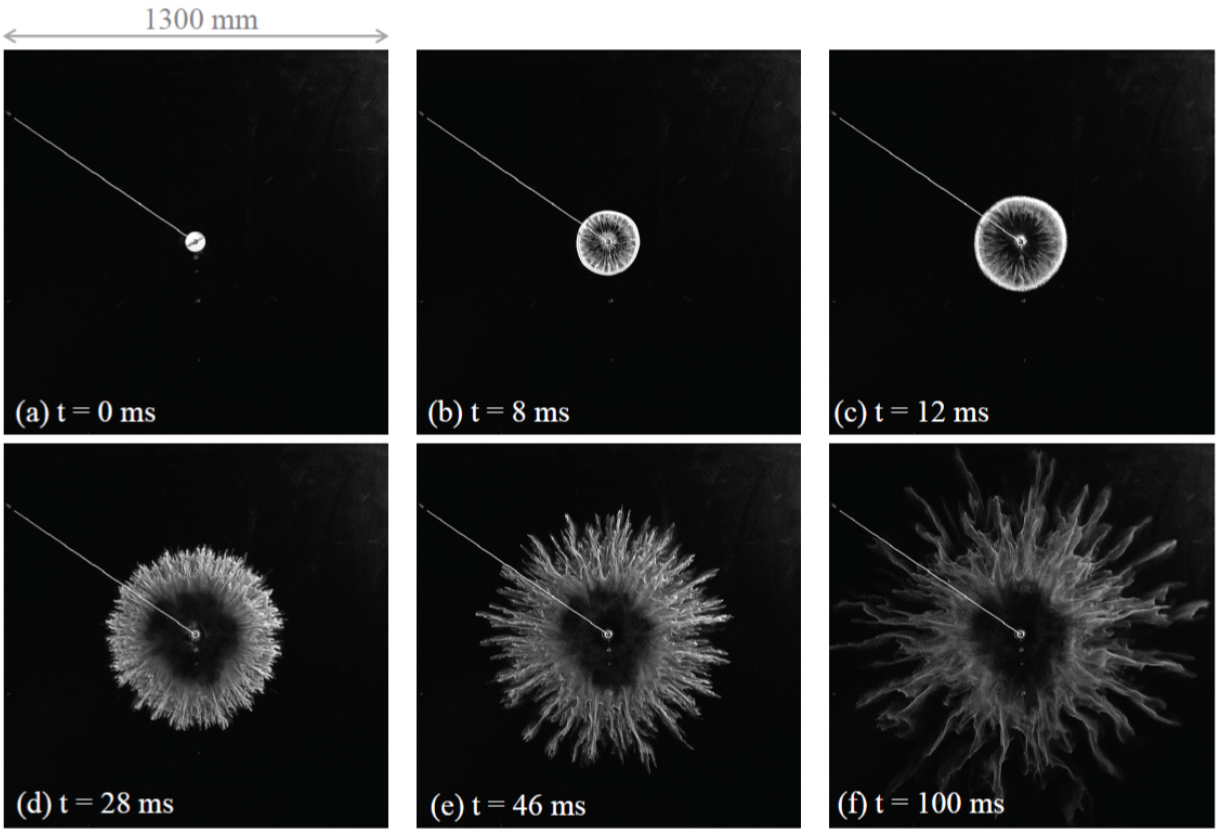

Figure 2.6: Sequence of snapshots looking at solid particle jet formation from a 1.16 Mach number shock wave through flour, from [68].

Chapter 3

Modelling Methodology

The problem that is investigated in this thesis is that of shock waves in granular gases. The current chapter presents the formulation for the model that is used to investigate this problem, and the numerical methods implemented to solve the model.

First, an overview is presented on the model that is being used to investigate shock waves in hard disks with activated inelastic collisions. The molecular dynamics (MD) model is introduced as it applies to this problem. The continuum description for the system is then given and implemented into a continuum solver, which is validated and compared with some test cases from MD and theory.

3.1 Model Overview

A model was constructed to investigate the problem of shock waves through granular gases using the classical formulation of piston driven shock waves. The current formulation assumes a system of smooth hard disks to model a granular material. A piston is driven into the system of disks, causing a shock wave to form, as sketched in Fig. 3.1. The driving piston is initially at rest and suddenly acquires a constant velocity u_{p} once the system of disks is thermalized.

The system of disks is composed of N colliding hard disks (in 2D), with identical masses

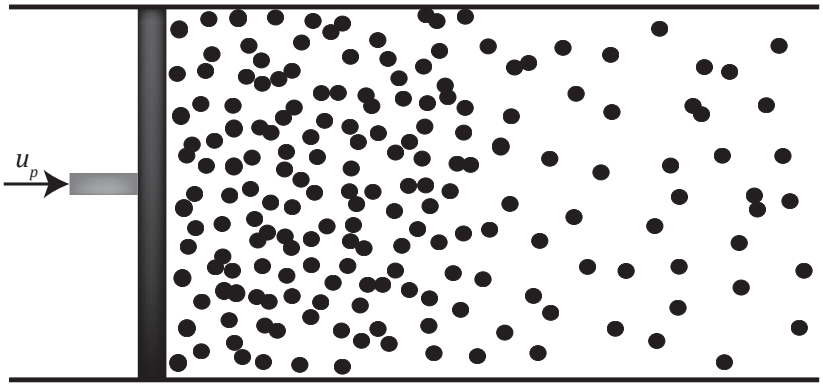

Figure 3.1: Sketch of a piston propagating at a velocity u_p through a system of hard particles.

m and diameters d, occupying an initial volume fraction η. Each disk propagates at a velocity $\boldsymbol{u}_\mathrm{i}$. The type of binary collision is determined by separating the velocities into normal and tangential velocities, denoted by subscripts N and T, respectively, as sketched out in Fig. 3.2 for colliding particles i and j. All collisions are assumed to be elastic, unless the impact velocity (difference in normal velocities) exceeds a velocity threshold u^*, i.e.,

$$\left|u_{\mathrm{i(N)}} - u_{\mathrm{j(N)}}\right| > u^*. \tag{3.1}$$

If the collision is inelastic, the disks collide with a constant coefficient of restitution ε, which gives the ratio of pre- and post-collision normal velocities:

$$\varepsilon = -\frac{\left(u'_{\mathrm{i(N)}} - u'_{\mathrm{j(N)}}\right)}{\left(u_{\mathrm{i(N)}} - u_{\mathrm{j(N)}}\right)} \quad \text{where} \quad 0 \leq \varepsilon \leq 1. \tag{3.2}$$

This is a simple treatment for viscoelastic collisions [34, 35].

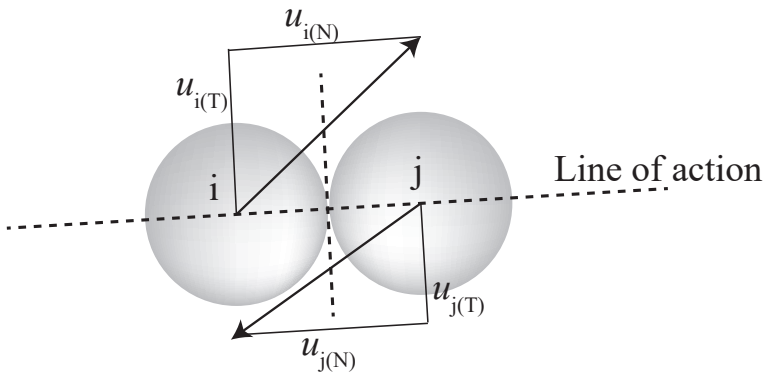

Figure 3.2: Sketch of a pairwise collision between two particles i and j, separating the velocity vectors into normal (N) and tangential (T) components of velocity with respect to the line of action.

3.2 Molecular Dynamics Model

The MD model was established by implementing the collision rules for inelastic and elastic encounters into an Event Driven Molecular Dynamics algorithm, as pioneered by Alder and Wainright [69, 70], and also described by Pöschel and Schwager [37]. For each simulation, N disks of diameter d are initialized with equal speeds and randomized trajectories. Collisions with the boundaries are treated as elastic. The particles are left to obtain Maxwell-Boltzmann statistics prior to allowing them to undergo inelastic collisions. This was shown to occur once the distribution of speeds converges to that expected from the Maxwell-Boltzmann distribution. The probability distribution function $f(v_\mathrm{i})$ for the Maxwell-Boltzmann distribution is given by (see B.1 for derivation):

$$f(v_\mathrm{i}) = \frac{mv_\mathrm{i}}{2RT} \exp\left(-\frac{mv_\mathrm{i}^2}{2RT}\right) \tag{3.3}$$

where m is the mass of the particle, v_i is the magnitude of the velocity, T is the temperature of the system, and R is the gas constant.

An example of the thermalization process, whereby the particles obtain Maxwell-Boltzmann

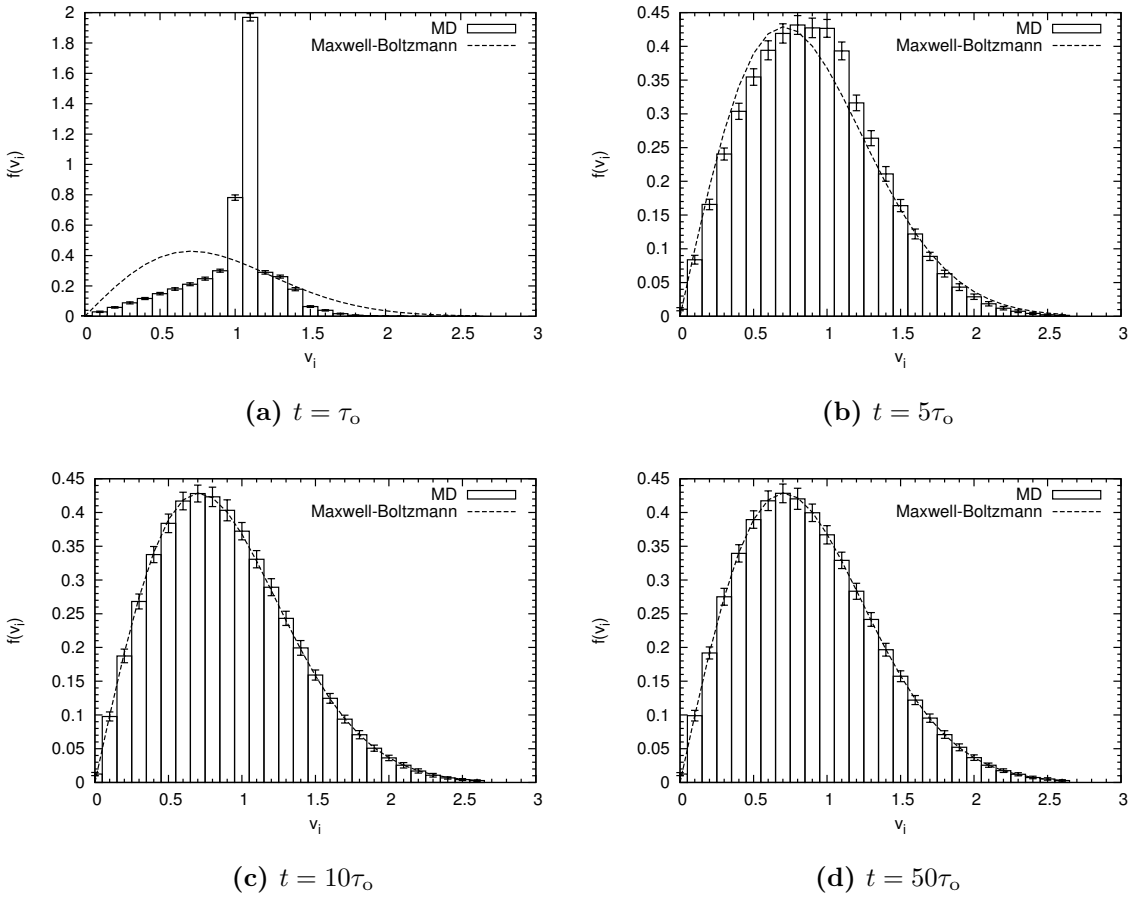

(a) $t = \tau_o$ **(b)** $t = 5\tau_o$

(c) $t = 10\tau_o$ **(d)** $t = 50\tau_o$

Figure 3.3: Probability distribution of speeds obtained from MD for different points in time for $N = 10000$ disks and ensemble averaged over 100 simulations, as compared to that expected from Maxwell-Boltzmann statistics. Error bars represent the standard deviation given from the ensemble average. Speeds are normalized by the initial speed of the disks and time is given in terms of the initial mean collision time τ_o.

statistics, is given in Fig. 3.3, which shows the probability density function of speed distributions obtained at different times from MD and compared with the Maxwell-Boltzmann distribution. MD results were obtained by ensemble averaging over 100 simulations for a system of $N = 10000$ disks. The error bars represent the standard deviation of the ensemble average for a particular speed. Results are represented in terms of the number of mean free times τ_o that elapsed since initialization. After one mean collision time, shown in Fig. 3.3(a), there is a large peak for the distributions at the initial speed of the disks. After five mean

collision times, shown in Fig. 3.3(b), the distribution approaches the Maxwell-Boltzmann distribution, although there is a plateau that still occurs at the initial speed of the disks. At ten mean collision times, shown in Fig. 3.3(c), the distribution of speeds converges to the Maxwell-Boltzmann distribution, and does not change over time, as shown by the distribution after fifty mean collision times in Fig. 3.3(d). This shows that the system comes to equilibrium after ten mean collision times, and this was found to be a sufficient time to equilibrate the system. Similar results were found for different number of disks in the system, with increasing noise for smaller systems.

Inelastic collisions are allowed after this initial thermalization process over ten mean collision times, which marks time zero. This also marks the time when the piston is suddenly accelerated to velocity u_p in the simulations.

Data Collection

The state variables are found by coarse-grain averaging the positions and velocities of the particles. This is done by separating the domain into vertical strips of width dx extending the height of the domain, or into boxes of size $dx \times dy$, as shown in Fig. 3.4. The one-dimensional distribution of macroscopic properties is found by coarse-grain averaging the microscopic properties within the strips of width $dx = 0.5\lambda_\mathrm{o}$, where λ_o is the initial mean free path, which will be described later in this chapter.

The local granular temperature $T(x)$ of each strip or box is calculated by averaging the kinetic energies in the x- and y-directions over all of the particles, within the coarse-grain averaged areas. The normalized local temperature, at position x, bounded by the strip of width dx, is written as:

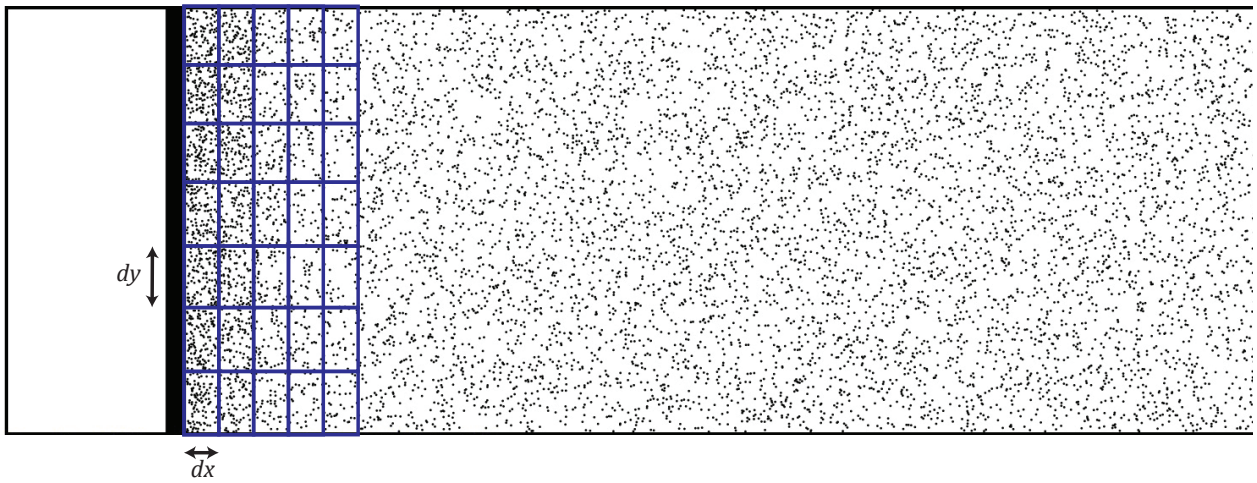

Figure 3.4: Example of particle distribution in an MD simulation with a sample grid used for coarse-grain averaging.

$$\begin{aligned} T(x) =& \frac{T_{\mathrm{x}} + T_{\mathrm{y}}}{2} \\ T_{\mathrm{x}}(x) =& \frac{1}{N(x)} \sum_{i=1}^{N(x)} \frac{1}{2} (u_{\mathrm{xi}} - \langle u_{\mathrm{x}} \rangle)^2 \\ T_{\mathrm{y}}(x) =& \frac{1}{N(x)} \sum_{i=1}^{N(x)} \frac{1}{2} (u_{\mathrm{yi}} - \langle u_{\mathrm{y}} \rangle)^2 \end{aligned} \tag{3.4}$$

where $N(x)$ is the number of hard disks at position x, bounded by the strip of width dx, and $\langle u_{\mathrm{x}} \rangle = \frac{1}{N(x)} \sum_{\mathrm{i}=1}^{N(x)} u_{\mathrm{xi}}$, $\langle u_{\mathrm{y}} \rangle = \frac{1}{N(x)} \sum_{\mathrm{i}=1}^{N(x)} u_{\mathrm{yi}}$, are the local mean velocities in the x- and y-directions, respectively.

The local number density in each strip, $n(x)$ is written as:

$$n(x) = \frac{N(x)}{dx \times L_{\mathrm{y}}} \tag{3.5}$$

Ensemble averaging is used to obtain accurate measurements of the coarse-grain averaged density and temperature. This is ddone by repeating the calculation with statistically different initial conditions, which is implemented by randomizing the trajectories of the particles.

Appendix A gives further details of the MD methodology.

3.3 Continuum Model

3.3.1 Governing Equations for a Granular Gas in Dimensional Form

Hydrodynamic Equations

For the continuum model, a two-dimensional granular gas is considered by modelling a system of smooth inelastic disks. For such a system, the hydrodynamic equations can be obtained starting with the inelastic Enskog kinetic equation [71]. For the fields of number density $\tilde{n}$, flow velocity $\tilde{\boldsymbol{u}}$, and granular temperature $\tilde{T}$, they are given as [10]:

$$\frac{\partial \tilde{n}}{\partial \tilde{t}} + \tilde{\boldsymbol{\nabla}} \cdot (\tilde{n}\tilde{\boldsymbol{u}}) = 0 \tag{3.6}$$

$$\tilde{n}\tilde{m}\left(\frac{\partial \tilde{\boldsymbol{u}}}{\partial \tilde{t}} + \left(\tilde{\boldsymbol{u}} \cdot \tilde{\boldsymbol{\nabla}}\right)\tilde{\boldsymbol{u}}\right) = \tilde{\boldsymbol{\nabla}} \cdot \tilde{\mathbf{P}} \tag{3.7}$$

$$\tilde{n}\left(\frac{\partial \tilde{T}}{\partial \tilde{t}} + \left(\tilde{\boldsymbol{u}} \cdot \tilde{\boldsymbol{\nabla}}\right)\tilde{T}\right) = -\tilde{\boldsymbol{\nabla}} \cdot \tilde{\boldsymbol{q}} - \tilde{\mathbf{P}} : \tilde{\boldsymbol{\nabla}}\tilde{\boldsymbol{u}} + \tilde{\zeta} \tag{3.8}$$

where $\tilde{(\,)}$ denotes a dimensional term. Equation (3.8) has a cooling rate term $\tilde{\zeta}$, which gives the rate of energy loss due to dissipative collisions. This important term for granular media is discussed later on in this chapter as it applies to the current model.

The heat flux is from heat conduction due to gradients in the granular temperature:

$$\tilde{\boldsymbol{q}} = -\tilde{\kappa}\tilde{\boldsymbol{\nabla}}\tilde{T}, \tag{3.9}$$

where $\tilde{\kappa}$ is the thermal conductivity. The pressure tensor $\tilde{\mathbf{P}}$ appearing in (3.7) and (3.8) is given as

$$\tilde{P}_{\mathrm{ij}} = -\tilde{p}\delta_{\mathrm{ij}} + (2\tilde{\mu}_1 - \tilde{\mu}_2)\sum_i \tilde{W}_{\mathrm{ii}}\delta_{\mathrm{ij}} + 2\tilde{\mu}_2\tilde{W}_{\mathrm{ij}} \tag{3.10}$$

where $\tilde{p}$ is the hydrostatic pressure, $\tilde{\mu}_1$ is the bulk viscosity, and $\tilde{\mu}_2$ is the shear viscosity.

The strain rate tensor takes the form:

$$\tilde{W}_{\mathrm{ij}} = \frac{1}{2}\left(\frac{\partial \tilde{u}_{\mathrm{i}}}{\partial \tilde{x}_{\mathrm{j}}} + \frac{\partial \tilde{u}_{\mathrm{j}}}{\partial \tilde{x}_{\mathrm{i}}}\right). \tag{3.11}$$

Transport Properties

For the Navier-Stokes (N-S) equations, the transport coefficients need to be given. One commonly used set of coefficients are those obtained by Jenkins and Richman by using Grad's moment method for a system of hard disks [40]. These coefficients are convenient in the current study as the terms are independent of ε and therefore are unaffected by the viscoelastic collision model. The transport coefficients from the Jenkins and Richman approach are given as

$$\tilde{\kappa} = \frac{\sqrt{\pi}}{2}\tilde{n}\tilde{d}\tilde{T}^{1/2}\left(\frac{1}{\eta g_2(\eta)} + 3 + \left(\frac{9}{4} + \frac{4}{\pi}\right)\eta g_2(\eta)\right) \tag{3.12}$$

for the thermal conductivity,

$$\tilde{\mu}_1 = \frac{2}{\sqrt{\pi}}\tilde{n}\tilde{d}\tilde{T}^{\frac{1}{2}}\eta g_2(\eta) \tag{3.13}$$

for bulk viscosity, and the shear viscosity by

$$\tilde{\mu}_2 = \frac{\sqrt{\pi}}{8}\tilde{n}\tilde{d}\tilde{T}^{\frac{1}{2}}\left[\frac{1}{\eta g_2(\eta)} + 2 + \left(1 + \frac{8}{\pi}\right)\eta g_2(\eta)\right], \tag{3.14}$$

where the pair correlation function for a granular gas in 2D is used [72]:

$$g_2(\eta) = \frac{1 - (7/16)\eta}{(1-\eta)^2}. \tag{3.15}$$

These terms have shown good agreement in comparing continuum and MD simulations for rapid granular flows (for example, see [3] and [36] for their implementation). An alternative set of coefficients has been derived by Garzo and Dufty [73] and Lutsko [74] with a dependence

on ε. However, these terms have not shown significant differences with the Jenkins and Richman coefficients when comparing with MD simulations [75]. Therefore, the current study only compares the MD simulations with the Jenkins and Richman coefficients as a first approximation.

Equation of State

To close the system of equations given thus far, the equation of state must be implemented. In a hard particle system, the internal energy $\tilde{e}$ of the system consists only of the translational kinetic energy modes, with $\frac{1}{2}\frac{\tilde{k}}{\tilde{m}}\tilde{T}$ per translational degree of freedom, where $\tilde{k}$ is the Boltzmann constant, $\tilde{m}$ the particle mass, and $\tilde{T}$ is the granular temperature. For a hard disk system, there are only two translational degrees of freedom, yielding the caloric equation of state given by

$$\tilde{e} = 2\left(\frac{1}{2}\frac{\tilde{k}}{\tilde{m}}\tilde{T}\right). \tag{3.16}$$

An equation of state relating the thermodynamic state variables may be written as

$$\tilde{p} = \tilde{\rho} Z \frac{\tilde{k}}{\tilde{m}}\tilde{T}, \tag{3.17}$$

where Z is the *compressibility factor*, which depends on the equation of state that is used. Thus for a hard disk system, combining (3.16) and (3.17), the general equation of state can be written as

$$\tilde{p} = \tilde{\rho} Z \tilde{e}. \tag{3.18}$$

To close the equation of state, the compressibility factor must be identified. In the dilute limit, the hydrostatic pressure can be approximated with $Z = 1$. However, for denser systems, the packing factor η becomes important. One simple equation of state for hard disks relating Z to η is that from Helfand *et al.* which was derived analytically using Scaled-Particle Theory

and takes the form [76]:

$$Z_{\text{Helfand}}(\eta) = \frac{1}{(1-\eta)^2} \tag{3.19}$$

A more accurate equation of state for hard disks has been proposed by Maeso *et al.* [77], which takes the form

$$\begin{aligned} Z_{\text{Maeso}}(\eta) =& \frac{10^3 - 947.989\eta + 128.018\eta^2 - 113.987\eta^3}{(1-0.947989\eta)(1-\eta)^2 10^3} \\ &+ \frac{-52.9722\eta^4 - 1.580596\eta^5}{(1-0.947989\eta)(1-\eta)^2 10^3}. \end{aligned} \tag{3.20}$$

This equation of state is obtained from the first seven virial coefficients and has an accuracy characterized by an average absolute deviation of 0.05%.

An equation of state which is dependent on ε has also been used in the literature [10, 40, 71], with the compressibility factor taking the form

$$Z_{\text{inelastic}}(\eta, \varepsilon) = \left(1 + (1+\varepsilon)\eta g_2(\eta)\right). \tag{3.21}$$

The three equations of state are compared in Fig. 3.5, with $\varepsilon = 1.0$ and 0.80 used to calculate the inelastic equation of state. At the dilute limit $\eta \to 0$, $Z = 1$ for all approximations, as expected. As η increases, Z increases, with differences becoming more prominent between the models. Interestingly, $\varepsilon = 1$ in the inelastic approximation shows a large discrepency of $\sim$25% at $\eta = 0.5$ when compared to Z_{Helfand} and Z_{Maeso} which were derived and validated for an elastic system of disks [78]. For values of $\varepsilon < 1$, $Z_{\text{inelastic}}$ is shown to decrease. This suggests that the inelastic equations of state may not be valid when considering the elastic limit. When comparing Z_{Helfand} and Z_{Maeso}, the compressibility factor given by Helfand *et al.*[76] is still shown to give reasonably accurate results.

Previously, the Helfand equation of state has been used to investigate shock waves in elastic hard disks, with the derived shock jump conditions using this approximation agreeing

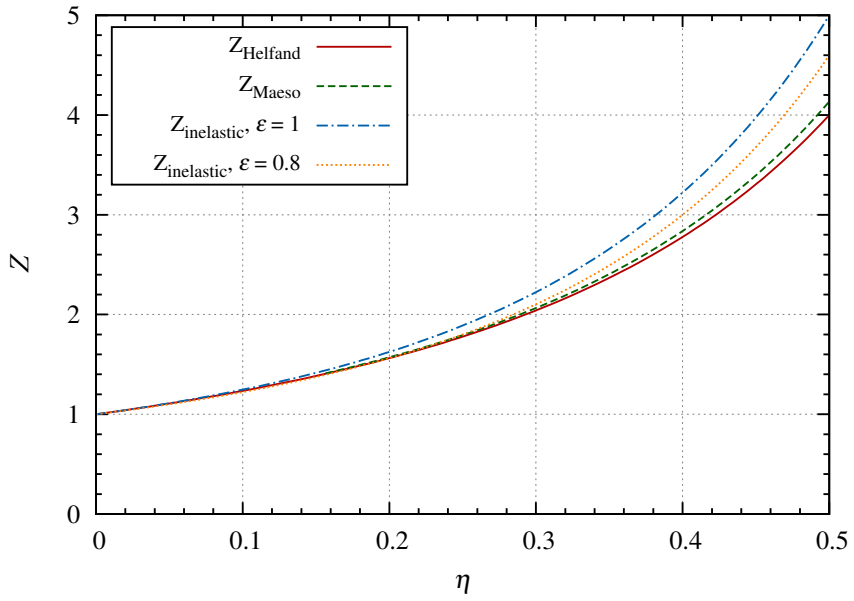

Figure 3.5: Relationships between compressibility factor Z and packing fractions η, comparing the approximations by Helfand *et al.* [76], Maeso *et al.* [77] and that used for inelastic disks [10].

with results obtained from MD [79]. Although it assumes all collisions are elastic, this equation of state is used as a first approximation for this study.

The Cooling Rate

The conservation of energy (3.8) has a source term $\tilde{\zeta}$ accounting for the energy losses due to dissipative collisions of particles. Assuming that all collisions are inelastic with a constant coefficient of restitution, the cooling rate takes the form [10]:

$$\tilde{\zeta} = -\frac{4}{\tilde{d}\sqrt{\pi}}\left(1-\varepsilon^2\right)\tilde{\rho}\tilde{T}^{3/2}\eta g_2(\eta). \tag{3.22}$$

This was modified and validated to treat activated inelastic collisions, as is shown later in this chapter.

3.3.2 Mean Free Path

An important scale that is considered throughout the thesis is the mean free path. The mean free path for a system of disks may be adapted from [10] as

$$\tilde{\lambda} = \frac{1}{\sqrt{2}\sqrt{\pi} g_2(\eta) \tilde{n} \tilde{d}} \quad . \tag{3.23}$$

Since the number density is $\tilde{n} = N/\tilde{A}$ and $\eta = \left(N\pi\tilde{d}^2\right) / \left(4\tilde{A}\right)$, this can be re-written more conveniently as

$$\tilde{\lambda} = \tilde{\lambda}\left(\tilde{d}, \eta\right) = \frac{\tilde{d}\sqrt{2}}{4\sqrt{\pi} g_2(\eta)\eta}. \tag{3.24}$$

3.3.3 Non-Dimensional Form of the Governing Equations

Scaling

The presented equations are non-dimensionalized by the initial density $\tilde{\rho}_\mathrm{o}$, the initial internal energy $\tilde{e}_\mathrm{o}$, and the initial mean free path $\tilde{\lambda}_\mathrm{o}$. Applying this scaling yields the following non-dimensional variables:

$$\begin{gathered} \rho = \frac{\tilde{\rho}}{\tilde{\rho}_\mathrm{o}} = \left(\frac{\tilde{n}\tilde{m}}{\tilde{n}_\mathrm{o}\tilde{m}} = n\right), \qquad e = \frac{\tilde{e}}{\tilde{e}_\mathrm{o}} = \left(\frac{\frac{k}{\tilde{m}}\tilde{T}}{\frac{k}{\tilde{m}}\tilde{T}_\mathrm{o}} = T\right), \qquad p = \frac{\tilde{p}}{\tilde{\rho}_\mathrm{o}\tilde{e}_\mathrm{o}}, \\ u = \frac{\tilde{u}}{\sqrt{\tilde{e}_\mathrm{o}}}, \qquad x = \frac{\tilde{x}}{\tilde{\lambda}_\mathrm{o}}, \qquad t = \frac{\tilde{t}}{\tilde{\lambda}_\mathrm{o}/\sqrt{\tilde{e}_\mathrm{o}}}, \qquad E_a = \frac{\tilde{E}_a}{\tilde{e}_\mathrm{o}} = \frac{\tilde{u}^{*2}}{\tilde{u}_o^2} \ . \end{gathered} \tag{3.25}$$

Here $\tilde{u_\mathrm{o}}$ represents the initial root mean squared velocity, where $\tilde{e}_\mathrm{o} = \frac{1}{2}\tilde{m}\tilde{u}_\mathrm{o}^2$.

3.3.4 Non-Dimensional Equations

Applying the described scaling, the non-dimensional hydrodynamics equations (3.6)-(3.8) are now given as

$$\frac{\partial \rho}{\partial t} + \boldsymbol{\nabla} \cdot (\rho \boldsymbol{u}) = 0 \tag{3.26}$$

$$\rho \left(\frac{\partial \boldsymbol{u}}{\partial t} + (\boldsymbol{u} \cdot \boldsymbol{\nabla}) \, \boldsymbol{u} \right) = \boldsymbol{\nabla} \cdot \mathbf{P} \tag{3.27}$$

$$\rho \left(\frac{\partial T}{\partial t} + (\boldsymbol{u} \cdot \boldsymbol{\nabla}) \, T \right) = -\boldsymbol{\nabla} \cdot \boldsymbol{q} - \mathbf{P} : \boldsymbol{\nabla} \boldsymbol{u} + \zeta \tag{3.28}$$

with heat flux

$$\boldsymbol{q} = -\kappa \boldsymbol{\nabla} T, \tag{3.29}$$

pressure tensor

$$P_{\mathrm{ij}} = -p\delta_{\mathrm{ij}} + (2\mu_1 - \mu_2) \sum_i W_{\mathrm{ii}} \delta_{\mathrm{ij}} + 2\mu_2 W_{\mathrm{ij}}, \tag{3.30}$$

and strain rate tensor

$$W_{\mathrm{ij}} = \frac{1}{2} \left(\frac{\partial u_{\mathrm{i}}}{\partial x_{\mathrm{j}}} + \frac{\partial u_{\mathrm{j}}}{\partial x_{\mathrm{i}}} \right) \tag{3.31}$$

The non-dimensionalized transport coefficients for thermal conductivity, bulk viscosity and shear viscosity now take the form, respectively,

$$\kappa = \frac{\sqrt{\pi}}{2} \rho d T^{1/2} \left(\frac{1}{\eta g_2(\eta)} + 3 + \left(\frac{9}{4} + \frac{4}{\pi} \right) \eta g_2(\eta) \right) \tag{3.32}$$

$$\mu_1 = \frac{2}{\sqrt{\pi}} \rho T^{\frac{1}{2}} \eta g_2(\eta) \tag{3.33}$$

$$\mu_2 = \frac{\sqrt{\pi}}{8} \rho d T^{\frac{1}{2}} \left[\frac{1}{\eta g_2(\eta)} + 2 + \left(1 + \frac{8}{\pi} \right) \eta g_2(\eta) \right]. \tag{3.34}$$

3.3.5 Conservative Form of Governing Equations

For the numerical implementation, it is necessary to recast the hydrodynamics equations (3.26)-(3.28) into conservative form. This is done by expanding and introducing the specific total energy

$$e_{\text{tot}} = T + \frac{1}{2}|\boldsymbol{u}|^2 = e + \frac{1}{2}|\boldsymbol{u}|^2. \tag{3.35}$$

With some manipulation (3.26)-(3.28) can be re-written for the conservation of mass, momentum, and energy as

$$\frac{\partial \rho}{\partial t} + \boldsymbol{\nabla} \cdot (\rho \boldsymbol{u}) = 0 \tag{3.36}$$

$$\frac{\partial \rho \boldsymbol{u}}{\partial t} + \boldsymbol{\nabla} \cdot (\rho \boldsymbol{u}\boldsymbol{u}) - \boldsymbol{\nabla} \cdot \mathbf{P} = 0 \tag{3.37}$$

$$\frac{\partial \rho e_{\text{tot}}}{\partial t} + \boldsymbol{\nabla} \cdot (\rho \boldsymbol{u} e_{\text{tot}}) - \mathbf{P} : \mathbf{W} - \boldsymbol{u} \cdot (\boldsymbol{\nabla} \cdot \mathbf{P}) + \boldsymbol{\nabla} \cdot \boldsymbol{q} = \zeta \tag{3.38}$$

This form of the equations was implemented into the numerical solver.

3.4 Numerical Implementation for Continuum Modelling

3.4.1 Hydrodynamic Solver

To solve Eqs. (3.36)-(3.38), the compressible flow solver *MG* was used [80, 81]. Full details of the discretization of the numerical solver can be found in Ref. [80]. *MG* uses a linear Riemann solver to treat the convective terms. Second-order time accuracy is achieved by using fractional time steps. Diffusion terms in Eqs. (3.37)-(3.38) are solved explicitly in time and are spatially discretized using central differences. The cooling rate term is also treated

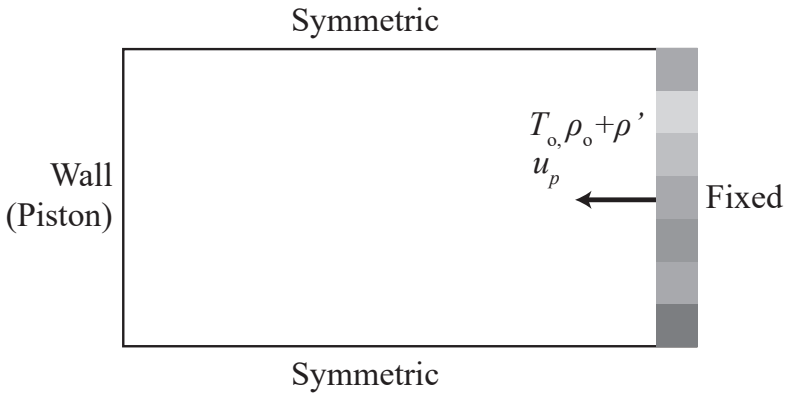

Figure 3.6: Sketch of the domain and boundary conditions used in the continuum solver to investigate the evolving shock structure in the piston frame of reference.

explicitly.

Adaptive mesh refinement is implemented in *MG* [81]. Cells are refined in regions where the primitive variables differ by 0.1% between grid levels. If a cell needs to be refined, a region extending 5-10 cells from this region is also refined from the current grid level [81].

A sketch of the computed domain is shown in Fig. 3.6. The hydrodynamics solver calculates the flow in the piston frame of reference. A reflective wall boundary is implemented on the left (piston face). The upper and lower boundaries have symmetric wall boundary conditions. The right boundary has free boundary conditions, where incoming flow is given an initial density and temperature and a velocity equal to the piston velocity $u_{\rm p}$. Any perturbations of the flow field are provided to the incoming density flow field, which is done by separating the flow into equal sized square bins with sides dx and prescribing some magnitude of fluctuations to the density.

3.4.2 Resolution Study

A resolution study was performed in order to determine the necessary resolution required for the simulations. The minimum resolution required was found by investigating the con-

vergence of the shock structure calculated for an elastic ($\varepsilon = 1$) system of disks in the given system of equations with diffusive effects.

Example shock structures at different resolutions are given in Fig. 3.7 for $u_\mathrm{p}/u_\mathrm{o} = 4.0$ and $\eta_\mathrm{o} = 0.012$, with the profiles of pressure, temperature and density.

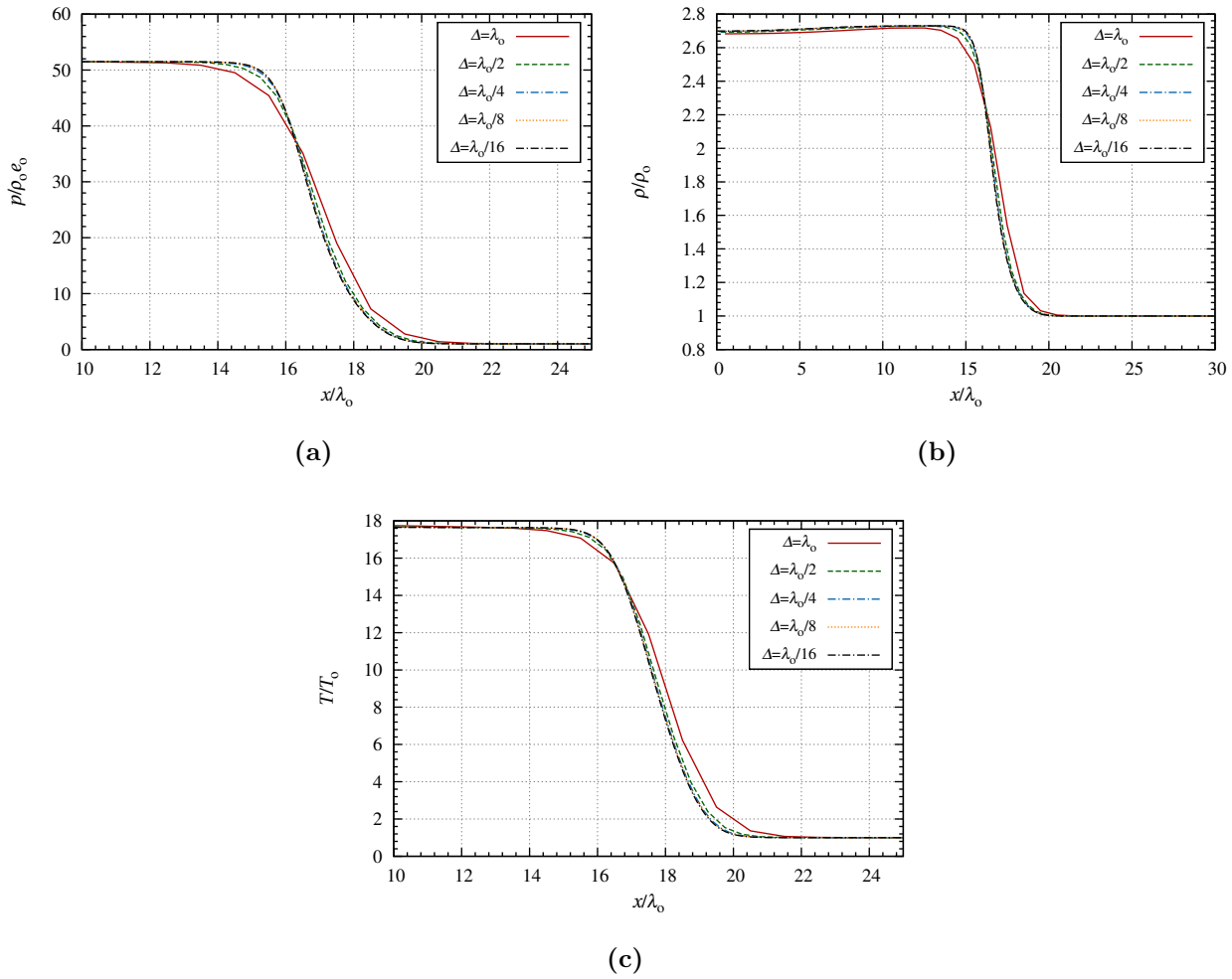

Figure 3.7: Comparison of *elastic* shock structure for (a) pressure, (b) density and (c) temperature, for various resolutions obtained from the hydrodynamic solver, with $u_\mathrm{p}/u_\mathrm{o} = 4.0$ and $\eta_\mathrm{o} = 0.012$.

The converged solution was determined by measuring the shock front thickness, which is where the sharpest gradients are expected to occur, and therefore require the finest resolution. The thickness is given by the ratio of the maximum gradient in density and the difference between the initial state (o) and post-stock state (∞):

$$\text{shock thickness} = \frac{\left(\frac{\partial \rho}{\partial x}\right)_{\max}}{(\rho_{\mathrm{o}} - \rho_{\infty})}. \tag{3.39}$$

Figure 3.8 shows how the shock thickness evolves for different piston velocities with different resolutions, for $\eta_{\mathrm{o}} = 0.012$. For a low piston velocity of $u_{\mathrm{p}}/u_{\mathrm{o}} = 1.0$, the thickness is shown to converge with a resolution $\Delta = \lambda_{\mathrm{o}}/4$. However, for higher piston velocities of $u_{\mathrm{p}}/u_{\mathrm{o}} = 4.0$ and 10.0, results indicate that a resolution of $\Delta = \lambda_{\mathrm{o}}/8$ is required at the most refined scale for a converged solution.

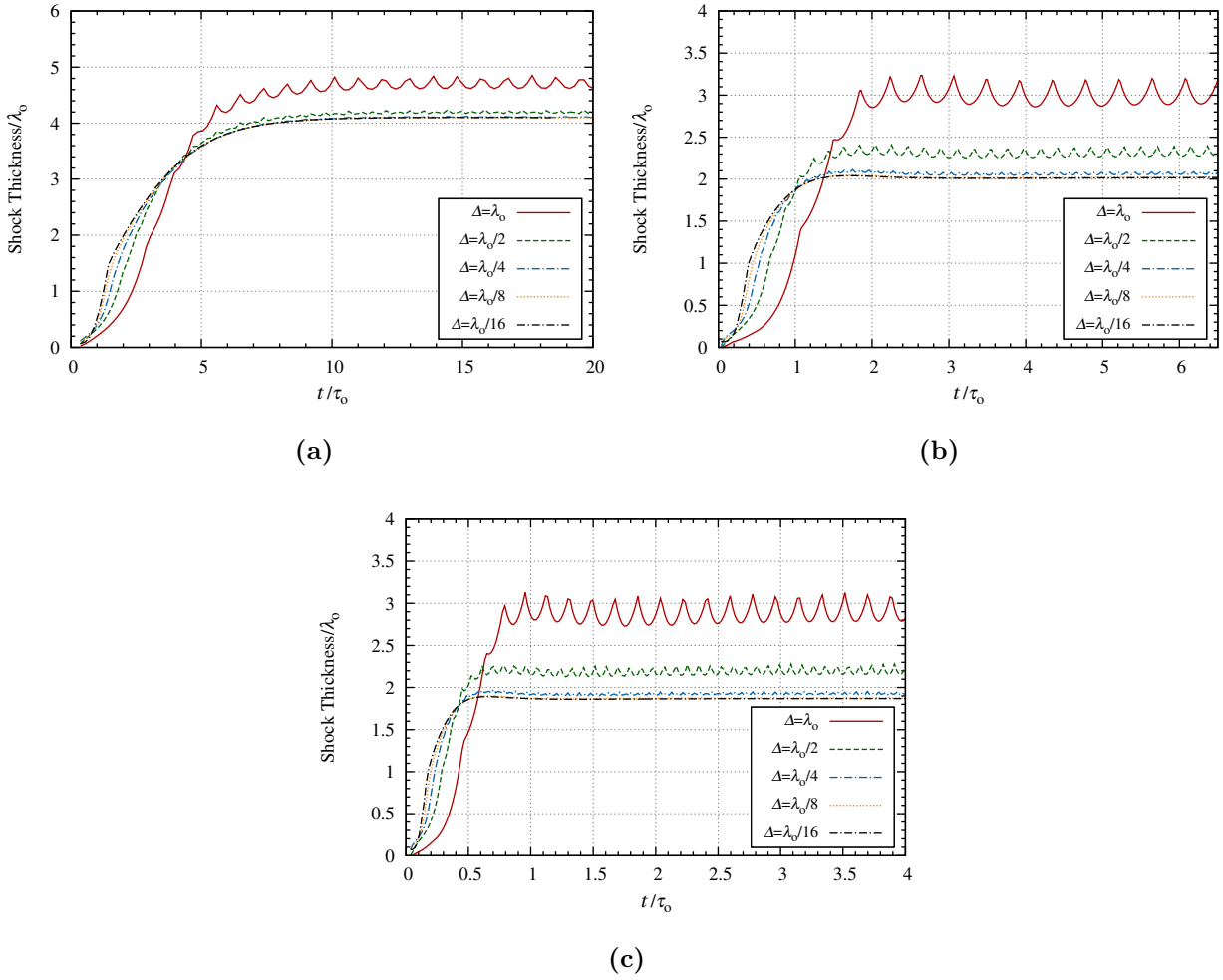

Figure 3.8: Comparison of *elastic* shock thickness obtained from the hydrodynamic solver for various resolutions with $\eta_{\mathrm{o}} = 0.012$ and (a) $u_{\mathrm{p}}/u_{\mathrm{o}} = 1.0$, (b) $u_{\mathrm{p}}/u_{\mathrm{o}} = 4.0$, and (c) $u_{\mathrm{p}}/u_{\mathrm{o}} = 10.0$.

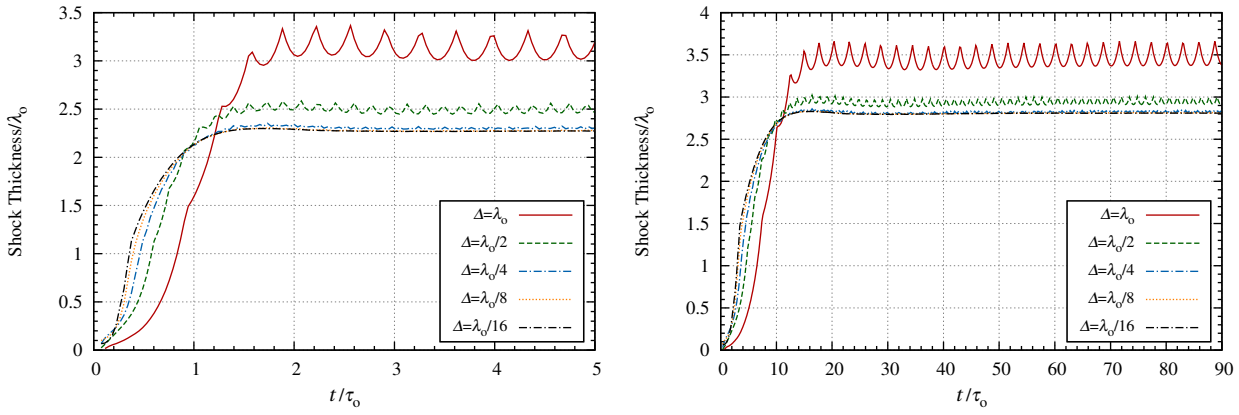

Figure 3.9: Comparison of *elastic* shock thickness obtained from the hydrodynamic solver for various resolutions with $u_p/u_o = 4.0$ and (a) $\eta_o = 0.05$ and (b) $\eta_o = 0.1$.

A minimum resolution of $\Delta = \lambda_o/8$ is also found to be needed for different values of η_o, as shown in Fig. 3.9 for $\eta_o = 0.05$ and 0.1, with a piston velocity of $u_p/u_o = 4.0$. Therefore, for the following chapters, when calculating shock waves using the continuum model, a resolution of $\Delta = \lambda_o/8$ was used.

3.4.3 Validation of Shock Jump Conditions

Past studies have been completed to derive the shock jump conditions for an elastic system of disks, given η_o and u_p [79]. The derivations are provided in Appendix C for completeness. In the current section, the continuum description is validated by comparing these expected shock jump conditions to those obtained from solving the N-S equations.

Figure 3.10 compares the theoretical shock jump conditions for density, pressure, and temperature with the shock structure obtained from the continuum solver, for a piston velocity of $u_p/u_o = 4$ and initial packing fractions of $\eta_o = 0.012$, 0.05, and 0.1. The results show that the post-shock conditions from the continuum solver agree with what is expected from the derived jump conditions, shown as dashed lines. Similar agreement between the

computed shock structure and theory is observed for different piston velocities, as shown in Fig. 3.11 for $\eta_o = 0.012$. These results confirm that the continuum model gives the jump conditions expected for a system of elastic disks.

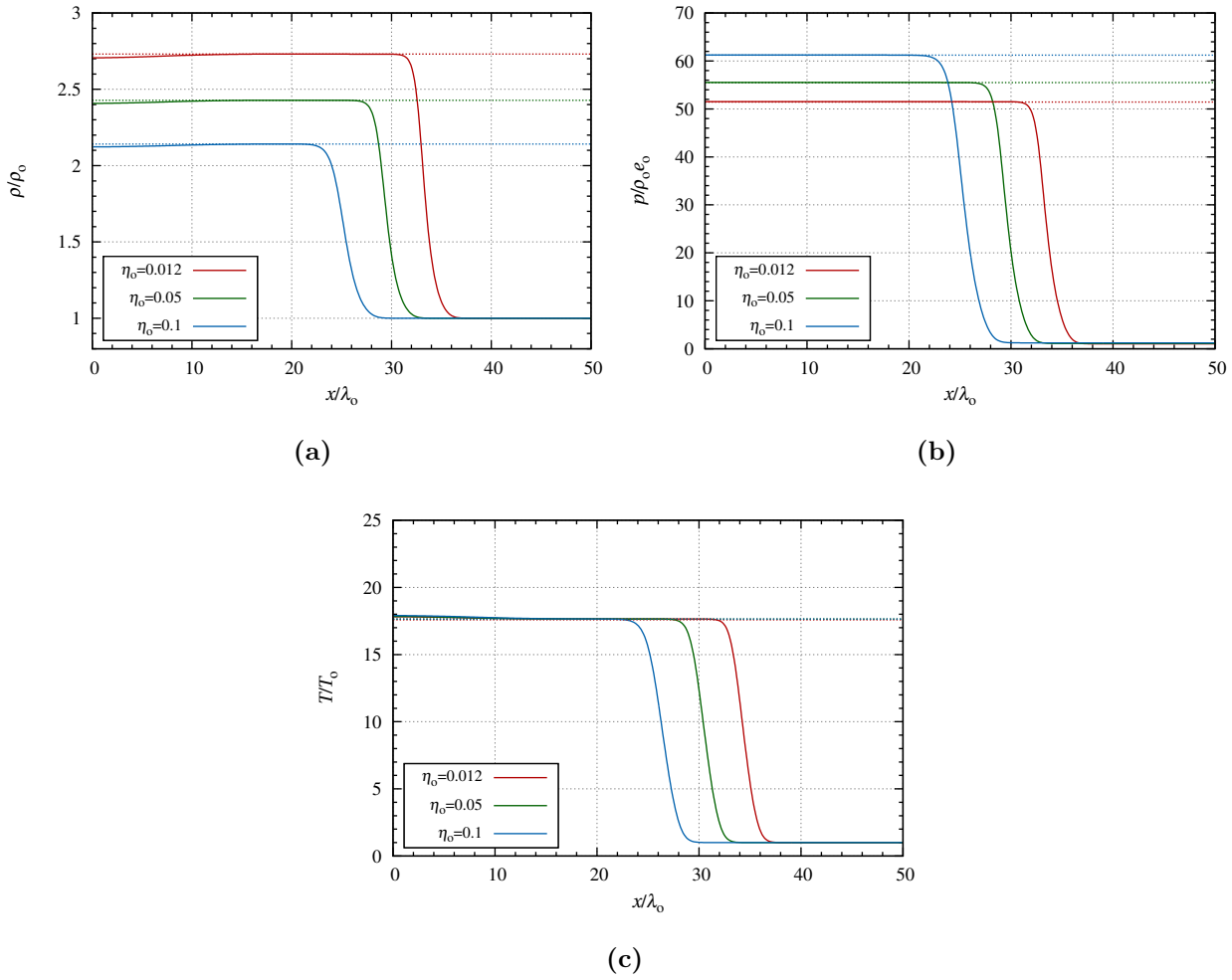

Figure 3.10: Profiles obtained numerically (in solid) for (a) density, (b) pressure and (c) temperature for a piston velocity of $u_p/u_o = 4$ and different initial packing fractions of $\eta_o = 0.1,\ 0.05$ and 0.012. The dashed lines represent the theoretical jump that is expected for the given parameters.

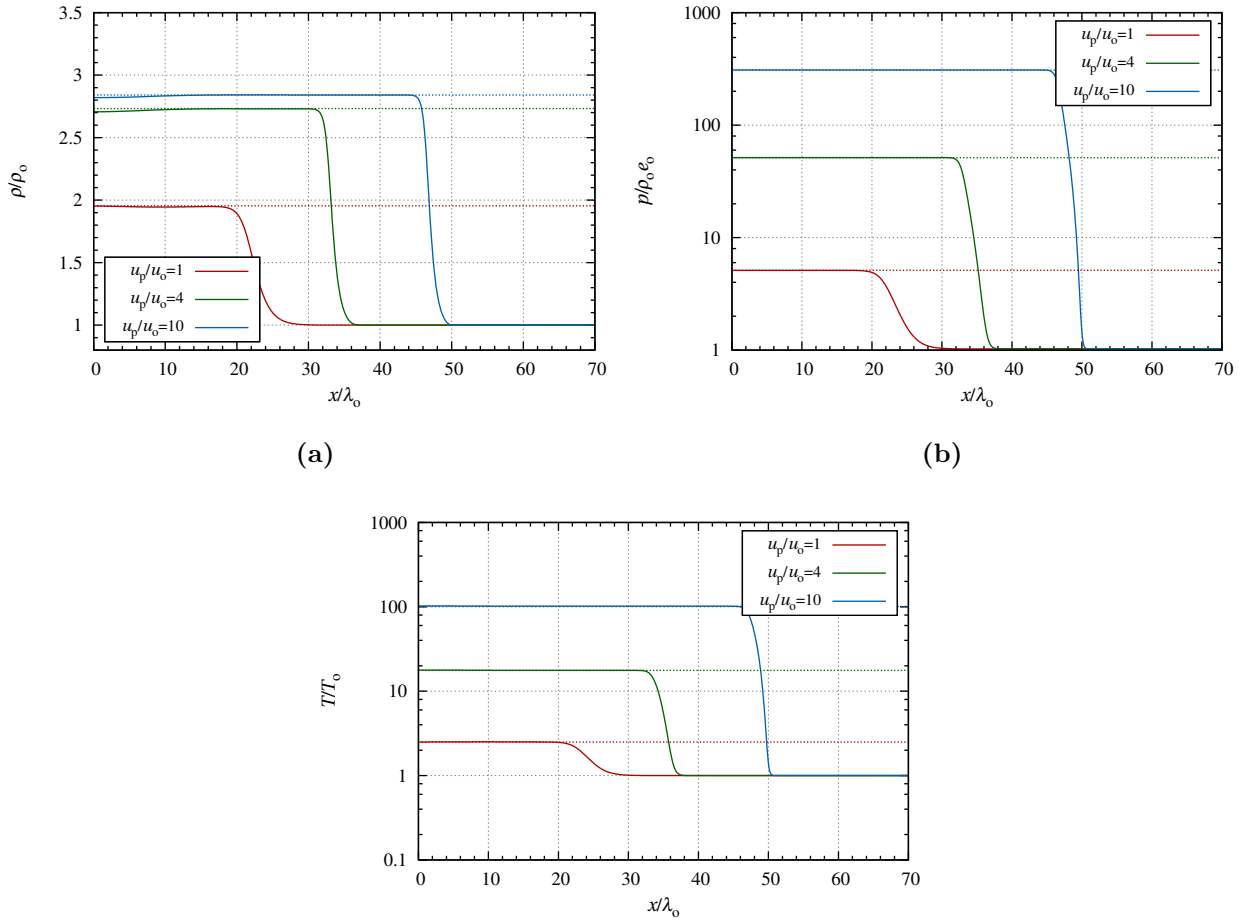

Figure 3.11: Profiles obtained numerically (in solid) for (a) density, (b) pressure and (c) temperature for piston velocities $u_p/u_o = 10$, 4 and 1, and $\eta_o = 0.012$. The dashed lines represent the theoretical jump that is expected for the given parameters.

3.5 Cooling Rate for Activated Inelastic Collisions

3.5.1 Modification of Cooling Rate

In the current model, which assumes activated inelastic collisions, inelastic collisions occur for only a fraction of collisions, making the cooling rate from (3.22) invalid. Therefore, a modification to the cooling rate is needed to solely account for the energy losses attributed

to inelastic collisions. To adjust the cooling rate, it is necessary to first examine the energy involved in collisions.

Details of the following derivation, including the underlying kinetic theory are presented in Appendix B.

To modify the cooling rate, it is appropriate to first obtain the rate of binary collisions per unit volume:

$$\tilde{n}^2\tilde{d}\frac{\tilde{m}}{2\tilde{k}\tilde{T}}\exp\left\{\frac{\tilde{m}\tilde{g}^2}{4\tilde{k}\tilde{T}}\right\}\tilde{g}^2\cos\psi d\tilde{g}d\psi. \tag{3.40}$$

This term gives the rate of binary collisions of a system of disks of mass $\tilde{m}$ with a number density $\tilde{n} = N/\tilde{A}$ that have a relative speed in the range of $\tilde{g}$ to $\tilde{g}+d\tilde{g}$, with an angle between the relative velocity and the line of action in the range of ψ to $\psi+d\psi$. Along the line of action, the relative velocity is $\tilde{u}_N = \tilde{g}\cos\psi$. Multiplying (3.40) by $\tilde{u}_N^2 = (\tilde{g}\cos\psi)^2$, and integrating over a range of $\tilde{u}_N$, one recovers the energy along the line of action for collisions with impact velocities within this range. Integrating $\tilde{u}_N$ from 0 to ∞ recovers the overall impact energy directly applicable to the initial cooling rate that assumes all collisions are inelastic (3.22). Integrating $\tilde{u}_N$ from $\tilde{u}^*$ to ∞ yields the energy involved along the line of action for impact velocities exceeding $\tilde{u}^*$. The *activation energy* $\tilde{E}_\mathrm{A}$ is found from the threshold $\tilde{u}^*$, which for disks of equal mass [82] are related with

$$\frac{1}{2}\frac{\tilde{u}^{*2}}{\tilde{u}_\mathrm{o}^2} = \frac{\tilde{E}_a}{\tilde{T}}. \tag{3.41}$$

To modify the cooling rate (3.22) that considers all collisions inelastic, the ratio of the average energy involved in activated collisions to the energy of all collisions is calculated as

$$\frac{\langle\tilde{u}_n^2\rangle(\tilde{u}_N > \tilde{u}^*)}{\langle\tilde{u}_n^2\rangle(\tilde{u}_N > 0)} = \exp\left\{\frac{\tilde{m}\tilde{u}^{*2}}{4\tilde{k}\tilde{T}}\right\}\left(1+\frac{\tilde{m}\tilde{u}^{*2}}{4\tilde{k}\tilde{T}}\right). \tag{3.42}$$

Since $\frac{1}{2}\tilde{m}\tilde{u}_\mathrm{o}^2 = \tilde{k}\tilde{T}$, multiplying this ratio with the cooling rate (3.22) yields the following

modified cooling rate in dimensional form:

$$\boxed{\tilde{\zeta}^* = -\frac{4}{\tilde{d}\sqrt{\pi}}\left(1-\varepsilon^2\right)\tilde{\rho}\tilde{T}^{3/2}\eta g_2(\eta)\exp\left\{-\frac{1}{2}\frac{\tilde{u}^{*2}}{\tilde{u}_\mathrm{o}^2}\right\}\left(1+\frac{1}{2}\frac{\tilde{u}^{*2}}{\tilde{u}_\mathrm{o}^2}\right).} \tag{3.43}$$

The non-dimensional modified cooling rate is

$$\boxed{\zeta^* = -\frac{4}{d\sqrt{\pi}}\left(1-\varepsilon^2\right)\rho T^{3/2}\eta g_2(\eta)\exp\left\{-\frac{1}{2}\frac{E_a}{T}\right\}\left(1+\frac{1}{2}\frac{E_a}{T}\right)} \tag{3.44}$$

where the activation energy $E_a/T = \frac{1}{2}u^{*2}/u_\mathrm{o}^2$. This cooling rate is applied to (3.38) for the continuum solver.

3.5.2 Comparison of Cooling Rate With Homogeneous Cooling Problem of Granular Gases

The newly derived cooling rate was validated by calculating the temperature evolution for the problem of a homogeneous cooling gas and compared with results from MD. In such a system, the energy equation (3.38) simplifies to

$$\frac{\mathrm{d}T}{\mathrm{d}t} = \frac{\zeta^*}{\rho} = -\frac{4}{d\sqrt{\pi}}\left(1-\varepsilon^2\right)T^{3/2}\eta g_2(\eta)\exp\left\{-\frac{1}{2}\frac{E_a}{T}\right\}\left(1+\frac{1}{2}\frac{E_a}{T}\right) \tag{3.45}$$

where $E_a/T = \frac{1}{2}u^{*2}/u_\mathrm{o}^2$. Equation (3.45) can therefore be numerically integrated and compared with MD to test its validity.

For the case where there is no activation threshold and there is a constant coefficient of restitution for colliding disks, the evolution of temperature follows Haff's law [10], which can be modified using the scaling previously introduced to be written as:

$$\frac{T(t)}{T_\mathrm{o}} = \frac{1}{\left(1+\frac{t}{2\sqrt{2}}\left(1-\varepsilon^2\right)\left(1+\frac{3}{16}a_2\right)\right)^2} \tag{3.46}$$

where

$$a_2 = \frac{16\,(1-\varepsilon)\,(1-2\varepsilon^2)}{57-25\varepsilon+30\varepsilon^2(1-\varepsilon)}. \tag{3.47}$$

The modified cooling rate was compared with results for disks with activated inelastic collisions from MD simulations with similar conditions. The evolution of temperature from MD was obtained by running simulations with $N = 10000$ disks and ensemble averaging the evolution over 10 simulations. The comparison of evolution for temperature with different initial packing factors and activation values u^* and η are shown in Fig. 3.12 for $\varepsilon = 0.95$ and Fig. 3.12 for $\varepsilon = 0.90$.

The results show that the modified cooling rate (3.45) (dashed lines) recovers what is obtained from MD (solid lines), for all conditions, with some minor discrepancies at large packing factors. For example, Fig. 3.12(a) for $\eta = 0.01$ and $\varepsilon = 0.95$, gives the same evolution for temperature between MD and theory for all cutoff values.

As η increases, and ε decreases, the differences between MD and the modified cooling rate show increasing differences, of approximately 5-10%. An example of these discrepancies is shown in Fig. 3.13(c) for $\eta = 0.1$ and $\varepsilon = 0.9$. It should be noted that MD is also shown to differ from Haff's law, where there is no cutoff value. This result has been previously attributed to a clustering phenomenon occurring due to non-homogeneity in the MD domain, causing a slower than expected cooling rate [83]. Therefore there may be a similar influence for the cases where there is an activation threshold.

These results indicate that the newly derived cooling rate accurately mimics the behaviour of colliding disks subject to activated inelastic collisions and is valid to compare with MD in subsequent chapters.

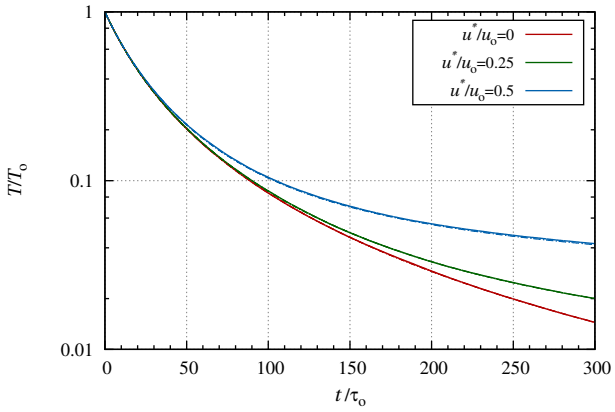

(a) $\eta = 0.01$

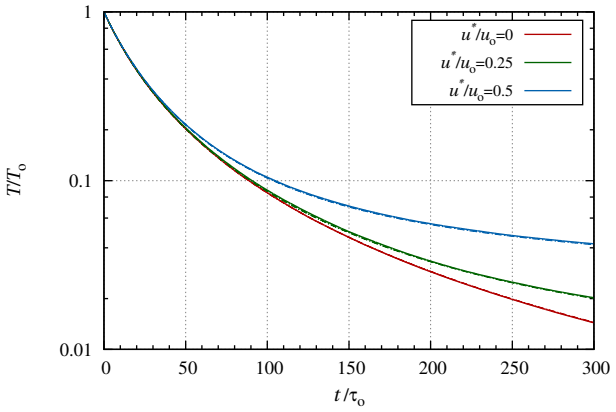

(b) $\eta = 0.05$

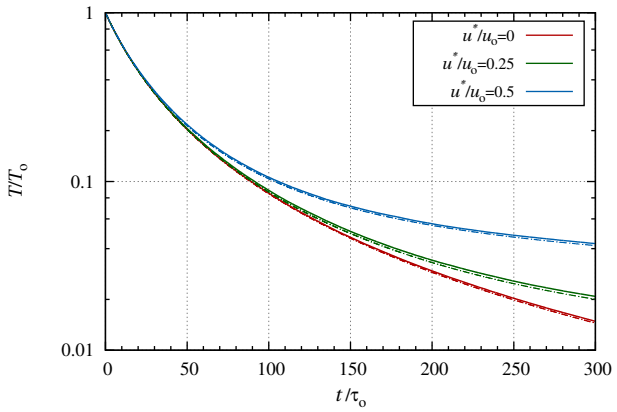

(c) $\eta = 0.1$

Figure 3.12: Comparison of temperature evolution for different values of u^* (normalized by u_o), where ε =0.95 and (a) $\eta = 0.01$, (b) $\eta = 0.05$, and (c) $\eta = 0.1$, with solid lines representing the MD results and dashed lines obtained from integrating the modified cooling rate.

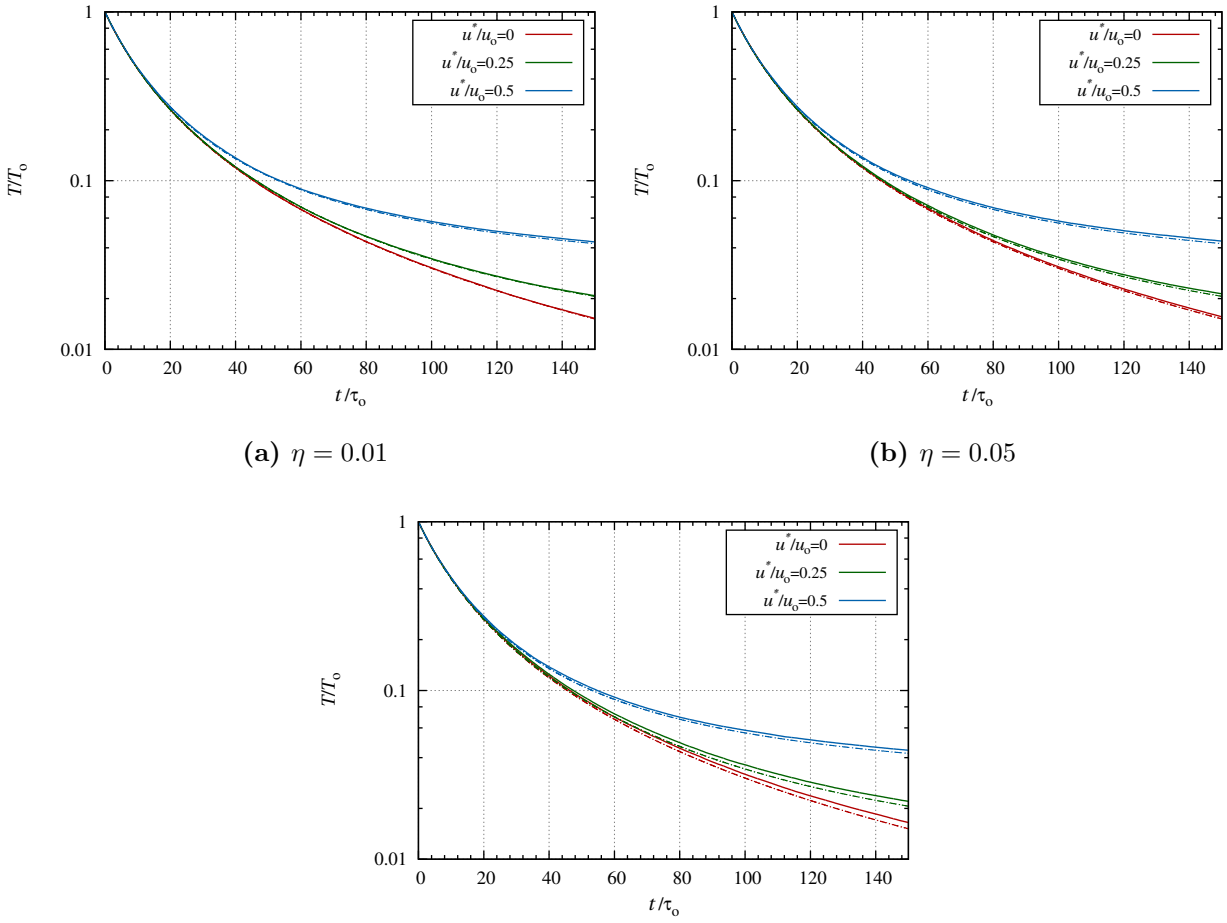

(a) $\eta = 0.01$

(b) $\eta = 0.05$

(c) $\eta = 0.1$

Figure 3.13: Comparison of temperature evolution for different values of u^* (normalized by u_o), where ε =0.90 and (a) $\eta = 0.01$, (b) $\eta = 0.05$, and (c) $\eta = 0.1$, with solid lines representing the MD results and dashed lines obtained from integrating the modified cooling rate.

3.6 Conclusions

The current chapter presented the details of the particle and continuum models that were used in this study. The continuum model was first validated by comparing the shock jump conditions with what is expected for elastic disks, yielding the expected results. The second validation test addressed the homogeneous cooling problem, which confirmed that the newly derived cooling rate used to treat activated inelastic collisions recovers what is calculated from MD. These two validation tests suggest that the two approaches can be combined in subsequent chapters, investigating piston driven shock waves *with* activated inelastic collisions.

Chapter 4

Structure and Properties of Steady State Shock Waves

4.1 Introduction

The current chapter presents the expected steady state structure for piston driven shock waves through systems of disks subject to inelastic activated collisions. This investigation was undertaken to compare with the two numerical modelling techniques. Deriving the steady state shock structure also allows for the stability of the shock wave to be investigated more thoroughly in later chapters.

The current analysis only considers the *inviscid* shock structure, where a frozen shock front is assumed, followed by a finite relaxation region. This is similar to the methodology used for the structure of exothermic shock waves (see, for example, [20]). The simplified inviscid structure that is considered is shown in Fig. 4.1. In the expected structure, a shock propagates into a medium at velocity D, where the initial state is characterized by subscript $(\,)_{\mathrm{o}}$. At the shock front, there is a sharp jump to the shocked state, denoted by subscript $(\,)_{\mathrm{s}}$. In the current analysis, a frozen shock jump is assumed, with no energy lost during this

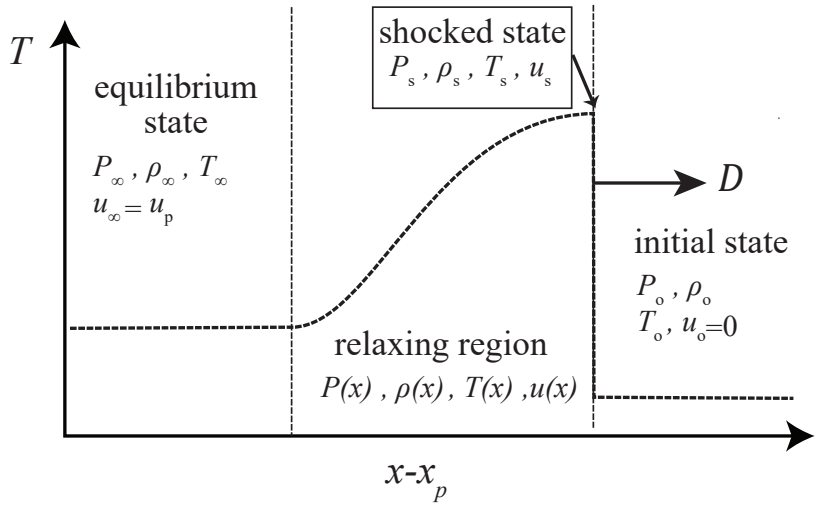

Figure 4.1: Expected inviscid steady-state structure of a piston driven shock wave propagating with speed D into an undisturbed medium (o). The structure is given in the piston frame of reference where the shock wave structure is given by the initial shocked state (s), followed by the relaxing region, and an equilibrium state at the piston (∞).

jump. Following the initial shock jump is the relaxing region, where the granular temperature decreases due to inelastic collisions, which is assumed to occur over a finite distance. The state within this region is variable in space, requiring the governing equations to be identified. Although there will always be a small fraction of inelastic collisions in the current model, the end of this relaxation region is identified as a region where there is a negligible number of collisions that are activated. At the end of the relaxation region is the 'equilibrium' state, denoted by subscript $(\,)_\infty$, which has speed u_p.

The first part presented in this chapter identifies the shock jump conditions for the shocked and equilibrium states, in terms of the initial state, and speeds D and u_p. The second part presents the details involved in obtaining the full structure by determining what occurs between the shock front and the equilibrium region. This was done by considering the travelling wave solution. After the structure was obtained, a parametric study was completed by varying the shock speed D, activation threshold u^*, coefficient of restitution ε, and initial packing factor η_o, to observe the effect each parameter has on the structure and various

properties.

4.2 The Shocked States

4.2.1 Initial Shock Jump State

To obtain the initial shock jump in a hard disk medium, the problem is considered whereby a shock wave propagates with velocity D and is supported behind the shock wave by some velocity u_s. In the absence of any inelastic collisions this supporting velocity is simply the piston velocity, $u_\mathrm{s} = u_\mathrm{p}$, with the derivation following that given in Appendix C and presented by Sirmas *et al.* [79]. Assuming diffusive fluxes are negligible in the pre- and post-shock states, the conservation of mass, linear momentum and energy, in the frame of reference of the shock yield [13]:

$$\frac{D}{v_\mathrm{o}} = \frac{(D - u_\mathrm{s})}{v_\mathrm{s}} \tag{4.1}$$

$$p_\mathrm{o} + \frac{D^2}{v_\mathrm{o}} = p_\mathrm{s} + \frac{(D - u_\mathrm{s})^2}{v_\mathrm{s}} \tag{4.2}$$

$$e_\mathrm{o} + p_\mathrm{o}v_\mathrm{o} + \frac{1}{2}D^2 = e_\mathrm{s} + p_\mathrm{s}v_\mathrm{s} + \frac{1}{2}(D - u_\mathrm{s})^2. \tag{4.3}$$

Combining (4.1),(4.2) and (4.3) to eliminate the two speeds, the accessible end states s across the shock wave can be represented by the shock Hugoniot relation [13]:

$$e_\mathrm{s}(p_\mathrm{s}, v_\mathrm{s}) - e_\mathrm{o}(p_\mathrm{o}, v_\mathrm{o}) = \frac{1}{2}(v_\mathrm{o} - v_\mathrm{s})(p_\mathrm{o} + p_\mathrm{s}). \tag{4.4}$$

This shock description is completely general, and depends on the equation of state $e(p, v)$ characterizing the particular medium.

Using Helfand's equation of state (3.19) and relation (3.18) with the definition of η, the

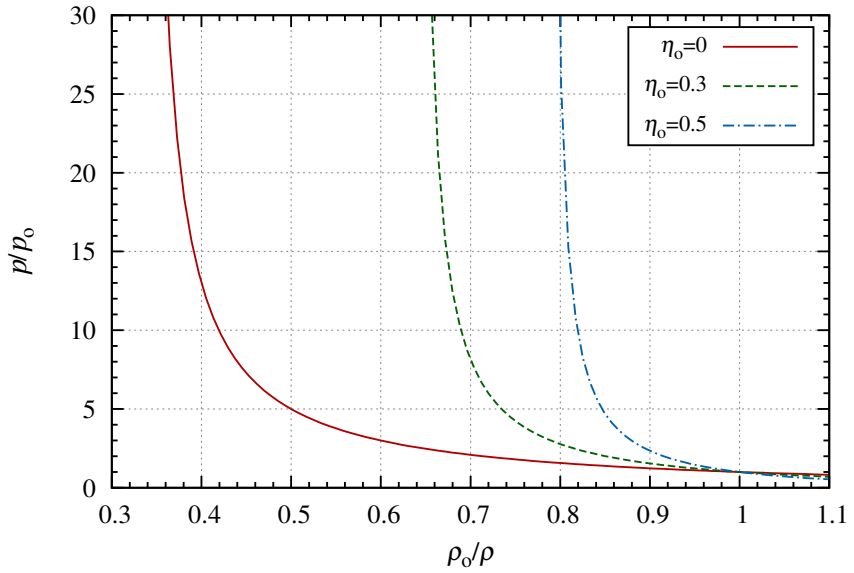

Figure 4.2: The relation between the shock overpressure and compression ratio represented on the shock Hugoniot for a hard disk medium in terms of the initial packing factor $\eta_{\rm o}$.

Hugoniot relation (4.4) can be used to express the variation of pressure with specific volume across the shock wave, yielding

$$\frac{p_{\rm s}}{p_{\rm o}} = \frac{\frac{1}{2}(1-\frac{v_{\rm s}}{v_{\rm o}}) + (1-\eta_{\rm o})^2}{\frac{v_{\rm s}}{v_{\rm o}}(1-\frac{v_{\rm o}}{v_{\rm s}}\eta_{\rm o})^2 - \frac{1}{2}(1-v_{\rm s}v_{\rm o})}. \tag{4.5}$$

Figure 4.2 displays the shock Hugoniot curves for three initial packing fractions. The maximum compression that can be achieved across the shock wave can be found by letting $\frac{p_{\rm s}}{p_{\rm o}} \to \infty$ in (4.5). This corresponds to letting the denominator in (4.5) equate to zero, yielding a quadratic for which the largest root is the physically attainable solution. The maximum compression achievable is thus

$$\left(\frac{v_{\rm s}}{v_{\rm o}}\right)_{\rm max} = \frac{1}{6}\left(1 + 4\eta_{\rm o} + \sqrt{(1-8(\eta_{\rm o}-1)\eta_{\rm o}}\right), \tag{4.6}$$

which is shown in Fig. 4.3 in terms of $\eta_{\rm o}$.

The shock jump conditions are now parameterized with the Mach number of the shock

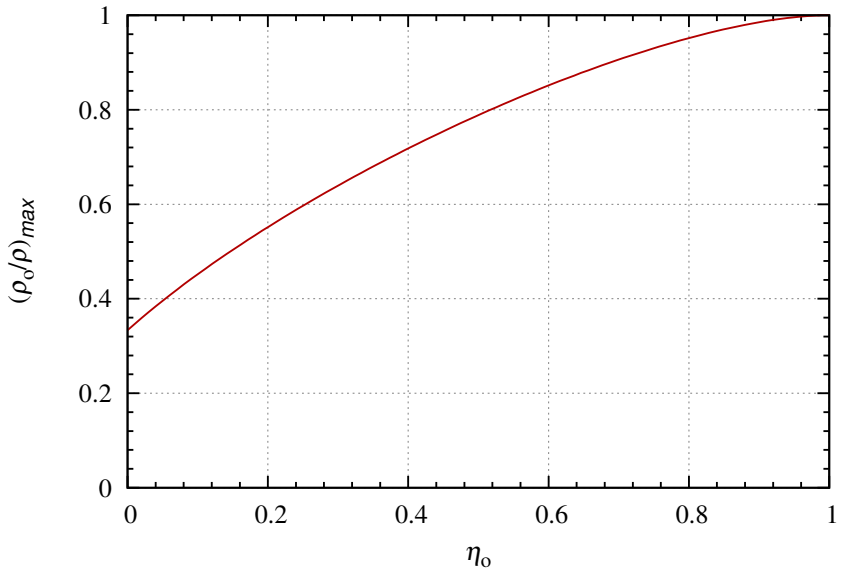

Figure 4.3: The maximum compression ratio achieved behind a frozen shock in terms of the initial packing factor η_o.

wave M_o. From the mass (4.1) and momentum (4.2) equations, and using (3.19) and relation (3.18), the overpressure can be expressed across the shock wave in terms of the shock Mach number and compression ratio across the shock. This yields the so-called Rayleigh line

$$\frac{p_s}{p_o} = 1 + \psi \left(1 - \frac{v_s}{v_o}\right) \tag{4.7}$$

where ψ is related to the shock Mach number and the initial value of the isentropic exponent γ:

$$\psi \equiv \frac{D^2}{p_o v_o} = \gamma_o \frac{D^2}{{c_o}^2} = \gamma_o {M_o}^2. \tag{4.8}$$

The properties across a shock wave for a given shock strength parameter ψ and the initial packing fraction η_o can be found by calculating the intersection of the Hugoniot curve and Raleigh line. By equating (4.5) and (4.7), the conditions behind the initial shock jump are

given as

$$\frac{v_\mathrm{s}}{v_\mathrm{o}} = \frac{4+\psi+4\psi+4\psi\eta_\mathrm{o}+\sqrt{-24\psi(1+\psi)\eta_\mathrm{o}^2+(4+\psi+4\psi\eta_\mathrm{o})^2}}{6\psi} \tag{4.9a}$$

$$\frac{p_\mathrm{s}}{p_\mathrm{o}} = 1+\psi\left(1-\frac{v_\mathrm{s}}{v_\mathrm{o}}\right) \tag{4.9b}$$

$$\frac{u_\mathrm{s}}{D} = 1-\frac{v_\mathrm{s}}{v_\mathrm{o}} \tag{4.9c}$$

$$\frac{T_\mathrm{s}}{T_\mathrm{o}} = \frac{p_\mathrm{s}}{p_\mathrm{o}}\frac{v_\mathrm{s}}{v_\mathrm{o}}\frac{(1-\eta_\mathrm{o}\frac{v_\mathrm{o}}{v_\mathrm{s}})^2}{(1-\eta_\mathrm{o})^2}. \tag{4.9d}$$

In the limit of a high Mach number, where $p_\mathrm{o} \to 0$ in (4.9b), the post shock pressure can be written as:

$$\frac{p_\mathrm{s}}{p_\mathrm{o}} = \frac{D^2}{p_\mathrm{o}v_\mathrm{o}}\left(1-\frac{v_\mathrm{s}}{v_\mathrm{o}}\right) = \frac{u_s^2}{p_\mathrm{o}v_\mathrm{o}}\frac{1}{\left(1-\frac{v_\mathrm{s}}{v_\mathrm{o}}\right)}. \tag{4.10}$$

This relationship, combined with the maximum compression ratio for a given η_o in (4.6), yields the initial shocked states in the limit of a high Mach number, which are a function of η_o and D only.

Alternatively, the temperature ratio can be written more conveniently with the post-shock velocity. This can be taken directly from the Hugoniot relation (4.4) which, after some manipulation, can be re-written as

$$\frac{T_\mathrm{s}}{T_\mathrm{o}} = \frac{e_\mathrm{s}}{e_\mathrm{o}} = 1+\frac{1-\frac{v_\mathrm{s}}{v_\mathrm{o}}}{(1-\eta_\mathrm{o})^2}+\frac{1}{2}\frac{{u_\mathrm{s}}^2}{e_\mathrm{o}}. \tag{4.11}$$

In the limit of a large shock velocity, the first two terms are bounded by the maximum compression ratio, whereas the final term will continue to grow from (4.9b). Therefore the temperature behind the shock front for a high shock strength can be approximated at this limit as

$$\frac{T_\mathrm{s}}{T_\mathrm{o}} \approx \frac{1}{2}\frac{{u_\mathrm{s}}^2}{e_\mathrm{o}}, \tag{4.12}$$

or, written alternatively with (4.9b) as

$$\frac{T_\mathrm{s}}{T_\mathrm{o}} \approx \frac{1}{2}\frac{D^2}{e_\mathrm{o}}\left(1-\left(\frac{v_\mathrm{s}}{v_\mathrm{o}}\right)_{\max}\right)^2. \tag{4.13}$$

This is a useful simplification, especially when determining whether a given piston velocity will provide sufficient energy to activate inelastic collisions.

4.2.2 Equilibrium State

The next set of needed jump conditions are those that relate the equilibrium state to the initial state. Since there will always be a small fraction of collisions that are inelastic, there will never be a state at true equilibrium. However, the present work assumes that the equilibrium region can be identified as the state where only a small fraction of collisions are activated. Quantitatively the equilibrium state was approximated as the point where the amount of energy involved in activated collisions only represents, at maximum, 1% of the overall energy involved in collisions. Although 1% is taken arbitrarily, it is shown later in this section that this value is sufficient to represent the equilibrium region. For the derived cooling rate (3.44) this percentage is represented in terms of the activation energy as:

$$X = \exp\left\{-\frac{1}{2}\frac{E_\mathrm{A}}{T}\right\}\left(1+\frac{1}{2}\frac{E_\mathrm{A}}{T}\right) \leq 0.01. \tag{4.14}$$

This gives an approximate temperature for the equilibrated state as

$$T_\infty \approx 0.075 E_\mathrm{A}. \tag{4.15}$$

With the temperature of the equilibrated state defined, the Hugoniot of all equilibrium states can be given as:

$$\frac{p_\infty}{p_\mathrm{o}} = 0.075 E_\mathrm{A} \frac{v_\mathrm{o}}{v_\infty} \left(\frac{1-\eta_\mathrm{o}}{1-\frac{v_\mathrm{o}}{v_\infty}\eta_\mathrm{o}} \right)^2 . \tag{4.16}$$

Based on the condition for equilibrium, the end state will only lie on this Hugoniot if T_s from (4.12) is greater than T_∞, which implies the presence of a relaxing structure. For the case where $T_\mathrm{s} < 0.075 E_\mathrm{A}$, the shock wave can be characterized by only the elastic collisions, and the shocked state presented in Sec. 4.2.1 will also represent the equilibrium state, with $u_\mathrm{s} = u_\mathrm{p}$.

Combined with (4.12), the minimum piston velocity that yields a relaxing structure can therefore be approximated as:

$$T_\mathrm{s} = 0.075 E_\mathrm{A} = \frac{1}{2} {u_\mathrm{p}}^2 \quad \rightarrow \quad u_\mathrm{p} \approx 0.39 E_\mathrm{A}^{1/2}. \tag{4.17}$$

With $E_\mathrm{A} = \frac{1}{2} u^{*2}$, the transition between elastic and relaxing structures can be related to the ratio u_p/u^* as

$$\frac{u_\mathrm{p}}{u^*} \approx 0.275. \tag{4.18}$$

Figure 4.4 shows the results for the fraction of energy involving inelastic collisions behind the shock wave based on the initial piston velocity, obtained by combining (4.14) and (4.12). The results demonstrate that the fraction of inelastic collisions drops dramatically below $u_\mathrm{p}/u^* = 0.2 - 0.3$. This means that even if a different threshold were taken (for example, 0.1% or 0.01% activated collisions), a transition point similar to that given by taking the 1% threshold would exist, and therefore (4.15) is valid for the current study.

Similar to the shocked state, the post-shock equilibrium properties may be found by equating the Rayleigh line and the Hugoniot. The Rayleigh line takes the same slope as that

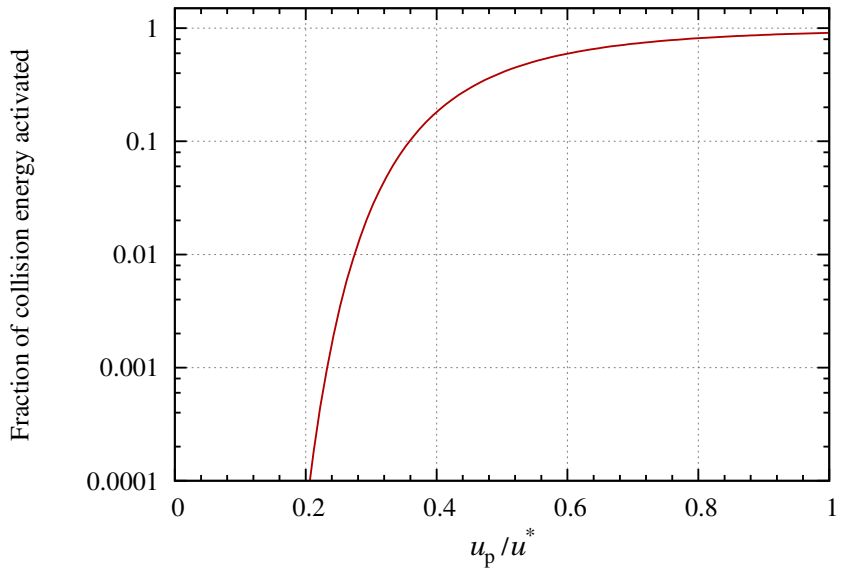

Figure 4.4: Relationship between the fraction of energy involved in activated collisions and the ratio of piston speed to activation threshold speed, assuming the velocity behind the shock wave is the piston speed.

used for the shocked state variables, with

$$\frac{p_\infty}{p_o} = 1 + \psi \left(1 - \frac{v_\infty}{v_o}\right). \tag{4.19}$$

A simple analytical result can not be obtained for the equilibrium states (as was done for the initial shocked state), although results obtained numerically are presented later in this chapter.

Limiting values can be given by considering the limit of a high Mach number, where p_o is negligible. Applying this to (4.16) yields

$$\left(\frac{v_\infty}{v_o}\right)_{\max} = \eta_o \tag{4.20}$$

and a simple relationship between D and u_p can be obtained by considering the conservation

of mass across the full structure, which can simplify to,

$$D = \frac{u_{\mathrm{p}}}{(1-\eta_{\mathrm{o}})}. \tag{4.21}$$

Finally, by taking $p_{\mathrm{o}} \to 0$ in (4.19) and combining with (4.8), (4.20) and (4.21), the equilibrium pressure in the limit of high Mach number can be given as

$$p_{\infty} = \frac{u_{\mathrm{p}}^2}{v_{\mathrm{o}}(1-\eta_{\mathrm{o}})}. \tag{4.22}$$

Alternatively, using the equation of state with $p_{\mathrm{o}} = \frac{e_{\mathrm{o}}}{v_{\mathrm{o}}(1-\eta_{\mathrm{o}})^2}$, the pressure can simply be written as

$$\frac{p_{\infty}}{p_{\mathrm{o}}} = \frac{u_{\mathrm{p}}^2}{e_{\mathrm{o}}}(1-\eta_{\mathrm{o}}). \tag{4.23}$$

4.3 The Shock Structure

The solution for the shock wave *structure* for the described system of disks undergoing activated inelastic collisions is presented in this section. It was obtained by deriving the equations describing the relaxing shock structure, and integrating between the boundary states obtained in Sec. 4.2.

4.3.1 Governing Equations

Consider a system of smooth inelastic disks. For such a system, the non-dimensional hydrodynamic equations for mass, momentum and energy from (3.38) can be re-written in material

derivative form for an inviscid medium:

$$\frac{\mathrm{D}\rho}{\mathrm{D}t} + \rho\boldsymbol{\nabla}\cdot\boldsymbol{u} = 0 \tag{4.24}$$

$$\rho\frac{\mathrm{D}\boldsymbol{u}}{\mathrm{D}t} + \boldsymbol{\nabla}p = 0 \tag{4.25}$$

$$\rho\frac{\mathrm{D}e_{tot}}{\mathrm{D}t} + \boldsymbol{\nabla}\cdot(p\boldsymbol{u}) = \zeta^* \tag{4.26}$$

where $\frac{\mathrm{D}(\ )}{\mathrm{D}t} = \frac{\partial(\ )}{\partial t} + \vec{u}\cdot\vec{\nabla}(\ )$, and the modified cooling rate accounting for the activation threshold u^* is taken as:

$$\zeta^* = -\frac{4}{d\sqrt{\pi}}\left(1-\varepsilon^2\right)\rho T^{3/2}\eta g_2(\eta)\exp\left\{-\frac{1}{2}\frac{E_\mathrm{A}}{T}\right\}\left(1+\frac{1}{2}\frac{E_\mathrm{A}}{T}\right). \tag{4.27}$$

Expanding the total energy to have an expression with internal energy, (4.26) may be re-written as:

$$\rho\frac{\mathrm{D}e}{\mathrm{D}t} + \rho\frac{1}{2}\frac{\mathrm{D}\boldsymbol{u}\cdot\boldsymbol{u}}{\mathrm{D}t} + \boldsymbol{\nabla}\cdot(p\boldsymbol{u}) = \zeta^*.$$

Since $\frac{1}{2}\frac{\mathrm{D}\boldsymbol{u}\cdot\boldsymbol{u}}{\mathrm{D}t} = \boldsymbol{u}\frac{\mathrm{D}\boldsymbol{u}}{\mathrm{D}t}$, using the conservation of momentum (4.25) and the chain rule, this equation is written as:

$$\rho\frac{\mathrm{D}e}{\mathrm{D}t} - \frac{p}{\rho}\frac{\mathrm{D}\rho}{\mathrm{D}t} = \zeta^*. \tag{4.28}$$

With the internal energy a function of ρ and p, the material derivative for $e(\rho,p)$ can be expanded as a perfect differential:

$$\frac{\mathrm{D}e}{\mathrm{D}t} = \frac{\mathrm{D}\rho}{\mathrm{D}t}\left(\frac{\partial e}{\partial\rho}\right)_\mathrm{p} + \frac{\mathrm{D}p}{\mathrm{D}t}\left(\frac{\partial e}{\partial p}\right)_\rho. \tag{4.29}$$

Plugging (4.29) into (4.28) yields:

$$\begin{aligned}
\rho\frac{\mathrm{D}\rho}{\mathrm{D}t}\left(\frac{\partial e}{\partial \rho}\right)_{\mathrm{p}} + \rho\frac{\mathrm{D}p}{\mathrm{D}t}\left(\frac{\partial e}{\partial p}\right)_{\rho} - \frac{p}{\rho}\frac{D\rho}{Dt} &= \zeta^* \\
\rho\frac{\mathrm{D}\rho}{\mathrm{D}t}\left(\left(\frac{\partial e}{\partial \rho}\right)_{\mathrm{p}} - \frac{p}{\rho^2}\right) + \rho\frac{\mathrm{D}p}{\mathrm{D}t}\left(\frac{\partial e}{\partial p}\right)_{\rho} &= \zeta^* \\
\frac{\mathrm{D}\rho}{\mathrm{D}t}\left(\frac{\left(\frac{\partial e}{\partial \rho}\right)_{\mathrm{p}} - \frac{p}{\rho^2}}{\left(\frac{\partial e}{\partial p}\right)_{\rho}}\right) + \frac{\mathrm{D}p}{\mathrm{D}t} &= \frac{\zeta^*}{\rho\left(\frac{\partial e}{\partial p}\right)_{\rho}}.
\end{aligned} \tag{4.30}$$

Given that the general sound speed squared c^2 is (from Appendix C.1)

$$c^2 = \left(\frac{\frac{p}{\rho^2} - \left(\frac{\partial e}{\partial \rho}\right)_{\mathrm{p}}}{\left(\frac{\partial e}{\partial p}\right)_{\rho}}\right), \tag{4.31}$$

and $\frac{\mathrm{D}\rho}{\mathrm{D}t}$ can be replaced from (4.24), (4.30) may be re-written as:

$$\frac{1}{\rho}\frac{\mathrm{D}p}{\mathrm{D}t} + c^2\boldsymbol{\nabla}\cdot\boldsymbol{u} = \frac{\zeta^*}{\rho^2\left(\frac{\partial e}{\partial p}\right)_{\rho}}. \tag{4.32}$$

The modified conservation equations used in constructing the steady shock structure are now:

$$\frac{D\rho}{Dt} + \rho\boldsymbol{\nabla}\cdot\boldsymbol{u} = 0 \tag{4.24}$$

$$\frac{D\boldsymbol{u}}{Dt} + \frac{1}{\rho}\boldsymbol{\nabla}p = 0 \tag{4.25}$$

$$\frac{1}{\rho}\frac{\mathrm{D}p}{\mathrm{D}t} + c^2\boldsymbol{\nabla}\cdot\boldsymbol{u} = \frac{\zeta^*}{\rho^2\left(\frac{\partial e}{\partial p}\right)_{\rho}}. \tag{4.32}$$

For a one-dimensional shock structure, (4.24),(4.25) and (4.32) may be re-written by expand-

ing the material derivative ($\frac{D}{Dt} = \frac{\partial}{\partial t} + u\frac{\partial}{\partial x}$), yielding:

$$\frac{\partial \rho}{\partial t} + u\frac{\partial \rho}{\partial x} + \rho\frac{\partial u}{\partial x} = 0 \tag{4.33}$$

$$\frac{\partial u}{\partial t} + u\frac{\partial u}{\partial x} + \frac{1}{\rho}\frac{\partial p}{\partial x} = 0 \tag{4.34}$$

$$\frac{\partial p}{\partial t} + u\frac{\partial p}{\partial x} + c^2\frac{\partial u}{\partial x} = \frac{\zeta^*}{\rho^2\left(\frac{\partial e}{\partial p}\right)_\rho}. \tag{4.35}$$

4.3.2 Travelling Wave Solution

The next step in the derivation is to convert the governing equations into the shock frame of reference. To change variables to the shock fixed frame of reference, coordinate z was introduced to measure the distance behind the shock front that is travelling at velocity D, i.e.,

$$z = x - \int_0^t D(t)dt \tag{4.36}$$

or for a constant D

$$z = x - Dt. \tag{4.37}$$

Time is also transformed in this reference, with $\tau = t$. The partial derivatives with respect to x and t are now written in terms of z and τ, which for some property f may be transformed with

$$\begin{aligned} \frac{\partial f}{\partial t} &= \frac{\partial f}{\partial z}\frac{\partial z}{\partial t} + \frac{\partial f}{\partial \tau}\frac{\partial \tau}{\partial t} = -D\frac{\partial f}{\partial z} + \frac{\partial f}{\partial \tau} \\ \frac{\partial f}{\partial x} &= \frac{\partial f}{\partial z}\frac{\partial z}{\partial x} + \frac{\partial f}{\partial \tau}\frac{\partial \tau}{\partial x} = \frac{\partial f}{\partial z}. \end{aligned} \tag{4.38}$$

Since the derivation is for the *steady state* structure, there are no changes with time (i.e., $\frac{\partial}{\partial \tau} = 0$), which simplifies the transformations to

$$\begin{aligned} \frac{\partial f}{\partial t} &= -D\frac{\mathrm{d}f}{\mathrm{d}z} \\ \frac{\partial f}{\partial x} &= \frac{\mathrm{d}f}{\mathrm{d}z}. \end{aligned} \tag{4.39}$$

Applying these transformations to (4.33)-(4.35) gives the following governing equations in the *shock frame* of reference:

$$\frac{\mathrm{d}\rho}{\mathrm{d}z}(u-D)+\rho\frac{\mathrm{d}u}{\mathrm{d}z} = 0 \tag{4.40}$$

$$\frac{\mathrm{d}u}{\mathrm{d}z}(u-D)+\frac{1}{\rho}\frac{\mathrm{d}p}{\mathrm{d}z} = 0 \tag{4.41}$$

$$\frac{1}{\rho}\frac{\mathrm{d}p}{\mathrm{d}z}(u-D)+c^2\frac{\mathrm{d}u}{\mathrm{d}z} = \frac{\zeta^*}{\rho^2\left(\frac{\partial e}{\partial p}\right)_\rho}. \tag{4.42}$$

Combining the equations and isolating for each differential yields

$$\frac{\mathrm{d}\rho}{\mathrm{d}z} = -\frac{\theta\rho}{\left(1-\frac{(D-u)^2}{c^2}\right)(D-u)} \tag{4.43}$$

$$\frac{\mathrm{d}u}{\mathrm{d}z} = \frac{\theta}{1-\frac{(D-u)^2}{c^2}} \tag{4.44}$$

$$\frac{\mathrm{d}p}{\mathrm{d}z} = -\frac{\theta\rho(D-u)}{1-\frac{(D-u)^2}{c^2}} \tag{4.45}$$

where the thermicity is defined as

$$\theta \equiv \zeta^*/c^2\rho^2\left(\frac{\partial e}{\partial p}\right)_\rho. \tag{4.46}$$

This set of equations gives the velocity in the lab frame of reference, but by replacing $D-u$ with u it can be written in a steady frame with the shock wave, giving

$$\boxed{\begin{aligned}\frac{\mathrm{d}\rho}{\mathrm{d}z} &= -\frac{\theta\rho}{\xi u} \qquad (4.47a)\\ \frac{\mathrm{d}u}{\mathrm{d}z} &= \frac{\theta}{\xi} \qquad (4.47b)\\ \frac{\mathrm{d}p}{\mathrm{d}z} &= -\frac{\theta\rho u}{\xi} \qquad (4.47c)\end{aligned}}$$

where $\xi = 1-M^2$ and $M = u/c$.

Equations (4.47)(a)-(c) can be used to integrate for the spatial evolution of density, velocity and pressure across the shock structure given the appropriate boundary conditions. Temperature can also found by using the appropriate equation of state.

4.3.3 Boundary Conditions

The boundary conditions must be considered in order to compute the steady state structure using (4.47). For the described system the two boundaries are the initial shocked state (at $z = 0$) and the equilibrium state (at $z \to -\infty$). The initial shocked state is defined by the shock-jump states obtained from (4.9). The rear boundary condition does not need to be defined, as it is automatically satisfied by the conservation laws.

4.4 Results for Shock Structure

The role that the parameters D, u^*, ε, and η_o play on the shock structures was investigated and is presented in the current section. The resulting structures were found by integrating (4.47) using a 4th order Runge-Kutta scheme.

4.4.1 Role of D on Shock Structure

Figure 4.5 shows the effect of the shock front speed D on the structure, with the macroscopic states (ρ, p, T, and u) shown for varying D, where $u^*/u_o = 10$, $\varepsilon = 0.95$ and $\eta_o = 0.012$. As expected for increasing D, the jumps in temperature and pressure are higher at the shock front. The density is not noticeably higher since the shock strengths are sufficiently strong to approach the maximum compaction for elastic disks. Following the shock front there are sharp changes in density, pressure, and temperature. Results show that increasing D causes the density to increase higher, which can be attributed to the larger cooling rate, also represented by a sharper drop in temperature. The velocity also decreases within the

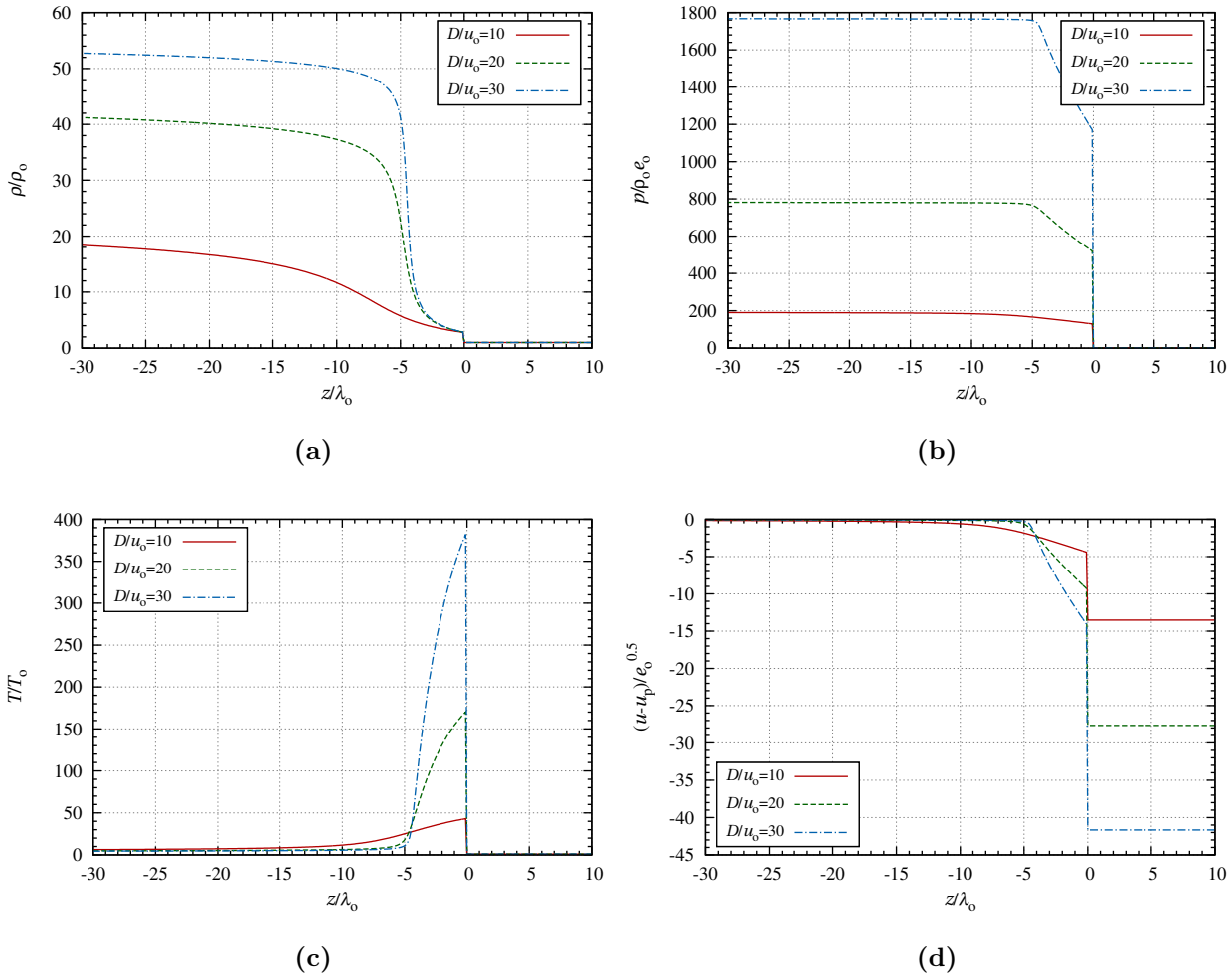

Figure 4.5: Steady state shock distribution of (a) density, (b) pressure, (c) temperature, and (d) velocity obtained for different shock speeds D (normalized by u_o), with $u^*/u_o = 10$, $\varepsilon = 0.95$ and $\eta_o = 0.012$.

relaxation region, approaching the velocity of the piston. In comparing the distance it takes for the temperature and pressure to stabilize to a near-equilibrium state, it can be seen that stronger shock waves yield a shorter relaxation region. Although the pressure appears to come to equilibrium, the density still increases, albeit at a slower rate, due to a small fraction of collisions still being inelastic.

4.4.2 Role of ε on Shock Structure

Figure 4.6 shows the resulting shock structures for varying ε, with $D/u_o = 20$, $u^*/u_o = 10$ and $\eta_o = 0.012$. The macroscopic states at the shock front are all equal for different values of ε, as expected for equal shock speeds and considering that the initial shock jump is independent of ε. The noticeable difference between the results is that the relaxation region becomes shorter with decreasing ε, represented by the sharper changes in all properties. The pressure in the equilibrium region is shown to be independent of ε, although the density and temperature show small differences. However, using the criteria for equilibrium (4.15), the approximated state at equilibrium is independent of ε since the elastic equation of state is used.

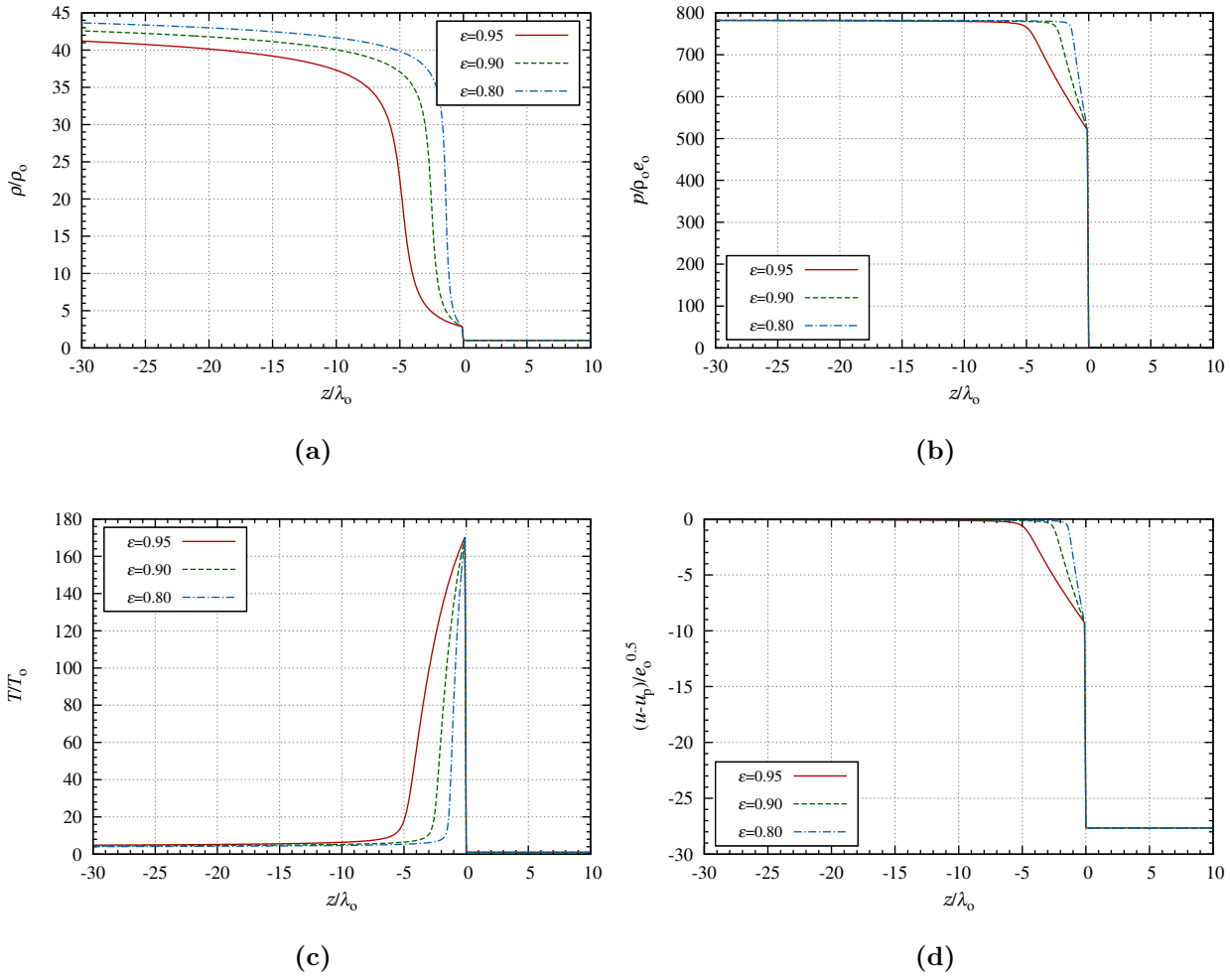

Figure 4.6: Steady state shock distribution of (a) density, (b) pressure, (c) temperature, and (d) velocity obtained for different values of ε, with $D/u_o = 20$, $u^*/u_o = 10$, and $\eta_o = 0.012$.

4.4.3 Role of η_o on Shock Structure

Figure 4.7 shows the resulting shock structures for varying initial packing ratio η_o, with $D/u_o = 20$, $u^*/u_o = 10$ and $\varepsilon = 0.95$. The density, pressure, and temperature are shown to decrease at the shock front with increasing η_o, which is expected from the elastic shock jump equations (4.9). Lower values of η_o show a shorter transition to equilibrium, representing a shorter relaxation region. The equilibrium region has a similar temperature for all η_o, but the density and pressure are lower with increasing η_o.

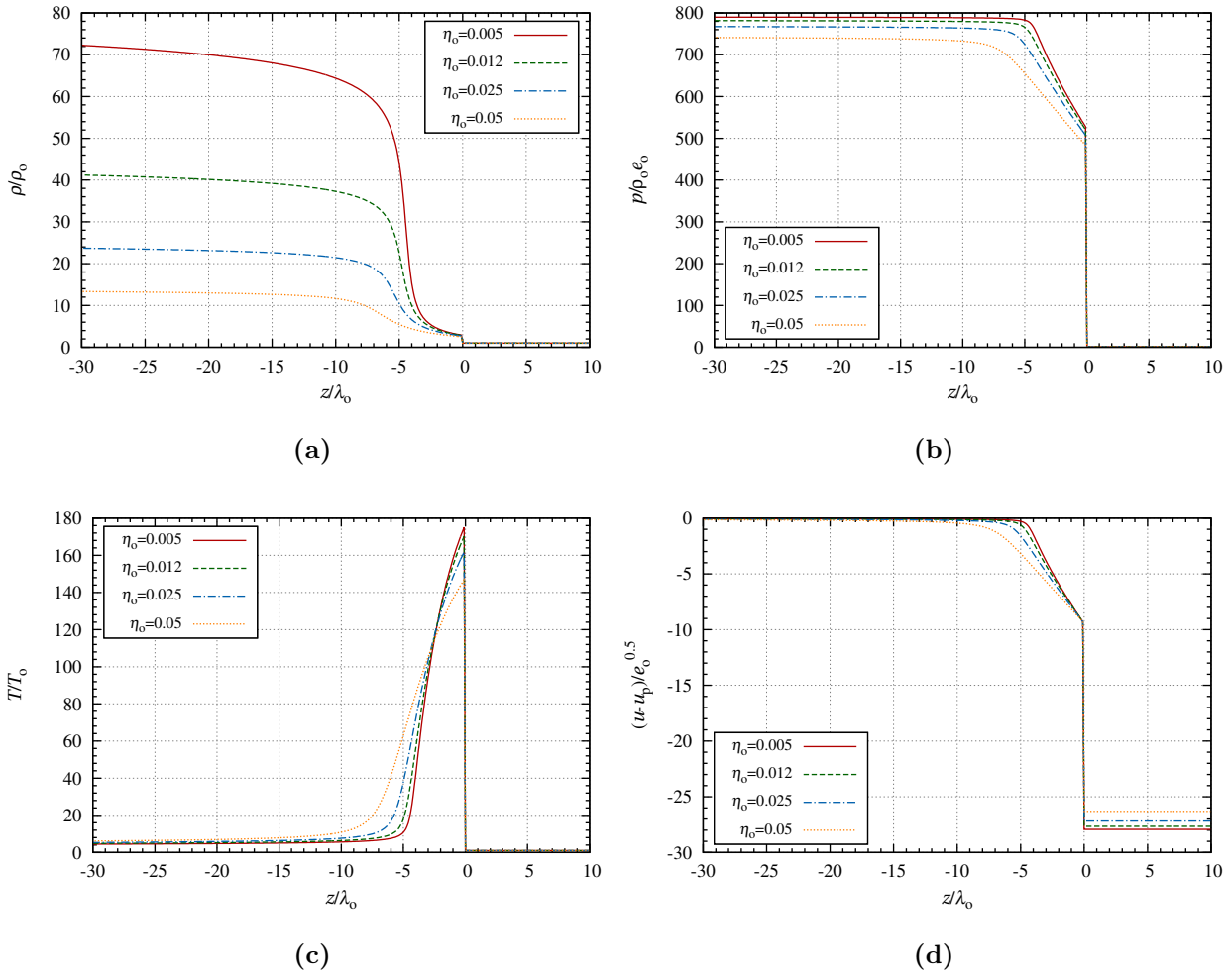

Figure 4.7: Steady state shock distribution of (a) density, (b) pressure, (c) temperature, and (d) velocity obtained for different values of η_o, with $D/u_o = 20$, $u^*/u_o = 10$, and $\varepsilon = 0.95$.

4.4.4 Role of D/u^* on Shock Structure

The effect that the relationship between D and u^* has on the shock structure is investigated using Figs. 4.8-4.10. Results are shown in Fig. 4.8 for the shock structures given for different values of u^*, where $D/u_o = 20$, $\eta_o = 0.012$ and $\varepsilon = 0.95$. Similar to previous results, the states at the shock front are the same for all values of u^*, since they are only dependent on the shock speed D and η_o. Following the shock front, the relaxation region is shown to decrease with decreasing u^*, represented by sharper gradients in all states. In the equilibrium region, the temperature is lower for decreasing u^*, as expected from (4.15). This yields a larger density for lower u^*, and also larger pressure, although to a smaller extent.

The two controllable velocities were combined to investigate the effect that maintaining a constant value of the ratio D/u^* has on the shock structure with different values of D and u^* taken to satisfy that ratio. Figure 4.9 shows the shock structures obtained for different values of D and u^* where $D/u^* = 2$, $\eta_o = 0.012$, and $\varepsilon = 0.95$. The distribution of density in Fig. 4.9(a) shows that there are identical structures of density for similar values of D/u^*, while keeping η_o and ε the same. The state at equilibrium is controlled by u^*, with pressure and temperature decreasing with u^*. Figure 4.10 repeats the results from Fig. 4.9, following the scaling used in the ratio D/u^*, with velocities scaled by u^* and energy by u^{*2}. By including this scaling, all profiles collapse to the same structure and only the initial state changes.

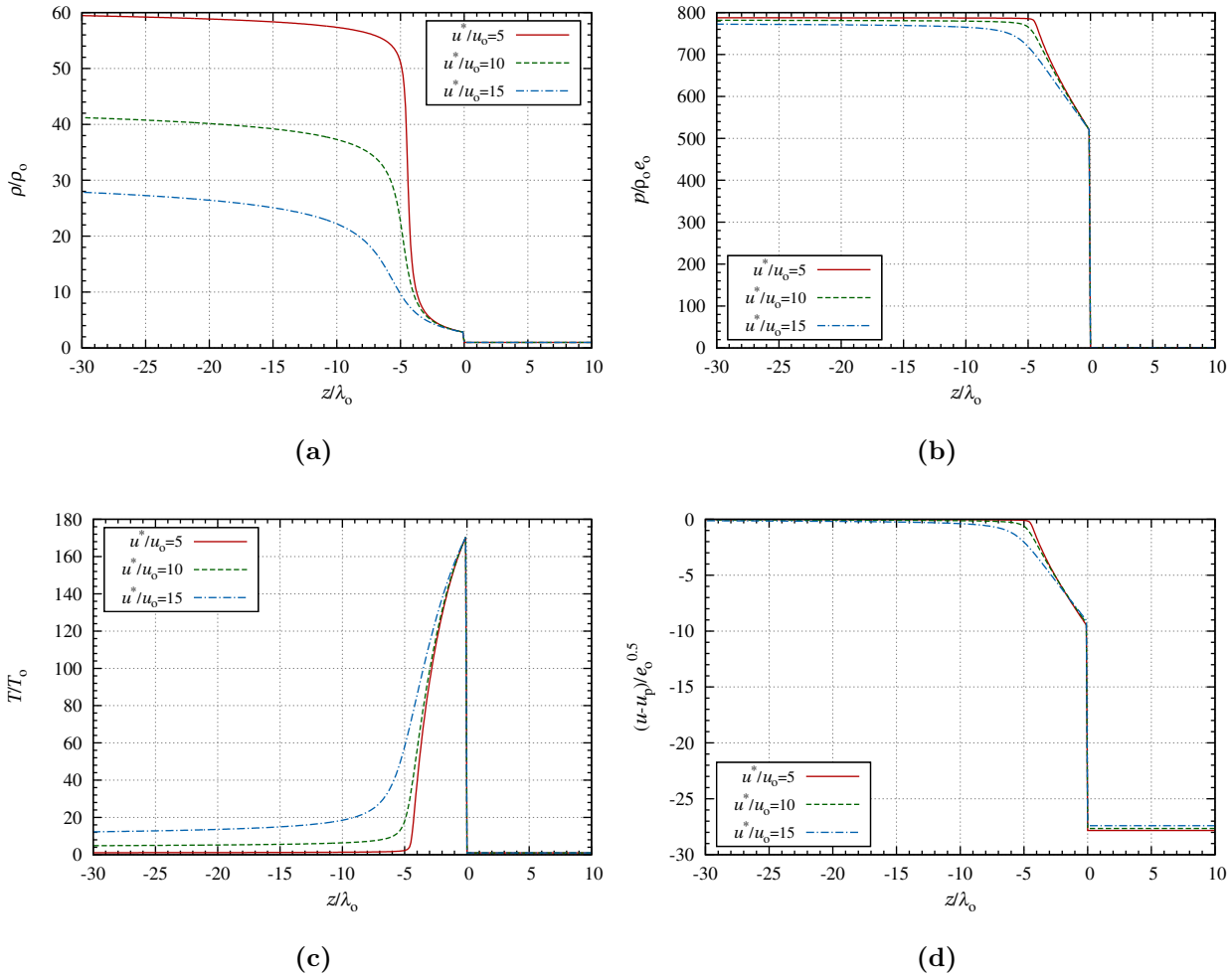

Figure 4.8: Steady state shock distribution of (a) density, (b) pressure, (c) temperature, and (d) velocity obtained for different values of u^*, with $D/u_o = 20$, $\eta_o = 0.012$ and $\varepsilon = 0.95$.

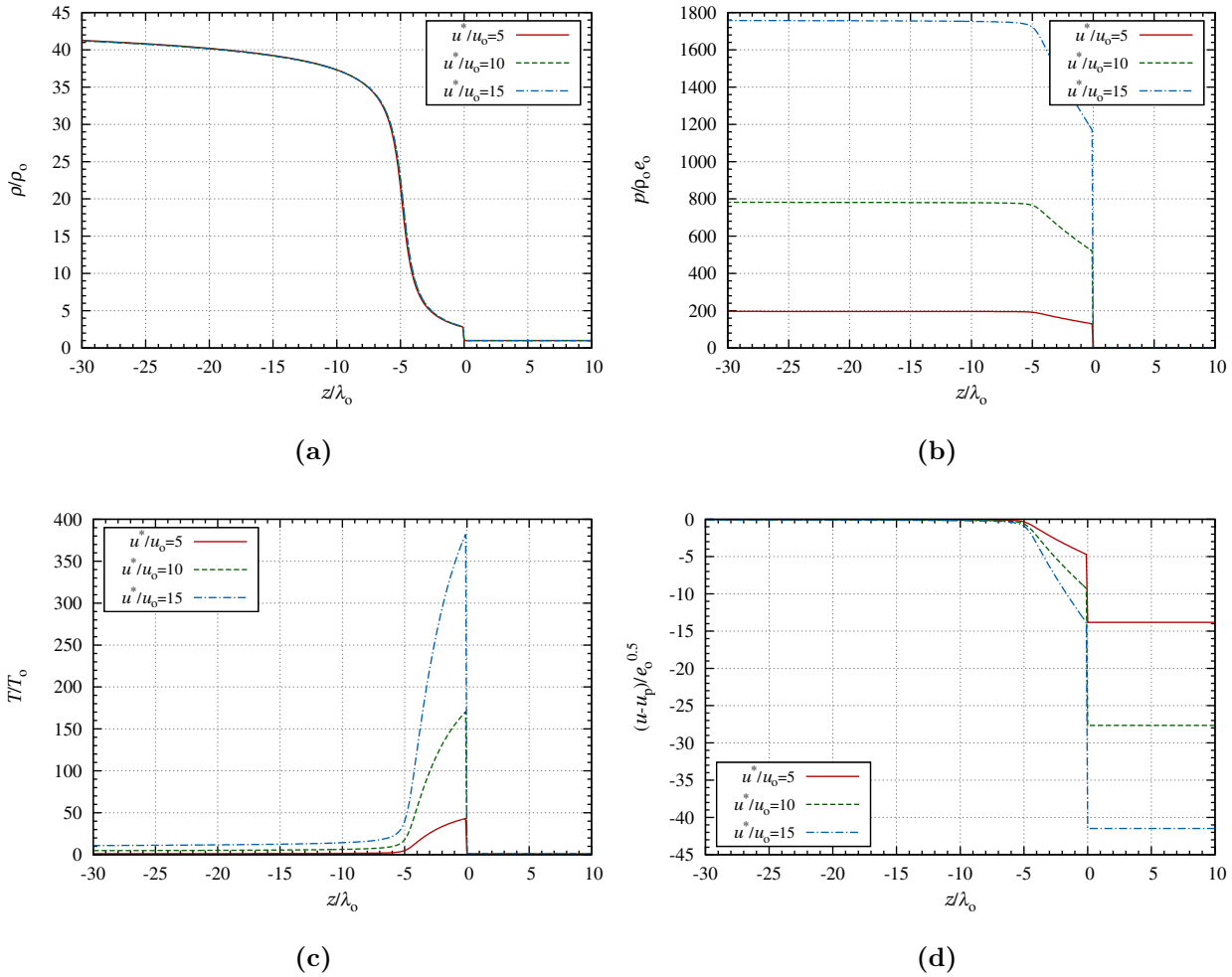

Figure 4.9: Steady state shock distribution of (a) density, (b) pressure, (c) temperature, and (d) velocity obtained for different values of D and u^* where $D/u^* = 2$, $\eta_o = 0.012$, and $\varepsilon = 0.95$.

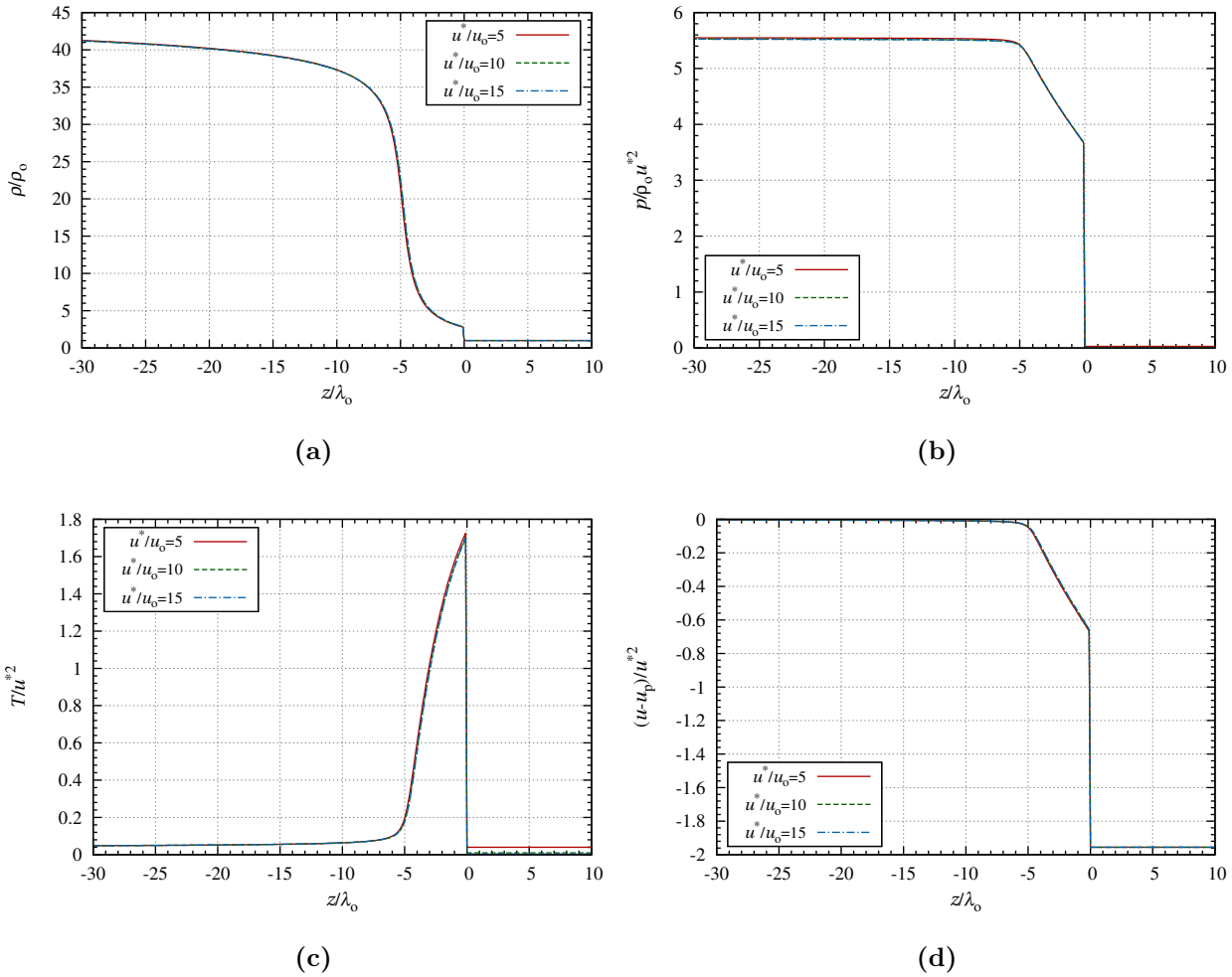

Figure 4.10: Steady state shock distribution of (a) density, (b) pressure, (c) temperature, and (d) velocity, *with energy and velocity scaled with* u^*, obtained for different values of D and u^* where $D/u^* = 2$, $\eta_o = 0.012$, and $\varepsilon = 0.95$.

4.5 Further Shock Properties

4.5.1 Influence of Piston Speed on Shock Speed

Up to this point the steady state shock structure has been related to the shock speed D, however, the simulations that are provided in the next chapters have shock waves controlled by the input piston velocity, u_p. Therefore, an important characteristic to consider is the

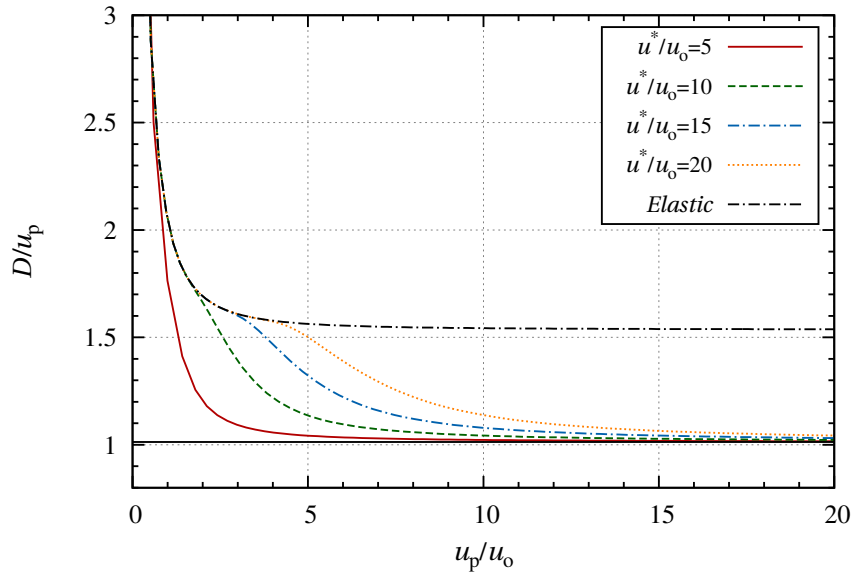

Figure 4.11: Relationship between the ratio D/u_p and $u_\mathrm{p}/u_\mathrm{o}$ for different values of u^*, with $\eta = 0.012$.

relationship between the shock speed and piston velocity. The following results assume that the velocity at the piston is equal to the velocity at the equilibrated state. Since the equilibrium state is independent of ε, it is not necessary to explore the role that ε has on the shock velocity in this section.

Figure 4.11 gives the relationship between D/u_p and u_p obtained for different values of u^*, where $\eta_\mathrm{o} = 0.012$. Initially, at low values of u_p, all values of u^* yield a similar relationship between D and u_p that follows what is obtained for an elastic system of disks (shown as the black dashed line). As u_p increases, the relaxing structure begins to form and the D/u_p diverges from the elastic limit. This is shown to first occur for u^*/u_o=5, and other values of u^* diverge at greater values of u_p. For large values of u_p, all cases of u^* are shown to eventually converge to some limiting value.

These results are shown again in Fig. 4.12, where the piston speed scaled by the activation threshold is shown along the x-axis. As has been shown with the analysis in Section 4.2.2, there is a noticeable transition after $u_\mathrm{p}/u^* \approx 0.3$ whereby all relaxing shocks are shown to

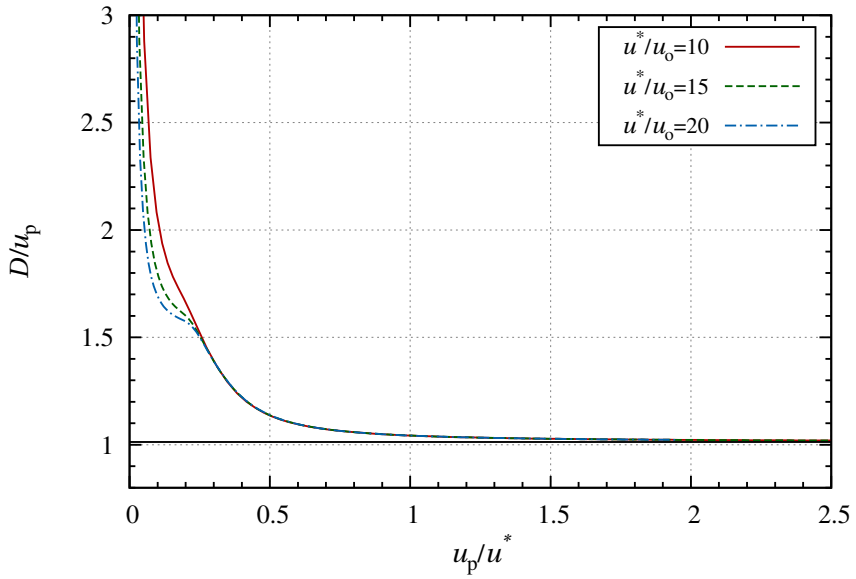

Figure 4.12: Relationship between the ratio D/u_p and u_p/u^* for different values of u^*, with $\eta = 0.012$.

have the same value of D/u_p. In this figure, to the left of this transition the velocities are represented by the elastic behaviour, and are independent of u^*. To the right of this transition, the velocity is shown to be independent of the initial energy (i.e., u_o). The relaxing region can further be separated into two regions. In the first zone, between $u_p/u^* \approx 0.3 - 2.0$, the shock wave is shown to slow down with respect to the piston speed as u_p increases. Eventually the ratio D/u_p is shown to asymptote to some limit near $u_p/u^* \approx 2.0$ (as shown in Fig. 4.13). The solid black line represents the limiting velocity obtained from the maximum compaction limit, as described by Eq. (4.21).

Figure 4.14 gives the resulting relationship between D/u_p and u_p/u^* for different values of η_o. The behaviour is similar to what was observed in the previous figure, with each value of η_o approaching some limiting velocity at $u_p/u^* \approx 2.0$. The curves converge to higher values of D/u_p with increasing η_o, as expected from (4.21).

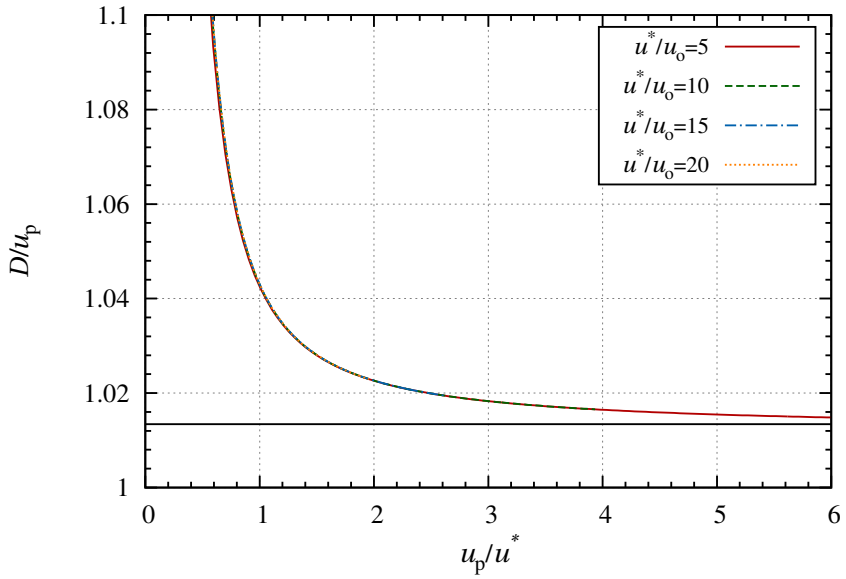

Figure 4.13: Relationship between the ratio D/u_p and u_p/u^* zoomed in near the minimum velocity limit (shown in solid black) for different values of u^*, with $\eta = 0.012$.

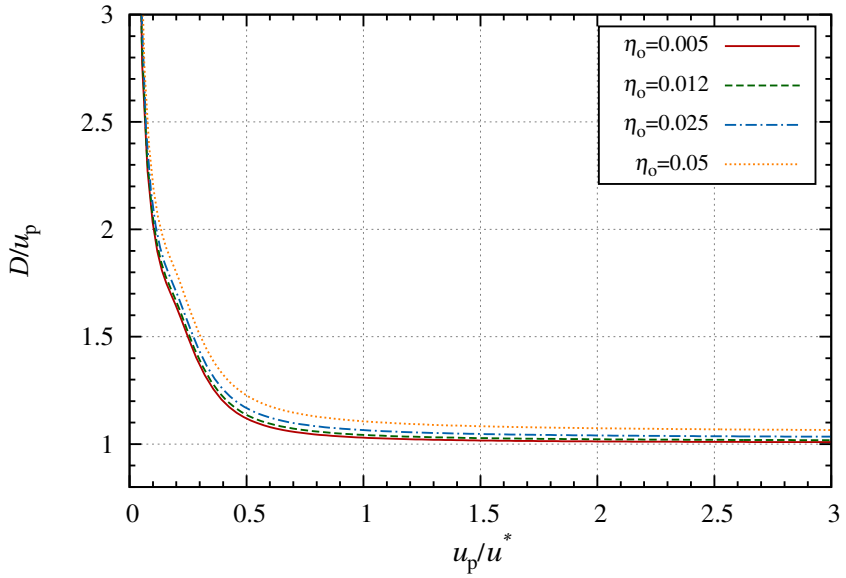

Figure 4.14: Relationship between the ratio D/u_p and u_p/u^* for different values of η_o, with $u^*/u_\mathrm{o} = 10$.

4.5.2 Relaxation Length

The relaxation length l_{R} was calculated to characterize the thickness of the relaxing region. This length scale is defined as the distance between the shock front ($z = 0$) and the beginning of the equilibrium zone, as represented by the criterion (4.15).

Results for l_{R} for different parameters are shown in Figs. 4.15-4.18. Figure 4.15 gives results for l_{R} with varying u_{p} and u^*, where $\varepsilon = 0.95$ and $\eta_{\mathrm{o}} = 0.012$. Results show that as u_{p} increases, l_{R} decreases, as previously observed. There exists a minimum value of u_{p} necessary for there to be a noticeable relaxation zone for each value of u^*, where the shock is expected to be purely elastic below that value.

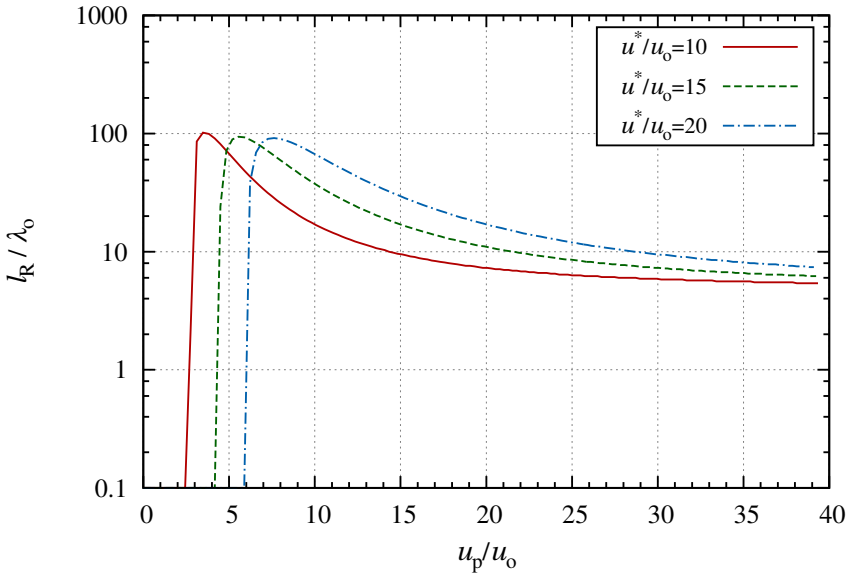

Figure 4.15: Relationship between the relaxation length normalized by the initial mean free path and the piston speed (*normalized by* u_o) for varying u^*, where $\varepsilon = 0.95$ and $\eta_{\mathrm{o}} = 0.012$.

Figure 4.16 shows the same results as Fig. 4.15, but with u_{p} scaled by u^*. The results show that values of l_{R} collapse to the same values in terms of u_{p}/u^*, confirming what was shown in Fig. 4.10. The results show that there is a transition between an elastic shock structure, with $l_{\mathrm{R}} = 0$, and a relaxing structure, at a value of $u_{\mathrm{p}}/u^* \approx 0.3$. As u_{p}/u^* increases, the results show that l_{R} begins to approach some limiting value, which for $\eta_{\mathrm{o}} = 0.012$ and $\varepsilon = 0.95$ is

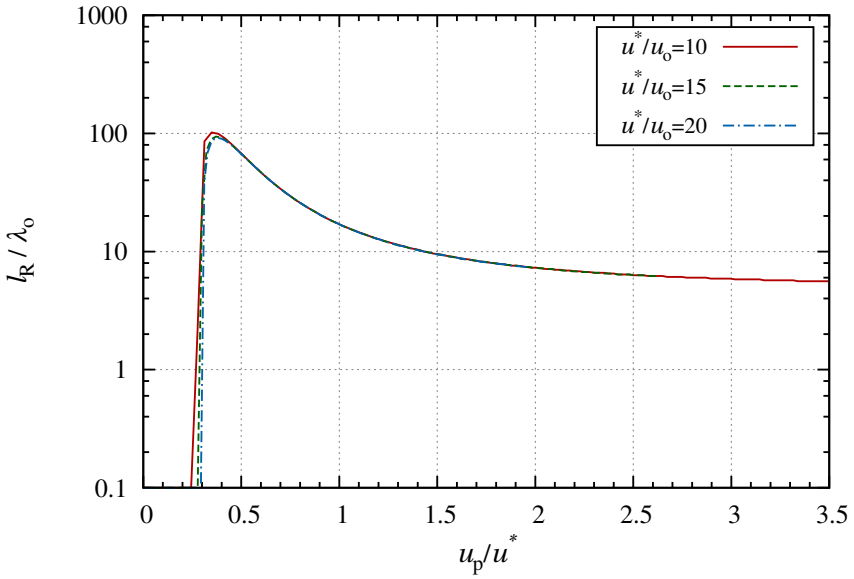

Figure 4.16: Relationship between the relaxation length normalized by the initial mean free path and the piston speed (*normalized by* u^*) obtained from the steady state shock structure for varying u^*, where $\varepsilon = 0.95$ and $\eta_o = 0.012$.

$l_R \approx 5.4\lambda_o$.

Figure 4.17 gives the results for l_R with varying u_p/u^* and η_o, where $\varepsilon = 0.95$. The results show that regardless of the packing factor, the transition between an elastic and a relaxing shock structure occurs at $u_p/u^* \approx 0.3$. For equal values of u_p/u^* the relaxation length is shown to decrease as η_o decreases, with the limiting value for l_R maintaining this trend.

Figure 4.18 shows how l_R varies with u_p/u^* and ε, where $\eta_o = 0.012$. The transition between an elastic to a relaxing shock structure is still shown to occur at $u_p/u^* \approx 0.3$. For similar values of u_p/u^* the relaxation length is shown to decrease as ε decreases, with the limiting value for l_R also following this trend.

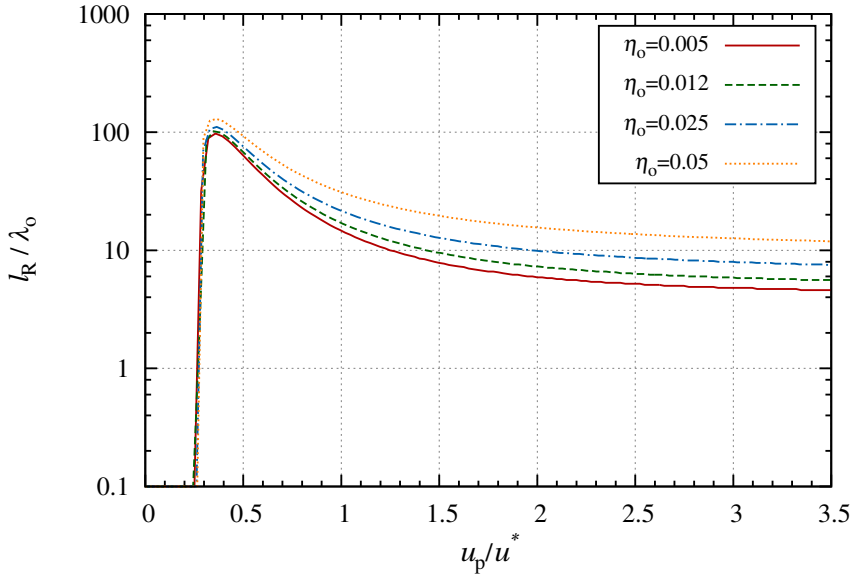

Figure 4.17: Relationship between the relaxation length normalized by the initial mean free path and the piston speed (*normalized by* u^*) obtained from the steady state shock structure for varying η_o, where $\varepsilon = 0.95$ and $u^*/u_o = 10.0$.

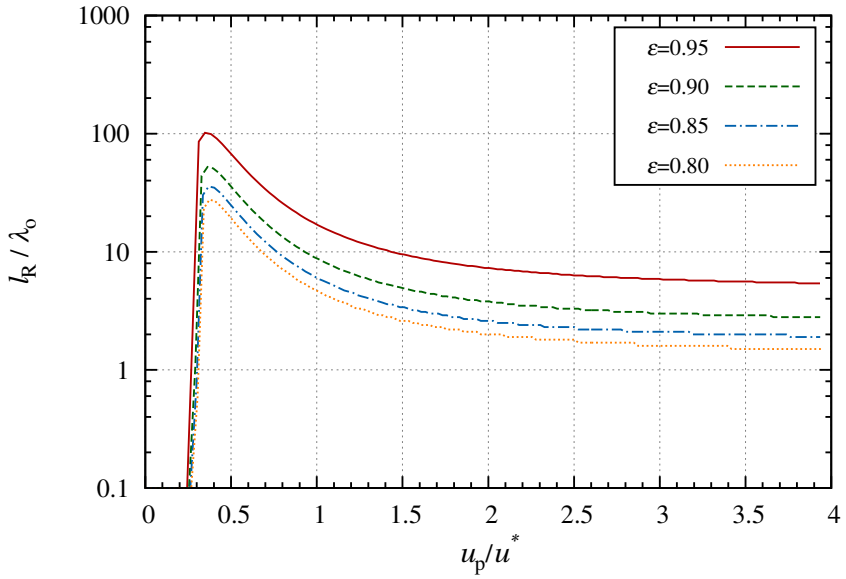

Figure 4.18: Relationship between the relaxation length normalized by the initial mean free path and the piston speed (*normalized by* u^*) obtained from the steady state shock structure for varying ε, where $\eta_o = 0.012$ and $u^*/u_o = 10.0$.

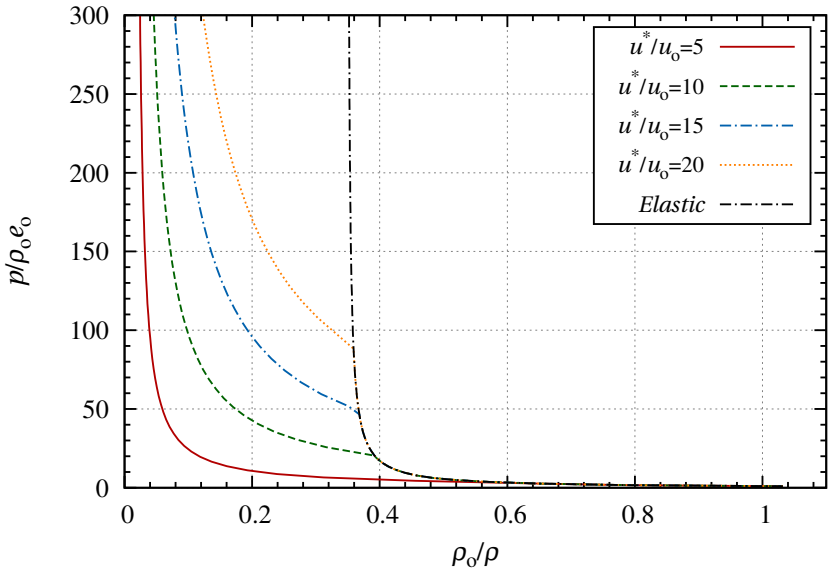

Figure 4.19: Shock Hugoniots obtained for different activation thresholds u^* (normalized by u_o) for η_o=0.012.

4.5.3 Shock Hugoniot

The shock Hugoniots were constructed by obtaining the equilibrium end states as given in Sec. 4.2.2. Figure 4.19 shows the resulting shock Hugoniot on a $p-v$ plot for different values of u^*, with η_o=0.012. The black dashed line represents the shock Hugoniot associated to elastic medium at this packing fraction, as represented by (4.9). All values of u^* show the transition between the elastic Hugoniot and the Hugoniot representing a relaxing shock wave, which occurs at $u_p/u^* = 0.275$. As u^* is increased, the transition between the two Hugoniots is shown to shift upward along the elastic Hugoniot, representing the higher jump in pressure and temperature that is required to relax at this level of u^*. These results further confirm what was shown in Fig. 4.8 for a single shock speed, where increasing u^*, while keeping all other parameters equal, yields a lower density and slightly lower pressure in the equilibrated state.

Figure 4.20 shows the shock Hugoniots obtained for different values of η_o, with $u^*/u_o = 10$. Increasing η_o is shown to shift the transition between relaxing and elastic Hugoniots at lower

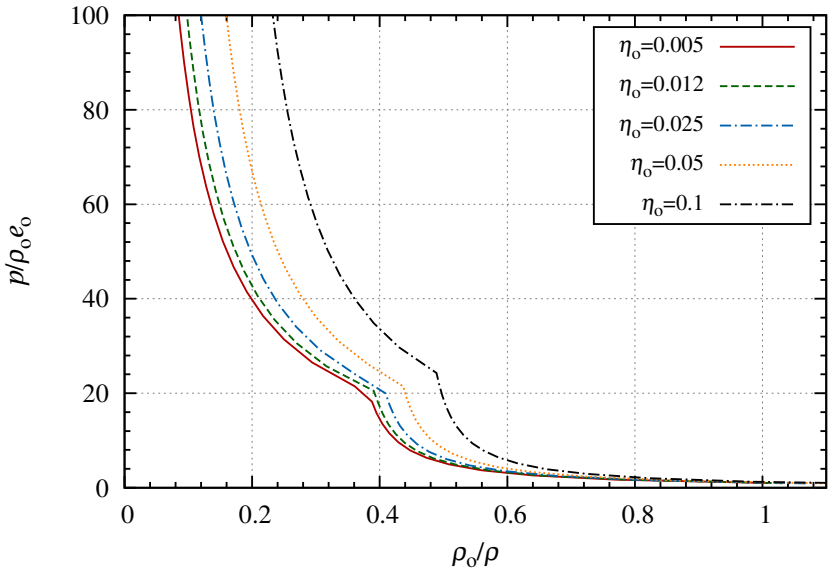

Figure 4.20: Shock Hugoniots obtained for different values of η_o, with u^*/u_o =10.

jumps in density and slightly higher jumps in pressure. The lower density jump can be attributed to the maximum compaction possible for elastic disks at a given η_o as given in (4.6).

The slightly different pressures required to transition between the elastic and relaxing structures can be attributed to the equation of state. The Hugoniot in Fig. 4.20 extends what was observed for a single shock speed in Fig. 4.7 for varying η_o, whereby increasing η_o is shown to decrease the density and pressure in the equilibrated state.

4.6 Invariance with u_p/u^*

The result that the relaxing structure depends on the ratio u_p/u^* is an important finding, as it simplifies the analyses in other chapters. It is worth demonstrating this invariance by addressing the governing equations controlling the shock structure. Beginning at the shock

front, in the limit of a high Mach number, as given in Sec. 4.2.1, the post shock states are:

$$f(\eta_o) = \left(\frac{v_s}{v_o}\right)_{max} = \frac{1}{6}\left(1 + 4\eta_o + \sqrt{(1 - 8(\eta_o - 1)\eta_o}\right) \tag{4.48}$$

$$\frac{u_s}{D} = (1 - f(\eta_o)) \tag{4.49}$$

$$p_s = \frac{D^2}{v_o}(1 - f(\eta_o)) \tag{4.50}$$

$$T_s = \frac{1}{2}D^2(1 - f(\eta_o))^2. \tag{4.51}$$

The first two relationships only depend on the initial packing factor, so in the limit of high Mach number, they are expected to be equal for any value of u_p and u^*. The final two relationships also include the shock strength, and are independent of the initial energy and pressure. By scaling with u^{*2} for pressure and temperature these can alternatively be written as:

$$\frac{p_s}{\rho_o u^{*2}} = \frac{D^2}{u^{*2}}(1 - f(\eta_o)) \tag{4.52}$$

$$\frac{T_s}{u^{*2}} = \frac{1}{2}\frac{D^2}{u^{*2}}(1 - f(\eta_o))^2. \tag{4.53}$$

This yields relationships for pressure and temperature as functions of only D/u^* and η_o. Equations (4.48), (4.49), (4.52), and (4.53) confirm that the the initial shock jump relations can be determined as a function of D/u^* only (or u_p/u^* by extension of Sec. 4.5.1) and η_o, as seen in Fig. 4.10.

Behind the initial shock jump, the differential equations for the change in density, pressure, temperature and velocity were shown to be controlled by the cooling rate. Using the initial shocked state at the beginning of the relaxing region, the cooling rate takes the form:

$$\zeta^* = -\frac{4}{d\sqrt{\pi}}\left(1 - \varepsilon^2\right)\rho_s T_s^{3/2}\eta_s g_2(\eta_s)\exp\left\{-\frac{1}{4}\frac{u^{*2}}{T_s}\right\}\left(1 + \frac{1}{4}\frac{u^{*2}}{T_s}\right). \tag{4.54}$$

Applying the relationship (4.48) and scaling with u^* yields:

$$\frac{\zeta^*}{u^{*3}} = -\frac{4}{d\sqrt{\pi}}\left(1-\varepsilon^2\right)\frac{1}{f(\eta_\mathrm{o})^2}\left(\frac{T_\mathrm{s}}{u^{*2}}\right)^{3/2}\eta_\mathrm{o}g_2\left(\frac{\eta_\mathrm{o}}{f(\eta_\mathrm{o})}\right)\exp\left\{-\frac{1}{4}\frac{u^{*2}}{T_\mathrm{s}}\right\}\left(1+\frac{1}{4}\frac{u^{*2}}{T_s}\right). \quad (4.55)$$

When implemented into the differential equations given in (4.47), the u^{*3} term cancels out via non-dimensionalization of the other terms. Therefore, it can be concluded from (4.55) that the rate of decay behind the shock is similar for equal values of η_o, ε and $\frac{T_\mathrm{s}}{u^{*2}}$; where $\frac{T_\mathrm{s}}{u^{*2}}$ is shown to be a function of u_p/u^*. Based on this alternative scaling, it is not surprising that the results presented in this chapter reveal that similar structures and properties can be given for equal values u_p/u^*, while maintaining the other variables constant.

4.7 Concluding Remarks on Shock Structure and Characteristics

This chapter presented the derivation and characterization of the steady state shock structure expected for a two-dimensional granular gas with activated inelastic collisions. The resulting shock structures demonstrated in Figs. 4.5-4.10 showed that for sufficiently strong shocks, the structure and properties are governed by three parameters: ε, η_o, and D/u^*; and are independent of the initial energy. This was verified by alternative scaling of the governing equations of the shock structure, as presented in Sec. 4.6.

By varying the parameters, it was shown that there exists a transition between elastic behaviour and relaxing shock behaviour at $u_\mathrm{p}/u^* \approx 0.3$. For values of u_p/u^* less than this value, the properties follow what is expected for an elastic medium, which is given by Eqs. (4.9). The parameter u^* has no effect within this regime. For values of $u_\mathrm{p}/u^* \geq 0.3$ the properties pertaining to a relaxing structure were obtained, whereby u_o was shown to not have any effect once velocities and energy are scaled with u^*. For very large values of u_p/u^*,

results for relaxation length and shock speed relative to a piston were shown to approach a limiting value. This asymptotic behaviour suggests that large values of u_{p}/u^{*} ($\gtrsim 2.0$) can be used to explore purely inelastic medium. The present model therefore gives a simplified method to explore all three regimes of shock structures: the elastic and purely inelastic structures, as well as a regime between these two extremes where activated collisions have a strong influence on the structures.

The independence from the initial kinetic energy of the granular medium for sufficiently strong shock waves is an important finding in the context of realistic mixtures, not unlike molecular gases for the strong shock approximation [13]. By demonstrating the independence from the initial energy, the analysis in this chapter and subsequent chapters can be applied to an initial state being fluidized *or* at rest.

Chapter 5

Dynamics of Shock Formation Process in 1D

5.1 Introduction

The current chapter presents the investigation of the evolution of the shock structure using the MD, N-S, and Euler models described in Ch. 3. This also serves as a method to validate whether the continuum description captures the same structure and behaviour as those predicted by MD.

Studies have been completed to investigate the evolution of a piston suddenly propagating into a medium at a constant velocity, although they have been limited to the cases where the medium is completely elastic or inelastic [9]. Sketches of these types of evolutions are shown in Fig. 5.1 where the position of the different zones of the shock wave are cast onto an $x - t$ diagram in the piston frame of reference.

Figure 5.1(a) demonstrates the general evolution observed for an elastic medium. After a piston begins moving into the mixture there is a short amount of time required for the shock structure to evolve into a steady structure. This development can be attributed to the

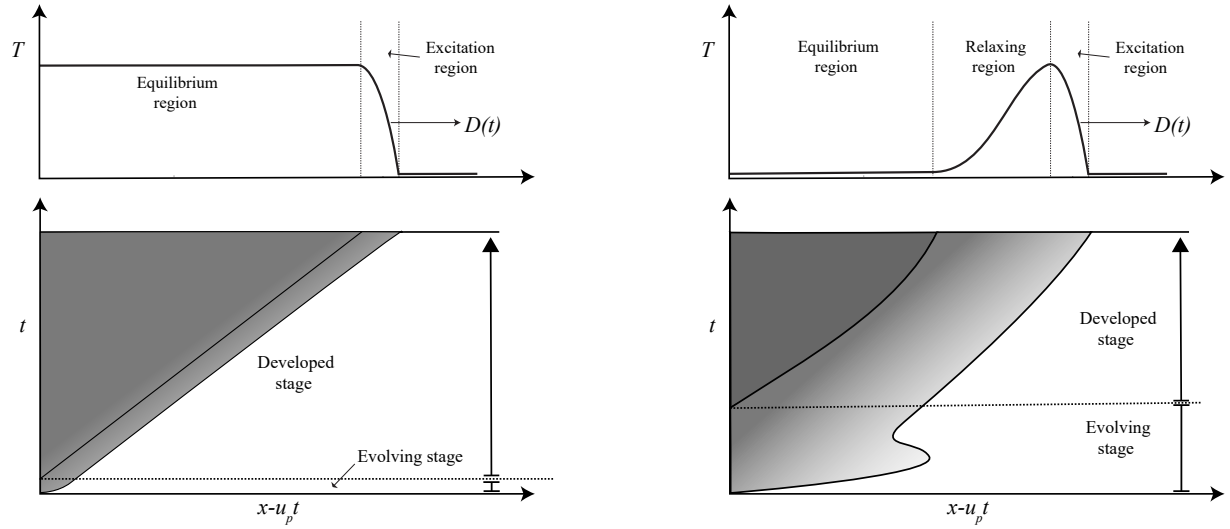

(a) Elastic **(b)** Inelastic

Figure 5.1: Expected steady state shock structure (top) and the structure's evolution (bottom) in the piston frame of reference for completely (a) elastic and (b) inelastic mixtures.

diffusive shock front taking shape. After this development, the shock wave propagates at a constant velocity ahead of the piston.

In contrast, the evolution of an inelastic shock structure is much more complex, as demonstrated by Kamenetsky *et al.* [9] and sketched out in Fig. 5.1(b). For such a structure, the evolving stage takes a longer amount of time due to the development of both the excitation region of the shock front and the relaxing region. At the beginning of this evolving stage there is a shock rapidly moving away from the piston. The shock front begins to slow down due to the relaxing effects behind the shock wave, which has even been shown to cause the shock front to pull back towards the piston for a short period [9]. Eventually, the equilibrium region forms along the piston, which is a dense, frozen state that extends from the piston. Once the equilibrium region is formed, the developed stage commences, where the shock structure follows what is expected from the steady state structure.

The evolving behaviours described above present two extremes for the evolution of shock waves. The present chapter expands on this work by investigating how the evolution is

affected by activated inelastic collisions, thus bridging the gap between purely inelastic and elastic gases. Additionally, the evolution in an inelastic mixture is still not well understood and is investigated more thoroughly in this chapter. For example, the reason for the shock front pulling back towards the piston and its implication on other shock phenomena are lacking.

5.2 Comparison of Molecular Dynamics and Continuum Models

This section compares the transient behaviour obtained from the MD, N-S and Euler continuum models for a single set of parameters. Further parametric study is presented in subsequent sections.

5.2.1 Snapshots of Shock Structure

Figure 5.2 gives the results for the one-dimensional distribution of density, pressure and temperature at different times, obtained for $u_{\mathrm{p}}/u_{\mathrm{o}} = 20$, $u^*/u_{\mathrm{o}} = 10$, $\varepsilon = 0.95$ and $\eta_{\mathrm{o}} = 0.012$. MD results were obtained by ensemble averaging over 50 simulations with each simulation containing 30,000 disks in a domain of $(L_x \times L_y)/\lambda_{\mathrm{o}} = 172 \times 17.2$.

At an early time ($t/\tau_{\mathrm{o}} = 0.32$) there is a small jump in density, and large jumps in pressure and temperature along the piston face. The behaviour is similar for all models. At $t/\tau_{\mathrm{o}} = 1.60$, the density rises sharply along the piston face, attributed to the drop in temperature, beginning to form the expected relaxing shock structure. This leads to a drop in pressure. At later times ($t/\tau_{\mathrm{o}} = 2.88$ and $t/\tau_{\mathrm{o}} = 5.44$), temperature and pressure begins to plateau to some value along the piston, representing the formation of the 'equilibrium' zone. Density continues to rise, albeit with a significantly lower gradient than in the relaxing region. The increase in density can be attributed to a small fraction of collisions still being

inelastic within the 'equilibrium' zone leading to a negligible change in temperature.

In general, the results shown in Fig. 5.2 demonstrate that the shock structures and their evolution are remarkably similar for the MD and continuum models. This similarity validates the use of continuum description as given in Sec. 3.3 and suggests it can be used for the cases considered in this study. Small differences between the MD and N-S results are noticeable, with N-S yielding a higher density along the piston face, as well as sharper gradients in pressure and temperature in the relaxing region. Euler simulations yield similar behaviour, although there is a sharp jump in macroscopic states at the shock front, which is expected due to the lack of diffusive effects.

5.2.2 Comparison with Steady State Structure

Figure 5.3 compares the shock structure for the inviscid case given in Fig. 5.2 with that expected from the steady state distribution as calculated in Ch. 4. The results show that at later times the solution is well approximated by the steady structure, with temperature, pressure and velocity agreeing well. The density is higher in the equilibrium zone for the theoretical distribution, which may be due to boundary effects or the structure not fully coming to the steady state structure.

5.2.3 Space-Time Evolution

Results were recast onto an $x - t$ plane in the piston frame of reference, similar to what is sketched out in Fig. 5.1. In addition to showing the macroscopic states on an $x - t$ plane, the family of characteristics are constructed in order to investigate the dynamics of the shock waves. The family of characteristics is represented by the particles paths (P), forward (C^+)

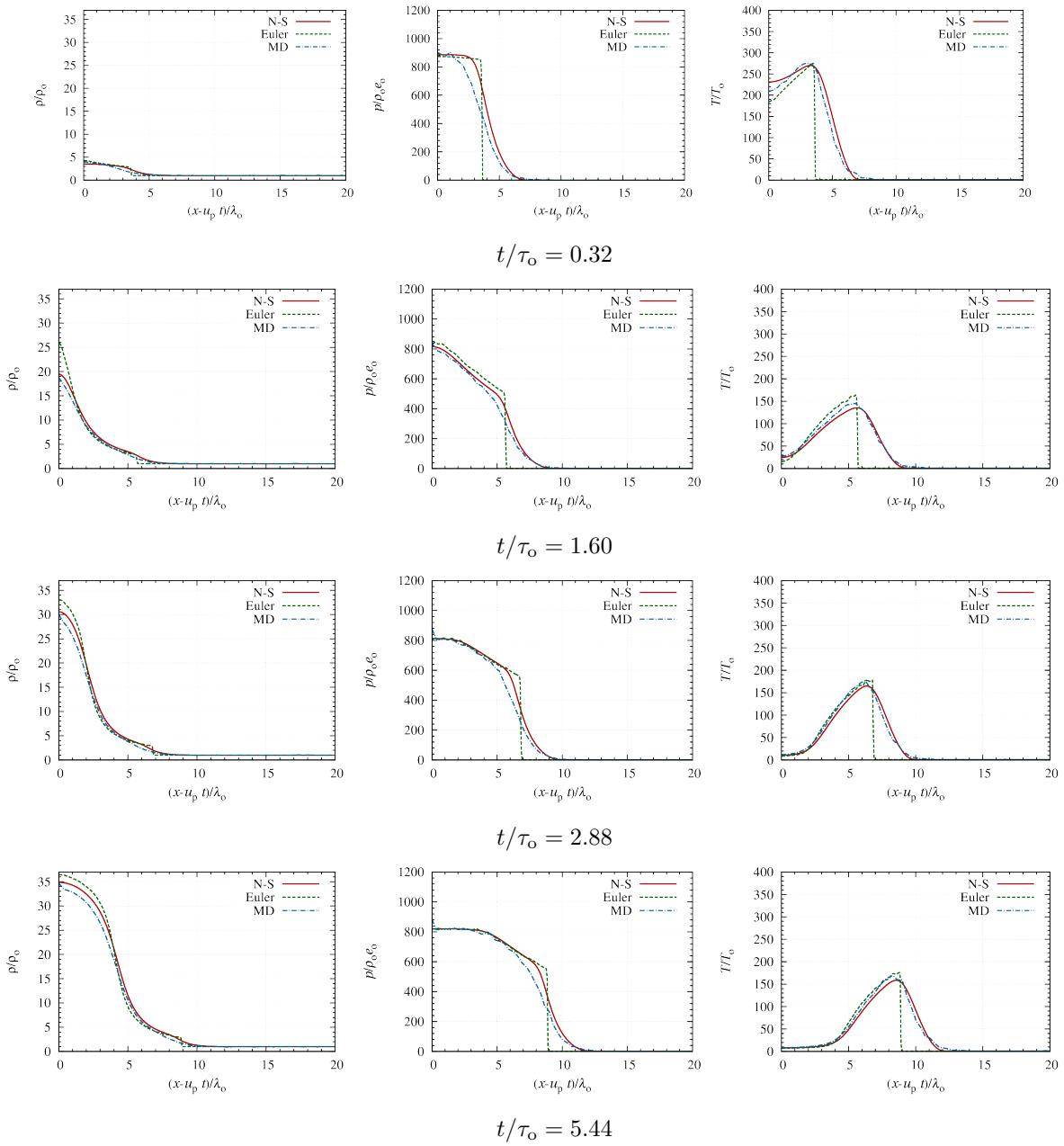

Figure 5.2: Evolution of one-dimensional distributions of density (left), pressure (center), and temperature (right), comparing MD (dot-dashed) and continuum inviscid (dashed) and viscous (solid) models for $u_p/u_o = 20$, $u^* u_o = 10$, $\varepsilon = 0.95$ and $\eta_o = 0.012$.

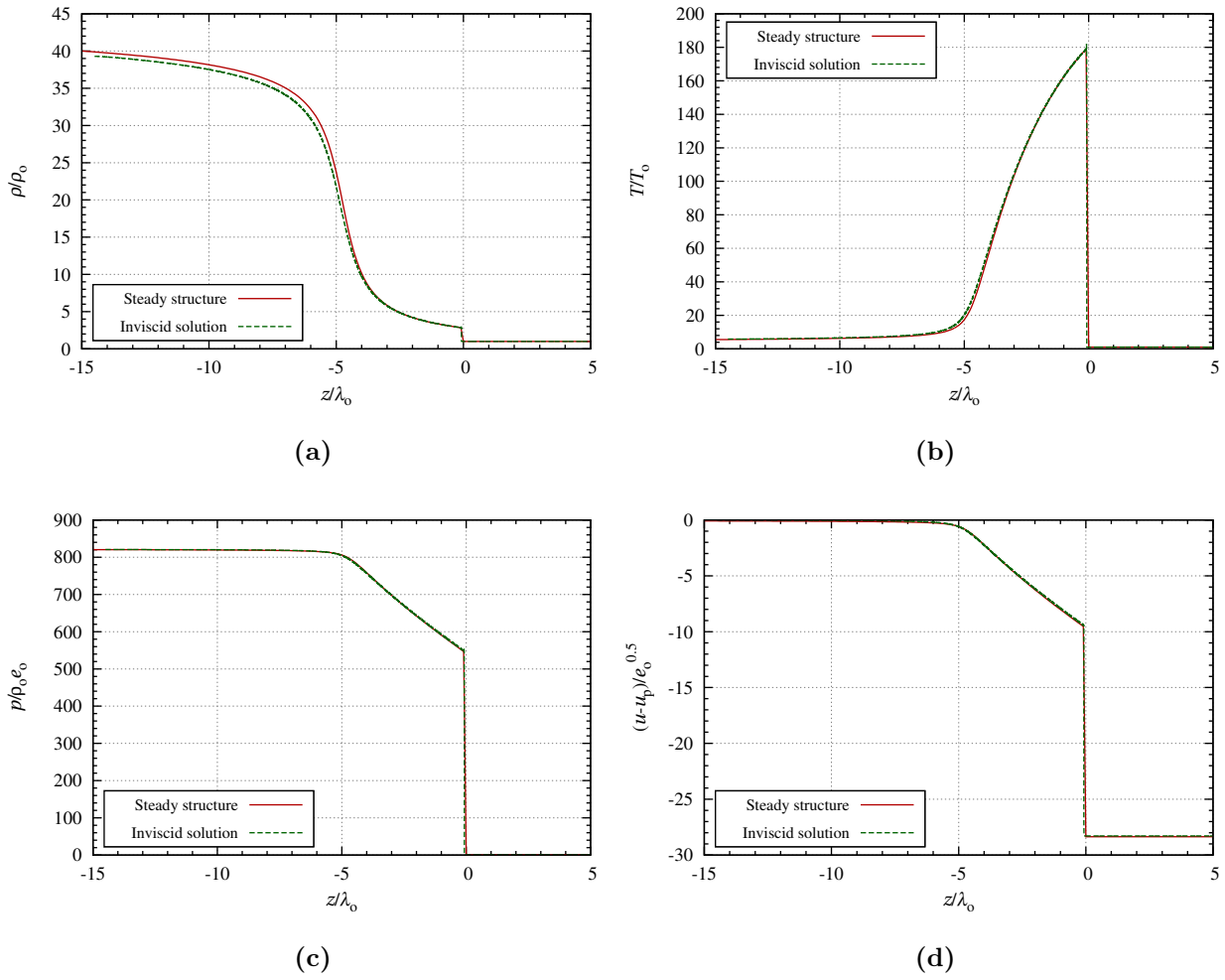

Figure 5.3: Comparison between distributions of (a) density, (b) temperature, (c) pressure, and (d) velocity, as obtained for the steady state structure and the inviscid solution after $t/\tau_o = 18.08$, where $u_p/u_o = 20$, $u^*/u_o = 10$, $\varepsilon = 0.95$, and $\eta_o = 0.012$.

and backward (C^-) running characteristics, which are given as:

$$P : \frac{dx_{\mathrm{p}}}{dt} = u \tag{5.1a}$$

$$C^+ : \frac{dx_+}{dt} = u + c \tag{5.1b}$$

$$C^- : \frac{dx_-}{dt} = u - c \tag{5.1c}$$

where u is the local particle velocity normal to the piston and c is the local speed of sound, at a given time. These paths represent the trajectories of fluid particles, right running pressure waves and left running pressure waves, respectively [22]. The scaled speed of sound for such a medium is (see Appendix C):

$$c = \sqrt{T(1 + (1-\eta)^{-2} + 2\eta(1-\eta)^{-1})}. \tag{5.2}$$

The local packing factor is taken from the density jump, $\eta = \eta_{\mathrm{o}}\rho/\rho_{\mathrm{o}}$.

The trajectories of the characteristics were obtained numerically by integrating (5.1). The C^+ characteristics were initiated from the piston face at specified intervals in time, while C^- characteristics were initiated from the shock front at similar time intervals. Particle paths were initialized at specified locations away from the initial piston position, denoted as $\xi = x(t = 0)$ for each path.

Figure 5.4 shows the evolution of density, pressure and temperature obtained from the MD and continuum models for the case shown in Fig. 5.2. The evolutions are shown with selected particle paths in white, C^+ characteristics extending from the piston in black, and C^- characteristics from the shock front in blue. Due to a sharp change in $u + c$ at the shock front, the C^+ characteristics converged along the shock front. All models give similar trends, although the Euler solution shows a sharp jump in density, pressure, and temperature at the shock front. This differs from the MD and N-S results where the macroscopic states

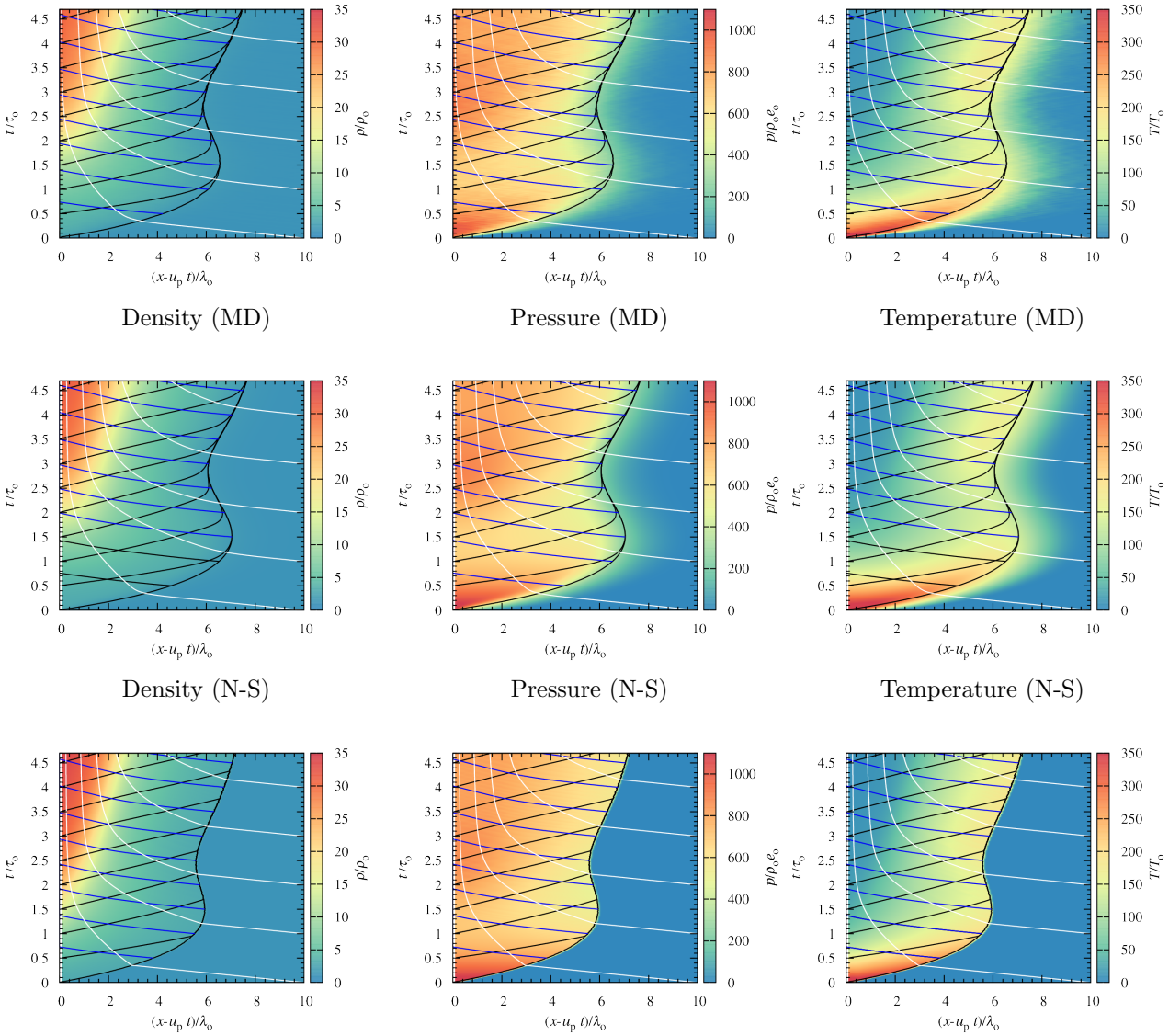

Figure 5.4: Evolution of density (left), pressure (center), and temperature (right) on an x vs. t plane, in the piston frame of reference, for $u_\mathrm{p}/u_\mathrm{o} = 20$, $u^*/u_\mathrm{o} = 10$, $\varepsilon = 0.95$, and $\eta_\mathrm{o} = 0.012$. Also shown are select particle paths (white), forward (black) and backward (blue) running characteristics.

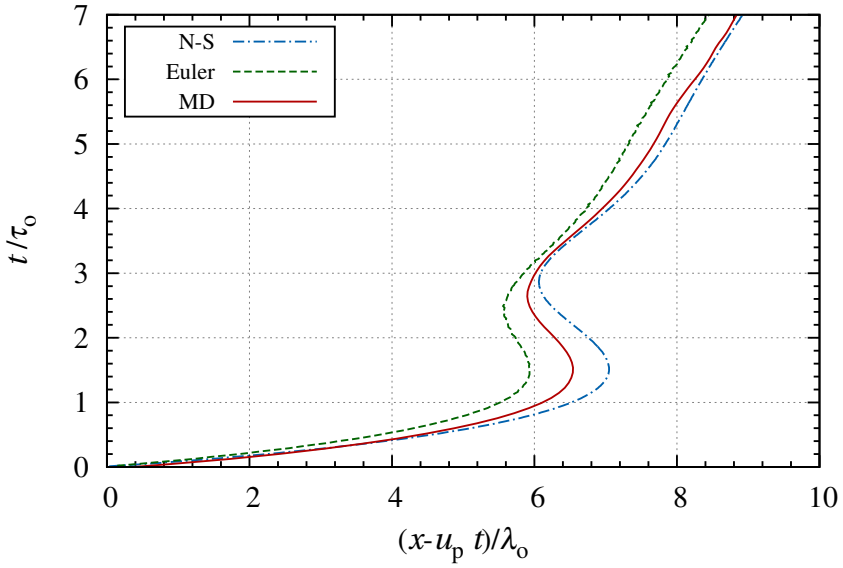

Figure 5.5: Comparison of shock front position obtained from MD, N-S, and Euler simulations with $u_p/u_o = 20$, $u^*/u_o = 10$, $\eta_o = 0.012$, and $\varepsilon = 0.95$.

were smeared on the shock front. Also seen from the shock trajectory is that there was no apparent unstable behaviour once the shock wave reached a steady structure.

The evolution of the shock structure can be broken into different stages based on the results given in Fig. 5.4. At the beginning of the shock development, there are large initial jumps in temperature and pressure, which give rise to a fast shock wave. Following this initial stage, the shock decelerates rapidly, eventually pulling back towards the piston at $t/\tau_o \approx 1.5$, thus recovering what is observed for purely inelastic media [9]. The shock then accelerates and tends to the developed structure at $t/\tau_o \approx 2.5$.

The positions of the shock fronts are shown in Fig. 5.5 for the different models. Results show that the time for the reversal of the shock front is the same for all models, although the shock front extends further forward in the N-S model, followed by the MD and Euler results.

To further investigate the stages of the evolution, including the reversal of the shock front to the piston, the interactions of characteristics with the evolution of temperature, density and pressure, were analyzed. A Lagrangian approach was taken to explain the transient stages

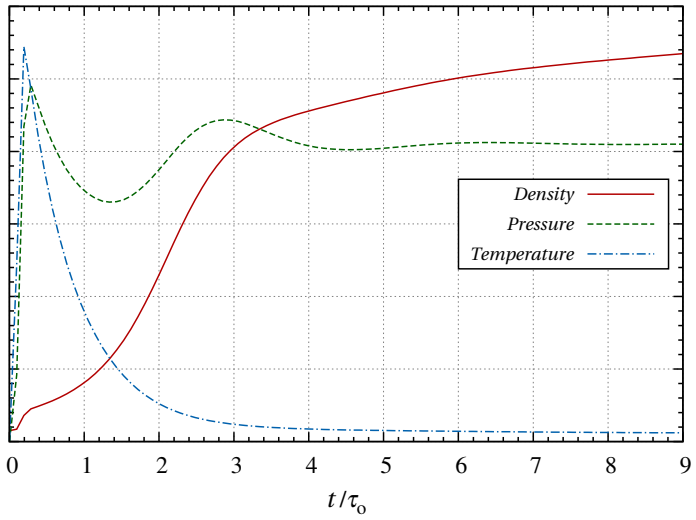

Figure 5.6: Comparison of particle path properties along the piston face obtained from N-S for $u_p/u_o = 20$, $u^*/u_o = 10$, $\eta_o = 0.012$, and $\varepsilon = 0.95$.

by tracking how properties of particle paths along the piston are communicated forward. Figure 5.6 gives the density, pressure and temperature for a particle path which originates close to the piston face, as obtained from the N-S simulation. Figure 5.7 gives a comparison between the evolution of shock front speed and the pressure along this particle path.

The first stages in the evolution can be related to the decay and pull-back of shock front. During these early stages, the initially shocked particle paths were shown to experience a strong temperature decay due to the inelastic collisions, as shown in Fig. 5.6. This decay in temperature leads to a drop in pressure and increase in density. The rapid decay experienced by these particle paths is communicated to the shock front via C^+ characteristics traversing through the particle paths, which causes the shock to slow down. The shock speed eventually becomes negative with respect to the piston at $t/\tau_o \approx 1.5$.

The next stage is attributed to a re-pressurization felt along the piston face. At $t/\tau_o \approx 1.3$, the pressure felt along the particle path stops decreasing and begins to increase, which can be attributed to the increasing density and compressibility factor playing a larger role than the decreasing temperature via the equation of state. This re-pressurization event can be

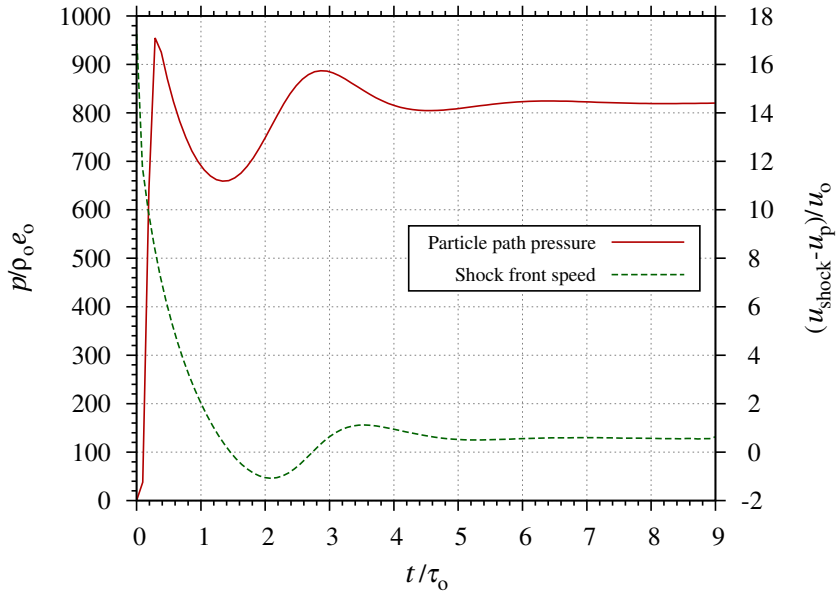

Figure 5.7: Comparison between pressure experienced by particle path along piston face and shock front velocity, obtained from N-S for $u_p/u_o = 20$, $u^*/u_o = 10$, $\eta_o = 0.012$, and $\varepsilon = 0.95$.

seen communicating forward to the shock front, causing the shock to accelerate at $t/\tau_o \approx 2.2$. The delay between the pressure increasing at $t/\tau_o \approx 1.3$ and the accelerating shock front at $t/\tau_o \approx 2.2$ in Fig. 5.7 can be explained by the time it takes for C^+ characteristics to be communicated from the piston to the shock front.

At $t/\tau_o \approx 2.8$ the pressure along the piston begins to decrease, leading to a deceleration of the shock front. The dropping pressure is attributable to the temperature decay having a larger effect via the equation of state than the density change on the pressure. The pressure eventually stops changing near $t/\tau_o \approx 4.5$, with the change in density and temperature counteracting to maintain a constant pressure. The constant pressure is attributable to the beginning of the 'equilibrium' region, which leads to a constant shock speed following shortly after. The steady state structure was formed once the 'equilibrium' region began extending from the piston.

Particle paths that traverse the shock front at later times, as shown in Fig. 5.8, do not experience the complex re-pressurization event and have no effect on changing the structure.

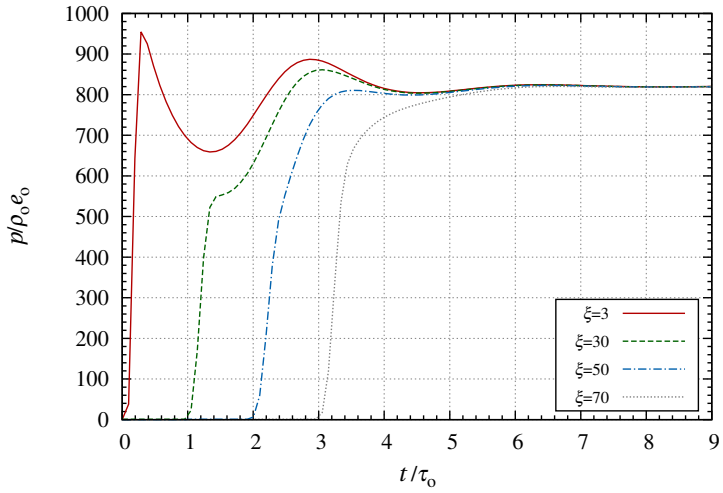

Figure 5.8: Comparison of pressure experienced by different particle paths obtained from N-S, where $\xi = x(t = 0)$, for $u_p/u_o = 20$, $u^*/u_o = 10$, $\eta_o = 0.012$, and $\varepsilon = 0.95$.

These results indicate that the knowledge of particle path states is important to consider as it directly contributes to the dynamics of the shock wave.

5.3 Parametric Study of Evolution

5.3.1 Role of u_p/u^* on Evolution

Figures 5.9-5.12 give the results for the evolutions obtained for different values of the ratio of the piston velocity to the impact velocity threshold, u_p/u^*. Figure 5.9 compares the position of the shock front, as obtained from the different models, for $u_p/u^* = 0.5$, 1.0, 1.5, and 2.0, where $u^*/u_o = 10$, $\eta = 0.012$, $\varepsilon = 0.95$. Figure 5.10 shows the evolution of pressure and the family of characteristics for this case, as obtained from N-S. Figure 5.11 gives the temperature, pressure and density felt along the early particle paths, and Fig. 5.12 compares the pressure along these particle paths with the speed of the shock front relative to the piston.

Figure 5.9(a) shows the resulting shock front position for $u_p/u^* = 0.5$ as obtained from MD and continuum models. For this case the shock front gradually slows down and does not experience any pullback towards the piston. Analysis of the characteristics shows that the early particle paths do not experience any rapid re-pressurization, leading to the shock front velocity remaining positive with respect to the piston, as seen in Fig. 5.12(a). Although there is a small decay in shock velocity, the trend is similar to that observed for elastic media. All models give a similar behaviour, although the N-S results extend the furthest away from the piston, while the Euler ones remain the closest. The same differences between the models exist for the other piston velocities.

Increasing to $u_p/u^* = 1.0$, with the evolution shown in Fig 5.9(b) and 5.10(b), there is a more rapid decay in the shock front velocity before obtaining a constant velocity. The properties of the particle path along the piston face, shown in Fig. 5.11(b) and Fig. 5.12(b) show that there is a gradual re-pressurization experienced at early times, with the drop in pressure not sufficient for the shock front velocity to slow down and pull back towards the piston before the re-pressurization is felt at the shock front.

Figures 5.9(c) and 5.10(c) show the evolution for $u_p/u^* = 1.5$. In this case, there is a

rapid decay in the shock front velocity, leading to the shock pulling back towards the piston in the N-S simulations and stalling in the Euler and MD simulations, before re-accelerating and obtaining a steady velocity. The properties of the particle path along the piston face are shown in Fig. 5.11(c) and Fig. 5.12(c). Results show that there is a rapid drop in pressure at early times, which is sufficient to cause the shock speed to become negative with respect to the piston before the re-pressurization is communicated forward causing the shock front to accelerate.

Finally, Figs. 5.9(d) and 5.10(d) show the evolution for $u_{\mathrm{p}}/u^* = 2.0$, as previously discussed. This case shows that increasing the ratio of u_{p}/u^* causes a larger pressure drop to be experienced by the early particle paths. This ultimately leads to the shock front velocity becoming negative with respect to the piston before the re-pressurization is able to be communicated forward to accelerate the shock front.

The results presented in Figs. 5.9-5.12 show that the behaviour of the shock wave evolution changes with u_{p}/u^*, which was shown to play an important part in the shock structure in Ch. 4. For large values of this ratio ($u_{\mathrm{p}}/u^* \geq 2.0$) the behaviour computed by Kamenetsky *et al.* [9] is recovered. However, decreasing this ratio leads to an increased number of elastic collisions during the evolution, leading to a transition between this purely inelastic behaviour and what is expected for elastic media.

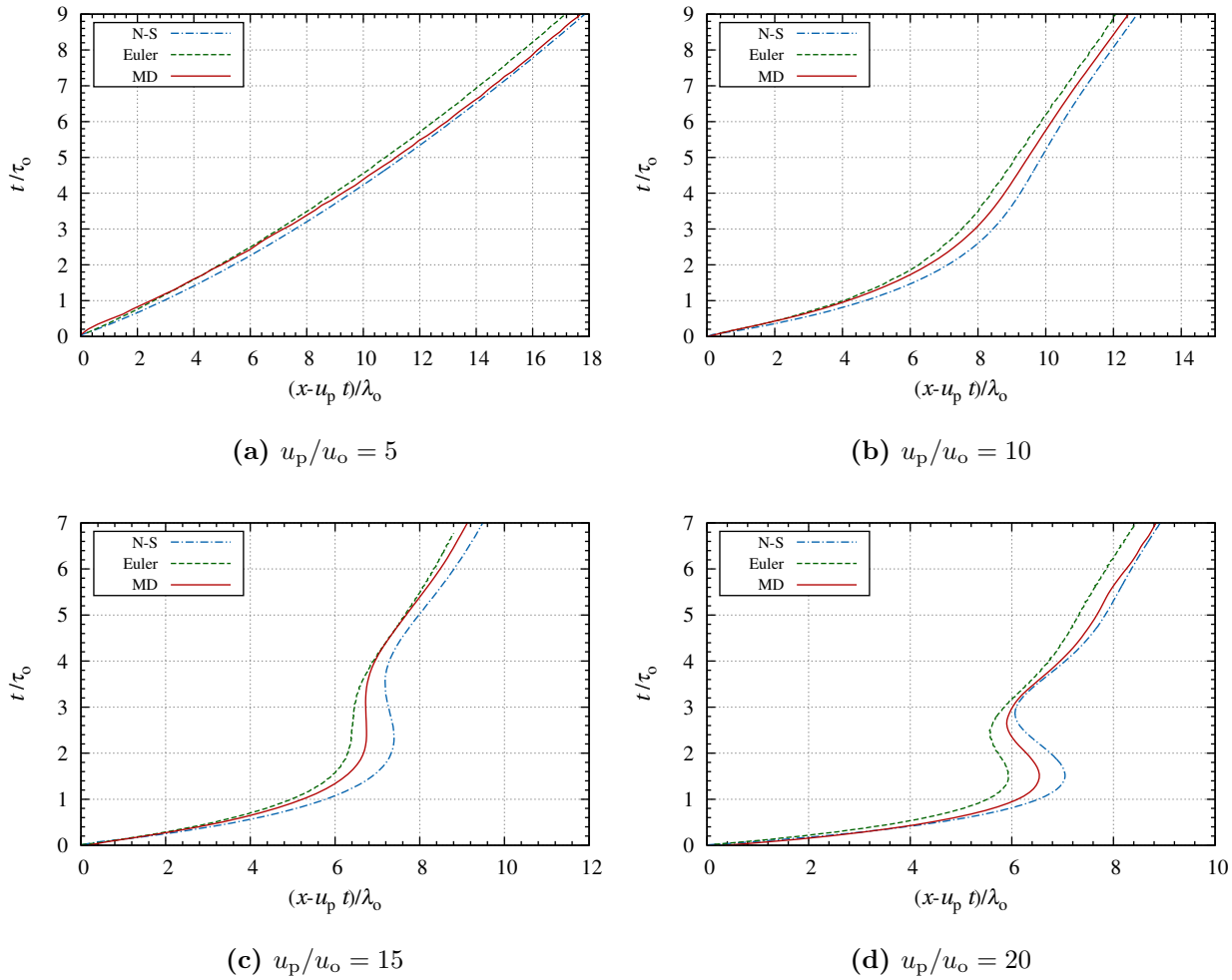

(a) $u_p/u_o = 5$ **(b)** $u_p/u_o = 10$

(c) $u_p/u_o = 15$ **(d)** $u_p/u_o = 20$

Figure 5.9: Comparison of shock front position obtained from MD, N-S, and Euler simulations with $u_p/u_o = 5$ (a), 10 (b), 15 (c), and 20 (d), $u^*/u_o = 10$, $\eta_o = 0.012$, and $\varepsilon = 0.95$.

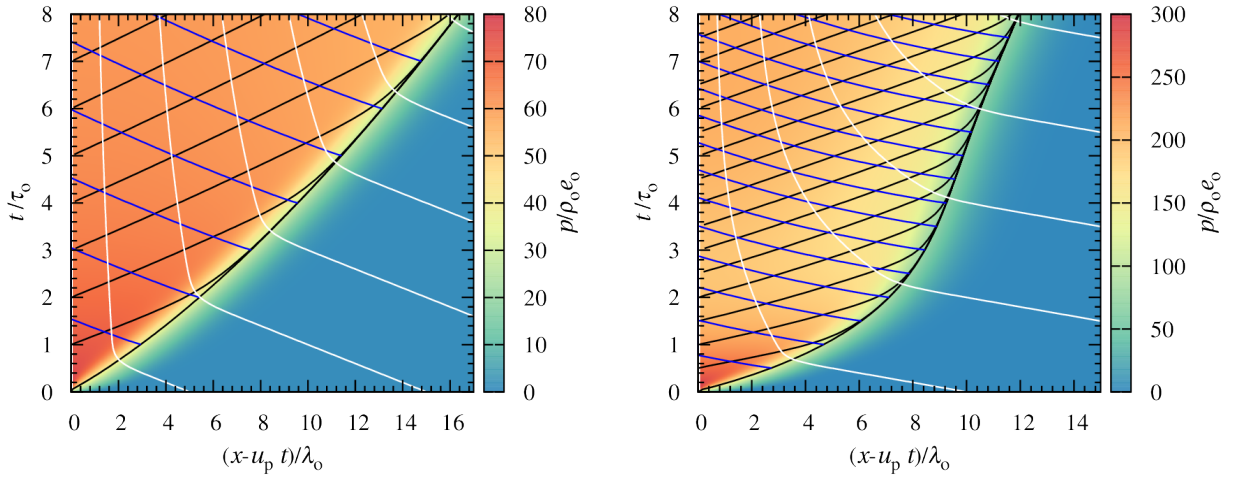

(a) $u_p/u_o = 5$ **(b)** $u_p/u_o = 10$

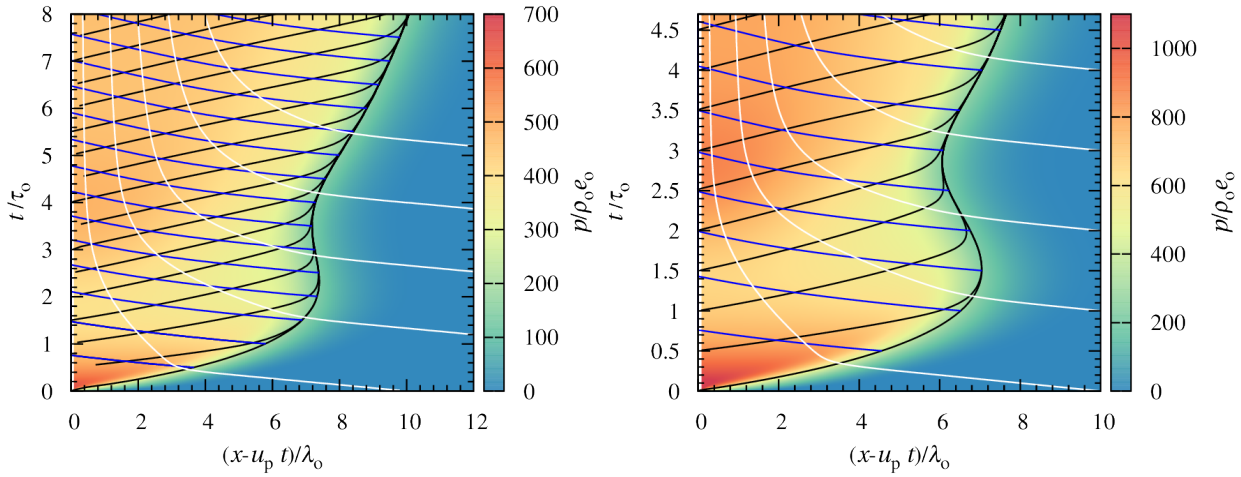

(c) $u_p/u_o = 15$ **(d)** $u_p/u_o = 20$

Figure 5.10: Comparison of the evolution of pressure and characteristics as obtained from N-S simulations for $u_p/u^* = 5.0$ (a), 1.0 (b), 1.5 (c), and 2.0 (d) for $u^*/u_o = 10$, $\eta_o = 0.012$, and $\varepsilon = 0.95$.

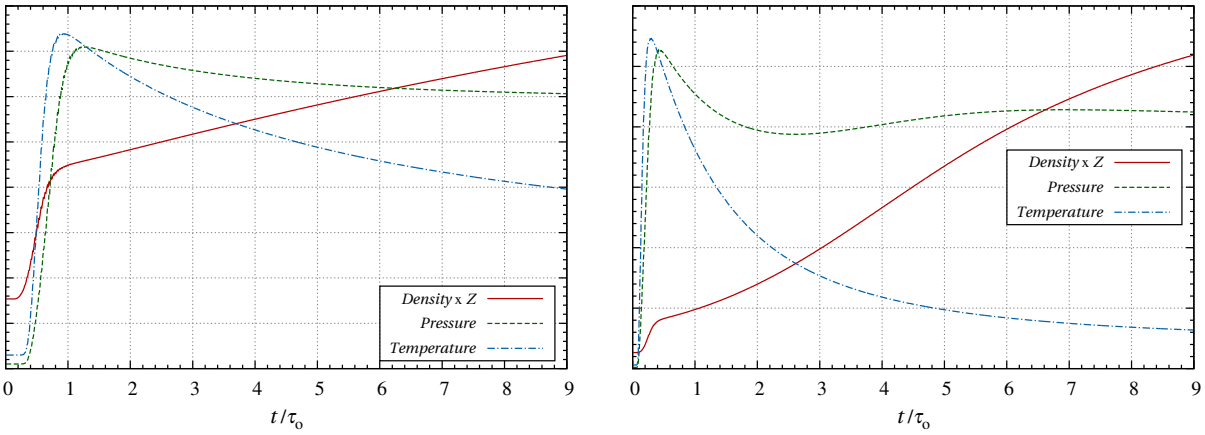

(a) $u_p/u_o = 5$ **(b)** $u_p/u_o = 10$

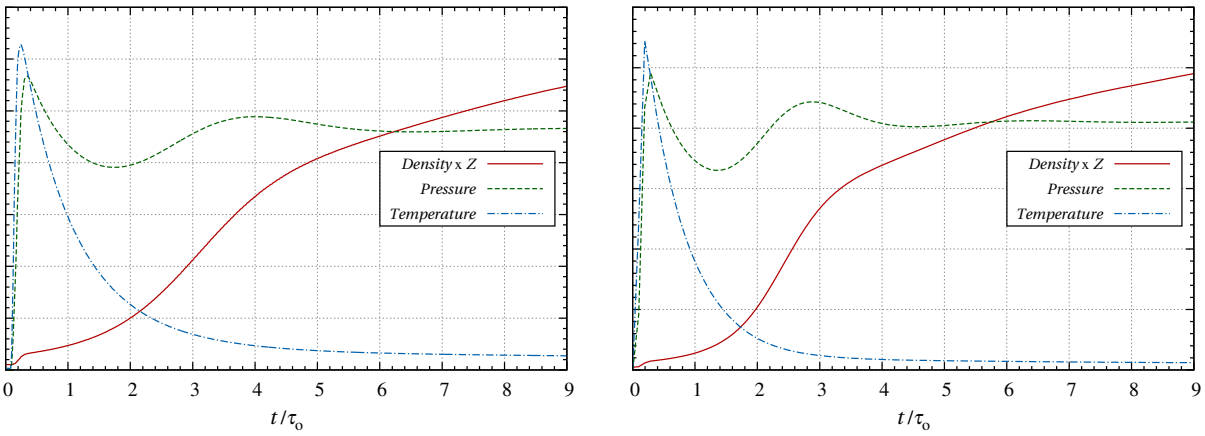

(c) $u_p/u_o = 15$ **(d)** $u_p/u_o = 20$

Figure 5.11: Comparison of particle path properties along the piston face obtained from N-S simulations for $u_p/u_o = 5$ (a), 10 (b), 15 (c), and 20 (d), $u^*/u_o = 10$, $\eta_o = 0.012$, and $\varepsilon = 0.95$.

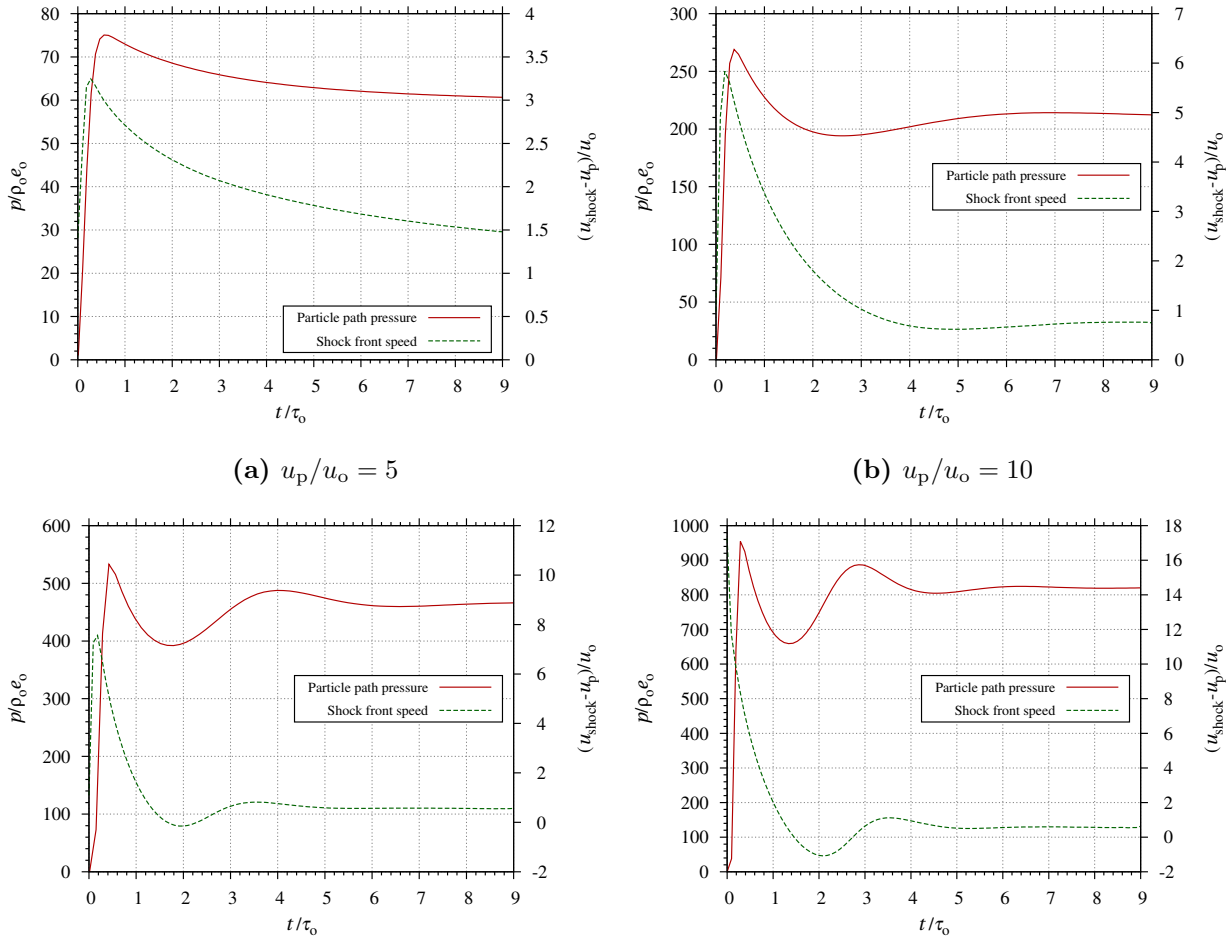

(a) $u_p/u_o = 5$ **(b)** $u_p/u_o = 10$

(c) $u_p/u_o = 15$ **(d)** $u_p/u_o = 20$

Figure 5.12: Comparison of pressure felt for particle paths along the piston face compared to the shock front velocity relative to the piston, as obtained from N-S simulations for $u_p/u_o = 5$ (a), 10 (b), 15 (c), and 20 (d), $u^*/u_o = 10$, $\eta_o = 0.012$, and $\varepsilon = 0.95$.

5.3.2 Role of ε on Evolution

Figure 5.13 compares how the shock fronts evolve for different values of the coefficient of restitution, ε, as obtained from MD and continuum models for $u_p/u_o = 20$, $u^*/u_o = 10$, $\eta_o = 0.012$. Results show that all values of ε give the same behaviour of the shock front pulling back towards the piston, although the time and distance from the piston for the pullback changes. Figure 5.13(a) shows that for $\varepsilon = 0.80$ the front turns to the piston at $t/\tau_o \approx 0.5$, at a distance ahead of the piston of $\sim 1.5\lambda_o$ for Euler and $\sim 2.6\lambda_o$ for N-S simulations.

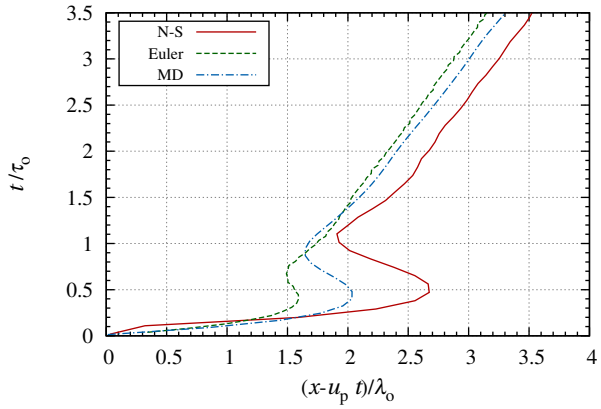

(a) $\varepsilon = 0.80$

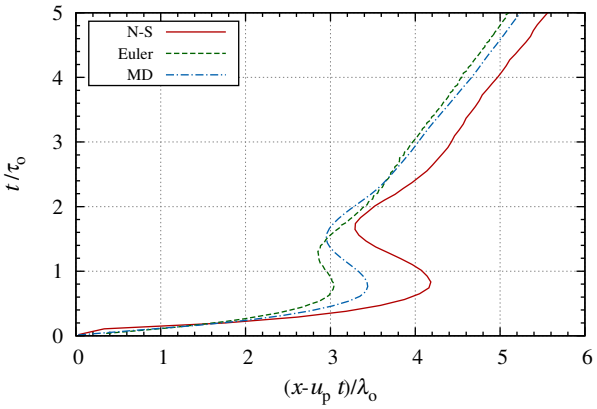

(b) $\varepsilon = 0.90$

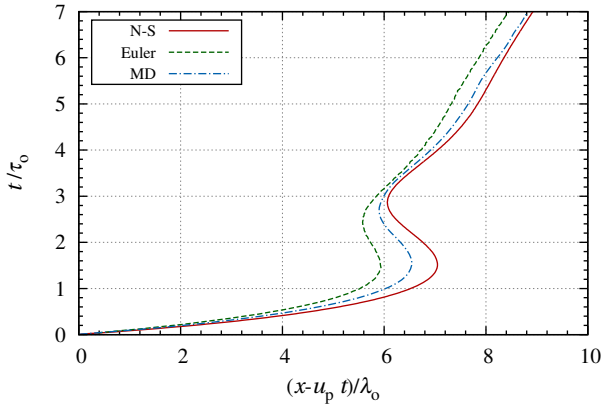

(c) $\varepsilon = 0.95$

Figure 5.13: Comparison of shock front position obtained from MD, N-S, and Euler simulations with $u_p/u_o = 20$, $u^*/u_o = 10$, $\eta_o = 0.012$, and varying ε.

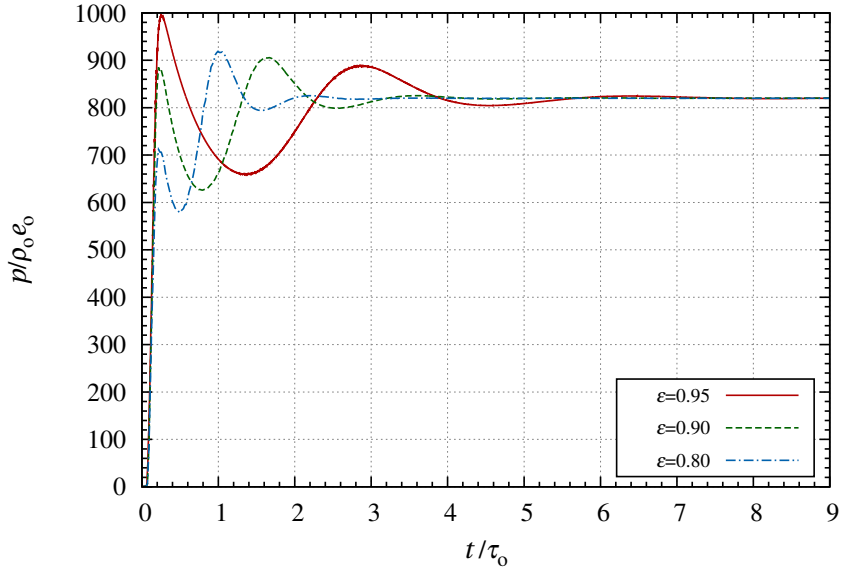

Figure 5.14: Evolution of pressure felt for particle paths along the piston face for different values of ε, as obtained from N-S simulations for $u_p/u_o = 20$, $u^*/u_o = 10$ and $\eta_o = 0.012$.

As in to the previous section, the behaviour of the shock front can be described by observing the pressure felt by the particle paths near the piston, which is shown in Fig. 5.14. The early particle paths along the piston experience a larger and more rapid pressure drop as ε is decreased, which can simply be attributed to a larger cooling rate. The overall dynamics are similar, with the presence of a large pressure drop, followed by a re-pressurization prior to coming to some steady value. The more rapid pressure drop leads to a quicker decrease in shock front velocity for lower ε, as shown in Fig. 5.15. Once the transient behaviour subsides, all values of ε obtain the same shock front velocity, as expected since the state in the equilibrium region is equal.

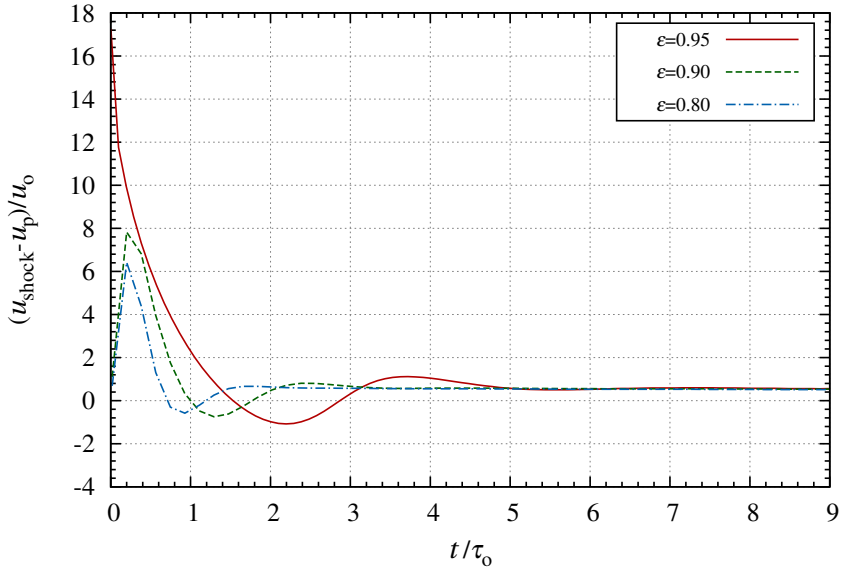

Figure 5.15: Evolution of shock front velocity relative to the piston for different values of ε, as obtained from N-S simulations for $u_p/u_o = 20$, $u^*/u_o = 10$ and $\eta_o = 0.012$.

5.3.3 Role of η_o on Evolution

Figure 5.16 compares the evolution of the shock front as obtained from N-S simulations for initial packing factors of η_o =0.005, 0.012, and 0.025, with u_p/u_o =20, u^*/u_o = 10, and ε = 0.95. Results show that the time for the shock front reversing towards the piston is unaffected by η_o, with each case reversing at $t/\tau_o \approx 1.5$. However, the distance ahead of the piston where the shock reverses to the piston increases with greater values of η_o, where for $\eta_o = 0.005$ it extends by $\sim 6.5\lambda_o$ ahead of the piston before reversing, while for $\eta_o = 0.025$ it extends by $\sim 8\lambda_o$. These differences can be attributed to the longer relaxation zone length expected for larger values of η_o, as shown in Ch. 4.

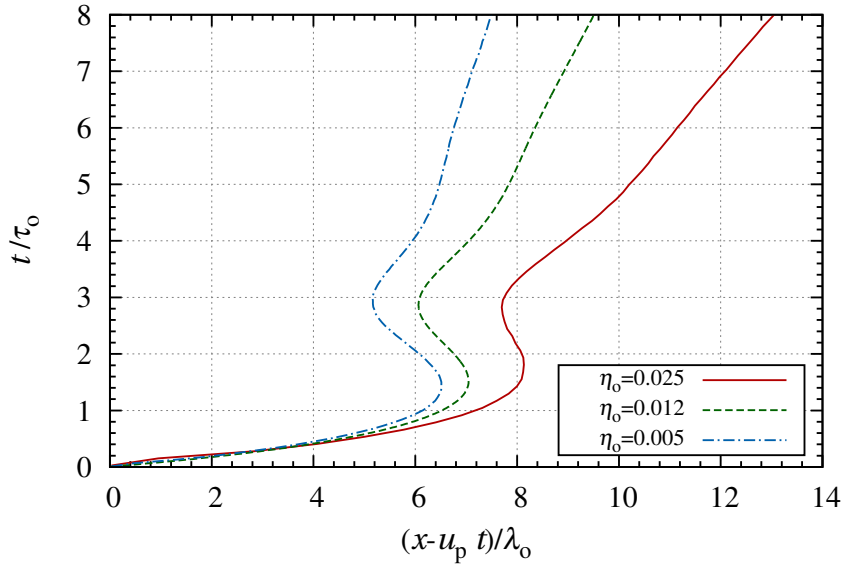

Figure 5.16: Comparison of shock front position obtained from N-S simulations, where η_o was varied, and u_p/u_o =20, $u^*/u_o = 10$, and $\varepsilon = 0.95$.

5.4 Scaling of Evolution with u^*

Results in Ch. 4 indicated that for $u_p/u^* \geq 0.3$, equal values of u_p/u^* yield the same shock *structure* once scaling is completed with the impact threshold u^* instead of u_o. Considering this finding, the *evolution* are compared for similar values of u_p/u^* with time scaled by $\tau^* = \lambda_o/u^*$.

Figure 5.17 shows the location of the shock front using such a time scaling for the cases where u_p and u^* are varied to satisfy $u_p/u^* = 2$, with $\eta_o = 0.012$ and $\varepsilon = 0.95$. The results show that under this scaling, the evolution of each shock structure are nearly identical. The distance and time of reversal towards the piston are equal, occurring at $7\lambda_o$ ahead of the piston at a time of $15\tau^*$.

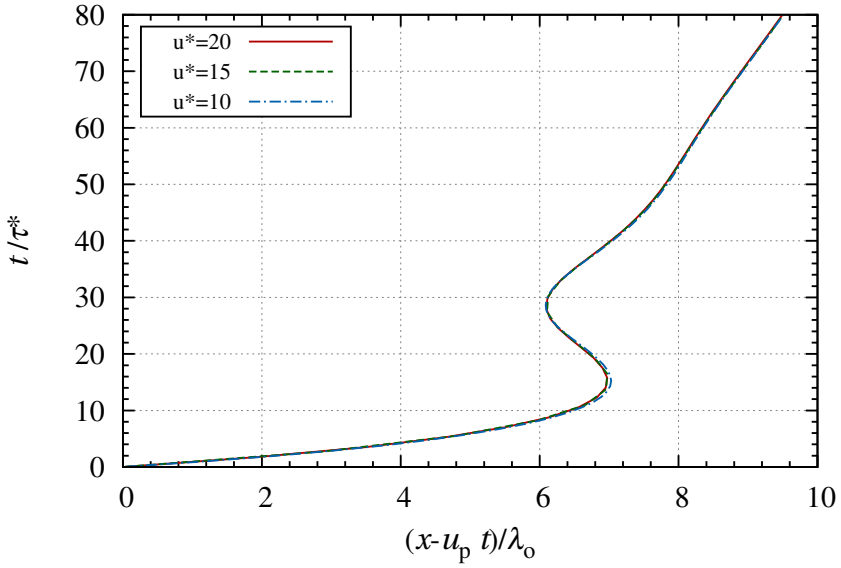

Figure 5.17: Comparison of shock front position obtained from N-S simulations, where u_p and u^* are varied, with u_p/u^* =2, $\eta_\mathrm{o} = 0.012$ and $\varepsilon = 0.95$.

5.5 Summary

The evolution of piston driven shock waves in a two-dimensional granular gas with activated inelastic collisions was investigated and presented in the current chapter. Results were obtained using the MD, N-S and Euler models. The results demonstrated that the N-S and Euler descriptions recover a similar evolution and shock structure as that obtained from MD, thus validating the use of the continuum description as given in Ch. 3.

Three different regimes of transient dynamics were found, which were controlled by u_p/u^*. For $u_\mathrm{p}/u^* \leq 0.5$, the shock wave experiences little decay, representing the behaviour of a nearly elastic shock wave. For sufficiently strong shock waves, with $u_\mathrm{p}/u^* \geq 2.0$, the shock wave experiences a very large decay. The large decay causes the shock front to pull back towards the piston during the early stages, a finding previously observed by Kamenetsky *et al.* [9] for all collisions being inelastic. Analysis of the family of characteristics revealed that the reason for this shock reversal was due to a large drop in pressure and subsequent re-pressurization experienced by particle paths along the piston face. The pressure felt by the

early particle paths is communicated to the shock front via forward running characteristics modifying the velocity of the shock front. The results for such strong shocks are also in agreement with findings from Ch. 4, whereby the evolution was shown to only depend on three parameters: u_{p}/u^*, η_{o} and ε, and becomes independent on the initial temperature.

As u_{p}/u^* is decreased from the strong shock regime, the behaviour of the evolution transitions from what is expected for a purely inelastic shock wave to what is expected for an elastic system of disks. Within this transitional regime, results showed that the shock front does not experience a negative velocity relative to the piston for decreasing values u_{p}/u^*, although a decay can still be experienced during the evolution. This behaviour is due to a lower pressure drop felt by early particle paths that are communicated to the shock front, which were unable to cause a pull back of the shock front. To the best of the author's knowledge, this is the first time this transitional, viscoelastic collision dominated, regime has been investigated.

Chapter 6

Dynamics of Shock Formation and Onset of Hydrodynamic Instabilities in 2D

The current chapter presents the results for the evolution of shock morphology obtained in two-dimensions using the MD, N-S, and Euler models described in Ch. 3. The goal is to investigate whether systems involving dissipative collisions can exhibit unstable shock behaviour. The definition of *instability* considered here is a multi-dimensional instability in the form of corrugations or non-homogeonous regions within the shock structure. For example, the structure sketched out in Fig. 6.1 is considered unstable.

The current chapter is organized as follows. First, the structure in two-dimensions for a

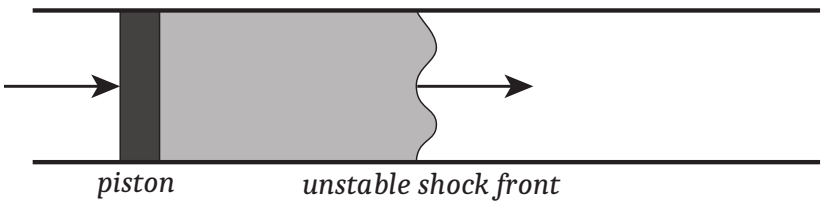

Figure 6.1: Sketch of a multi-dimensional unstable shock structure.

piston propagated shock wave obtained using the MD model is investigated. This case is used as a baseline case for the comparison with the continuum descriptions. Once the structure of the shock in two-dimensions is recovered using MD, the conditions under which a similar structure can be recovered at the continuum level are explored. Finally, the evolution of the steady-state structure is evaluated using the continuum models, to further address the stability of the shock structure and the contributing factors of the instability.

6.1 Evolution of Shock Structure Predicted at the Microscopic Level

Figure 6.2 shows the evolution of the two-dimensional shock structure obtained from MD, showing the position of each disk obtained for a single realization, where $u_{\rm p}/u_{\rm o} = 20$, $u^*/u_{\rm o} = 10$, $\varepsilon = 0.95$, and $\eta_{\rm o} = 0.012$. In this example, there are $N = 30000$ disks in a domain of $(l_x \times l_y)/\lambda_{\rm o} = 172 \times 17.2$. Each subsequent image represents the position at a time interval of $\Delta t = 0.90\tau_{\rm o}$ later.

The development of the shock wave is similar to what was seen from the one-dimensional structure. Initially, a shock wave extends ahead of the piston, representing a small jump in density (number of disks). In the fourth frame, density is shown to start increasing along the piston face. As the density continues to increase behind the shock wave, there is a birth of high density clusters that extend ahead.

Figure 6.3 compares the one-dimensional distribution of temperature and density obtained from Ch. 5 to the two-dimensional structure shown at $t/\tau_{\rm o} = 8.12$. Streamlines of velocity are also shown overlayed on the particle distributions.

Comparing with the one-dimensional structure, once the state begins transitioning to the equilibrium region, the flow becomes unstable with the formation of high density non-uniformities. The velocity streamlines show the presence of convective rolls within these

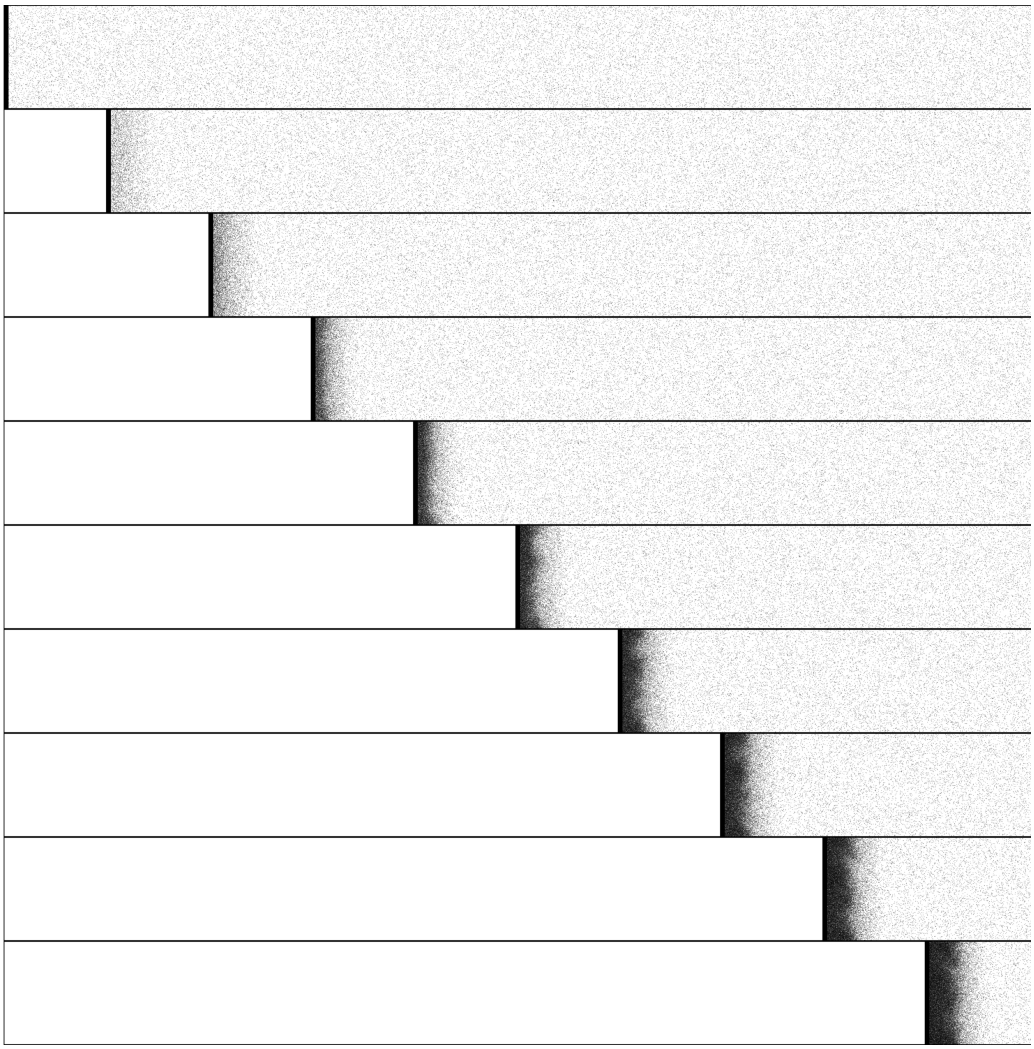

Figure 6.2: Evolution of shock morphology from MD simulations with each snapshot at intervals of $\Delta t/\tau_{\rm o} = 0.90$, where $u_{\rm p}/u_{\rm o} = 20$, $u^*/u_{\rm o} = 10$, $\varepsilon = 0.95$ and $\eta_{\rm o} = 0.012$.

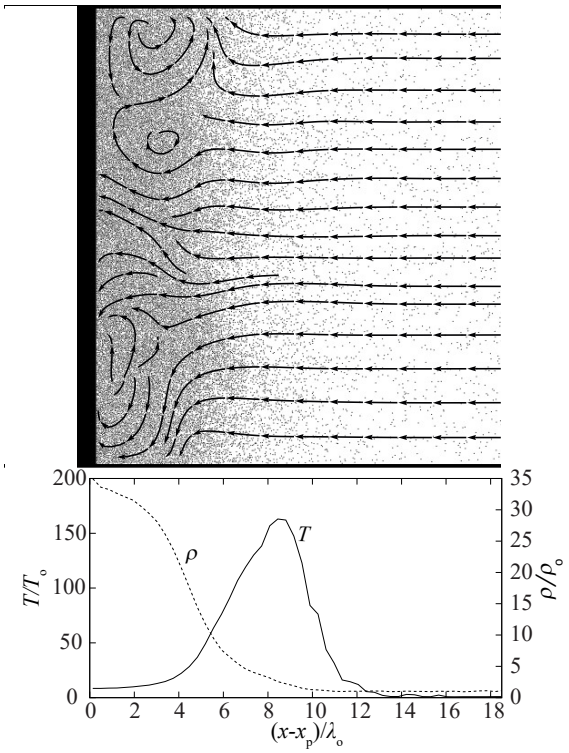

Figure 6.3: Two-dimensional particle distribution and coarse-grained stream-lines from MD (upper), with coarse-grained one-dimensional distribution of temperature and density (lower) at $t = 8.12\tau_o$ for $u_p/u_o = 20$, $u^*/u_o = 10$, $\varepsilon = 0.95$ and $\eta_o = 0.012$.

clusters. Further analysis of the shock structure reveals that the wavelength of these patterns is similar in magnitude to the relaxation length for these parameters, which for this case is $l_R/\lambda_o \approx 7.3$, as given in Ch. 4. This relationship is explored further in future sections, but is an important characteristic to note when comparing with the continuum results.

6.2 Evolution of Shock Structure in Continuum Models

6.2.1 'Stable' Shock Structure

The incoming flow field was perturbed in the continuum models over a short period to investigate whether instabilities would form. Figure 6.4 shows the results for inviscid continuum simulations with the same parameters explored in the MD example from Fig. 6.3. For this

case, the incoming flow's density was perturbed during the times $t/\tau_o = 0$ to 1.0, with the density perturbed in square bins of sides $dx = \lambda_o$ and fluctuations with a standard deviation of $\sigma = 0.33\rho_o$. A contour line was chosen arbitrarily at $\rho/\rho_o = 29$ to visualize instabilities.

The results in Fig. 6.4 show that the structure does become unstable when the incoming flow field is perturbed. However, as the perturbations stop, the instabilities decay and smear along the piston face. Similar results can be observed for the N-S simulations, although the instabilities diffuse out rapidly once the perturbations end.

This example demonstrates that perturbing the flow is not sufficient for instabilities to grow, as the flow remains unstable *only* when the incoming flow provides perturbations.

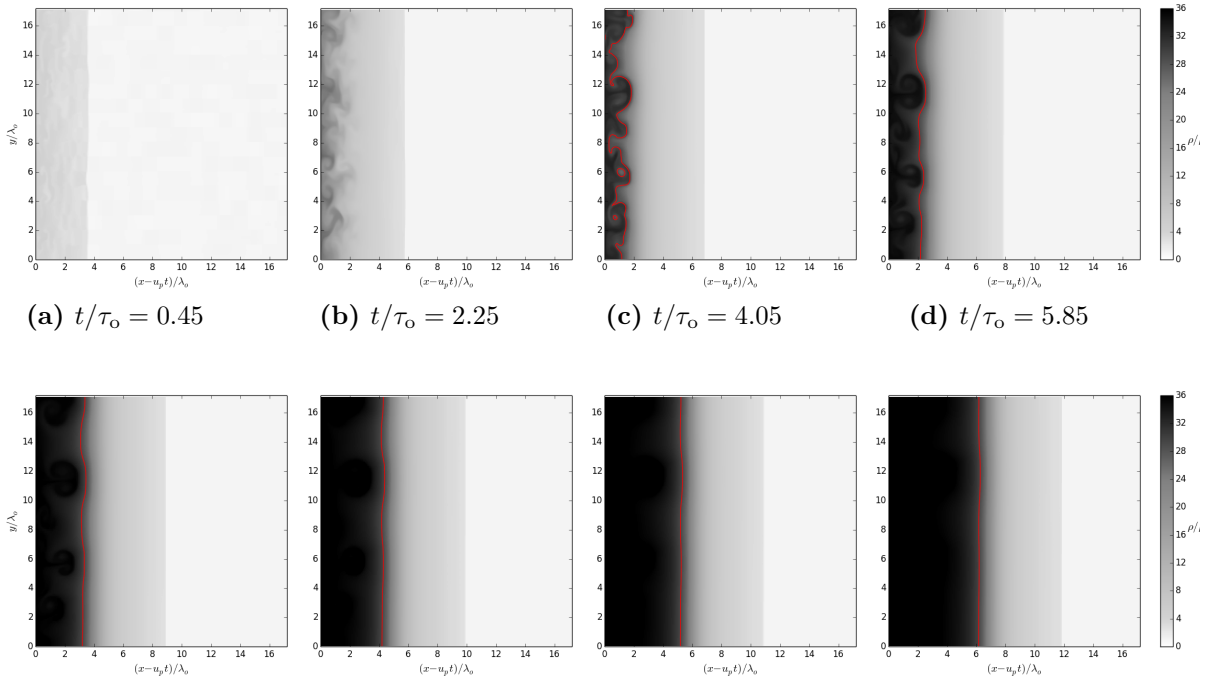

(a) $t/\tau_o = 0.45$ **(b)** $t/\tau_o = 2.25$ **(c)** $t/\tau_o = 4.05$ **(d)** $t/\tau_o = 5.85$

(e) $t/\tau_o = 7.65$ **(f)** $t/\tau_o = 9.45$ **(g)** $t/\tau_o = 11.25$ **(h)** $t/\tau_o = 13.05$

Figure 6.4: Evolution of shock structure obtained from Euler simulations where incoming flow is perturbed from $t/\tau_o = 0$ to 1.0 for $u_p/u_o = 20$, $u^*/u_o = 10$, $\varepsilon = 0.95$ and $\eta_o = 0.012$. Incoming flow is perturbed in bins of sides $dx = \lambda_o$ and a standard deviation of $\sigma = 0.33\rho_o$.

6.2.2 Influence of Noise on Shock Structure

The continuum models assume that matter is continuously distributed without any fluctuations. This is not valid when comparing with MD, as there are fluctuations inherent with the distribution of disks. Indeed, it can be shown that, if a domain of disks is divided into bins of size dx, the variance in number density can be significant for small enough areas [38]. When looking at a system of disks, the standard deviation in number density can be written as (see Appendix D):

$$\sigma = \frac{\rho_o d\sqrt{\pi}}{2\sqrt{\eta} dx}. \tag{6.1}$$

Since it is evident that there are large fluctuations in the MD simulations, the next step was to adopt these fluctuations into the continuum models to investigate the role they may play. To account for the statistical fluctuations, perturbations were introduced into the incoming density flow field as discussed in Sec. 3.4.1. This was simply done by separating the domain and incoming flow into bins of size $dx \times dx$ and perturbing the density with some value ρ', i.e., $\rho = \rho_o + \rho'$. A schematic of these perturbed cells is shown in Fig. 6.5, which compares the representative cell size in MD to the perturbed bins that are introduced in the continuum model. The amplitude of the perturbation was taken randomly within the range $-2\sigma \leq \rho' \leq 2\sigma$, where σ was given from (6.1). This range was chosen for the simple step-wise distribution used here to recover the same standard deviation given in the actual distribution from MD.

Figure 6.6 gives the results for the evolution of two-dimensional structure obtained from Euler and N-S with the inclusion of these fluctuations, for the case where $u_p/u_o = 20$, $u^*/u_o = 10$, $\varepsilon = 0.95$ and $\eta_o = 0.012$. For comparison, the coarse-grain averaged density distribution from MD is also shown. In this case, the perturbed bins in the continuum models were given a size of $dx = \lambda_o$, which corresponds to a standard deviation of $\sigma = 0.33\rho_o$.

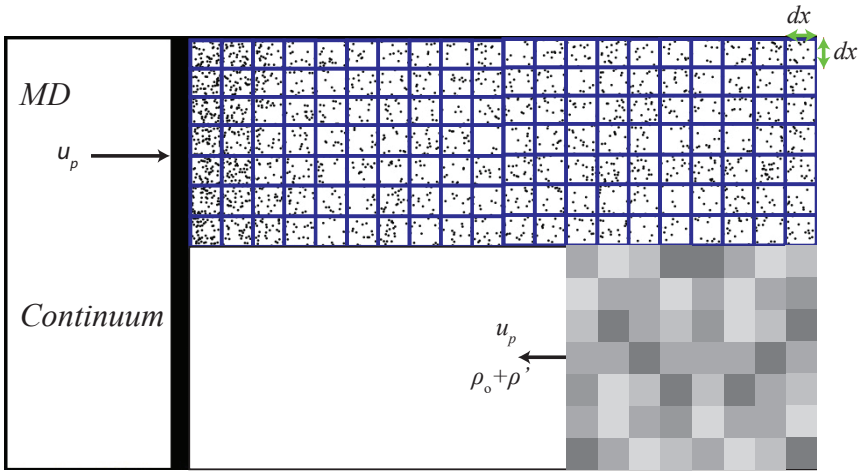

Figure 6.5: Schematic comparing the MD and continuum domains, where continuum simulations are perturbed in bins of size $dx \times dx$ with amplitudes in agreement with the statistical fluctuations observed in MD being split into bins of similar dimensions.

At initial times, a noisy flow can be seen moving towards the piston face, which lead to a jump in density with the formation of the shock wave. As time progresses, density rises rapidly at the piston face, as seen in Fig. 6.6(b), for $t/\tau_o = 2.71$. Instabilities form in the Euler simulations at this time. At later times ($t/\tau_o = 5.41$ and 8.12), N-S and MD yield instabilities with bumps forming near the piston face and extending ahead.

Figure 6.7 further compares the developed structure from N-S to MD, where streamlines and the pattern formation are outlined. Results for N-S simulations show that the model recovers the same formation of convective rolls within the higher density regions, as exhibited by MD in Fig. 6.3. These results demonstrate that the continuum models can indeed recover the same instability seen in MD if fluctuations are included. Also given in Fig. 6.7 is the relaxation length scale under these parameters, $l_R \approx 7.3\lambda_o$, as obtained in Ch. 4. As can be seen, both MD and N-S yield a size of these bumps similar to l_R.

To investigate if the wavelength of the patterns is locked to the domain size, a larger domain of $y/\lambda_o = 25$ was considered, with results shown in Fig. 6.8, as compared to $y/\lambda_o = 17$

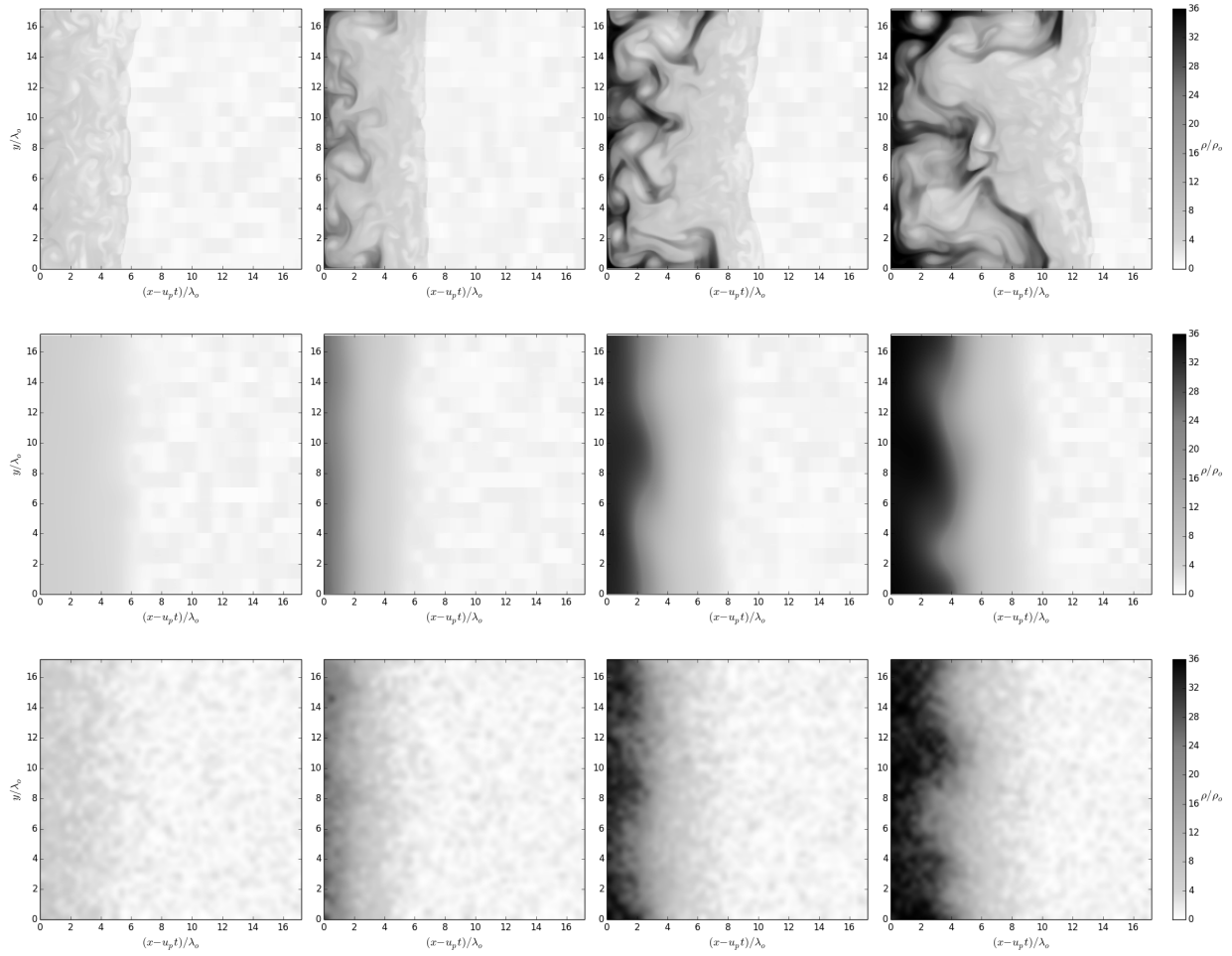

(a) $t/\tau_o = 0.90$ **(b)** $t/\tau_o = 2.71$ **(c)** $t/\tau_o = 5.41$ **(d)** $t/\tau_o = 8.12$

Figure 6.6: Evolution of shock morphology obtained at different times from Euler (top), N-S (middle) and MD (bottom) simulations with $u_p/u_o = 20$, $u^*/u_o = 10$, $\varepsilon = 0.95$ and $\eta_o = 0.012$. Continuum simulations have perturbation size of $dx = \lambda_o$, which corresponds to a standard deviation of $\sigma = 0.33\rho_o$.

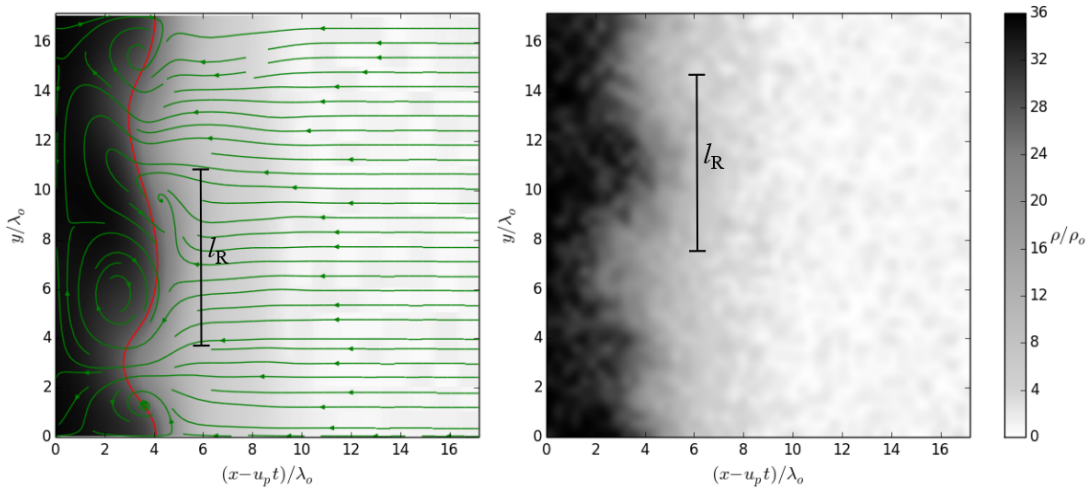

(a) N-S **(b)** MD

Figure 6.7: Comparison of shock morphology obtained at $t/\tau_o = 8.12$ for (a) N-S and (b) MD simulations, where $u_p/u_o = 20$, $u^*/u_o = 10$, and $\varepsilon = 0.95$. Also shown is the relaxation length for these conditions, $l_R \approx 7.3\lambda_o$. N-S simulations are perturbed with bins of size $dx = \lambda_o$, which corresponds to a standard deviation of $\sigma = 0.33\rho_o$.

in Fig. 6.7. The results from N-S show that the amplitude and wavelength of the instabilities are independent of the domain size, recovering a similar structure to what was seen for the smaller domain.

Simulations with different resolutions were computed to determine whether the instabilities are an artifact of unresolved simulations. Figure 6.9 shows the results obtained from N-S for the case presented in Fig. 6.6, with the finest resolution after refinement varied from $\Delta = \lambda_o/4$ to $\Delta = \lambda_o/16$. As can be seen, the structures are qualitatively similar, all being capable of recovering the unstable shock formation of approximately 1.5-2 wavelengths within the current domain. Little difference is observed between the simulations using resolutions of $\Delta = \lambda_o/8$ in Fig. 6.9(b) and $\Delta = \lambda_o/12$ in Fig. 6.9(c), thus confirming that using a resolution of at least $\Delta = \lambda_o/8$, as identified in Sec. 3.4.2, is sufficient.

To confirm that the resulting shock structures are not fixed to the amplitude and the bin sizes of the perturbations, other bin sizes were computed with their respective variance

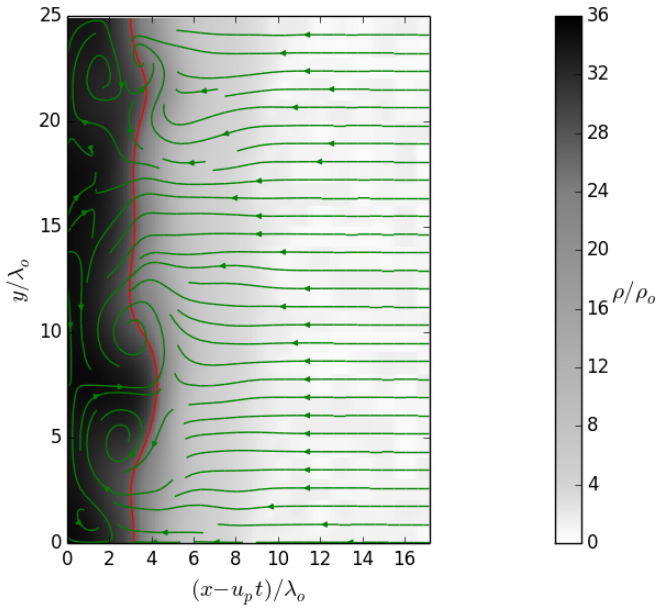

Figure 6.8: Comparison of shock morphology obtained from N-S for a taller domain, of y/λ_o ranging from 0 to 25, at $t/\tau_o = 8.12$, where $u_p/u_o = 20$, $u^*/u_o = 10$, $\varepsilon = 0.95$, and perturbations implemented in bins of size $dx = \lambda_o$, corresponding to $\sigma = 0.33\rho_o$.

provided from Eq. 6.1. Fig. 6.10 shows the developed shock structures obtained from N-S simulations for the case shown in Fig. 6.6 for bin sizes of $dx/\lambda_o = 0.75,\ 1.0,\ 1.5$, representing standard deviations of approximately $0.56\rho_o$, $0.33\rho_o$, and $0.22\rho_o$, respectively.

The results show that using bins different than $dx/\lambda_o = 1.0$ with the amplitude of perturbations adjusted accordingly recovers a similar pattern formation. This indicates that a similar structure and spacing of these patterns is recoverable while perturbations for the respective bin sizes are in agreement with Eq. 6.1.

The case where the amplitude of perturbations was not in agreement with Eq. 6.1 was also considered for a given bin size to further validate the need for perturbations to agree with spatial fluctuations present in MD. Figure 6.11 shows the developed shock structure for $u_p/u^* = 2.0$, $\varepsilon = 0.95$, and $\eta_o = 0.012$, with $dx = \lambda_o$ and three different amplitudes of perturbations. The expected standard deviation of $0.33\rho_o$ is shown in Fig. 6.11(a) and is compared with lower than expected standard deviations of $0.16\rho_o$ in Fig. 6.11(b) and $0.025\rho_o$

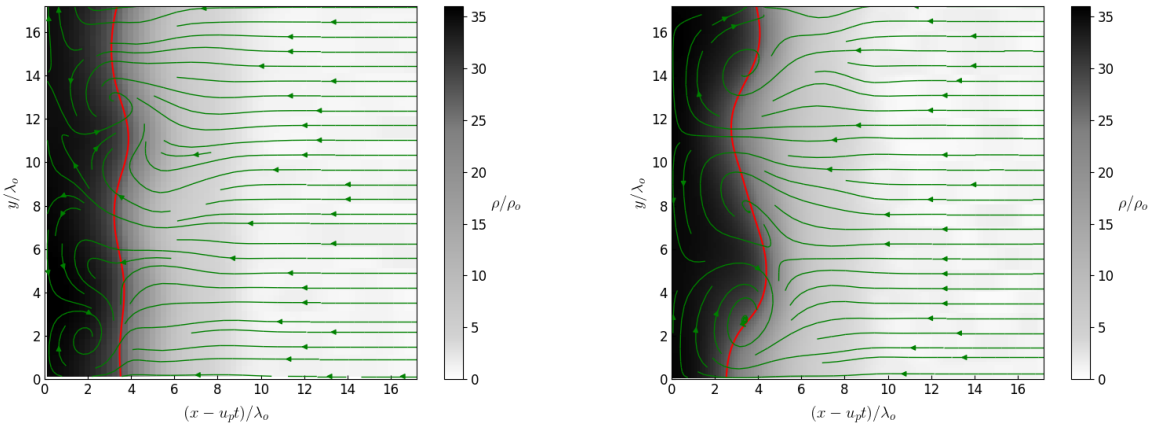

(a) $\Delta = \lambda_o/4$ **(b)** $\Delta = \lambda_o/8$

(c) $\Delta = \lambda_o/12$ **(d)** $\Delta = \lambda_o/16$

Figure 6.9: Developed shock structures obtained from N-S simulations for different resolutions, with the finest resolution after refinement of (a) $\Delta = \lambda_o/4$, (b) $\Delta = \lambda_o/8$, (c) $\Delta = \lambda_o/12$, and (d) $\Delta = \lambda_o/16$. All cases are shown at a time of $t/\tau_o = 8.12$ where $u_p/u_o = 20$, $u^*/u_o = 10$, $\varepsilon = 0.95$, $\eta_o = 0.012$, and perturbed with bins of size $dx = \lambda_o$, which corresponds to a standard deviation of $\sigma = 0.33\rho_o$.

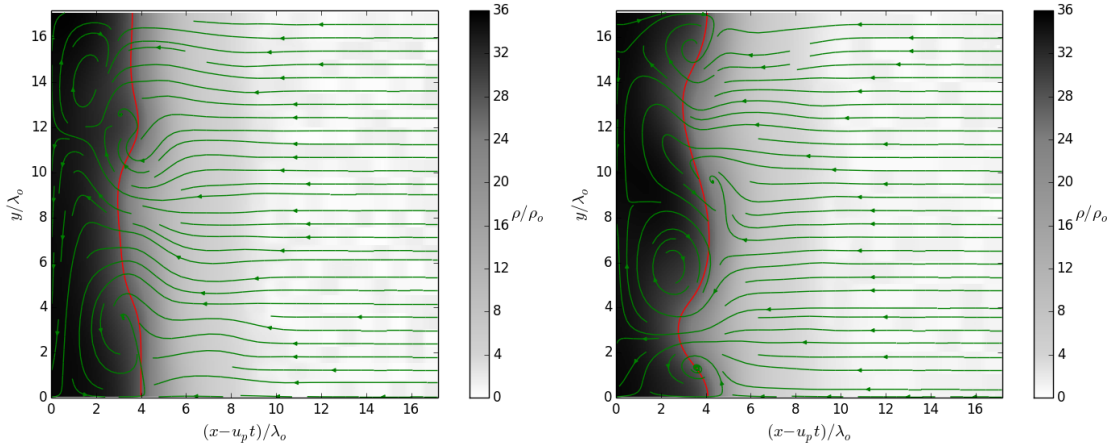

(a) $dx = 0.75\lambda_o$ **(b)** $dx = \lambda_o$

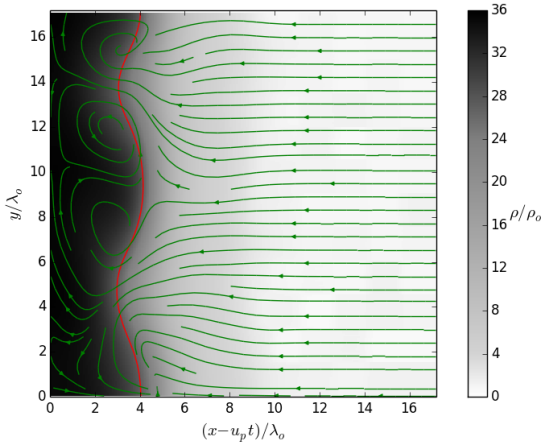

(c) $dx = 1.5\lambda_o$

Figure 6.10: Developed shock structures obtained from N-S simulations for different perturbation bin sizes of (a) $dx = 0.75\lambda_o$, (b) $dx = \lambda_o$, and (c) $dx = 1.5\lambda_o$, with $u_p/u_o = 20$, $u^*/u_o = 10$, $\varepsilon = 0.95$ and $\eta_o = 0.012$.

in Fig. 6.11(c).

The case shown in Fig. 6.11(b) has a standard deviation half of what is expected for the given dimensions. In this case, the structure is still shown to become unstable, with the presence of convective rolls and bumps along the piston, although the bumps do not extend significantly ahead of the piston face. Further decreasing the standard deviation in Fig. 6.11(c) shows that there is no noticeable instability, with a planar shock structure and no convective rolls along the piston face. These results suggest that the amplitude of perturbations must be in agreement with Eq. 6.1 to reproduce the instabilities seen in MD.

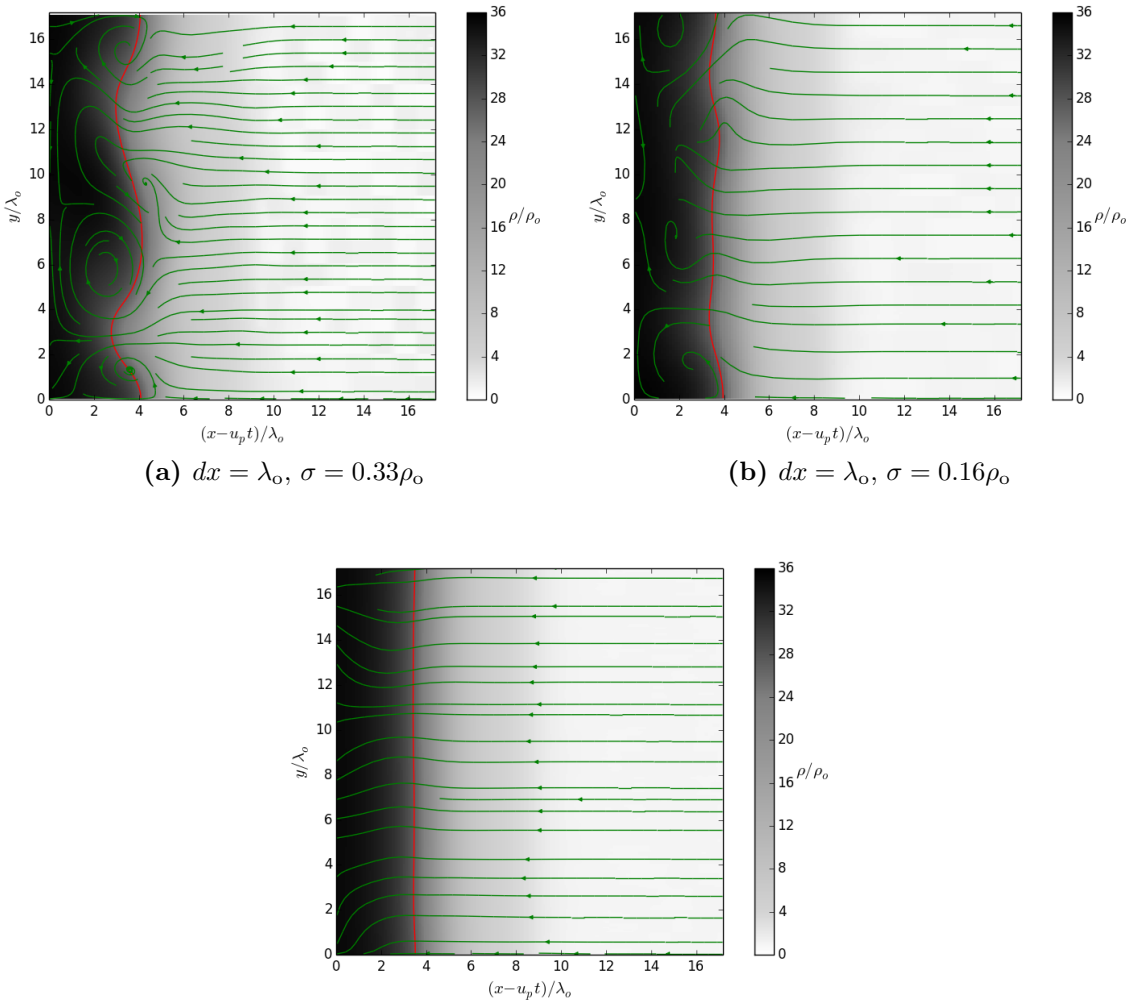

(a) $dx = \lambda_o$, $\sigma = 0.33\rho_o$

(b) $dx = \lambda_o$, $\sigma = 0.16\rho_o$

(c) $dx = \lambda_o$, $\sigma = 0.025\rho_o$

Figure 6.11: Developed shock structures obtained from N-S simulations for similar perturbation bin sizes of $dx = \lambda_o$, where the standard deviation of perturbations is (a) in agreement with statistics, with $\sigma = 0.33\rho_o$, and lower than expected from statistics, with (b) $\sigma = 0.16\rho_o$ and (c) $\sigma = 0.025\rho_o$. All cases are shown at a time of $t/\tau_o = 8.12$ where $u_p/u_o = 20$, $u^*/u_o = 10$, $\varepsilon = 0.95$ and $\eta_o = 0.012$.

6.3 Parametric Study

A parametric study of the multi-dimensional instability was performed using the MD and continuum models. This was also completed to see if there are any discrepancies between the microscopic and macroscopic models under different sets of parameters. In this section, results for varying u_{p}/u^*, ε and η_{o} are investigated, similar to the investigations completed for the one-dimensional structure in Ch. 5. Since the previous section showed a connection between the instability scales and the relaxation length scales, all results in this section are compared with the relaxation length scales obtained in Ch. 4.

6.3.1 Role of u_{p}/u^* on Shock Structure

Figure 6.12 shows the resulting density distribution from N-S and MD for $u_{\mathrm{p}}/u^* = 3.0$, $u^*/u_{\mathrm{o}} = 10$, $\varepsilon = 0.95$, and $\eta_{\mathrm{o}} = 0.012$. Under these conditions $l_{\mathrm{R}} \approx 5.8\lambda_{\mathrm{o}}$, which is shown in the images. Results from MD show bumps with a similar wavelength to l_{R}. Results from N-S show that the structure still remains unstable, although the wavelength of the instability from N-S is larger than l_{R} for these parameters. Results from N-S and MD still show fair agreement, demonstrating that an increasing value of u_{p}/u^* yields a more compact unstable structure.

Figure 6.13 shows the results for $u_{\mathrm{p}}/u^* = 1.0$, with other parameters the same as before. Under these conditions, $l_{\mathrm{R}} \approx 16.8\lambda_{\mathrm{o}}$, which is shown in the images. Unstable patterns are difficult to see in MD, although the results from N-S demonstrate that under these parameters, the flow still becomes unstable, with convective rolls and bumps forming along the piston face. The spacing of these patterns is shown to be similar to the relaxation length.

Results from N-S are shown in Figs. 6.14 and 6.15 for $u_{\mathrm{p}}/u_{\mathrm{o}} = 7.5$ and 5.0, respectively, with $u^*/u_{\mathrm{o}} = 10$, $\varepsilon = 0.95$, and $\eta_{\mathrm{o}} = 0.012$. The coarse-grain averaged properties in MD are too noisy to interpret any instabilities, and are not included. For the case where $u_{\mathrm{p}}/u^* = 0.75$

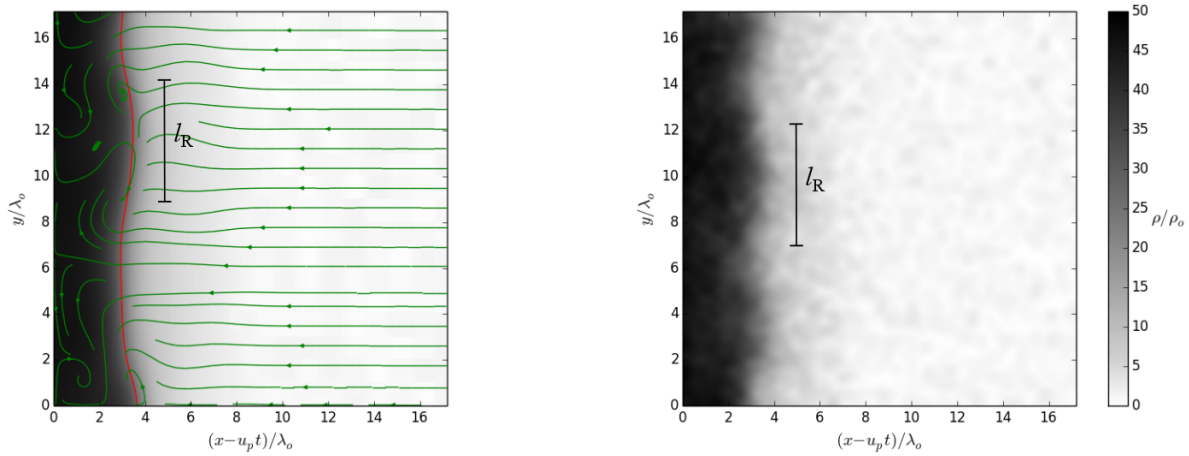

(a) NS **(b)** MD

Figure 6.12: Comparison of shock morphology obtained at $t/\tau_o = 5.40$ for (a) N-S and (b) MD simulations, where $u_p/u_o = 30$, $u^*/u_o = 10$, $\varepsilon = 0.95$, and $\eta_o = 0.012$. Also shown is the relaxation length for these conditions, $l_R \approx 5.8\lambda_o$. N-S simulations perturbed with bins of size $dx = \lambda_o$, corresponding to $\sigma = 0.33\rho_o$.

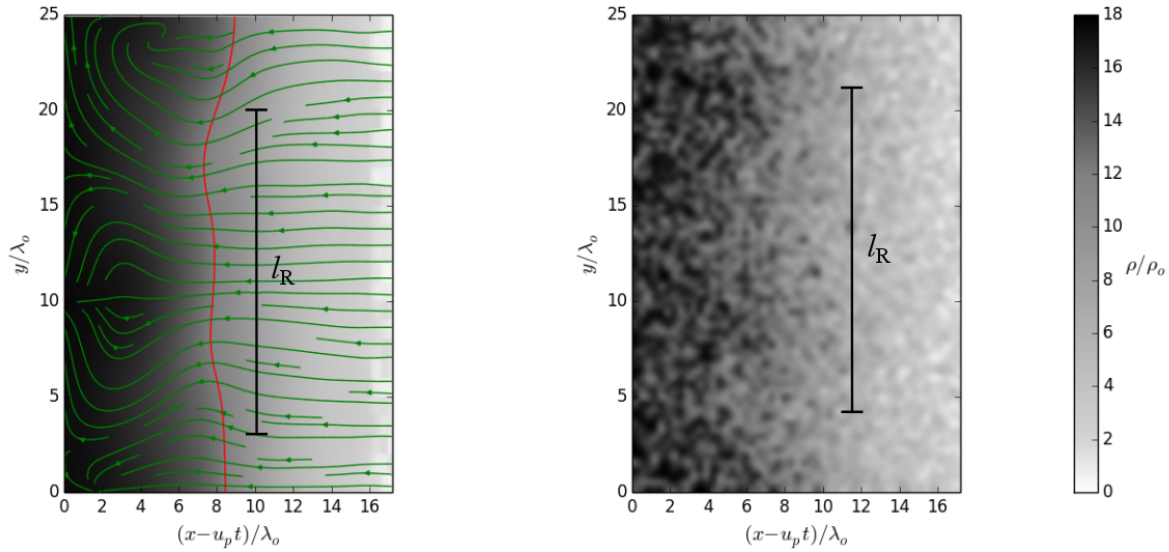

(a) N-S **(b)** MD

Figure 6.13: Comparison of shock morphology obtained at $t/\tau_o = 16.24$ for (a) N-S and (b) MD simulations, where $u_p/u_o = 10$, $u^*/u_o = 10$, $\varepsilon = 0.95$, and $\eta_o = 0.012$. Also shown is the relaxation length for these conditions, $l_R \approx 16.8\lambda_o$. N-S simulations perturbed with bins of size $dx = \lambda_o$, corresponding to $\sigma = 0.33\rho_o$.

in Fig. 6.14, convective rolls are still seen to occur along the piston face, which are shown to occur over lengths similar to the relaxation length, which is $29.5\lambda_o$ for these parameters.

However, as u_p/u^* was decreased to 0.50 in Fig. 6.15, convective rolls are no longer seen along the piston face, yielding a stable structure. For this case the relaxation length is $65.5\lambda o$. These results indicate a transition between the unstable and stable structures occurring at $u_p/u^* \approx 0.75$ for this value of η_o and ε.

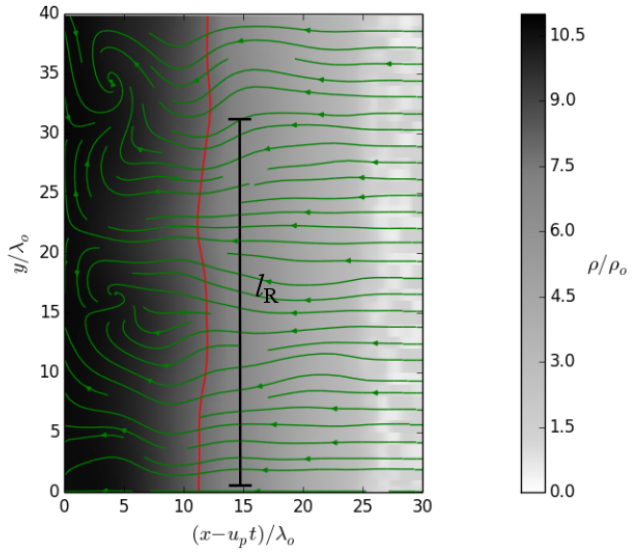

Figure 6.14: Shock morphology obtained from N-S for $u_p/u_o = 7.5$, $u^*/u_o = 10$, $\varepsilon = 0.95$, and $\eta_o = 0.012$. Also shown is the relaxation length for these conditions, $l_R \approx 29.5\lambda_o$. Simulation perturbed with bins of size $dx = \lambda_o$, corresponding to $\sigma = 0.33\rho_o$.

6.3.2 Results with Differing ε

Figure 6.16 shows the structures obtained for $\varepsilon = 0.90$, with $u_p/u_o = 20$, $u^*/u_o = 10$, and $\eta_o = 0.012$. Under these parameters, the relaxation length scale is $3.8\lambda_o$. Both N-S and MD results demonstrate an unstable structure with the characteristic bumps seen in the previous cases. For MD, the bumps are similar in size to the relaxation length. However, for N-S, the resulting bump size is shown to be larger than the relaxation length.

A similar result is observed for $\varepsilon = 0.80$, as shown in Fig. 6.17, where the relaxation length

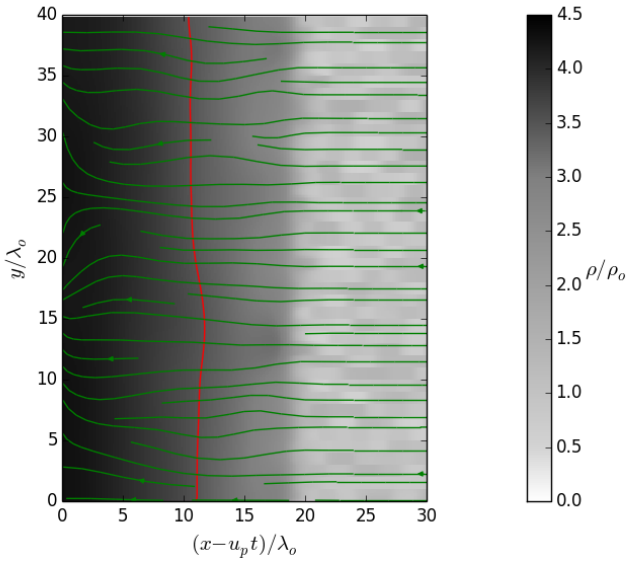

Figure 6.15: Shock morphology obtained from N-S for $u_\mathrm{p}/u_\mathrm{o} = 5$, $u^*/u_\mathrm{o} = 10$, $\varepsilon = 0.95$, and $\eta_\mathrm{o} = 0.012$. Simulation perturbed with bins of size $dx = \lambda_\mathrm{o}$, corresponding to $\sigma = 0.33\rho_\mathrm{o}$.

is approximately $2.0\lambda_\mathrm{o}$. MD results for these parameters show a more compact instability, with bumps similar in scale to the relaxation length. N-S recovers a dense unstable structure, although the bumps are larger than the relaxation length scale.

These results show that the instability becomes more compact with decreasing ε, following the trend given for l_R in Ch. 4.

6.3.3 Results with Differing η_o

The final parameter that was investigated was the initial packing factor η_o. In addition to $\eta_\mathrm{o} = 0.012$ shown in Fig. 6.7, $\eta_\mathrm{o} = 0.025$ and 0.005 were investigated, with $\varepsilon = 0.95$, $u_\mathrm{p}/u_\mathrm{o} = 20$ and $u^*/u_\mathrm{o} = 10$.

Figure 6.18 shows results for the dense case, where $\eta_\mathrm{o} = 0.025$, and the relaxation length scale is approximately $9.9\lambda_\mathrm{o}$. Both the N-S and MD results show large bumps similar to the size of the relaxation length, exhibiting an unstable structure.

For the dilute case of $\eta_\mathrm{o} = 0.005$, shown in Fig. 6.19, the unstable patterns are more

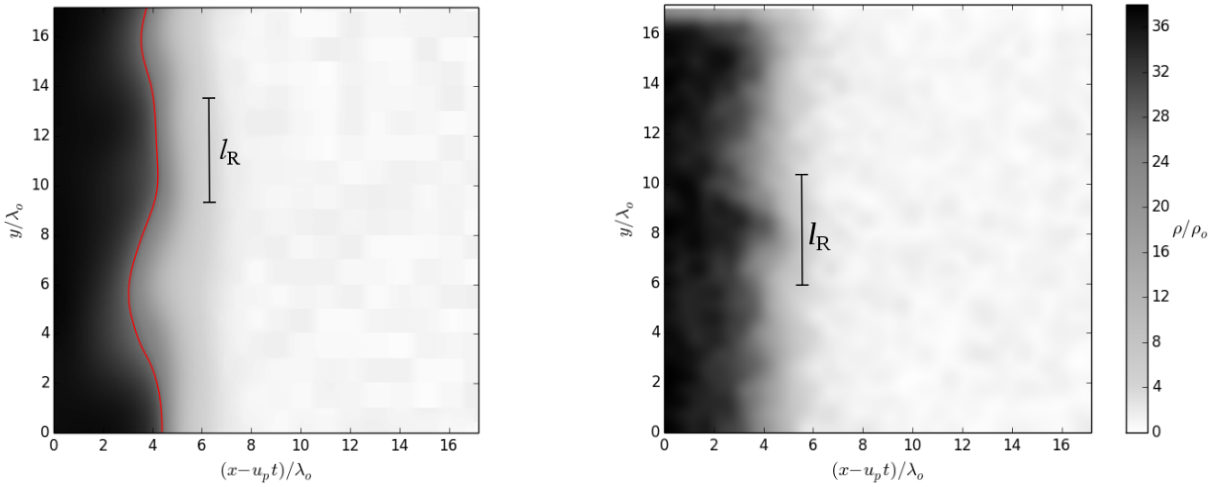

(a) N-S **(b)** MD

Figure 6.16: Developed shock structures obtained from N-S and MD simulations at $t/\tau_o = 8.12$ for $\varepsilon = 0.90$, $u_p/u_o = 20$, $u^*/u_o = 10$, and $\eta_o = 0.012$. Also shown is the relaxation length for these conditions, $l_R \approx 3.8\lambda_o$. N-S simulations perturbed with bins of size $dx = \lambda_o$, corresponding to $\sigma = 0.33\rho_o$.

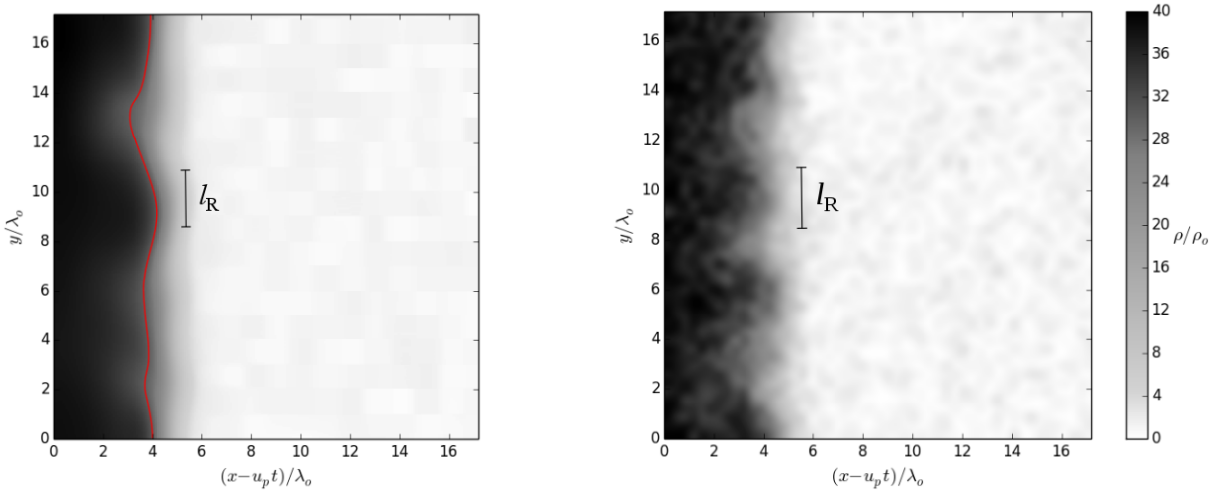

(a) N-S **(b)** MD

Figure 6.17: Developed shock structures obtained from N-S and MD simulations at $t/\tau_o = 8.12$ for $\varepsilon = 0.80$, $u_p/u_o = 20$, $u^*/u_o = 10$, and $\eta_o = 0.012$.Also shown is the relaxation length for these conditions, $l_R \approx 2.0\lambda_o$. N-S simulations perturbed with bins of size $dx = \lambda_o$, corresponding to $\sigma = 0.33\rho_o$.

compact, and comparable in size to the relaxation length, which is approximately $5.9\lambda_o$. Under these conditions both the N-S and MD models yield similar sized pattern formations.

As for the other parameters, varying η_o modifies the shock structure in accordance with the relaxation length scale. These results show that the trend applies to both the dilute and dense gas regimes.

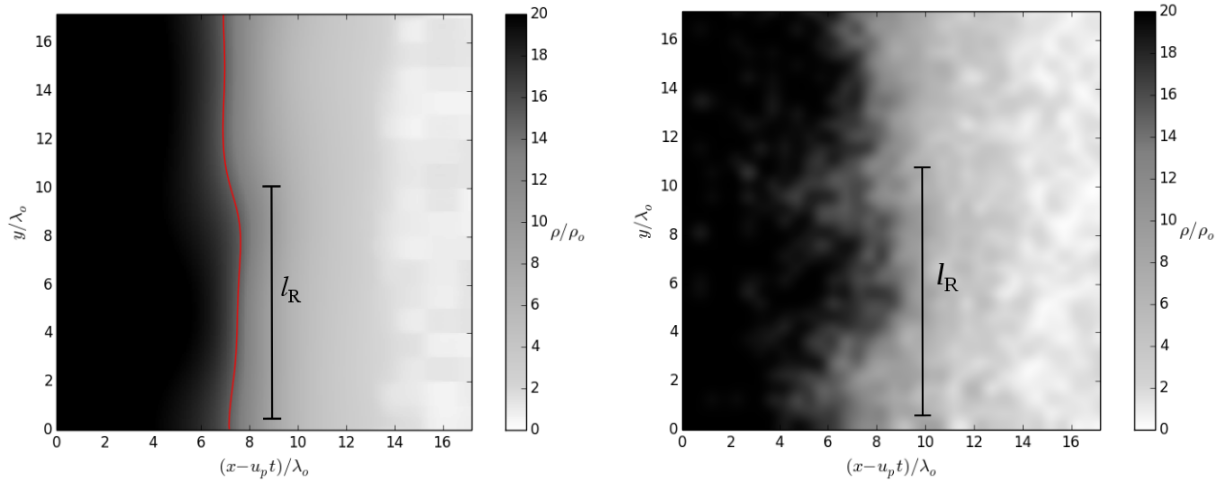

(a) N-S **(b)** MD

Figure 6.18: Developed shock structures obtained from N-S and MD simulations at $t/\tau_o = 8.92$ for $\eta_o = 0.025$, $\varepsilon = 0.95$, $u_p/u_o = 20$ and $u^*/u_o = 10$. Also shown is the relaxation length for these conditions, $l_R \approx 9.9\lambda_o$. N-S simulations perturbed with bins of size $dx = \lambda_o$, corresponding to $\sigma = 0.33\rho_o$.

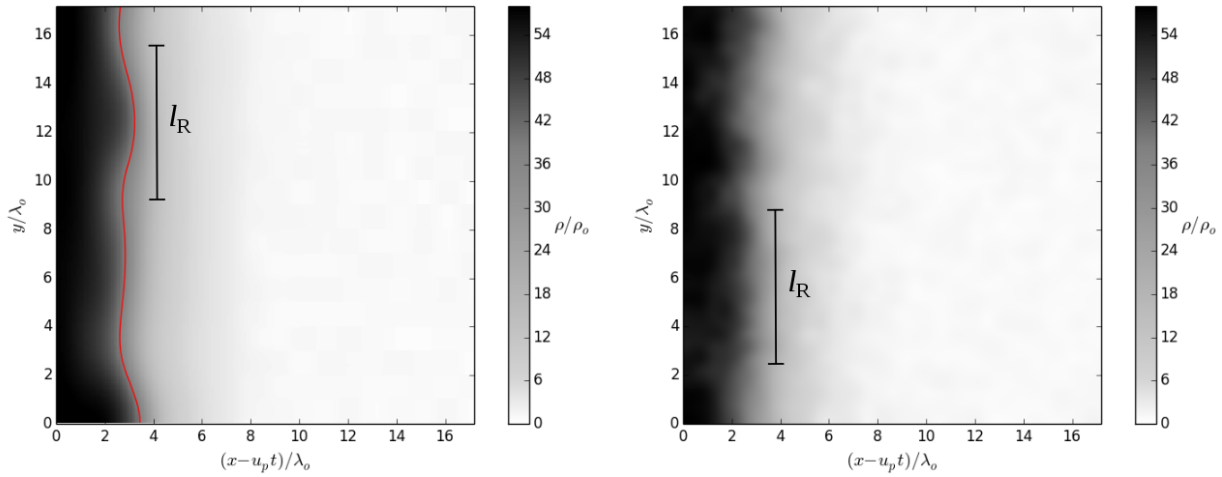

(a) N-S **(b)** MD

Figure 6.19: Developed shock structures obtained from N-S and MD simulations at $t/\tau_o = 9.8$ for $\eta_o = 0.005$, $\varepsilon = 0.95$, $u_p/u_o = 20$ and $u^*/u_o = 10$. Also shown is the relaxation length for these conditions, $l_R \approx 5.9\lambda_o$. N-S simulations perturbed with bins of size $dx = \lambda_o$, corresponding to $\sigma = 0.33\rho_o$.

6.4 Non-Linear Stability of Steady-State Structure

The steady-state structure was investigated using the continuum description to determine if the absence of the initial evolving stage still gives instabilities.

6.4.1 Stability Analysis

The stability of the shock structure was investigated by perturbing the steady state structure derived in Ch. 4 for a short duration and observing whether the perturbations grow or decay. This procedure is similar to ones used in investigations of multi-dimensional instabilities in *exothermic* shock waves (i.e. detonations) (see, for example, Ref. [84]).

Figure 6.20 shows a sequence of images for the resulting evolution of the inviscid steady-state structure with $D/u_o = 20$, $u^*/u_o = 10$, $\varepsilon = 0.95$ and $\eta_o = 0.012$ which was perturbed between the times $t/\tau_o = 0$ to 0.9 following the methodology described in Sec. 3.4.1. Initially,

instabilities form after perturbations are introduced, as seen at $t/\tau_o = 0.180$ in Fig. 6.20(b), and up to $t/\tau_o = 7.22$ in Fig. 6.20(f). Once the perturbations stop being applied, the front flattens out. During this time, instabilities are pushed back into the shock structure, and do not amplify. From this sequence it can be seen that the traditional method to investigate such an instability recovers a stable structure.

6.4.2 Implementation of Noise on Steady Structure

Statistical noise was implemented into the steady structure to compare with the transient piston problem above.

Figure 6.21 shows the evolution of the inviscid shock structure perturbed continuously after $t/\tau_o = 0$ with bins of $dx = \lambda_o$, corresponding to a standard deviation of $\sigma = 0.33\rho_o$. Similar to the previous case, $D/u_o = 20$, $u^*/u_o = 10$, $\varepsilon = 0.95$ and $\eta_o = 0.012$. The results show that the structure begins forming instabilities immediately, visible at $t/\tau_o = 1.80$. As time progresses, the instabilities continue to grow and extend back in the negative z direction. This agrees with what was seen for the transient case in the previous section, whereby the inviscid results remain unstable in the presence of a continuous source of fluctuations.

The connection between the relaxation length scales and unstable patterns was also addressed using the steady-state structure. For this case, the viscous solution was considered. Although the steady-state structure was not obtained for the viscous case, the inviscid structure forms a diffusive structure once implemented into the N-S solver and given enough time to evolve. For the case given here, the diffusive structure was shown to form after $t/\tau_o = 2.1$. Therefore, in order to investigate the stability of the viscous steady-state structure, perturbations are implemented after the time required for a steady viscous structure to form.

Figure 6.22 gives the evolving shock structure from N-S for $D/u_o = 20$, $u^*/u_o = 10$, $\varepsilon = 0.95$ and $\eta_o = 0.012$. Perturbations are initiated after $t/\tau_o = 2.1$ in bins of size $dx = \lambda_o$, corresponding to a standard deviation of $\sigma = 0.33\rho_o$. The results show that instabilities do

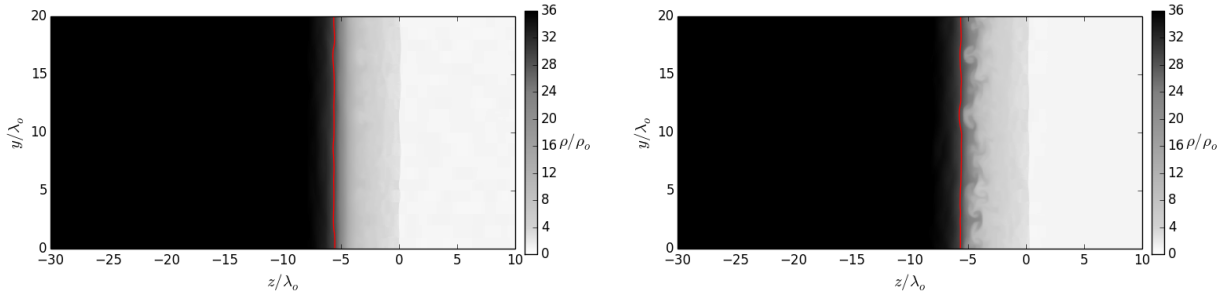

(a) $t/\tau_o = 0.90$

(b) $t/\tau_o = 1.80$

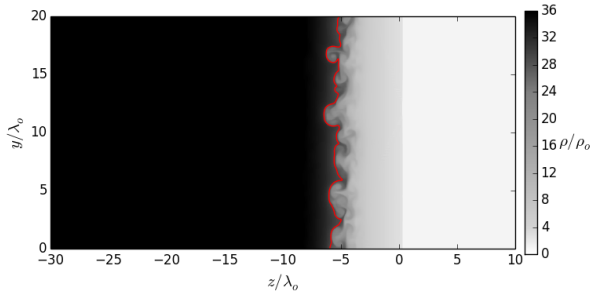

(c) $t/\tau_o = 2.71$

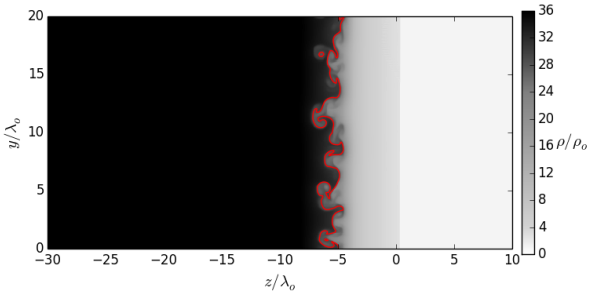

(d) $t/\tau_o = 3.61$

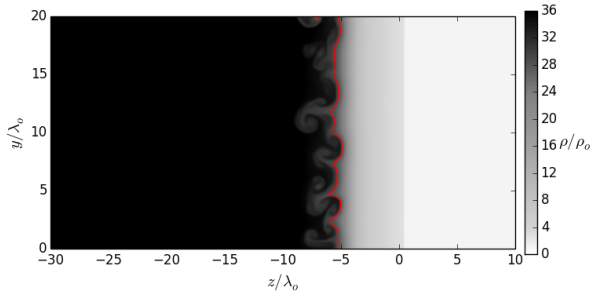

(e) $t/\tau_o = 5.41$

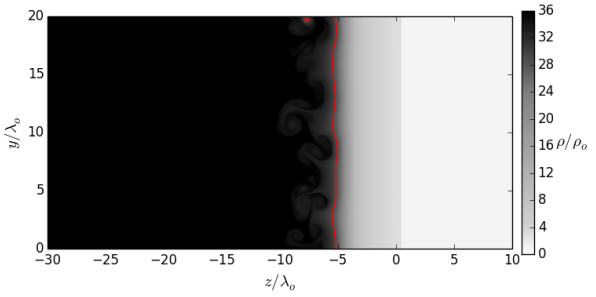

(f) $t/\tau_o = 7.22$

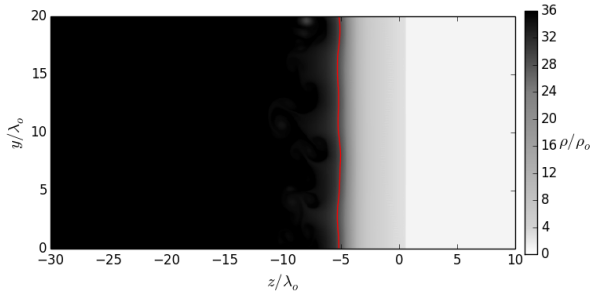

(g) $t/\tau_o = 9.02$

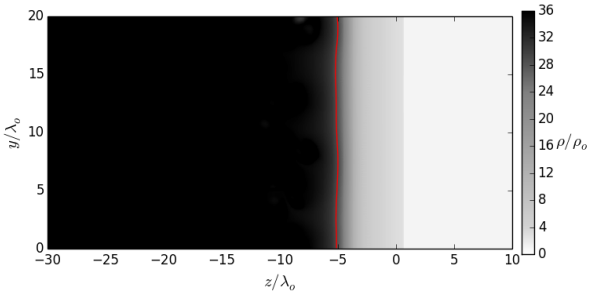

(h) $t/\tau_o = 10.82$

Figure 6.20: Evolution of steady-state structure in Euler simulations where incoming flow is perturbed from $t/\tau_o = 0 - 0.9$ for $D/u_o = 20$, $u^*/u_o = 10$, $\varepsilon = 0.95$ and $\eta_o = 0.012$.

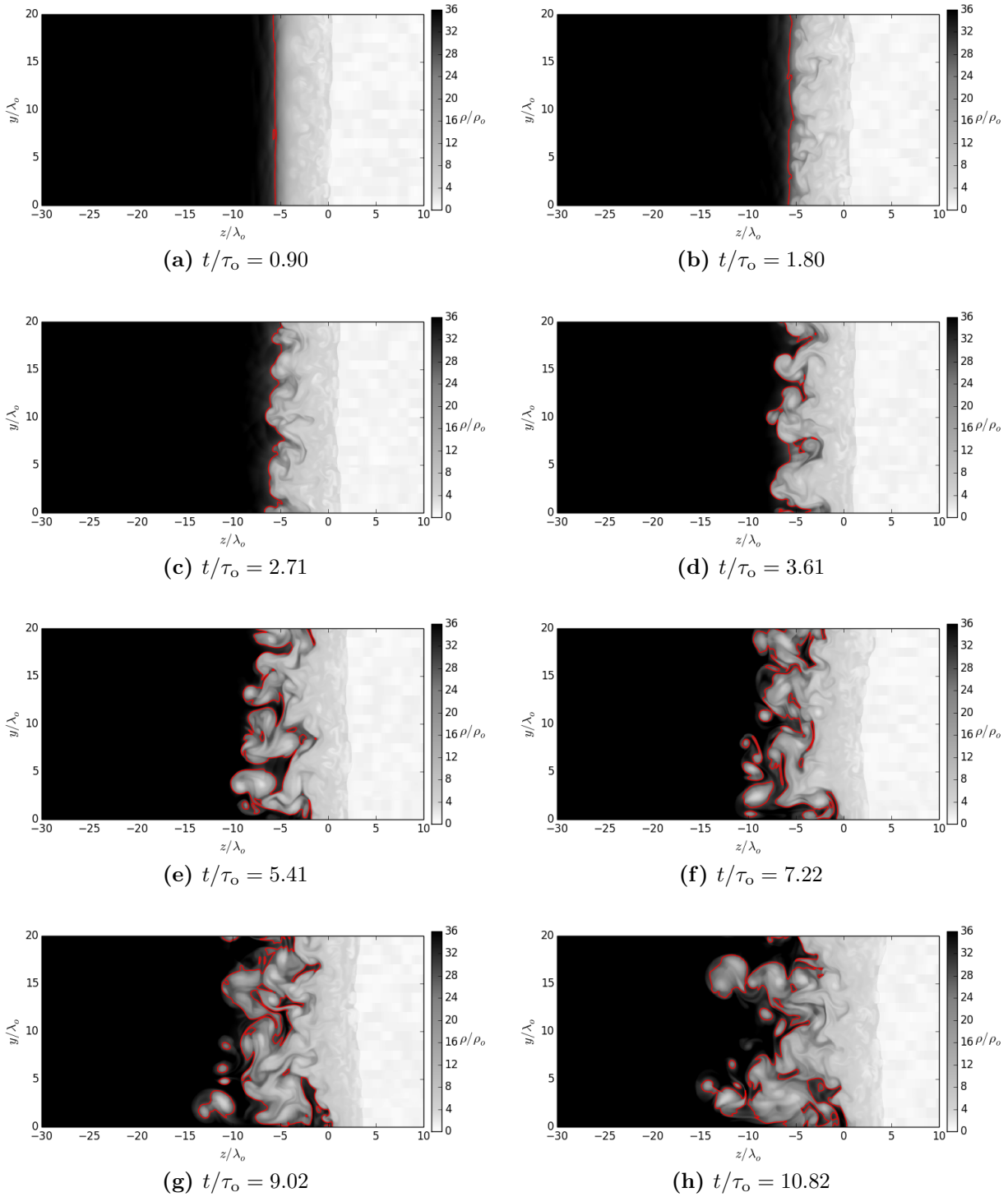

(a) $t/\tau_o = 0.90$ **(b)** $t/\tau_o = 1.80$

(c) $t/\tau_o = 2.71$ **(d)** $t/\tau_o = 3.61$

(e) $t/\tau_o = 5.41$ **(f)** $t/\tau_o = 7.22$

(g) $t/\tau_o = 9.02$ **(h)** $t/\tau_o = 10.82$

Figure 6.21: Evolution of steady-state structure in Euler simulations where incoming flow is perturbed continuously from $t/\tau_o = 0$ for $D/u_o = 20$, $u^*/u_o = 10$, $\varepsilon = 0.95$ and $\eta_o = 0.012$. Incoming flow is perturbed in bins of $dx = \lambda_o$, corresponding to $\sigma = 0.33\rho_o$.

indeed form, although at a slower rate than for the inviscid model. After $t/\tau_o = 6.50$, shown in Fig. 6.22(e), the characteristic unstable pattern seen in the previous section was observed. Figure 6.22(h) shows that the bumps are similar in size to the relaxation length, which for this case is approximately $7.5\lambda_o$.

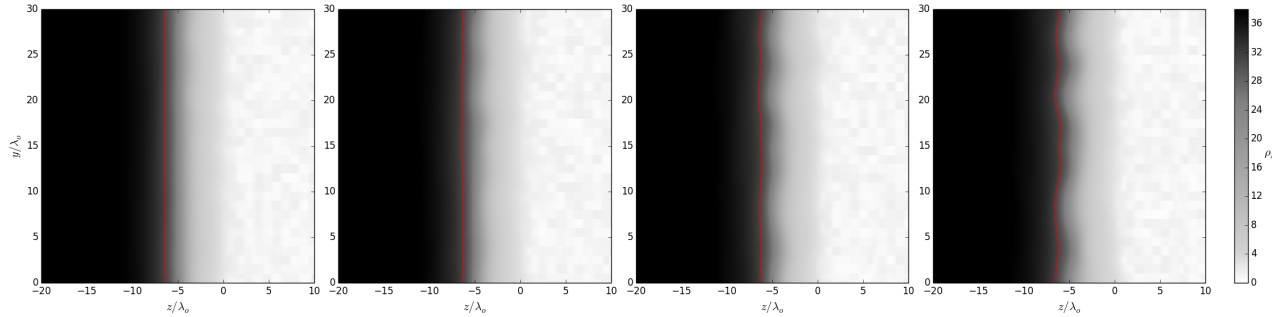

(a) $t/\tau_o = 3.61$ **(b)** $t/\tau_o = 4.33$ **(c)** $t/\tau_o = 5.05$ **(d)** $t/\tau_o = 5.77$

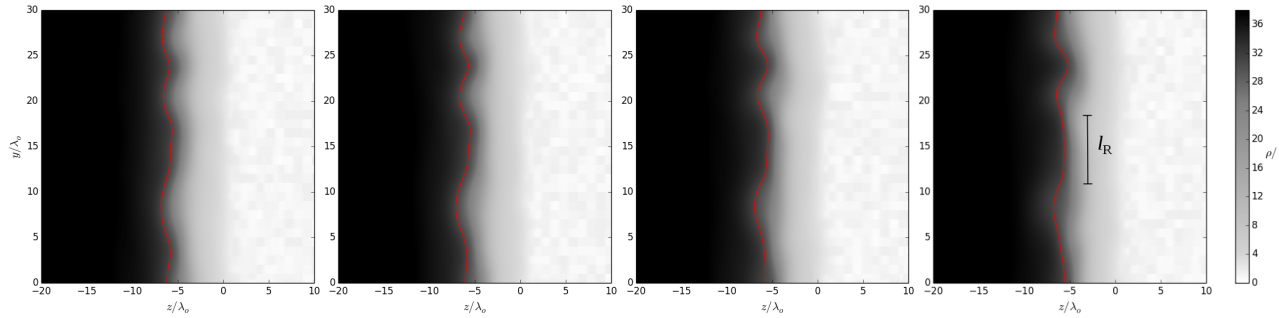

(e) $t/\tau_o = 6.50$ **(f)** $t/\tau_o = 7.22$ **(g)** $t/\tau_o = 7.94$ **(h)** $t/\tau_o = 8.66$

Figure 6.22: Evolution of steady-state structure in N-S simulations for $D/u_o = 20$, $u^*/u_o = 10$, $\varepsilon = 0.95$ and $\eta_o = 0.012$. Incoming flow is perturbed continuously in bins of $dx = \lambda_o$, corresponding to $\sigma = 0.33\rho_o$, after $t/\tau_o = 2.1$, which is the time chosen in order for the diffusive structure of the steady-state structure to have formed. The relaxation length shown in later times is $l_R/\lambda_o \approx 7.5$.

6.5 Summary

The current chapter presented the investigation of the multi-dimensional stability of shock waves in a two-dimensional granular gases with activated inelastic collisions. Results from MD for the piston driven structure demonstrated that the shock structure does indeed become

unstable for sufficiently strong shock waves. The instabilities took the form of high density convective rolls near the piston face, where the rolls were similar in size to the relaxation length under similar conditions. Continuum models were also shown to become unstable, but *only* if the incoming flow field was perturbed. It was determined that these perturbations must be in accordance with the statistical fluctuations inherent in MD. For moderate relaxation lengths, the instabilities shown in N-S and MD were of similar wavelengths. However, for shorter relaxation lengths, N-S was shown to give larger than expected patterns, whereas MD still yielded instabilities similar to the relaxation length. This suggests an invalidity for the continuum model for small characteristic scales.

Finally, the steady-state structure was analyzed in order to determine whether the instability was due to the shock structure evolving from the piston or only an artifact of the perturbations. Structures did again become unstable in the presence of a continuous source of perturbations. The structure obtained for N-S demonstrated that the instabilities still manifest themselves on scales similar to the relaxation length.

Chapter 7

Discussion on Instability

Simulations at both the microscopic and macroscopic levels using MD and continuum models have shown that shock structures can indeed become unstable with the presence of activated inelastic collisions. The results have shown that the instabilities occur if the driving piston velocity u_{p} is on the order of the activation threshold u^*. The wavelength of these instabilities was similar in magnitude to the relaxation length of the shock wave structure, suggesting a possible link. The instability was also present in the steady travelling wave, ruling out transient mechanisms such as the Richtmyer-Meshkov type instabilities, which had recently been proposed as the controlling mechanism based on the results first obtained in MD [85].

The current chapter further analyzes this instability to offer an explanation as to what controls it. The first part discusses whether the reconstruction of the shock Hugoniot predicts unstable patterns, a common method to predict shock instability [20]. The next part discusses the connection between the relaxation length and the instabilities.

7.1 Analysis of Shock Hugoniot

Standard explanations for shock instability are related to the shock Hugoniot [13, 20, 22]. Two of the common mechanisms of instability based on the equilibrium end states are the

D'Yakov-Kontorovich instability, or if the fluid undergoes phase transitions.

7.1.1 D'yakov-Kontorovich Instability

For the instability known as the D'yakov-Kontorovich instability, certain conditions have been shown to cause perturbed shock waves in non-ideal gases to become unstable by emitting undamped sound and entropy-vortex waves [21]. For the D'yakov-Kontorovich instability, the end states lying along sections of the Hugoniot having a positive slope are expected to have a corrugation type instability [22].

Figure 7.1 shows the Hugoniot and Rayleigh lines obtained from Ch. 4 for $\eta_{\mathrm{o}} = 0.012$ and $u^*/u_{\mathrm{o}} = 10$, with the Rayleigh line representing a shock wave with $u_{\mathrm{p}}/u^* = 1.0$. From the previous results, it was observed that these conditions become unstable. The Hugoniot and Rayleigh lines shown in Fig. 7.1 show that the Rayleigh line does not intersect at a section with a positive slope, thus ruling out the D'yakov-Kontorovich instability as an influencing mechanism.

7.1.2 Instability from Shock Splitting

Shock splitting, which causes instability, is expected when the Rayleigh line, representing the state across the shock wave, intersects multiple points on the Hugoniot [20]. Such a behaviour is possible near the transition for $u_p/u^* \approx 0.3$, as obtained in Ch. 4. However, results demonstrated that it was for greater values of u_{p}/u^* that the shocks became unstable. As seen in Fig. 7.1 for $u_p/u^* = 1.0$, the Rayleigh line was far from this transition and does not intersect the Hugoniot in multiple locations, thus ruling out the instability associated with shock splitting. Therefore, these mechanisms can be ruled out.

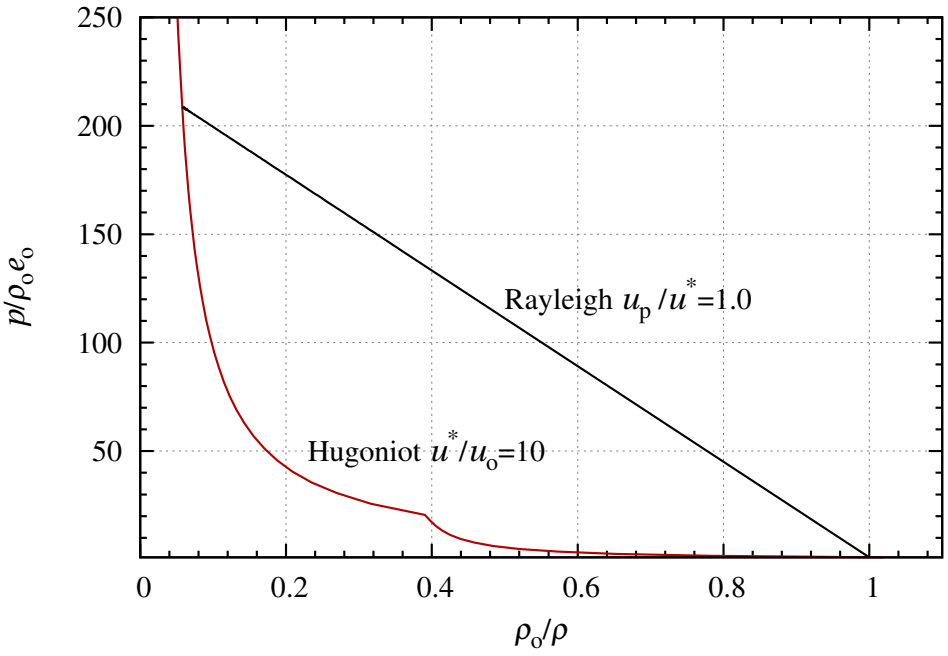

Figure 7.1: Representation of the Hugoniot and Rayleigh lines as obtained from Ch. 4 for $\eta_o = 0.012$ and $u^*/u_o = 10$, with the Rayleigh line representing a shock wave with $u_p/u^* = 1.0$.

7.2 Relaxation Length Scales and the Role of Fluctuations

The results have shown that the multi-dimensional structure is closely linked to the relaxation length scale l_R, suggesting that it is a governing length scale for the current problem. As this governing length scale decreased, the role of fluctuations was shown to become important, and discrepancies between the continuum and microscopic models became more evident.

These results suggest that the *rarefied* effects for the current problem must be considered, which implies that characteristic length scales that are short compared to the mean free path can lead to issues in modelling at the continuum level, and particle fluctuations become important [38].

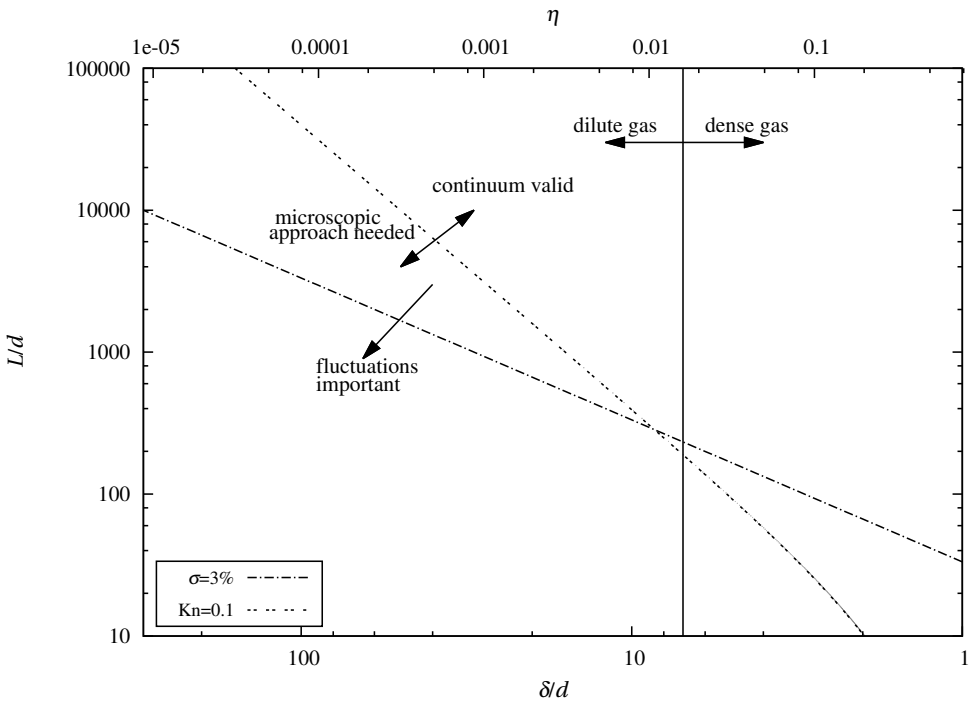

Figure 7.2: The limiting length scales based on the relationships between the characteristic dimension L, the particles diameter d, the mean distance between particles δ, and the packing fraction η.

7.2.1 Limiting Length Scales for a Hard Disk Gas

There are three limiting length scales that must be considered, which are shown in Fig. 7.2 and summarized below.

Rarefied Limit

The first limit of interest is the rarefied limit. This limit identifies whether continuum models are valid or whether a microscopic approach must be used for a specific problem. This limit is based on the Knudsen number,

$$\mathrm{Kn} = \lambda / L, \tag{7.1}$$

which relates the length scale of interest L to the mean free path of the particles, λ. Generally, it is assumed that continuum models are invalid when [38]:

$$\mathrm{Kn} < 0.1 - 0.2 \tag{7.2}$$

In the context of the current problem, this would require that $l_{\mathrm{R}} > 5\lambda_{\mathrm{o}} - 10\lambda_{\mathrm{o}}$.

Limit for Statistical Fluctuations

Another limit of interest is the limit that identifies whether statistical fluctuations play an important role on the dynamics of the problem. Bird argues that fluctuations must be considered if a box constructed with sides of the given length scale yields a standard deviation, σ, of approximately 3% [38]. The reasoning behind the magnitude of this standard deviation was not discussed by Bird, although it does give a meaningful length scale to consider. This regime is particularly important for flows close to the dense gas regime where continuum assumption still holds, for example, in microelectromechanical systems [86].

In the current 2D system, by applying Eq. (D.8), the limit is found as:

$$\sigma = \frac{\delta}{L} \quad \rightarrow \quad L_{crit} = \frac{\delta}{0.03} \tag{7.3}$$

where δ is the mean spacing between particles. Given this limit, length scales exceeding this value are not expected to be influenced by particle fluctuations, while fluctuations must be considered for length scales lower than this value.

Dilute-Dense Gas Limit

Another limit is the assumption that the gas can be treated as a dilute gas. In the limit of a dilute gas, it is assumed that there are only binary collisions, which simplifies the derivations from kinetic theory. The dilute gas assumption assumes that $\delta \gg d$, with the approximate

limit given as [38]:

$$\frac{\delta}{d} = 7 \tag{7.4}$$

Since $\eta = \frac{\pi}{4}\left(\frac{d}{\delta}\right)^2$ from (D.6), this yields a limiting packing factor of

$$\eta_{\text{dilute}} \lesssim 0.016. \tag{7.5}$$

7.2.2 Analysis of Results in Context of Limiting Length Scales

The relaxation length scales l_{R} that were found in Ch. 4 were compared to the limiting length scales. Results from Ch. 6 showed that instabilities occurred when the value of $u_{\text{p}}/u^* \geq 0.75$ (specifically seen for $\eta_{\text{o}} = 0.012$ and $\varepsilon = 0.95$). Figure 7.3 compares the resulting length scales for $\varepsilon = 0.95$ obtained for different packing factors, and compared with the limits discussed above. The solid symbols represent the cases where $u_{\text{p}}/u^* \geq 0.75$, while the empty symbols are for piston velocities below this ratio.

The results show that for low values of u_{p}/u^*, l_{R} lies above the limits associated to the continuum limit and limit for particle fluctuations. As u_{p}/u^* increases, however, all values of η_{o} begin crossing these limits. The transition at $u_{\text{p}}/u^* = 0.75$ approaches the limiting boundaries while running parallel to the limit associated with particle fluctuations. Large values of u_{p}/u^* yielded lower values of l_{R} that drop below these limits, signifying that fluctuations are important to consider and that the continuum model may not be valid. While the relaxation length was taken with some arbitrary equilibrium state in Ch. 4, these results nevertheless show a clear connection between the size of the relaxation zone, and the need to consider particle fluctuations.

Chapter 6 demonstrated that results were in fair agreement when comparing the 2D structure obtained from the continuum and MD models for $\varepsilon = 0.95$. However, results in Sec. 6.3.2 showed that as ε was decreased, instabilities were still shown to occur, although the

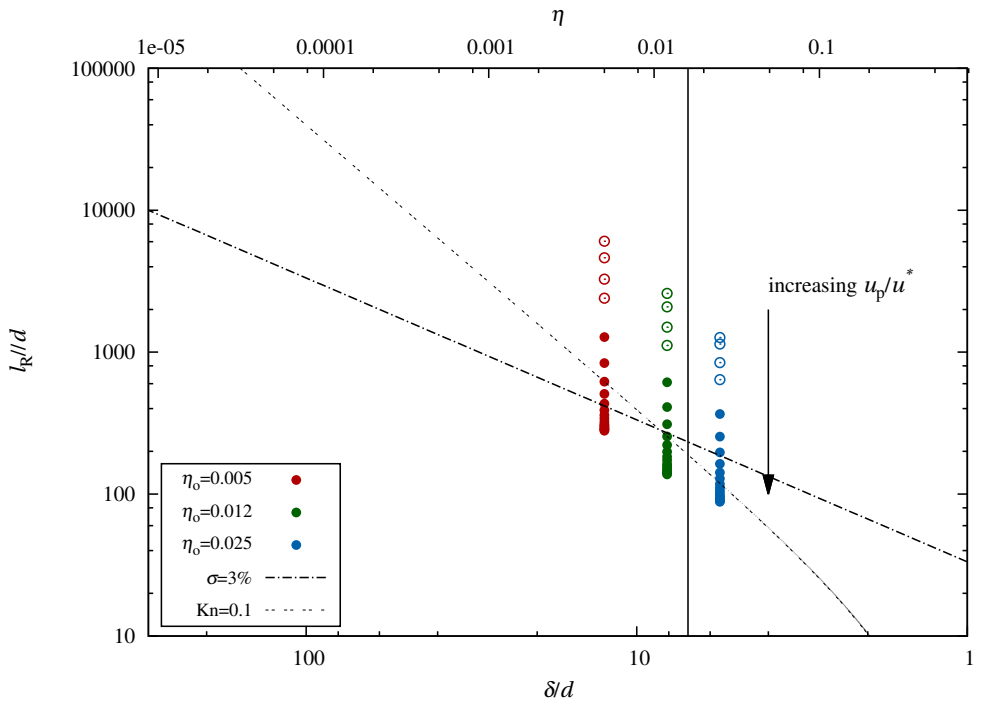

Figure 7.3: Comparison between limits in approximations with the characteristic length scale represented by relaxation length relaxation length scales obtained from simulations for different values of u_p/u^* and η_o, with $\varepsilon = 0.95$. The solid symbols represent the cases where $u_p/u^* \geq 0.75$, while the empty symbols are for piston velocities below this ratio.

wavelengths of instabilities from MD and N-S were in disagreement. This discrepancy can be explained by comparing with the limits presented above. Figure 7.4 shows the values l_R for different values of ε, with $\eta_o = 0.012$ and $u_p/u^* = 2.0$, as compared to the limiting boundaries. The results demonstrate that a decreasing value of ε significantly decreased the value of l_R, with those given for $\varepsilon = 0.90$ and 0.80 lying well below the limit of Kn = 0.1. These results show that fluctuations continue to be important for such small relaxation lengths, although the continuum model may not be valid, which agrees with what was observed in Sec. 6.3.2. Although $\varepsilon = 0.95$ still lies below these limits, the results from both Ch. 5 and Ch. 6 show that MD and continuum agree well, which may suggest that the definition of the relaxation length may need to be modified in future work.

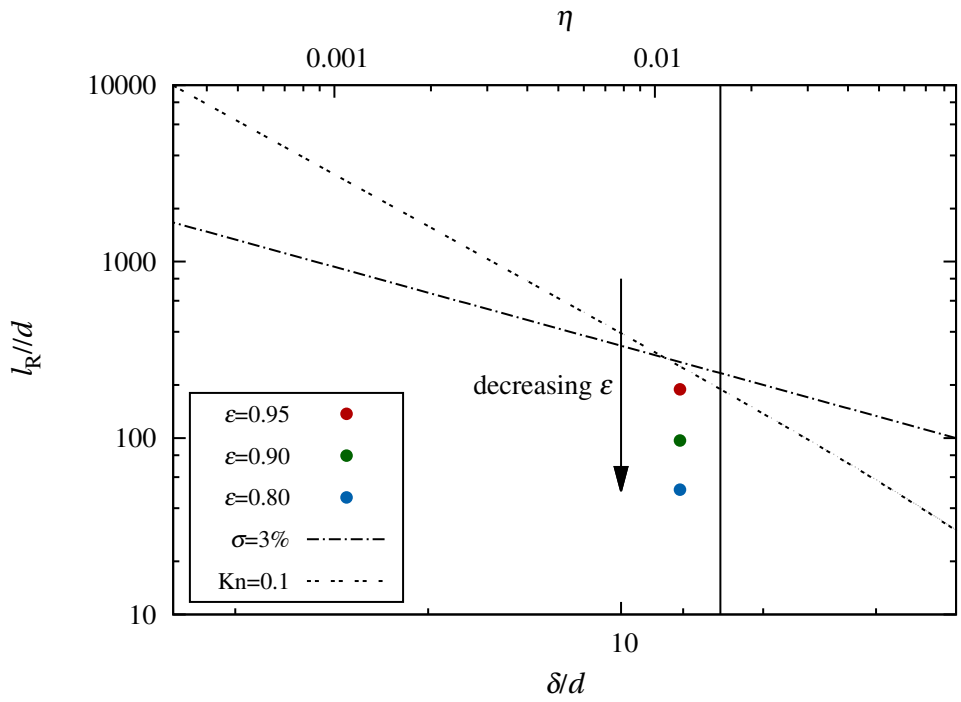

Figure 7.4: Comparison between limits in approximations with the characteristic length scale represented by relaxation length obtained from simulations for different values of ε, with $\eta_o = 0.012$ and $u_p/u^* = 2.0$.

Chapter 8

Conclusions and Recommendations

In this thesis, the effect that dissipative collisions have on the evolution and stability of shock waves was investigated. The problem was addressed numerically at the microscopic and macroscopic levels by investigating a model of a piston propagating into a system of disks (2D) that undergo activated inelastic collisions. The current chapter summarizes the findings from this study and what conclusions can be made. Final remarks are given on recommendations for future study.

8.1 Summary

The first part of this thesis, as presented in Ch. 3, established the model and numerical methodologies used in the study at the microscopic and macroscopic levels. The problem was defined for a piston propagating with a velocity u_{p} into a system of smooth disks occupying an initial area fraction η_{o}. Binary collisions were elastic unless their impact velocity exceeded some threshold u^*, where the particles then collided inelastically with a coefficient of normal restitution ε. The MD methodology was established for this model in Sec. 3.2 using the Event-Driven Molecular Dynamics method. The continuum model was formulated in Sec. 3.3 using the hydrodynamic equations for granular gases at the Navier-Stokes (N-S) level, which

required the modification and validation of a new cooling rate term ζ^* that included u^*.

Chapter 4 provided the derivation and analysis of the steady state shock structure for the described model using the inviscid hydrodynamic equations from Ch. 3. The results demonstrated that shock waves can be treated as completely elastic if $u_\mathrm{p}/u^* < 0.3$. For values of $u_\mathrm{p}/u^* \geq 0.3$ the properties pertaining to a relaxing structure were obtained, whereby the structure was shown to be independent of the initial energy.

The transient dynamics and structure of the shock wave were then investigated using the MD and continuum models. Firstly, results were obtained in 1D in Ch. 5. The results demonstrated that the MD and continuum models yield similar behaviour for the evolution and structure of the shock wave. Analysis of the evolutions yielded three different behaviours, which are controlled by u_p/u^*. For $u_\mathrm{p}/u^* \leq 0.5$, the shock wave demonstrates behaviour of a nearly elastic shock wave. For sufficiently strong shock waves, with $u_\mathrm{p}/u^* \geq 2.0$, the shock waves are shown to experience a very large decay, which causes the front to pull back towards the piston during the early stages, a finding previously observed by Kamenetsky *et al.* [9] for all collisions being inelastic. The third regime lies between these limits, where it is shown that as u_p/u^* is decreased from the strong shock regime, the behaviour transitions from what is predicted for a purely inelastic shock wave to that for an elastic system of disks.

The dynamics and evolving structure were extended to 2D in Ch. 6. Results for MD showed that for sufficiently strong shock waves, a multi-dimensional instability can form with high density non-uniformities and convective rolls within the relaxing region. Similar instabilities were observed in the N-S results *only* with the inclusion of statistical fluctuations to density mimicking what was seen in MD. The size of the instabilities obtained from N-S and MD were shown to scale with the relaxation length expected for the relaxing structure. Similar instabilities were observed by including fluctuations to the steady state structure in N-S, representing an independence from any transient effects for the instability.

The mechanism for instability observed in this work was addressed in Ch. 7. Traditional

methods for predicting shock instability via the Hugoniot and Rayleigh lines were addressed in Sec. 7.1, which showed that a stable structure is predicted. The close link between the relaxation length and the instability was then addressed in terms of the rarefied effects of the problem in Sec. 7.2. The cases that were shown to become unstable yielded a relaxation length scale whereby statistical fluctuations were shown to become important, following the description for this regime by Bird [38].

8.2 Conclusions and Contributions to Original Knowledge

Previous studies investigating shock waves in granular media have been limited to purely inelastic media [8, 9]. To the best of the author's knowledge, this study is the first to investigate shock waves for granular media with activated inelastic collisions, although such a formulation has previously been used to study viscoelastic collisions in a homogeneous cooling granular gas [34]. The inclusion of the activation threshold offered a method to more closely mimic granular collisions, and more importantly gave a controllable parameter to tailor the magnitude of dissipation present in the shock waves. Ultimately, the results revealed that this parameter plays a strong role on the evolution and structure of the shock waves.

The first part of this study was to obtain the inviscid steady state structure for the given problem, as well as other shock properties. A meaningful finding from this section was that a relaxing shock structure is only expected when $u_\mathrm{p}/u^* \geq 0.3$. Beyond this limit it was concluded that the initial energy plays no role on the structure, and that it is controlled only by the ratio u_p/u^*, ε and η_o. The independence from the initial kinetic energy is an important finding in the context of the present work, as it implies that the results and analysis presented here for an initial *fluidized* state also hold for an initially *frozen* state where the particles

have no initial kinetic energy contributing to the granular temperature. This result is similar to the strong shock limit for molecular gases, which shows an independence from the initial energy of the system [13].

The one-dimensional shock wave structure and development with MD and continuum models were investigated in Ch. 5. One of the first findings from this chapter, as represented in Sec. 5.2, was that the continuum description is able to capture the structure given from MD remarkably well. From this result, it can be concluded that the continuum description involving Jenkins and Richman transport terms, the modified cooling rate, and the equation of state is valid.

Results for the evolving structure were obtained for the varying parameters of the model. Prior to this work, the only other work regarding the evolution of shock structure in granular media was that presented by Kamenetsky *et al.* [9], which was limited to purely inelastic media. By including the activation threshold for inelastic collisions, this work expanded on the previous work by Kamenetsky *et al.* One finding from the work by Kamenetsky *et al.* that needed clarification was that the shock wave can experience a negative velocity relative to the piston during the early transient stages. The present work addressed this issue by investigating the dynamics more carefully, which was done by reconstructing the family of characteristics of the problem. From this, it was concluded that the cause for the pull-back was due to a large re-pressurization felt by early particle paths, which were in turn communicated to the shock wave via forward running characteristics. The results indicated that the amplitude of re-pressurization can be controlled by the ratio u_p/u^*, whereby values of $u_\mathrm{p}/u^* \geq 2.0$ recovered this pull-back behaviour. The cases where $0.5 < u_\mathrm{p}/u^* < 2.0$ formed a newly explored regime which exhibits strong relaxation effects leading to a decay of the shock wave, although not to the extent where the shock pulls back towards the piston.

The study then turned to investigating the structure of the shock waves in two dimensions in Ch. 6. From the results obtained with MD and continuum models, it was concluded that

shock waves can indeed become unstable with the presence of activated inelastic collisions. By including the activation threshold, instabilities were shown to only exist for sufficiently strong piston velocities, with the transition occurring at $u_{\mathrm{p}}/u^{*} \approx 0.75$. Beyond this limit, the unstable structures were shown to be similar in size to the relaxation length scale of the shock wave.

Extending this work to the continuum level allowed for the instability to be further analyzed. The traditional hydrodynamic treatment, as presented in Ch. 3, assumes that the initial state is continuous and homogeneously dispersed. However, the continuum results revealed that such a medium does not exhibit an unstable shock formation. It was only when statistical fluctuations were included in the incoming flow field that instabilities appeared. Remarkably, the same instability could be seen for different sized bins as long as the amplitude of the perturbations for these bins yielded a similar variance in density to equally sized bins occupying the MD model. Although the treatment of these fluctuations was simple, it may be of interest to other problems where fluctuations may be important. The steady state analysis in 2D using the N-S model revealed that the structure still exhibits the same instability with the presence of statistical fluctuations. This finding implies that the instability is not a transient effect, and is unaffected by the transient dynamics shown in Ch. 5.

The final conclusion regarding the instability is that it is related to the statistical fluctuations and the rate of relaxation behind the shock wave. As previously explained by Bird [38], fluctuations can become important for sufficiently small characteristic length scales. In the context of the present problem, fluctuations can be shown to become important for small relaxation lengths, which is controlled closely by changing u_{p}/u^{*}, and it is these cases that were shown to become unstable.

Overall, the current work identified the role that dissipative collisions can play on shock wave stability and dynamics in both 1D and 2D. These results may have implications to dissipative shock behaviour in both granular media and molecular gases.

In the context of granular media, the inclusion of activated inelastic collisions allowed for the behaviour of shock waves in realistic granular mixtures that may undergo viscoelastic collisions to be investigated. The connection between the relaxation length scale and ensuing instabilities is something that should now be considered in physical phenomena of rapid granular flows exhibiting finger-like instabilities.

In the context of molecular gases, the current study may shed light on the dynamics involved in relaxing shock waves. In a realistic molecular gas, a strong shock wave may be followed by strong relaxation effects before coming to some equilibrium state [13]. The current model offers an analogous system mimicking this behaviour, whereby the activation threshold yields a method to control the temperature in the equilibrium zone, while the coefficient of restitution can be used to tailor the relaxation zone length. Considering this, it may be of interest to investigate the length scales involved in the cases where shock waves have been shown to become unstable and the mechanisms controlling instability are not fully understood [16, 18] to see if a similar mechanism to that found in this study may be influencing the dynamics.

8.3 Recommendations

The present study offered a simple model to investigate piston driven shock waves through a dissipative gas; however, improvements could be made to gain further insight or to mimic physical systems more accurately.

The largest simplification in this study was that the system was treated as a 2D medium, while the physical cases where instabilities are seen are in 3D. The main reason for this simplification was due to its simplicity and to save computational time. The system of hard disks was also previously investigated for elastic shock waves, which allowed for simple analytical expressions for shock jump equations using the Helfand equation of state to be used.

Although a three-dimensional medium would be more complex, it is anticipated that the overall behaviour would be similar. Studies in granular media have shown that phenomena in 2D still hold in 3D; one example is the clustering instability in cooling granular gases seen in 2D [87] and 3D [83]. To address this problem in 3D, modifications to the hydrodynamic description would be needed for the equation of state, the cooling rate, and the transport terms.

The results and analysis from Ch. 6 and Ch. 7 revealed that statistical fluctuations play an important role on the shock stability. The method used to include fluctuations in the continuum models was simple and perhaps unrealistic. It may be of interest to implement more realistic fluctuation fields, perhaps with variable wavelengths of perturbations instead of the sharp, piecewise, distribution given here. Alternatively, hydrodynamic descriptions that include fluctuations should be considered, such as the *fluctuating Navier-Stokes equations* that have recently been formulated for inelastic hard spheres and gases [88, 89].

One physical concept that was not discussed but may be of interest in investigating the instabilities presented in this thesis is that of compressible turbulence and the interaction with density fluctuations [90, 91]. Morkovin's hypothesis, for example, argues that the effects of density fluctuations, specifically along shear layers, should be considered for sufficiently high Mach number flows [91]. Therefore, future work should also be completed to investigate whether turbulent mechanisms control the instabilities observed in the current study.

The obvious extension to this work would be to investigate whether the results can be recovered experimentally, with a focus on the correlation between the relaxation length and ensuing instabilities. For granular media, the first step would be to obtain the relaxation length scales for the cases that experience shock dynamics, such as in oscillating granular beds [2, 43] or in rapidly dispersed granular media due to an explosive or shock wave in air [6, 7, 62, 65, 68]. This will give a meaningful length scale to compare with the wavelength of instabilities that are observed. For molecular gases, the relaxation length scales should be

obtained for shock waves undergoing relaxation effects (for example, vibrational relaxation, dissociation and ionization) and exhibit unstable behaviour. These length scales can then be compared to the length scales of the medium (mean free path and molecular spacing) to determine if the results obtained in this study are related.

Appendix A

Event-Driven Molecular Dynamics Model

In the hard particle molecular dynamics model that is used, molecules are represented as hard disks in free flight within a bounded volume. The hard disks are chosen since there are no force potentials between the molecules, which enables easy calculation of the kinematics of the system. Since there are no external forces or inter-molecular forces, the velocity of the hard particles remain constant unless in contact with a boundary, or another particle.

This section summarizes the dynamics of collisions for the hard particle molecular dynamics model, where the collision properties are explained for activated inelastic collisions.

A.1 Mechanics of Collisions

The post-collision velocities $\vec{u_i'}$ are calculated for colliding i particles travelling at velocity $\vec{u_i}$. These collisions are separated into either *boundary collisions* or *pairwise collisions*.

A.1.1 Boundary Collisions

Collisions between hard disks and boundaries are elastic, whereby the disks collide specularly with the walls. The post-collision velocities for disks are separated into the tangential velocity component (u_{Ti}), which remains constant, and the normal component (u_{Ni}), which reflects in the opposite direction, i.e.,

$$\begin{aligned} u'_{\mathrm{Ti}} =& u_{\mathrm{Ti}} \\ u'_{\mathrm{Ni}} =& -u_{\mathrm{Ni}} \end{aligned} \tag{A.1}$$

Collisions with the piston are also elastic, where the piston is travelling with a velocity u_{p} and assumed to have an infinite mass. The post-collision velocities are separated into the tangential and normal components, with the piston propagating into the domain from the negative x-direction with speed u_{p}. The post-collision velocities are given by:

$$\begin{aligned} u'_{\mathrm{T(i)}} =& u'_{\mathrm{yi}} = u_{\mathrm{yi}} \\ u'_{\mathrm{N(i)}} =& u'_{\mathrm{xi}} = 2u_{\mathrm{p}} - u_{\mathrm{xi}} \end{aligned} \tag{A.2}$$

A.1.2 Pairwise Collisions

Figure A.1 shows a pairwise collision at the point of impact. The pre- and post-collision velocities are broken up into normal and tangential components at the point of impact. The normal components lie along the *line of action*, connecting the centers of mass of the colliding particles.

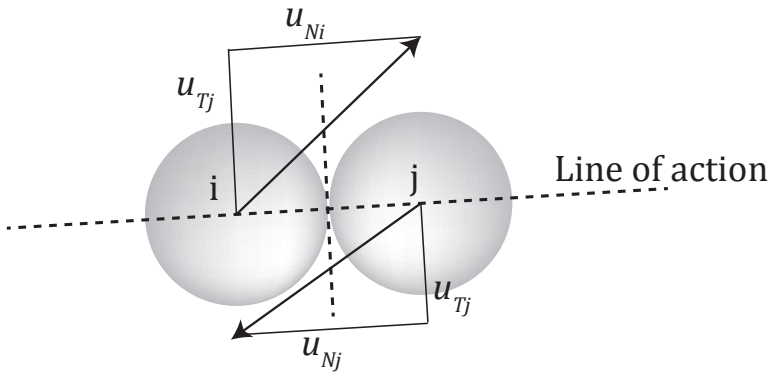

Figure A.1: Sketch of a pairwise collision between two particle demonstrating the normal and tangential components of velocity with respect to the line of action

The particles are smooth disks, which mean that there is no dissipation due to friction during collisions. This translates to no change in the tangential components during the collision, i.e.,

$$\begin{aligned} u'_{\mathrm{Ti}} &= u_{\mathrm{Ti}} \\ u'_{\mathrm{Tj}} &= u_{\mathrm{Tj}} \end{aligned} \tag{A.3}$$

The velocities in the normal direction are found by manipulating the conservation of momentum equation for the collision in the normal direction. To account for the inelasticity, the coefficient of restitution ε^* is used, where $0 \leq \varepsilon^* \leq 1$. This represents the ratio of pre- and post-collision normal velocities:

$$\varepsilon^* = -\frac{\left(u'_{\mathrm{Ni}} - u'_{\mathrm{Nj}}\right)}{\left(u_{\mathrm{Ni}} - u_{\mathrm{Nj}}\right)} \quad \text{where} \quad 0 \leq \varepsilon^* \leq 1 \tag{A.4}$$

This gives the following post-collision velocities along the normal direction for disks i and j, which take the form:

$$\begin{aligned} u'_{\mathrm{Ni}} =& u_{\mathrm{Ni}} - \frac{(1+\varepsilon^*)}{2}\left(u_{\mathrm{Ni}} - u_{\mathrm{Nj}}\right) \\ u'_{\mathrm{Nj}} =& u_{\mathrm{Nj}} + \frac{(1+\varepsilon^*)}{2}\left(u_{\mathrm{Ni}} - u_{\mathrm{Nj}}\right) \end{aligned} \tag{A.5}$$

In order to emulate activated inelastic collisions for the current study, inelastic collisions with $\varepsilon^* < 1$ only occur when the relative impact velocity exceeds a threshold, u^*. All other pairwise collisions are elastic, i.e.,

$$\varepsilon^* = \begin{cases} 1 & \text{if} \quad |u_{\mathrm{Ni}} - u_{\mathrm{Nj}}| < u^* \\ \varepsilon & \text{if} \quad |u_{\mathrm{Ni}} - u_{\mathrm{Nj}}| \geq u^* \end{cases}$$

where the predefined u^* and ε remain constant during each simulation.

A.2 Model Implementation

The hard particle molecular dynamics model using the collision properties discussed in the previous section is implemented by using Event Driven Molecular Dynamics method [69]. The model used in the current study follows the algorithm as presented by [37]. For the *event-driven* algorithm, the simulation propagates to the next time step where an event occurs, which is either a collision with a boundary, or a pairwise collision between disks. In contrast, if there were forces acting on the molecules (force-based algorithms), then small time steps would have to be taken to account for the change in acceleration of molecules, resulting in significantly longer computational times and Event Driven Molecular Dynamics method could not be easily implemented.

A.2.1 Event Driven Molecular Dynamics Algorithm

The MD algorithm follows a simple set of steps to advance the system of particles in time. More efficient algorithms to what is presented here can be seen in [37] and are implemented

in the code used for this study. A simplified Event Driven Molecular Dynamics algorithm to investigate piston propagated shock waves through hard particles is demonstrated by the following set of steps:

1. The system is initialized ($t = 0$) with N hard disks at their respective positions (x_{io}, y_{io}) and velocities (u_{xi}, u_{yi})

2. Schedule of events are computed by calculating the collision times for all pairwise collisions and when each hard disk will collide with a boundary, with the length of time to the nearest collision time denoted as t^* (see Figure A.2 for a simple schematic of this step)

3. The $i = 1, 2...N$ particles are propagated to their new positions ($x_{\mathrm{i}}, y_{\mathrm{i}}$) from position ($x_{\mathrm{io}}, y_{\mathrm{io}}$):

$$\begin{aligned} x_{\mathrm{i}} &= x_{\mathrm{io}} + u_{\mathrm{xi}} t^* \\ y_{\mathrm{i}} &= y_{\mathrm{io}} + u_{\mathrm{yi}} t^* \end{aligned} \tag{A.6}$$

   Piston travelling at velocity u_{p} is propagated to position x_p:

$$x_{\mathrm{p}} = x_{\mathrm{po}} + u_{\mathrm{p}} t^* \tag{A.7}$$

4. Post collision velocities u'_{xi} and u'_{yi} calculated for boundary collisions, and u'_{xi}, u'_{yi}, u'_{xj}, u'_{yj} calculated for pairwise collisions between i and j. These velocities are updated in the algorithm.

5. Time is set to $t = t + t^*$ and positions set to $x_{\mathrm{io}} = x_i$, $y_{\mathrm{io}} = y_i$ for $i = 1, 2...N$

6. Return to Step 2.

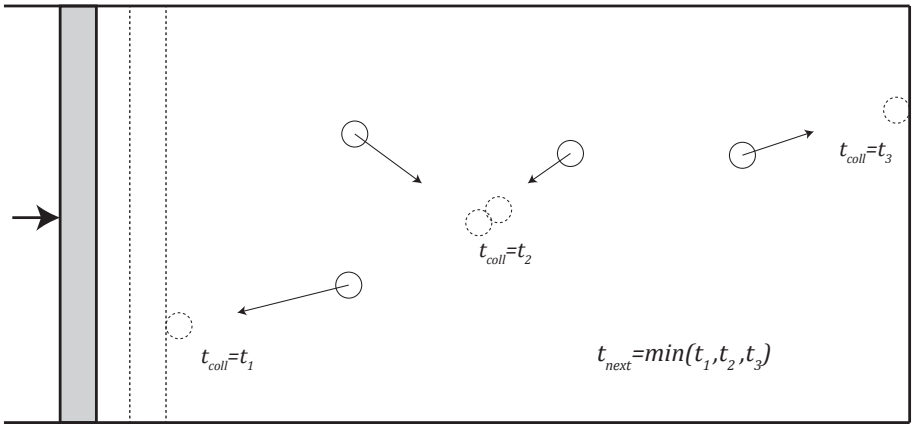

Figure A.2: Sketch demonstrating the scheduling used for the Event Driven Molecular Dynamics algorithm, calculating the minimum time to a collision within a set of disks

To follow this algorithm, the time between collisions and the properties of collisions must be calculated, which are explained in the following sections.

A.2.2 Kinematics of Particles and Boundaries

The novelty of the Event Driven algorithm is the scheduling of collision times for all possible collisions. This allows for the propagation of the system to the next collision, thus avoiding the need to integrate over discrete, small time steps.

Since there are no forces acting on the molecules, the equations of motion are easily expressed for the hard disks and moving boundaries (piston). This allows for the time between events to be easily calculated. The trajectories for the centre of each hard disk can be expressed in terms of the velocities (u_y, u_x) and the position at the time of calculation (x_o, y_o):

$$\begin{aligned} x_i(t) &= x_{\mathrm{io}} + u_{\mathrm{xi}} t \\ y_i(t) &= y_{\mathrm{io}} + u_{\mathrm{yi}} t \end{aligned} \tag{A.8}$$

Pairwise collisions between two hard disks with radius R occur when their centres are located at a distance of $2R$ from each other. A collision occurs between an i and j hard disk

at the time calculated by the following:

$$d_{\mathrm{ij}} = \sqrt{(x_i(t^*_{\mathrm{ij}}) - x_j(t^*_{\mathrm{ij}}))^2 + (y_i(t^*_{\mathrm{ij}}) - y_j(t^*_{\mathrm{ij}}))^2} = 2R \tag{A.9}$$

Since the velocities and positions are known for each hard disk at the time of calculations, the time of collision t^*_{ij} can be calculated. For a calculated $t^*_{\mathrm{ij}} < 0$, no collision between hard disk i and j will occur without other collisions occurring first. For $i, j = 1, 2.....N$, the time for all possible pairwise collisions is calculated in order to determine which event occurs first.

Similarly, collisions times between hard disks and the boundaries are calculated. In this case, the collisions can occur with the walls if the centres of the hard disks are a distance R away from the boundary. The boundaries of the system are three stationary walls at the upper (y_{upper}), lower (y_{lower}) and right (x_{right}) boundaries, and a moving boundary from the left representing a piston at the time dependent position $x_p(t)$. The piston propagates at constant velocity, u_{p}, such that the position of the piston at any time is:

$$x_{\mathrm{p}}(t) = x_{\mathrm{po}} + u_{\mathrm{p}}t \tag{A.10}$$

The time until collisions with the boundaries are separated into the time to collide with the surfaces in the y-direction (t^*_{iy}) and time to collide with surfaces in the x-direction (t^*_{ix}). For $v_{\mathrm{yi}} > 0$ the collision will occur with the upper wall at time $t^*_{\mathrm{upper(i)}}$, and for $u_{\mathrm{yi}} < 0$ the collision will occur with the lower wall at $t^*_{\mathrm{lower(i)}}$,

$$\begin{aligned} t^*_{\mathrm{upper(i)}} &= \frac{y_{\mathrm{upper}} - y_{\mathrm{io}} - R}{u_{\mathrm{yi}}} \\ t^*_{\mathrm{lower(i)}} &= \frac{y_{\mathrm{lower}} - y_{\mathrm{io}} + R}{u_{\mathrm{yi}}} \end{aligned} \tag{A.11}$$

Collisions in the x-direction depend on the direction of a hard disk trajectories, and the relative velocity to the piston. If $u_{\mathrm{xi}} < 0$, a collision with the piston will occur at $t^*_{\mathrm{ix}} = t^*_{\mathrm{piston(i)}}$.

If $u_{\mathrm{xi}} > 0$ the time to collide with piston will be the minimum time between a collision with the right wall or with the piston, i.e., $t^*_{\mathrm{ix}} = \min(t^*_{\mathrm{piston(i)}}, t^*_{\mathrm{right(i)}})$. These times are calculated as:

$$\begin{aligned} t^*_{\mathrm{piston(i)}} &= \frac{x_{\mathrm{po}} - x_{\mathrm{io}} + R}{u_{\mathrm{p}} - u_{\mathrm{xi}}} \\ t^*_{\mathrm{right(i)}} &= \frac{x_{\mathrm{right}} - x_{\mathrm{io}} - R}{u_{\mathrm{xi}}} \end{aligned} \tag{A.12}$$

Therefore, hard disk i will collide with the boundaries at the minimum value between t^*_{ix}, t^*_{iy}, denoted as the time $t^*_{\mathrm{wall(i)}}$.

Calculating t^*_{ij} and $t^*_{\mathrm{wall(i)}}$ for $i, j = 1, 2...N$ allows for a schedule of all events to be compiled.

A.3 Data Collection

Throughout the simulations, the velocities and positions of every disk are tracked, capturing the macroscopic state of the system. Data is output after a specified time step, or distance travelled by the piston. At each of these times, the model outputs various files recording the state of the system.

First, a scalar vector graphic (.svg) image file is output, displaying the position of all the particles and the evolution of the shock waves. The background of Figure A.3 shows an example of this output, where the distribution of particles is shown, along with the position of the piston at that time.

The macroscopic properties of the flow are found by coarse-grain averaging the positions and velocities of the particles. This is done by separating the domain into vertical strips of width dx extending the height of the domain, or into boxes of size $dx \times dy$, as shown in Figure A.3. The one-dimensional distribution of macroscopic properties are found by coarse-grain averaging the microscopic properties within the strips, which are x- and y-directions

are collected within the square boxes with sides approximately equal to $2\lambda_1$.

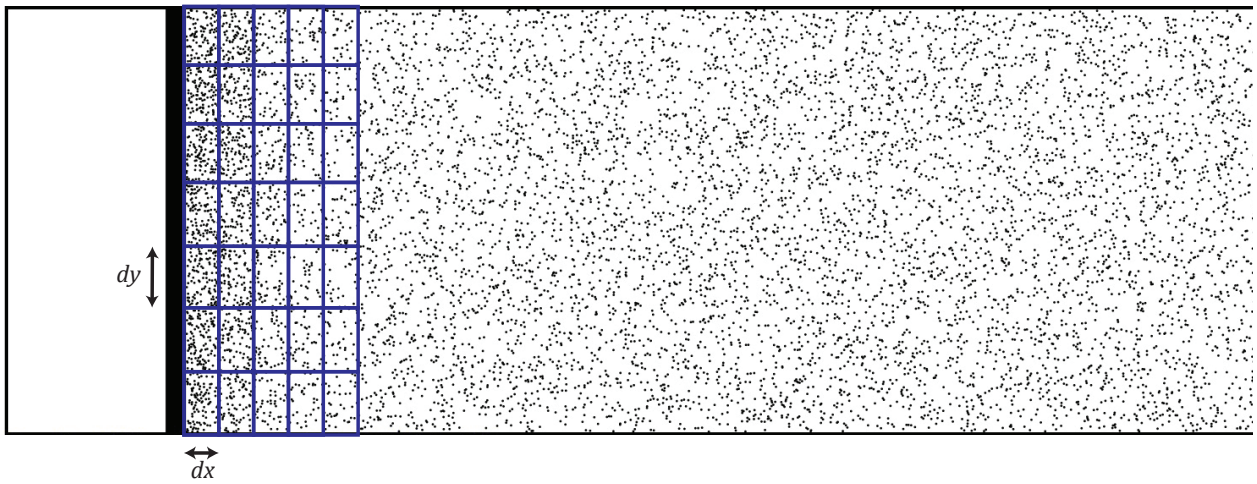

Figure A.3: Example of particle distribution in MD simulation with a sample grid used for coarse-grain averaging

The local granular temperature $T(x)$ of each strip or box is calculated by averaging the kinetic energies in the x- and y-directions over all of the particles, within the coarse-grain averaged areas. The normalized local temperature, at position x, bounded by the strip of width dx, is written as:

$$\begin{aligned} T(x) =& \frac{T_{\mathrm{x}} + T_{\mathrm{y}}}{2} \\ T_{\mathrm{x}}(x) =& \frac{1}{N(x)} \sum_{\mathrm{i}=1}^{N(x)} \frac{1}{2} (u_{\mathrm{xi}} - \langle u_{\mathrm{x}} \rangle)^2 \\ T_{\mathrm{y}}(x) =& \frac{1}{N(x)} \sum_{\mathrm{i}=1}^{N(x)} \frac{1}{2} (u_{\mathrm{yi}} - \langle u_{\mathrm{y}} \rangle)^2 \end{aligned} \tag{A.13}$$

where $N(x)$ is the number of hard disks at position x, bounded by the strip of width dx, and $\langle u_{\mathrm{x}} \rangle = \frac{1}{N(x)} \sum_{\mathrm{i}=1}^{N(x)} u_{\mathrm{xi}}$, $\langle u_{\mathrm{y}} \rangle = \frac{1}{N(x)} \sum_{\mathrm{i}=1}^{N(x)} u_{\mathrm{yi}}$, are the local mean velocities in the x- and y-directions, respectively.

The local number density in each strip, $n(x)$ is written as:

$$n(x) = \frac{N(x)}{dx \times L_{\mathrm{y}}} \tag{A.14}$$

Ensemble averaging is used to obtain accurate measurements of the coarse-grained density and temperature. This is done by repeating the calculation with statistically different initial conditions, which is implemented by randomizing the initial positions and directions of motion for each simulation.

Appendix B

Kinetic Theory for Hard Disks

The following section presents the derivation of some statistics of a hard disk medium using kinetic theory. Much of the derivations follow the methodology presented for kinetic theory of hard particles, such as that presented by Vincenti and Kruger [82].

B.1 Maxwell-Boltzmann distribution in 2D

It is well know that the distribution of velocities for a system of particles takes the form

$$f(\boldsymbol{v}_\mathrm{i}) = A \exp\left(-B\boldsymbol{v}_\mathrm{i}^2\right). \tag{B.1}$$

In order to solve for A and B in (B.1), it must be acknowledged that the integral over all velocities is equal to unity, i.e.,

$$\int_{-\infty}^{\infty} f(\boldsymbol{v}_\mathrm{i}) d\boldsymbol{v}_\mathrm{i} = 1. \tag{B.2}$$

Applying the expected form from (B.1) yields

$$\int_{-\infty}^{\infty} A \exp\left(-B\boldsymbol{v}_\mathrm{i}^2\right) d\boldsymbol{v}_\mathrm{i} = 1. \tag{B.3}$$

To solve this requires a conversion to polar coordinates for the 2D space and integrating:

$$A \int_0^{\infty} \int_0^{2\pi} v_\mathrm{i} \exp\left(-B {v_\mathrm{i}}^2\right) d\theta dv_\mathrm{i} = 1 \tag{B.4}$$

$$A 2\pi \int_0^{\infty} v_\mathrm{i} \exp\left(-B {v_\mathrm{i}}^2\right) dv_\mathrm{i} = 1 \tag{B.5}$$

$$A 2\pi \left(\frac{1}{2B}\right) = 1, \tag{B.6}$$

or

$$A = \frac{B}{\pi}. \tag{B.7}$$

Another identity that can be used is that

$$\bar{v_\mathrm{i}}^2 = \frac{2kT}{m} = \int_0^{\infty} \boldsymbol{v}_\mathrm{i}^2 f(\boldsymbol{v}_\mathrm{i}) d\boldsymbol{v}_\mathrm{i}. \tag{B.8}$$

Plugging in the expected form from (B.1) and converting to polar coordinates gives the following integral to solve:

$$\begin{aligned}
\frac{2kT}{m} &= A \int_0^{2\pi} \int_0^{\infty} v_\mathrm{i}^3 \exp\left(-B v_\mathrm{i}^2\right) d\theta dv_\mathrm{i} \\
&= \frac{B}{\pi} \int_0^{2\pi} \int_0^{\infty} v_\mathrm{i}^3 \exp\left(-B v_\mathrm{i}^2\right) d\theta dv_\mathrm{i} \\
&= 2B \int_0^{\infty} v_\mathrm{i}^3 \exp\left(-B v_\mathrm{i}^2\right) dv_\mathrm{i} \\
&= 2B \left(\frac{1}{2B^2}\right),
\end{aligned}$$

yielding

$$B = \frac{m}{2kT} \tag{B.9}$$

and

$$A = \frac{m}{2\pi kT}. \tag{B.10}$$

Therefore, the distribution of velocities $\boldsymbol{v}_\mathrm{i}$ is:

$$f(\boldsymbol{v}_\mathrm{i}) = \frac{m}{2\pi kT} \exp\left(\frac{-m\boldsymbol{v}_\mathrm{i}^2}{2kT}\right) \tag{B.11}$$

or in terms of the magnitude v_i, since

$$f(\boldsymbol{v}_\mathrm{i})d\boldsymbol{v}_\mathrm{i} = \int_0^{2\pi} \frac{m}{2\pi kT} \exp\left(\frac{-m\boldsymbol{v}_\mathrm{i}^2}{2kT}\right) v_\mathrm{i} dv_\mathrm{i} d\theta \tag{B.12}$$

is

$$\boxed{f(v_\mathrm{i}) = \frac{mv_\mathrm{i}}{2\pi kT} \exp\left(\frac{-m{v_\mathrm{i}}^2}{2kT}\right).} \tag{B.13}$$

This equation gives the probability that a hard disk of mass m, in a mixture with temperature T will have a velocity magnitude v_i.

B.2 Collision Frequency for System of Disks

The collision frequency of disks is now derived. This begins by considering the frame of reference of a disk i impacting a disk j. At the moment of impact, the center of j must lie on the circle of influence of i. The *line of centers* connect the centers of i and j, which is at an angle ψ with the relative velocity vector $\boldsymbol{g}_\mathrm{ij}$. Where the magnitude of this vector is

$$g = \sqrt{(v_\mathrm{xj}^2 - v_\mathrm{xi}^2) + (v_\mathrm{yj}^2 - v_\mathrm{yi}^2)}. \tag{B.14}$$

The frequency of collisions is now needed for particles of class $\boldsymbol{v}_\mathrm{i}$ and $\boldsymbol{v}_\mathrm{j}$, whose line of centers lie in the range ψ to $\psi + d\psi$. At the moment of impact, the center of j must lie on

the surface of the circle of influence with length $d_{\mathrm{ij}}d\psi$. During a short time dt, for a collision to occur, the center must lie in the area of the parallelapiped:

$$dA = gdt \times d\cos\psi d\psi. \tag{B.15}$$

Considering all molecules of type $\boldsymbol{v}_{\mathrm{i}}$ with such an area, gives $nf(\boldsymbol{v}_{\mathrm{i}})d\boldsymbol{v}_{\mathrm{i}}$ molecules. This gives a total area for all molecules as

$$nf(\boldsymbol{v}_{\mathrm{i}})gd\cos\psi d\psi dt d\boldsymbol{v}_{\mathrm{i}}. \tag{B.16}$$

Therefore, the number of collisions of specific type, per unit area, per unit time is this area multiplied by the distribution of type $\boldsymbol{v}_{\mathrm{j}}$ disks, yielding

$$n^2 f(\boldsymbol{v}_{\mathrm{i}})f(\boldsymbol{v}_{\mathrm{j}})gd\cos\psi d\psi dt d\boldsymbol{v}_{\mathrm{i}}d\boldsymbol{v}_{\mathrm{j}}. \tag{B.17}$$

For two different species, the frequency of collisions can be written as:

$$n_{\mathrm{A}}n_{\mathrm{B}}f_{\mathrm{A}}(\boldsymbol{v}_{\mathrm{i}})f_{\mathrm{B}}(\boldsymbol{v}_{\mathrm{j}})gd_{\mathrm{AB}}\cos\psi d\psi dt d\boldsymbol{v}_{\mathrm{i}}d\boldsymbol{v}_{\mathrm{j}} \tag{B.18}$$

where

$$d_{\mathrm{AB}} = \frac{d_{\mathrm{A}} + d_{\mathrm{B}}}{2}. \tag{B.19}$$

From the previous section, the Maxwellian distribution in 2D is given as

$$f(\boldsymbol{v}_{\mathrm{i}}) = \frac{m}{2\pi kT}\exp\left(\frac{-m\boldsymbol{v}_{\mathrm{i}}^2}{2kT}\right) \tag{B.20}$$

Plugging this into the collision frequency above yields

$$n_{\mathrm{A}} n_{\mathrm{B}} \frac{m_{\mathrm{A}} m_{\mathrm{B}}}{(2\pi kT)^2} \exp\left(-\frac{m_{\mathrm{A}} v_{\mathrm{i}}^2 + m_{\mathrm{B}} v_{\mathrm{j}}^2}{2kT}\right) g d_{\mathrm{AB}} \cos\psi d\psi dt d\boldsymbol{v}_{\mathrm{i}} d\boldsymbol{v}_{\mathrm{j}}. \tag{B.21}$$

This equation can be integrated over all space and velocities to get the collision frequency. However, this is difficult due to g, so it is simplified first.

The velocity components of the molecules are now transformed to the components of the relative velocity and the velocity of the center of mass. The $x-$component of relative velocity can be expressed as:

$$g_{\mathrm{x}} = v_{\mathrm{jx}} - v_{\mathrm{ix}} \tag{B.22}$$

and the $x-$coordinate of the center of mass is

$$x_{\mathrm{c}} = \frac{m_{\mathrm{A}} x_{\mathrm{A}} + m_{\mathrm{B}} x_{\mathrm{B}}}{m_{\mathrm{A}} + m_{\mathrm{B}}}. \tag{B.23}$$

Taking $\frac{dx_{\mathrm{c}}}{dt}$ gives the $x-$component of the velocity, v_{cx} of the center of mass:

$$v_{\mathrm{cx}} = \frac{dx_{\mathrm{c}}}{dt} = \frac{m_{\mathrm{A}} v_{\mathrm{Ax}} + m_{\mathrm{B}} v_{\mathrm{Bx}}}{m_{\mathrm{A}} + m_{\mathrm{B}}}. \tag{B.24}$$

From (B.23) and (B.24):

$$\begin{aligned} v_{\mathrm{Ax}} &= v_{\mathrm{cx}} - \frac{m_{\mathrm{B}}}{m_{\mathrm{A}} + m_{\mathrm{B}}} g_{\mathrm{x}} \\ v_{\mathrm{Bx}} &= v_{\mathrm{cx}} + \frac{m_{\mathrm{A}}}{m_{\mathrm{A}} + m_{\mathrm{B}}} g_{\mathrm{x}}. \end{aligned} \tag{B.25}$$

The following can now be written:

$$m_{\mathrm{A}} v_{\mathrm{Ax}}^2 + m_{\mathrm{B}} v_{\mathrm{Bx}}^2 = (m_{\mathrm{A}} + m_{\mathrm{B}}) v_{\mathrm{cx}}^2 + \frac{m_{\mathrm{A}} m_{\mathrm{B}}}{m_{\mathrm{A}} + m_{\mathrm{B}}} g_{\mathrm{x}}^2. \tag{B.26}$$

Introducing the reduced mass, $\mu_{\mathrm{AB}} = \frac{m_{\mathrm{A}} m_{\mathrm{B}}}{m_{\mathrm{A}} + m_{\mathrm{B}}}$ and doing this transformation in all directions,

the sum in the exponential of (B.21) can be re-written as:

$$\frac{1}{2}m_{\mathrm{A}}v_{\mathrm{A}}^2+\frac{1}{2}m_{\mathrm{B}}v_{\mathrm{B}}^2=\frac{1}{2}(m_{\mathrm{A}}+m_{\mathrm{B}})v_c^2+\frac{1}{2}\mu_{\mathrm{AB}}g^2. \tag{B.27}$$

The differentials now need to be transformed. In the $x-$direction, $dv_{\mathrm{Ax}}dv_{\mathrm{Bx}}$ needs to be transformed, where:

$$dv_{\mathrm{Ax}}dv_{\mathrm{Bx}}=\frac{\partial(v_{\mathrm{Ax}},v_{\mathrm{Bx}})}{\partial(v_{\mathrm{cx}},g_{\mathrm{x}})}dv_{\mathrm{cx}}dg_{\mathrm{x}}. \tag{B.28}$$

The Jacobian, $\frac{\partial(v_{\mathrm{Ax}},v_{\mathrm{Bx}})}{\partial(v_{\mathrm{cx}},g_{\mathrm{x}})}$ can be calculated from (B.25):

$$\frac{\partial(v_{\mathrm{Ax}},v_{\mathrm{Bx}})}{\partial(v_{\mathrm{cx}},g_{\mathrm{x}})}=\begin{vmatrix}\frac{\partial v_{\mathrm{Ax}}}{\partial v_{\mathrm{cx}}} & \frac{\partial v_{\mathrm{Ax}}}{\partial g_{\mathrm{x}}}\\ \frac{\partial v_{\mathrm{Bx}}}{\partial v_{\mathrm{cx}}} & \frac{\partial v_{\mathrm{Bx}}}{\partial g_{\mathrm{x}}}\end{vmatrix}=\begin{vmatrix}1 & -\frac{m_{\mathrm{B}}}{m_{\mathrm{A}}+m_{\mathrm{B}}}\\ 1 & \frac{m_{\mathrm{A}}}{m_{\mathrm{A}}+m_{\mathrm{B}}}\end{vmatrix}=1. \tag{B.29}$$

Therefore, $dv_{\mathrm{Ax}}dv_{\mathrm{Bx}}=dv_{\mathrm{cx}}dg_{\mathrm{x}}$. Doing the transformations in all directions, (B.21) can be re-written as:

$$n_{\mathrm{A}}n_{\mathrm{B}}d_{\mathrm{AB}}^2\frac{(m_{\mathrm{A}}m_{\mathrm{B}})}{(2\pi kT)^3}g\exp\left(-\frac{1}{2kT}\left((m_{\mathrm{A}}+m_{\mathrm{B}})v_c^2+\mu_{\mathrm{AB}}g^2\right)\right)\cos\psi d\psi dv_{\mathrm{cx}}dv_{\mathrm{cy}}dg_{\mathrm{x}}dg_{\mathrm{y}}. \tag{B.30}$$

Converting to polar coordinates and modifying with the following:

$$\begin{aligned}dv_{\mathrm{cx}}dv_{\mathrm{cy}}&=v_cd\theta_cdv_c\\ dg_{\mathrm{x}}dg_{\mathrm{y}}&=gd\theta_gdg\end{aligned} \tag{B.31}$$

yields

$$\begin{aligned}n_{\mathrm{A}}n_{\mathrm{B}}d_{\mathrm{AB}}^2\frac{m_{\mathrm{A}}m_{\mathrm{B}}}{(2\pi kT)^2}\exp\left(-\frac{1}{2kT}\left((m_{\mathrm{A}}+m_{\mathrm{B}})v_c^2+\mu_{\mathrm{AB}}^2g^2\right)\right)\\ \times g^2v_c\cos\psi d\psi d\theta_cdv_cd\theta_gdg.\end{aligned} \tag{B.32}$$

Integrating over all velocities of the center of mass gives the following integral:

$$\int_0^{2\pi}\int_0^{\infty} v_c \exp\left(-\frac{1}{2kT}(m_\mathrm{A}+m_\mathrm{B})v_c^2\right)d\theta_c dv_c = 2\pi\frac{2kT}{2(m_\mathrm{A}+m_\mathrm{B})} = 2\frac{2\pi kT}{(m_\mathrm{A}+m_\mathrm{B})}. \tag{B.33}$$

Plugging it back into (B.32) yields,

$$n_\mathrm{A}n_\mathrm{B}d_\mathrm{AB}^2\left(\frac{\mu_\mathrm{AB}}{2\pi kT}\right)\exp\left(-\frac{1}{2kT}\mu_\mathrm{AB}g^2\right)g^2\cos\psi d\psi d\theta_g dg. \tag{B.34}$$

Accounting for all directions of the relative velocity by integreting θ_g from 0 to 2π yields:

$$2\pi n_\mathrm{A}n_\mathrm{B}d_\mathrm{AB}^2\left(\frac{\mu_\mathrm{AB}}{2\pi kT}\right)\exp\left(-\frac{1}{2kT}\mu_\mathrm{AB}g^2\right)g^2\cos\psi d\psi dg. \tag{B.35}$$

This gives the frequency of collision between molecules A and B with relative velocities in the range g to $g+dg$ and angular centers lying in the range ψ to $\psi+d\psi$ from the direction of g. This can be used for collision theory involving chemical reaction rates, where the reactions will depend on the magnitude of the collision (represented by g and ψ).

To get the overall collision frequency between A and B molecules Z_AB requires integration over all relative velocities, and for ψ from 0 to $\pi/2$:

$$\begin{aligned}
Z_\mathrm{AB} = &\int_{-\pi/2}^{\pi/2}\int_0^{\infty} 2\pi n_\mathrm{A}n_\mathrm{B}d_\mathrm{AB}\left(\frac{\mu_\mathrm{AB}}{2\pi kT}\right)\exp\left(-\frac{1}{2kT}\mu_\mathrm{AB}g^2\right)g^2\cos\psi d\psi dg \\
= &\ 4\pi n_\mathrm{A}n_\mathrm{B}d_\mathrm{AB}\left(\frac{\mu_\mathrm{AB}}{2\pi kT}\right)\frac{1}{4}\frac{\pi^{1/2}}{(\mu_\mathrm{AB}/2kT)^{3/2}} \\
= &\ n_\mathrm{A}n_\mathrm{B}d_\mathrm{AB}\left(\frac{\mu_\mathrm{AB}}{2\pi kT}\right)\left(\frac{2\pi kT}{\mu_\mathrm{AB}}\right)^{3/2} \\
= &\ n_\mathrm{A}n_\mathrm{B}d_\mathrm{AB}\left(\frac{2\pi kT}{\mu_\mathrm{AB}}\right)^{1/2}.
\end{aligned} \tag{B.36}$$

This can be more appropriately written as:

$$Z_{\mathrm{AB}} = \frac{n_{\mathrm{A}} n_{\mathrm{B}}}{s} d_{\mathrm{AB}} \left(\frac{2\pi kT}{\mu_{\mathrm{AB}}} \right)^{1/2}. \tag{B.37}$$

Where s is a symmetry factor, which is equal to 1 for $A \neq B$ and 2 for $A = B$. This is due to the fact that collisions between like molecules are counted twice during integration, although they are indistinguishable. Therefore the collision frequency among like particles is divided by 2.

B.2.1 Collision Frequency with Activation Threshold

The collision frequency is now derived for collisions where the velocity along the line of centers exceeds some threshold u^*, i.e, when

$$g \cos\psi \geq u^* \qquad \rightarrow \qquad \psi = \cos^{-1}\left(\frac{u^*}{g}\right). \tag{B.38}$$

Recall that the collision rate is written as:

$$Z_{\mathrm{AB}}(g,\psi) = 2\pi n_{\mathrm{A}} n_{\mathrm{B}} d_{\mathrm{AB}} \left(\frac{\mu_{\mathrm{AB}}}{2\pi kT}\right) \exp\left(-\frac{1}{2kT}\mu_{\mathrm{AB}} g^2\right) g^2 \cos\psi d\psi dg.$$

ψ must now be replaced in term of this activation threshold, and the relative velocity. To do this, $\cos\psi$ must first be integrated from -$\cos^{-1}\left(\frac{u^*}{g}\right)$ to $\cos^{-1}\left(\frac{u^*}{g}\right)$:

$$\int_{-\cos^{-1}\left(\frac{u^*}{g}\right)}^{\cos^{-1}\left(\frac{u^*}{g}\right)} \cos\psi d\psi = \sin\psi \Big|_{-\cos^{-1}\left(\frac{u^*}{g}\right)}^{\cos^{-1}\left(\frac{u^*}{g}\right)} = 2\sqrt{1 - \frac{u^{*2}}{g^2}}. \tag{B.39}$$

This now gives the integral for the collision frequency from u^* to ∞:

$$\begin{aligned} Z_{\mathrm{AB}} &= \int_{u^*}^{\infty} 2n_{\mathrm{A}}n_{\mathrm{B}}d_{\mathrm{AB}}\left(\frac{\mu_{\mathrm{AB}}}{kT}\right)\exp\left(-\frac{1}{2kT}\mu_{\mathrm{AB}}g^2\right)g^2\sqrt{1-\frac{u^{*2}}{g^2}}dg \\ &= 2n_{\mathrm{A}}n_{\mathrm{B}}d_{\mathrm{AB}}\left(\frac{\mu_{\mathrm{AB}}}{kT}\right)\frac{\exp\left(-\frac{\mu_{\mathrm{AB}}u^{*2}}{2kT}\right)\sqrt{\pi}}{4\left(\frac{\mu_{\mathrm{AB}}}{2kT}\right)^{3/2}} \\ &= 2n_{\mathrm{A}}n_{\mathrm{B}}d_{\mathrm{AB}}\left(\frac{\mu_{\mathrm{AB}}}{kT}\right)\left(\frac{2kT}{\mu_{\mathrm{AB}}}\right)^{3/2}\exp\left(-\frac{\mu_{\mathrm{AB}}u^{*2}}{2kT}\right)\frac{\sqrt{\pi}}{4} \\ &= 2n_{\mathrm{A}}n_{\mathrm{B}}d_{\mathrm{AB}}\left(\frac{kT}{\mu_{\mathrm{AB}}}\right)^{1/2}\sqrt{\frac{\pi}{2}}\exp\left(-\frac{\mu_{\mathrm{AB}}u^{*2}}{2kT}\right). \end{aligned} \tag{B.40}$$

B.3 Energy Involved in Collisions

To consider the energy involved along the line of action for identical disks with equal mass and diameter, one can re-write rate of binary collisions per unit volume:

$$f(g,\psi) = n^2 d\frac{m}{2kT}\exp\left\{\frac{mg^2}{4kT}\right\}g^2\cos\psi dg d\psi \tag{B.41}$$

which gives the rate of binary collisions of a system of disks of mass m with a number density $n = N/A$ that have a relative speed in the range of g to $g + dg$, with an angle between the relative velocity and the line of action in the range of ψ to $\psi + d\psi$. Along the line of action, the relative velocity is

$$u_{\mathrm{N}} = g\cos\psi. \tag{B.42}$$

Multiplying (B.41) by $u_{\mathrm{N}}^2 = (g\cos\psi)^2$, and integrating over a range of u_{N}, one recovers the energy along the line of action for collisions with impact velocities within this range. Integrating u_{N} from 0 to ∞ recovers the overall impact energy directly. Integrating u_{N} from u^* to ∞ yields the energy involved along the line of action for impact velocities exceeding u^*, which is

$$\langle u_{\mathrm{N}}^2 \rangle (u_{\mathrm{N}} > u^*) = \underbrace{2\sqrt{\pi} n^2 d \left(\frac{kT}{m}\right)^{1/2} \exp\left(-\frac{mu^{*2}}{4kT}\right)}_{Z_{\mathrm{AB}}(u_{\mathrm{N}} > u^*)} \frac{4kT}{m} \left(1 + \frac{mu^{*2}}{4kT}\right). \tag{B.43}$$

The first term represents the rate of binary collisions exceeding impact velocity u^*, and the following terms are related to the energy involved in those collisions.

The ratio of the average energy involved in activated collisions to the energy of all collisions can be calculated as

$$\frac{\langle u_{\mathrm{n}}^2 \rangle (u_{\mathrm{N}} > u^*)}{\langle u_{\mathrm{n}}^2 \rangle (u_{\mathrm{N}} > 0)} = \exp\left\{\frac{mu^{*2}}{4kT}\right\} \left(1 + \frac{mu^{*2}}{4kT}\right). \tag{B.44}$$

which can be applied to transform the rate of cooling that is calculated for all collisions being activated to only those collisions exceeding a threshold u^*.

Appendix C

Thermodynamics and Shock Wave Properties for Elastic Disks

The current Appendix provides details for the thermodynamics of a system of elastic disks, as well as the shock wave properties for such a medium. This work has previously been published in the *Shock Waves* journal [79].

C.1 Thermodynamic Properties

C.1.1 Equation of State for a Hard Disk Gas

In elastic hard particle systems, there is no internal structure, therefore the internal energy e consists of only the translational kinetic energy. The energy for each translational degree of freedom is $\frac{1}{2}\frac{k}{m}T$. For a hard disk system, there are two translational degrees of freedom, giving the internal energy as,

$$e = \frac{k}{m}T. \tag{C.1}$$

An equation of state is needed to relate the hydrostatic pressure p, the specific volume v and the temperature T, written as [78]:

$$pv = Z\frac{k}{m}T \tag{C.2}$$

where Z is the compressibility factor, which tends to 1 for an ideal gas.

Combining (C.1) and (C.2), the internal energy e can be written in terms of p and v:

$$e = \frac{pv}{Z}. \tag{C.3}$$

The compressibility factor Z is usually expressed in terms of the packing factor η. The caloric equation of state can then be expressed as:

$$e(p, v) = \frac{pv}{Z(\eta)}. \tag{C.4}$$

For a hard-disk medium, the exact equation of state is not known in closed form, requiring an infinite virial expansion. Various equations of state ahve been proposed for a hard particle system (see, for example [78]). One equation of state proposed in hard disks is that by Helfand *et al.* [76], which is accurate, physically meaningful and analytically simple. This simple expression takes the form

$$Z(\eta) = \frac{1}{(1-\eta)^2}. \tag{C.5}$$

This equation of state shall be used to analytically investigate the effect that the initial compaction η_o has on the medium's compressibility.

C.1.2 Isentropic Exponent and Sound Speed

The change in the compressibility of medium is best described by the isentropic exponent γ, which describes the relation between changes in density and changes in pressure for isentropic

processes. It is defined as

$$\gamma \equiv \left(\frac{\partial \ln p}{\partial \ln \rho}\right)_{\mathrm{s}}. \tag{C.6}$$

The sound speed in the medium is directly related to γ, i.e.:

$$c^2 \equiv \left(\frac{\partial p}{\partial \rho}\right)_{\mathrm{s}} = \gamma \frac{p}{\rho}. \tag{C.7}$$

Note that γ is *not* the ratio of specific heats, which in this case is simply 2 for any compaction ratio, as can be deduced from (C.1) and the definition of enthalpy. To determine the dependence of c or γ on the state variables p and v (or ρ), one makes use of the Gibbs thermodynamic equations relating p, v and the entropy s. The first and second law of thermodynamics for a control system yield Gibbs equation written in terms of the density as

$$de(p,\rho) = Tds + \frac{p}{\rho^2} d\rho \tag{C.8}$$

alternatively, $e(p,\rho)$ can also be written as a perfect differential as

$$de(p,\rho) = \left(\frac{\partial e}{\partial p}\right)_{\rho} dp + \left(\frac{\partial e}{\partial \rho}\right)_{\mathrm{p}} d\rho. \tag{C.9}$$

Comparing (C.8) and (C.9), this can be re-written as

$$dp = \frac{\frac{p}{\rho^2} - \left(\frac{\partial e}{\partial \rho}\right)_{\mathrm{p}}}{\left(\frac{\partial e}{\partial p}\right)_{\rho}} d\rho + \frac{T}{\left(\frac{\partial e}{\partial p}\right)_{\rho}} ds. \tag{C.10}$$

Writing $p(\rho, s)$ as a perfect differential yields

$$dp(\rho,s) = \left(\frac{\partial p}{\partial \rho}\right)_{\mathrm{s}} d\rho + \left(\frac{\partial p}{\partial s}\right)_{\rho} ds. \tag{C.11}$$

Comparing (C.10) with (C.11) gives

$$c^2 = \left(\frac{\partial p}{\partial \rho}\right)_{\mathrm{s}} = \frac{\frac{p}{\rho^2} - \left(\frac{\partial e}{\partial \rho}\right)_{\mathrm{p}}}{\left(\frac{\partial e}{\partial p}\right)_{\rho}}. \tag{C.12}$$

This expression is general for any medium. By using the Helfand equation of state, the sound speed may be expressed in terms of the local state of the medium and the local packing factor η

$$c^2 = pv\left(1 + (1-\eta)^{-2} + 2\eta(1-\eta)^{-1}\right) \tag{C.13}$$

and from (C.7) the isentropic exponent is obtained as

$$\gamma = 1 + (1-\eta)^{-2} + 2\eta(1-\eta)^{-1}. \tag{C.14}$$

Figure C.1 shows the variation of the isentropic exponent with the local packing fraction. In the dilute limit of an ideal gas, i.e., $\eta \to 0$, the isentropic exponent of a two-dimensional hard disk gas of $\gamma = 2$ is recovered. However, with increasing packing fraction, the isentropic exponent grows significantly, reflecting the incompressibility of the medium. A small change in density requires a very large change in pressure, a characteristic of nearly *incompressible* media like liquids and solids.

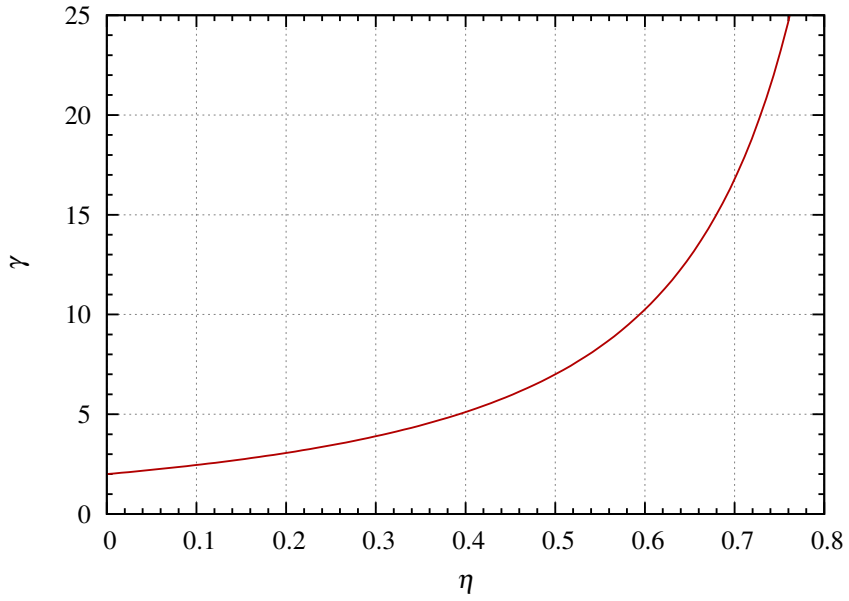

Figure C.1: The variation of the isentropic exponent with the local packing factor η.

C.2 Shock Waves in a Hard Disk Medium

To investigate shock jumps in a hard disk medium, the classic problem is considered whereby a piston is suddenly accelerated from zero velocity to a constant velocity u_p into a medium initially at rest. A shock wave is formed, which propagates with velocity D. If diffusive fluxes are negligible in the pre- and post-shock states, and letting the subscript s denote the uniform state of the medium behind the shock wave, the conservation of mass, linear momentum and energy, in the frame of reference of the shock yield [13]:

$$\frac{D}{v_\mathrm{o}} = \frac{(D-u_\mathrm{p})}{v_\mathrm{s}} \tag{C.15}$$

$$p_\mathrm{o} + \frac{D^2}{v_\mathrm{o}} = p_\mathrm{s} + \frac{(D-u_\mathrm{p})^2}{v_\mathrm{s}} \tag{C.16}$$

$$e_\mathrm{o} + p_\mathrm{o}v_\mathrm{o} + \frac{1}{2}D^2 = e_\mathrm{s} + p_\mathrm{s}v_\mathrm{s} + \frac{1}{2}(D-u_\mathrm{p})^2. \tag{C.17}$$

Combining the equation of mass (C.15), momentum (C.16) and energy (C.17) to eliminate the two speeds, the accessible end states s across the shock wave can be represented by the shock Hugoniot relation in the (p, v) plane [13]:

$$e_{\mathrm{s}}(p_{\mathrm{s}}, v_{\mathrm{s}}) - e_{\mathrm{o}}(p_{\mathrm{o}}, v_{\mathrm{o}}) = \frac{1}{2}(v_{\mathrm{o}} - v_{\mathrm{s}})(p_{\mathrm{o}} + p_{\mathrm{s}}). \tag{C.18}$$

This shock description is completely general, and depends on the equation of state $e(p, v)$ characterizing the particular medium.

Using Helfand's equation of state (C.5) and relation (C.4) with the definition of η, the Hugoniot relation (C.18) can be used to express in closed form the variation of pressure with specific volume across the shock wave, yielding

$$\pi = \frac{\frac{1}{2}(1 - \varsigma) + (1 - \eta_{\mathrm{o}})^2}{\varsigma(1 - \frac{\eta_{\mathrm{o}}}{\varsigma})^2 - \frac{1}{2}(1 - \varsigma)}, \tag{C.19}$$

where π, ς and η_{o} are, respectively, the non-dimensional pressure ratio across the shock wave, non-dimensional specific volume ratio across the shock wave, and the initial packing fraction of the medium.

$$\pi = \frac{p_{\mathrm{s}}}{p_{\mathrm{o}}}, \varsigma = \frac{v_{\mathrm{s}}}{v_{\mathrm{o}}}, \eta_{\mathrm{o}} = \frac{(V_{\mathrm{a}}/m)}{v_{\mathrm{o}}}. \tag{C.20}$$

Figure C.2 displays the shock Hugoniot curves for three initial packing fractions. As the packing fraction is increased, a higher pressure is generated for the same compression ratio. Alternatively, the same pressure is achieved with less compression in an initially higher packed medium. This mimics very well the real properties of shocks in less compressible media such as liquids and solids [13].

The maximum compression that can be achieved across a shock wave can be found by letting $\pi \to \infty$ in (C.19). This corresponds to letting the denominator in (C.19) equate to zero, yielding a quadratic for which the largest root is the physically attainable solution. The

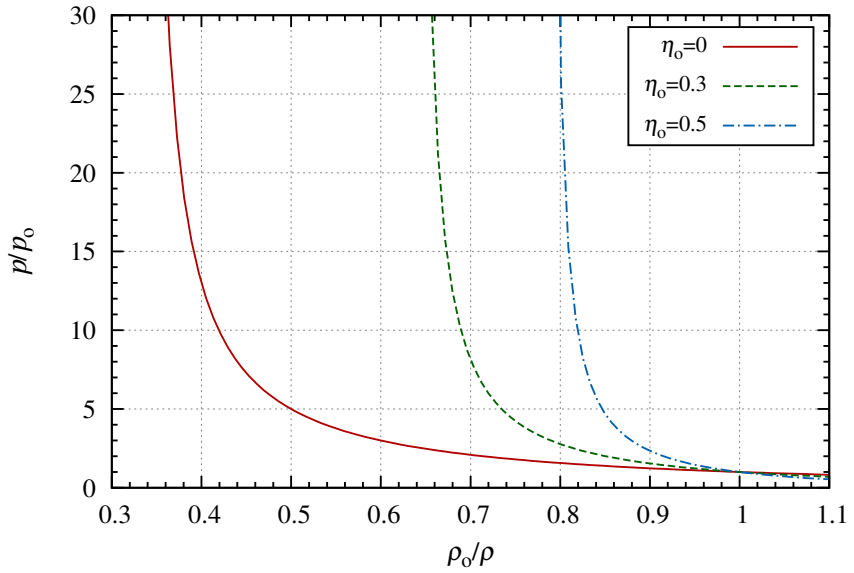

Figure C.2: The relation between the shock overpressure and compression ratio represented on the shock Hugoniot for a hard disk medium in terms of the initial packing factor η_o.

maximum compression achievable is thus

$$\varsigma_{\max} = \frac{1}{6}(1 + 4\eta_o + \sqrt{(1 - 8(\eta_o - 1)\eta_o}), \tag{C.21}$$

which is shown in Fig. C.3.

The shock jump conditions are now parametrized with the Mach number of the shock wave M_o. From the mass (C.15) and momentum (C.16) equations and using (C.4), (C.5) and (C.20), the overpressure can be expressed across the shock wave in terms of the shock Mach number and compression ratio across the shock, yielding the so-called Rayleigh line

$$\pi = 1 + \psi(1 - \varsigma) \tag{C.22}$$

where ψ is simply related to the shock Mach number and the initial value of γ:

$$\psi \equiv \frac{D^2}{p_o v_o} = \gamma_o \frac{D^2}{{c_o}^2} = \gamma_o {M_o}^2. \tag{C.23}$$

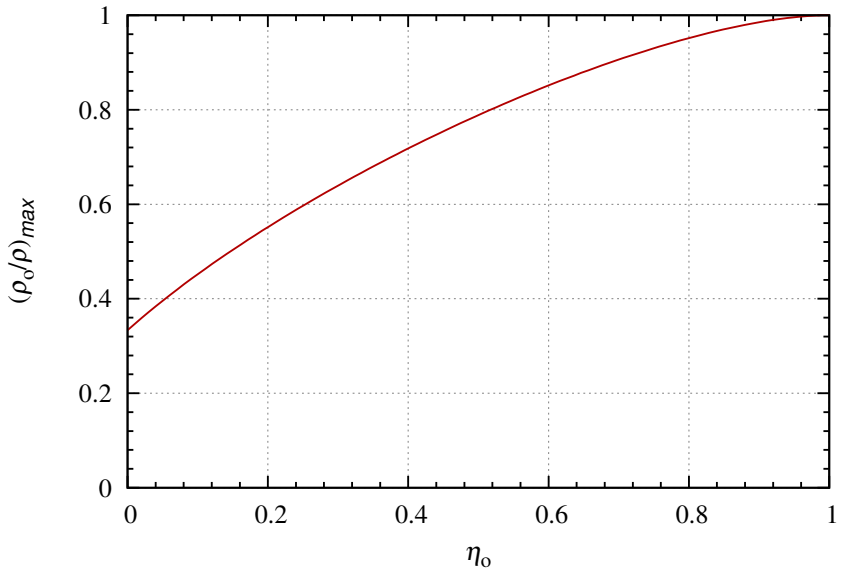

Figure C.3: The maximum compression ratio achieved by shock compression in terms of the initial packing factor η_o.

Equating (C.19) to (C.22) yields the shock jump conditions in closed form in terms of the shock strength parameter ψ, and the initial packing fraction η_o:

$$\frac{v_s}{v_o} = \varsigma = \frac{4 + \psi + 4\psi + 4\psi\eta_o}{6\psi} + \frac{\sqrt{-24\psi(1+\psi)\eta_o^2 + (4 + \psi + 4\psi\eta_o)^2}}{6\psi} \tag{C.24a}$$

$$\frac{p_s}{p_o} = \pi = 1 + \psi(1 - \varsigma) \tag{C.24b}$$

$$\frac{u_p}{D} = 1 - \varsigma \tag{C.24c}$$

$$\frac{T_s}{T_o} = \pi\varsigma\frac{(1 - \frac{\eta_o}{\varsigma})^2}{(1 - \eta_o)^2}. \tag{C.24d}$$

In order to better compare with the simulated results, this solution may be paramaterized in terms of the piston velocity, instead of the Mach number. To do this,the square of the piston speed is used, representing the kinetic energy addition by the piston motion as a parameter,

given by

$$\beta \equiv \frac{1}{2}\frac{{u_\mathrm{p}}^2}{e_\mathrm{o}} \equiv \frac{{u_\mathrm{p}}^2}{u_{\mathrm{rms(o)}^2}}. \tag{C.25}$$

Expressions (C.24) can be expressed implicitly in terms of β using (C.24c), which can be re-written as

$$\beta = \frac{\psi}{2}\frac{(1-\varsigma)^2}{(1-\eta_\mathrm{o})^2}. \tag{C.26}$$

Even in the closely packed regimes, the temperature ratio is very well approximated by the ideal gas expression. To account for this finding, the temperature ratio can be written directly from the Hugoniot relation (C.18) which, after some manipulation, can be re-written as

$$\frac{T_\mathrm{s}}{T_\mathrm{o}} = \frac{e_\mathrm{s}}{e_\mathrm{o}} = 1 + \frac{1-\varsigma}{(1-\eta_\mathrm{o})^2} + \frac{1}{2}\frac{{u_\mathrm{p}}^2}{e_\mathrm{o}} \tag{C.27}$$

The second term on the right hand side of (C.27), labeled A, is bounded as $u_\mathrm{p} \to \infty$, while the third term, labeled B, grows without bounds as $u_\mathrm{p} \to \infty$, hence dominates the temperature increase across the shock wave. Formally taking the ratio of these two terms yields

$$\frac{A}{B} = \frac{2}{(1-\varsigma)\gamma M^2} \tag{C.28}$$

In the limit of a large shock Mach number, $\varsigma \to \varsigma_\mathrm{max}$ (from (C.21)) and hence $A/B \to 0$. Likewise, this term also vanishes for arbitrary shock Mach numbers when the initial compaction ratio is increased. Indeed, the isentropic exponent increases very rapidly with packing factor, as shown in Figure C.1. Under these conditions, the internal energy and temperature, according to (C.27), are thus incremented by the kinetic energy of the piston, resulting into an equipartition of the available energy into the mean motion (mean kinetic energy of the medium) and thermal energy.

$$\frac{T_\mathrm{s}}{T_\mathrm{o}} = \frac{e_\mathrm{s}}{e_\mathrm{o}} \cong 1 + \frac{1}{2}\frac{{u_\mathrm{p}}^2}{e_\mathrm{o}}. \tag{C.29}$$

This result was also obtained by [13] by neglecting the upstream pressure of an arbitrary medium in the governing equations. Instead, the condition that the term given in (C.28) be small can be considered as the strong shock condition in a hard disk fluid. Generally, it was numerically found that the correction for low Mach numbers is very weak, suggesting that (C.29) serves as a very good approximation for all initial compaction ratios of the medium, ranging from the dilute ideal gas to a solid packed medium of hard disks.

Appendix D

Spacial Properties in System of Disks

This Appendix presents some details regarding spacial properties for a system of disks. The derivations follow what is completed by Bird [38] for spheres.

Mean Particle Spacing

From [38], it is noted that the mean particle spacing is

$$\delta = n^{-1/f}, \tag{D.1}$$

where f is the number of dimensions, and the number density is

$$.n = \frac{N}{A} \tag{D.2}$$

For a system of disks (2D) the spacing is

$$\delta = \left(\frac{N}{A}\right)^{-\frac{1}{2}}, \tag{D.3}$$

which can be combined with the packing fraction of disks

$$\eta = \frac{\pi N d^2}{4A} \tag{D.4}$$

to yield

$$\delta = \left(\frac{4\eta}{\pi d^2}\right)^{1/2} = \frac{\sqrt{\pi} d}{2\sqrt{\eta}}. \tag{D.5}$$

This can also be written as

$$\frac{\delta}{d} = \frac{\sqrt{\pi}}{2\sqrt{\eta}}, \tag{D.6}$$

which is a value that is shown to play an important role in differentiating between dilute and dense gases, and whether continuum assumptions are valid [38].

Standard Deviation for Number Density

The standard deviation for number density in a volume, or area in this case, is given as:

$$\sigma = \frac{1}{\sqrt{nA}}. \tag{D.7}$$

Since $1/\sqrt{n} = \delta$ from (D.1), this can be written as

$$\sigma = \frac{\delta}{\sqrt{A}}. \tag{D.8}$$

Using δ from D.5, yields:

$$\sigma = \frac{d\sqrt{\pi}}{2\sqrt{\eta}\sqrt{A}}, \tag{D.9}$$

or if A is a square with sides dx, the standard deviation is

$$\sigma = \frac{d\sqrt{\pi}}{2\sqrt{\eta} dx}. \tag{D.10}$$

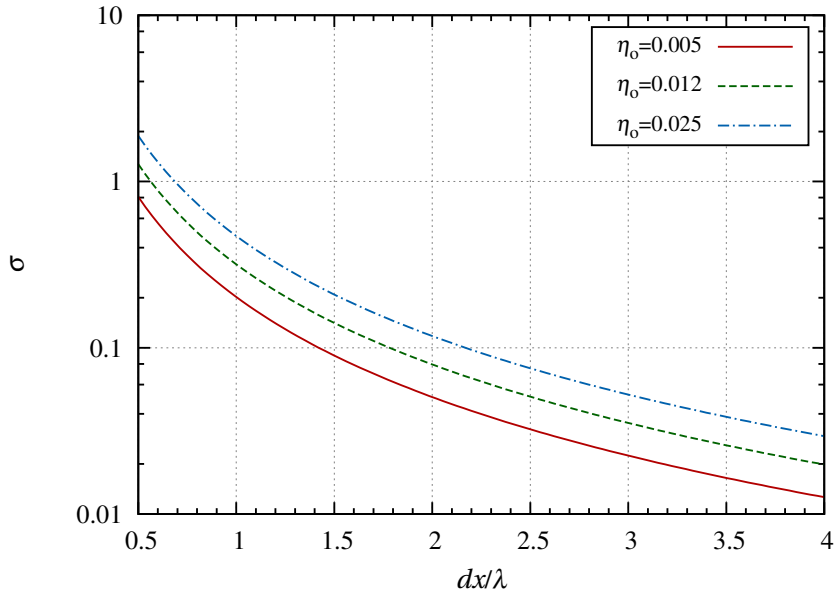

Figure D.1: Standard deviation in number density of disks in a given area $dx \times dx$ for different packing fractions η.

The standard deviation in number density using this relationship for a given area $dx \times dx$ and different packing fractions η is given in Fig. D.1, where dx is normalized by the initial mean free path, as given in Ch. 3:

$$\lambda = \frac{d\sqrt{2}}{4\sqrt{\pi} g_2(\eta)\eta}. \tag{D.11}$$

Bibliography

[1] Heinrich M. Jaeger, Sidney R. Nagel, and Robert P. Behringer. Granular solids, liquids, and gases. *Rev. Mod. Phys.*, 68(94):1259–1273, 1996.

[2] C. Bizon, M. D. Shattuck, J. B. Swift, W. D. McCormick, and Harry L. Swinney. Patterns in 3D vertically oscillated granular layers: Simulation and experiment. *Phys. Rev. Lett.*, 80(1):57–60, 1998.

[3] José A. Carrillo, Thorsten Pöschel, and Clara Salueña. Granular hydrodynamics and pattern formation in vertically oscillated granular disk layers. *J. Fluid Mech.*, 591:199–144, 2008.

[4] J. F. Boudet and H. Kellay. Unstable blast shocks in dilute granular flows. *Phys. Rev. E*, 87, 2013.

[5] Olivier Pouliquen, Jean Delour, and Stuart B. Savage. Fingering in granular flows. *Nature*, 386(6627):816, 1997.

[6] David L. Frost, Yann Gregoire, Oren Petel, Samuel Goroshin, and Fan Zhang. Particle jet formation during explosive dispersal of solid particles. *Phys. Fluids*, 29(9):091109, 2012.

[7] V. Rodriguez, R. Saurel, G. Jourdan, and L. Houas. Solid-particle jet formation under shock-wave acceleration. *Phys. Rev. E*, 88:063011, 2013.

[8] A. Goldshtein, M. Shapiro, and C. Gutfinger. Mechanics of collisional motion of granular materials 3. Self-similar shock wave propagation. *J. Fluid Mech.*, 316:29–51, 1996.

[9] V. Kamenetsky, A. Goldshtein, M. Shapiro, and D. Degani. Evolution of a shock wave in a granular gas. *Phys. Fluids*, 12(11):3036–3049, 2000.

[10] N. Brilliantov and Thorsten Pöschel. *Kinetic theory of granular gases*. Oxford University Press, Oxford, 2004.

[11] Rosa Ramírez, Thorsten Pöschel, Nikolai V. Brilliantov, and Thomas Schwager. Coefficient of restitution of colliding viscoelastic spheres. *Phys. Rev. E*, 60:4465–4472, Oct 1999.

[12] Frank G. Bridges, A. Hatzes, and D.N.C. Lin. Structure, stability and evolution of saturn's rings. *Nature*, 309(5966):333–335, 1984.

[13] Ya. B. Zeldovich and Ya. P. Raizer. *Physics of shock waves and high-temperature hydrodynamic phenomena*. Academic Press, New York, 1966.

[14] J. Grun, J. Stamper, C. Manka, J. Resnick, R. Burris, J. Crawford, and B. H. Ripin. Instability of Taylor-Sedov blast waves propagating through a uniform gas. *Phys. Rev. Lett.*, 66(21):2738–2741, 1991.

[15] I.I. Glass and W. S. Liu. Effects of hydrogen impurities on shock structure and stability in ionizing monatomic gases. 1. argon. *J. Fluid Mech.*, 84:55–77, 1978.

[16] R. W. Griffiths, R. J. Sandeman, and H. G. Hornung. Stability of shock waves in ionizing and dissociating gases. *J. Phys. D Appl. Phys.*, 9(12):1681–1691, 1976.

[17] G. I. Mishin, A. P. Bedin, N. I. Yushchenkova, G. E. Skvortsov, and A. P. Ryazin. Anomalous relaxation and the instability effect of shock waves in gases. *Zhurnal Tekhnicheskoi Fiziki*, 51(11):2315–2324, 1981.

[18] H. G. Hornung and P. Lemieux. Shock layer instability near the Newtonian limit of hypervelocity flows. *Phys. Fluids*, 13(8):2394–2402, 2001.

[19] A. Semenov, M. Berezkina, and I. Krassovskaya. Classification of pseudo-steady shock wave reflection types. *Shock Waves*, 22:307–316, 2012. 10.1007/s00193-012-0373-z.

[20] Wildon Fickett and William Chester Davis. *Detonation: Theory and Experiment*. Dover Publications, Mineola, N.Y., 2000.

[21] Jason W. Bates and David C. Montgomery. The D'Yakov-Kontorovich instability of shock waves in real gases. *Phys. Rev. Lett.*, 84(6):1180–1183, 2000.

[22] L. D. Landau and E. M. Lifshitz. *Fluid Mechanics*. Butterworth-Heinemann, 2nd. edition, 1987.

[23] Martin Brouillette. The Richtmyer-Meshkov Instability. *Annu. Rev. Fluid Mech.*, 34(1):445–468, 2002.

[24] G. Dimonte and P. Ramaprabhu. Simulations and model of the nonlinear Richtmyer-Meshkov instability. *Phys. Fluids*, 22(1):014104, 2010.

[25] M. J. Keskinen, A. L. Velikovich, and A. Schmitt. Multimode evolution of the ablative richtmyer-meshkov and landau-darrieus instability in laser imprint of planar targets. *Phys. Plasmas*, 13(12):122703, 2006.

[26] A. Bezett, V. Bychkov, E. Lundh, D. Kobyakov, and M. Marklund. Magnetic Richtmyer-Meshkov instability in a two-component Bose-Einstein condensate. *Phys. Rev. A*, 82:043608, 2010.

[27] Arkady Petchenko, Vitaly Bychkov, V'yacheslav Akkerman, and Lars-Erik Eriksson. Violent folding of a flame front in a flame-acoustic resonance. *Phys. Rev. Lett.*, 97:164501, 2006.

[28] J. Bougie, Sung Joon Moon, J. B. Swift, and Harry L. Swinney. Shocks in vertically oscillated granular layers. *Phys. Rev. E*, 66:051301, 2002.

[29] M. G. Kapper and J. L. Cambier. Ionizing shocks in argon. Part II: Transient and multi-dimensional effects. *J. Appl. Phys.*, 109(11), 2011.

[30] M. Mond, I. Rutkevich, and E. Toffin. Stability of ionizing shock waves in monatomic gases. *Phys. Rev. E*, 56(5):5968–5978, 1997.

[31] Charles S. Campbell. Rapid granular flows. *Annu. Rev. Fluid Mech.*, 22(1):57–90, 1990.

[32] M. L. Tan and I. Goldhirsch. Rapid granular flows as mesoscopic systems. *Phys. Rev. Lett.*, 81(14):3022, 1998.

[33] I. Goldhirsch. Rapid granular flows. *Annu. Rev. Fluid Mech.*, 35:267–293, 2003.

[34] Thorsten Pöschel, Nikolai V. Brilliantiov, and Thomas Schwager. Long-time behavior of granular gases with impact-velocity dependent coeffcient of restitution. *Physica A*, 325:274–283, 2003.

[35] Goro Kuwabara and Kimitoshi Kono. Restitution coefficient in a collision between two spheres. *Jap. J. Appl. Phys.*, 26(8R):1230, 1987.

[36] E. C. Rericha, C. Bizon, M. D. Shattuck, and H. L. Swinney. Shocks in supersonic sand. *Phys. Rev. Lett.*, 88(1), 2002. doi:10.1103/PhysRevLett.88.014302.

[37] Thorsten Pöschel and Thomas Schwager. *Computational granular dynamics: models and algorithms*. Springer-Verlag, Berlin New York, 2005.

[38] G.A. Bird. *Molecular Gas Dynamics and the Direct Simulation of Gas Flows*. Oxford University Press, Oxford, 1999.

[39] J.T. Jenkins and S.B. Savage. A theory for the rapid flow of identical, smooth, nearly elastic, spherical particles. *J. Fluid Mech.*, 130:187–202, 1983.

[40] J. Jenkins and M. Richman. Kinetic theory for plane flows of a dense gas of identical, rough, inelastic, circular disks. *Phys. Fluids*, 28(12):3485–3494, 1985.

[41] A. Vilquin, J. F. Boudet, and H. Kellay. Structure of velocity distributions in shock waves in granular gases with extension to molecular gases. *Phys. Rev. E*, 94:022905, 2016.

[42] Michael Faraday. On a peculiar class of acoustical figures; and on certain forms assumed by groups of particles upon vibrating elastic surfaces. *Philosophical transactions of the Royal Society of London*, 121:299–340, 1831.

[43] Paul B Umbanhowar, Francisco Melo, and Harry L Swinney. Localized excitations in a vertically vibrated granular layer. *Nature*, 382(6594):793–796, 1996.

[44] J.A.C. Gallas, H.J. Herrmann, and S. Sokołowski. Convection cells in vibrating granular media. *Phys. Rev. Lett.*, 69(9):1371, 1992.

[45] Sean McNamara and Stefan Luding. Energy flows in vibrated granular media. *Phys. Rev. E*, 58(1):813, 1998.

[46] Y-h. Taguchi. New origin of a convective motion: Elastically induced convection in granular materials. *Phys. Rev. Lett.*, 69:1367–1370, 1992.

[47] J. Bougie and K. Duckert. Continuum simulations of shocks and patterns in vertically oscillated granular layers. *Phys. Rev. E*, 83(1):011303, 2011.

[48] C. Bizon, M. D. Shattuck, and J. B. Swift. Linear stability analysis of a vertically oscillated granular layer. *Phys. Rev. E*, 60(6):7210–7216, 1999.

[49] Krishna Kumar and Laurette S Tuckerman. Parametric instability of the interface between two fluids. *J. Fluid Mech.*, 279:49–68, 1994.

[50] Krishna Kumar. Linear theory of faraday instability in viscous liquids. *Proceedings of the Royal Society of London. Series A: Mathematical, Physical and Engineering Sciences*, 452(1948):1113–1126, 1996.

[51] Kolumban Hutter and Thilo Koch. Motion of a granular avalanche in an exponentially curved chute: experiments and theoretical predictions. *Philosophical Transactions of the Royal Society of London. Series A: Physical and Engineering Sciences*, 334(1633):93–138, 1991.

[52] K. Hutter, M. Siegel, S.B. Savage, and Y. Nohguchi. Two-dimensional spreading of a granular avalanche down an inclined plane part i. theory. *Acta Mech.*, 100(1-2):37–68, 1993.

[53] Ralf Greve and Kolumban Hutter. Motion of a granular avalanche in a convex and concave curved chute: experiments and theoretical predictions. *Philosophical Transactions of the Royal Society of London. Series A: Physical and Engineering Sciences*, 342(1666):573–600, 1993.

[54] K. Hutter, T. Koch, C. Pluüss, and SB. Savage. The dynamics of avalanches of granular materials from initiation to runout. Part II. experiments. *Acta Mech.*, 109(1-4):127–165, 1995.

[55] J.M.N.T. Gray and K. Hutter. Pattern formation in granular avalanches. *Continuum Mech. Thermodyn.*, 9(6):341–345, 1997.

[56] Yih-Chin Tai, S. Noelle, J.M.N.T. Gray, and Kolumban Hutter. Shock-capturing and front-tracking methods for granular avalanches. *J. Comp. Phys.*, 175(1):269–301, 2002.

[57] Shiva P. Pudasaini and Christian Kröner. Shock waves in rapid flows of dense granular materials: Theoretical predictions and experimental results. *Phys. Rev. E*, 78(4):041308, 2008.

[58] Azita Soleymani, Piroz Zamankhan, and William Polashenski. Supersonic dense granular materials in a duct flow. *Appl. Phys. Lett.*, 84(22):4409–4411, 2004.

[59] Piroz Zamankhan. Shock waves in dense granular flows down a chute. *Shock Waves*, 17(5):337–349, 2008.

[60] Y. Amarouchene, J. F. Boudet, and H. Kellay. Dynamic sand dunes. *Phys. Rev. Lett.*, 86:4286–4289, 2001.

[61] Yacine Amarouchene and Hamid Kellay. Speed of sound from shock fronts in granular flows. *Phys. Fluids*, 18:031707, 2006.

[62] F. Zhang, D.L. Frost, P.A. Thibault, and S.B. Murray. Explosive dispersal of solid particles. *Shock Waves*, 10(6):431–443, 2001.

[63] J.H. Geng, A. van de Ven, Q. Yu, F. Zhang, and H. Grnig. Interaction of a shock wave with a two-phase interface. *Shock Waves*, 3(3):193–199, 1994.

[64] Robert Ripley, Laura Donahue, and Fan Zhang. Jetting instabilities of particles from explosive dispersal. *AIP Conf. Proc.*, 1426:1615, 2012.

[65] Kun Xue, Fangfang Li, and Chunhua Bai. Explosively driven fragmentation of granular materials. *Eur. Phys. J. D*, 36(8):1–16, 2013.

[66] L.T. Zhang, H.H. Shi, C. Wang, R.L. Dong, H.X. Jia, X.N. Zhang, and S.Y. Yue. Aerodynamic characteristics of solid particles acceleration by shock waves. *Shock Waves*, 21(3):243–252, 2011.

[67] M. Kellenberger, C. Johansen, G. Ciccarelli, and F. Zhang. Dense particle cloud dispersion by a shock wave. *Shock Waves*, 23(5):415–430, 2013.

[68] V. Rodriguez, R. Saurel, G. Jourdan, and L. Houas. External front instabilities induced by a shocked particle ring. *Phys. Rev. E*, 90:043013, 2014.

[69] B. J. Alder and T. E. Wainwright. Phase transition for a hard sphere system. *J. Chem. Phys.*, 27(5):1208–1209, 1957.

[70] B. J. Alder and T. E. Wainwright. Studies in molecular dynamics. 1. General method. *J. Chem. Phys.*, 31(2):459–466, 1959.

[71] Alexander Goldshtein and Michael Shapiro. Mechanics of collisional motion of granular materials. part 1. general hydrodynamic equations. *J. Fluid Mech.*, 282:75–114, 1995.

[72] S. Torquato. Nearest-neighbor statistics for packings of hard spheres and disks. *Phys. Rev. E*, 51:3170–3182, 1995.

[73] V Garzó and J.W. Dufty. Dense fluid transport for inelastic hard spheres. *Phys. Rev. E*, 59(5):5895, 1999.

[74] James F. Lutsko. Transport properties of dense dissipative hard-sphere fluids for arbitrary energy loss models. *Phys. Rev. E*, 72(2):021306, 2005.

[75] Lidia Almazán, Clara Salueña, Vicente Garzó, José A. Carrillo, Thorsten Pöschel, Michel Mareschal, and Andrés Santos. Hydrodynamics at the navier-stokes level applied to fast, transient, supersonic granular flows. In *AIP Conference Proceedings-American Institute of Physics*, volume 1501, page 993, 2012.

[76] E. Helfand, H. L. Frisch, and J. L. Lebowitz. Theory of two- and one-dimensional rigid sphere fluids. *J. Chem. Phys.*, 34(3):1037–1042, 1961.

[77] M. Maeso, J. Solana, J. Amoros, and E. Villar. Equations of state for d-dimensional hard sphere fluids. *Material Chemistry and Physics*, 30:39–42, 1991.

[78] A Mulero, C. A. Galan, M. I. Parra, and F. Cuadros. Equations of state for hard spheres and hard disks. *Lect. Notes Phys.*, 753:37–109, 2008.

[79] Nick Sirmas, Marian Tudorache, Javier Barahona, and Matei Ioan Radulescu. Shock waves in hard disk fluids. *Shock Waves*, 22(3):237–247, 2012.

[80] S.A.E.G. Falle. Self-similar jets. *Mon. Not. R. Astron. Soc.*, 250(3):581–596, 1991.

[81] S.A.E.G. Falle and S.S. Komissarov. An upwind numerical scheme for relativistic hydrodynamics with a general equation of state. *Mon. Not. R. Astron. Soc.*, 278(2):586–602, 1996.

[82] Walter Guido Vincenti and Charles H. Kruger. *Introduction to Physical Gas Dynamics*. Krieger, 1975.

[83] Peter P. Mitrano, Steven R. Dahl, Daniel J. Cromer, Michael S. Pacella, and Christine M. Hrenya. Instabilities in the homogeneous cooling of a granular gas: A quantitative assessment of kinetic-theory predictions. *Phys. Fluids*, 23(9):093303, 2011.

[84] Mark Short and D Scott Stewart. Cellular detonation stability. part 1. a normal-mode linear analysis. *J. Fluid Mech.*, 368:229–262, 1998.

[85] N. Sirmas and M. I. Radulescu. Evolution and stability of shock waves in dissipative gases characterized by activated inelastic collisions. *Phys. Rev. E*, 91:023003, 2015.

[86] Mohamed Gad-el Hak. *The MEMS handbook*. CRC press, 2001.

[87] I. Goldhirsch and G. Zanetti. Clustering instability in dissipative gases. *Phys. Rev. Lett.*, 70(11):1619–1622, 1993.

[88] J Javier Brey, P Maynar, and MI Garcia De Soria. Fluctuating hydrodynamics for dilute granular gases. *Phys. Rev. E*, 79(5):051305, 2009.

[89] J. Javier Brey, P. Maynar, and M.I. García de Soria. Fluctuating navier-stokes equations for inelastic hard spheres or disks. *Phys. Rev. E*, 83(4):041303, 2011.

[90] Sanjiva K Lele. Compressibility effects on turbulence. *Annu. Rev. Fluid Mech.*, 26(1):211–254, 1994.

[91] Peter Bradshaw. Compressible turbulent shear layers. *Annu. Rev. Fluid Mech.*, 9(1):33–52, 1977.